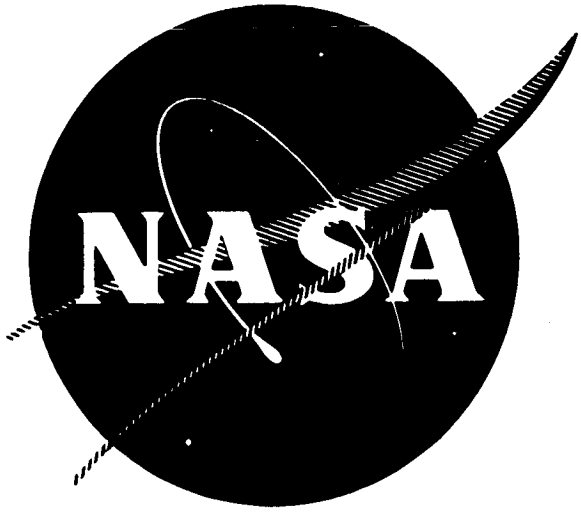

REPORT NO.
NASA-CR-54358
WESTINGHOUSE
WAED 66.33E
MARCH 1966

DEVELOPMENT AND EVALUATION OF MAGNETIC AND ELECTRICAL MATERIALS CAPABLE OF OPERATING IN THE 800° TO 1600°F TEMPERATURE RANGE

Fifth Quarterly Report

edited by

P. E. Kueser et al

prepared for

NATIONAL AERONAUTICS AND SPACE ADMINISTRATION
LEWIS RESEARCH CENTER
UNDER CONTRACT NAS3-6465

Westinghouse Electric Corporation
AEROSPACE ELECTRICAL DIVISION
LIMA, OHIO

NOTICE

This report was prepared as an account of Government-sponsored work. Neither the United States nor the National Aeronautics and Space Administration (NASA), nor any person acting on behalf of NASA:

A) Makes any warranty or representation, expressed or implied, with respect to the accuracy, completeness, or usefulness of the information contained in this report, or that the use of any information, apparatus, method, or process disclosed in this report may not infringe privately-owned rights; or

B) Assumes any liabilities with respect to the use of, or for damages resulting from the use of any information, apparatus, method or process disclosed in this report.

As used above, "person acting on behalf of NASA" includes any employee or contractor of NASA, or employee of such contractor, to the extent that such employee or contractor of NASA or employee of such contractor prepares, disseminates, or provides access to, any information pursuant to his employment or contract with NASA, or his employment with such contractor.

AVAILABILITY NOTICE

Qualified requestors may obtain copies of this report from:

National Aeronautics and Space Administration
Office of Scientific and Technical Information
Washington 25, D.C.
Attn: AFSS-A

Report No. 66.33E

9 March 1966

DEVELOPMENT AND EVALUATION OF MAGNETIC AND ELECTRICAL MATERIALS CAPABLE OF OPERATING IN THE 800° TO 1600°F TEMPERATURE RANGE

FIFTH QUARTERLY REPORT
(DECEMBER 1, 1965 - FEBRUARY 28, 1966)

sponsored by

NATIONAL AERONAUTICS AND SPACE ADMINISTRATION
CONTRACT NAS 3-6465

Project Management
NASA - Lewis Research Center
Space Power Systems Division
R. A. Lindberg

Prepared by:

P. E. Kueser, et al
Manager, NASA Materials Study
and Research Program

Approved by:

N. W. Bucci, Jr.
Manager, Engineering
Systems Research and
Development Department

Westinghouse Electric Corporation
Aerospace Electrical Division
Lima, Ohio

PREFACE

The work reported here was sponsored by the Space Power Systems Division of the NASA Lewis Research Center under Contract NAS 3-6465. Mr. R. A. Lindberg of NASA has provided the Project Management for the program. His review and suggestions as well as those of Mr. T. A. Moss, also of NASA, are gratefully acknowledged. The Westinghouse Aerospace Electrical Division (WAED) is responsible for the over-all Technical Direction of the program. The Westinghouse Research and Development Center (WR & D) is conducting Tasks 1, 2, and 4 of Program I on Optimized Magnetic Materials for Application in the 1000 to 1200°F Range, the Investigation for Raising the Alpha to Gamma Transformation, and Creep Testing of Rotor Materials. Eitel-McCullough (EIMAC) is responsible for the Bore Seal Development, Task 1 of Program III. All other tasks are being conducted at the Westinghouse Aerospace Electrical Division (WAED).

In a program of this magnitude a large group of engineers and scientists are involved in its progress. An attempt to recognize those who are contributing directly, together with their area of endeavor, follows:

Program I - Magnetic Materials for High-Temperature Operation

Task 1 - Optimized Precipitation Hardened Magnetic Materials for Application in the 1000 to 1200°F Range

Dr. K. Detert (WR & D); J. W. Toth (WAED)

Task 2 - Investigation for Raising the Alpha to Gamma Transformation Temperature in Cobalt-Iron Alloys

Dr. K. Detert (WR & D); J. W. Toth (WAED)

Task 3 - Dispersion-Strengthened Magnetic Materials for Application in the 1200 to 1600°F Range

Dr. R. J. Towner (WAED)

Task 4 - Creep Testing

M. Spewock (WR & D); D. H. Lane (WAED)

Program II - High Temperature Capacitor Feasibility

R. E. Stapleton (WAED)

Program III - Bore Seal Development and Combined Material Investigation Under a Space Simulated Environment

Task 1 - Bore Seal Development

R. C. McRae, Dr. L. Reed (EIMAC); J. W. Toth (WAED)

Tasks 2, 3, 4 - Stator and Bore Seal, Transformer and Solenoid

W. L. Grant, H. E. Keneipp, D. H. Lane, R. P. Shumate J. W. Toth (WAED)

Dr. A. C. Beiler (WAED) and Dr. G. W. Wiener (WR & D) are acting as consultants on Program I.

SUMMARY

This is the fifth quarterly report on Contract NAS 3-6465 for the Development and Evaluation of Magnetic and Electrical Materials capable of Operating in the Temperature Range from 800 to 1600°F. Advance Space Electric Power Systems are the area of eventual application.

Program I is directed at the development of high-temperature magnetic materials with satisfactory strength for use in the solid rotors of electrical generators. Two strengthening mechanisms are being studied to develop better magnetic materials. These are precipitation-hardening in the range from 800 to 1200°F and dispersion strengthening from 1200 to 1600°F. In the precipitation-hardening area, both martensitic alloys and cobalt-base alloys are being evaluated. The best martensitic alloys which have both adequate strength and magnetic properties has the following basic composition: iron; nickel, 10 to 15 weight percent; cobalt, 20 to 30 weight percent (1 weight percent chromium may replace 2 weight percent nickel up to a total of 5 weight percent chromium). Additions to this base composition to obtain hardening include: tantalum, 3 to 4 weight percent; tungsten, 0 to 2 weight percent; aluminum, 0.5 weight percent; titanium, 0.5 weight percent.

The cobalt-type base composition has: cobalt; nickel, 10 to 15 weight percent; iron, 5 weight percent. Additions to this base composition to achieve the gamma prime hardening include: Aluminum, 1.0 to 1.5 weight percent; tantalum, 2 to 4 weight percent; and zirconium, 0.3 weight percent. In the early screening phases of the dispersion-strengthened magnetic material program, the composition observed with the highest strength in the 1200 to 1600°F range was Co + 1.1 w/o B + 4.4w/o Cb. It was hot extruded from the prealloyed atomized powders. The material was strengthened by the tau ($Cr_{23}C_6$ structure) ternary boride compound. While the dispersion-strengthening of iron-27% cobalt-base materials provide better magnetic properties than cobalt-base materials, the tensile strength of these materials is less than the cobalt type. Creep testing has continued on Nivco alloy and one sample has achieved 4122 hours at 1100°F and the environmental pressure is 2.6×10^{-9} torr. The applied stress is 37,500 psi and the present elongation is 0.44 percent.

Program II will determine the feasibility of high-temperature capacitors using high-quality dielectric materials. A pyrolytic boron-nitride capacitor has several orders of magnitude better RC product than teflon, mica, mylar,

and vitreous enamel capacitors. It also has shown the best stability represented by the least change in capacitance over the temperature range from room temperature to 1100°F.

Program III incorporates developments on alkali-metal compatible ceramic-to-metal seals and combinations of materials designed into a stator and a bore seal, transformer, and the solenoid for investigations of compatibility under electrical and magnetic stress at elevated temperature and under high vacuum. Bend tests on Cb-1Zr joined to beryllia ceramics by the active-metal braze, 60Zr-25V-15Cb, retained flexural strengths of greater than 15,000 psi after 500 hour exposure at 1600°F in potassium. This braze system also has a ductility greater than any other active-metal braze system tested to date as determined by the tab peel tests which are an indication of it's notch sensitivity. The stator, transformer, and solenoid test vehicles, which will provide data on the stability of materials applied to typical electrical designs, continued their test program. No degradation has been noted in either the electrical conductivity of the conductor systems or in the electrical insulation systems selected. The stator has achieved 2032 hours at 1100°F and is operating at an environmental pressure of 1.4×10^{-8} torr. The transformer and solenoid have achieved 1800 hours at 1100°F and are operating at a pressure of 4.8×10^{-8} torr.

TABLE OF CONTENTS

TABLE OF CONTENTS - Continued

TABLE OF CONTENTS - Concluded

LIST OF FIGURES

LIST OF FIGURES - Continued

LIST OF FIGURES - Continued

LIST OF FIGURES - Continued

LIST OF FIGURES - Continued

LIST OF FIGURES - Continued

LIST OF FIGURES - Continued

LIST OF FIGURES - Concluded

LIST OF TABLES

LIST OF TABLES - Continued

LIST OF TABLES - Concluded

SECTION I

INTRODUCTION

This is the fifth quarterly report on Contract NAS 3-6465 for the Development and Evaluation of Magnetic and Electrical Materials Capable of Operating in the Temperature Range from 800 to 1600°F. The period of performance is from December 1, 1965 through February 28, 1966. The program consists of three Programs with their related tasks as follows:

Program I - Magnetic Materials for High-Temperature Operation

- Task 1 - Optimized Precipitation Hardened Magnetic Materials for Application in the 1000 to 1200°F Range
- Task 2 - Investigation for Raising the Alpha to Gamma Transformation Temperature in Cobalt-Iron Alloys (completed)
- Task 3 - Dispersion-Strengthened Magnetic Materials for Application in the 1200 to 1600°F Range
- Task 4 - Creep Testing

Program II - High-Temperature Capacitor Feasibility

Program III - Bore Seal Development and Combined Material Investigation Under a Space Simulated Environment

- Task 1 - Bore Seal Development
- Task 2 - Stator and Bore Seal
- Task 3 - Transformer
- Task 4 - Solenoid

In Program I, limitations in magnetic material performance at elevated temperature have been recognized from Contract NAS 3-4162 and the development of materials incorporating improved magnetic and mechanical properties is being pursued. In most cases, high-strength compromises the magnetic properties; therefore, a balance between these two variables is sought.

Program II is directed at determining the feasibility of applying high-quality dielectric materials and their processes to a high-temperature (1100°F) capacitor which is lightweight and suitable for static power conditioning apparatus used in space applications.

Program III incorporates development on ceramic-to-metal seals and on combinations of materials previously evaluated under Contract NAS 3-4162 into a stator with a bore seal, a transformer, and a solenoid for investigations of compatibility under electrical and magnetic stress at elevated temperature and high vacuum.

The three programs will be reported consecutively in Sections II, III, and IV. Section II and Section IV are further divided into their respective tasks. Each task is reported separately and includes a summary of technical progress, a discussion, and the program for the next quarter so the reader may obtain an understanding of each task.

The first, second, third, and fourth quarterly reports were issued as NASA-CR-54354, 55, 56, and 57 respectively. These reports are extensively referenced in this report and fully titled in Section V. Other references identified by number in the discussion of each task are contained in Section V. These are identified in Section V by the program and task for which the reference is applicable.

SECTION II

PROGRAM I - MAGNETIC MATERIALS FOR HIGH-TEMPERATURE OPERATION

Program I is directed at improvement and further understanding of magnetic materials suitable for application in the rotor of a generator or motor in advanced space electric power systems.

Task 1 is concerned with precipitation-hardened magnetic materials in the 1000 to 1200°F range. These materials are of the iron-cobalt-nickel ternary system. The two specific areas of interest are the iron and cobalt corners of the ternary system.

Task 2 is a small research investigation for determining the feasibility of raising the alpha to gamma transformation temperature in the iron-cobalt system; thereby increasing the useful magnetic temperature of this system. This investigation is completed and the final results were given in the third quarterly report. Selected alloy additions of 3 to 5 weight percent increased the transformation temperature approximately 9°F (5°C) for each weight percent added. Magnetic saturation was lowered by each addition. If only a 45°F increase in alpha to gamma transformation temperature is desired, at a slight sacrifice in magnetic saturation, several alloying agents are satisfactory.

Task 3 is directed at applying dispersion-strengthening mechanisms to magnetic materials to achieve useful and stable mechanical and magnetic properties in the 1200 to 1600°F range. Because both variables are influenced differently by particle size and spacing, a compromise is sought thereby tailoring the materials to the need of dynamic electric machines.

Task 4 is a creep program on Nivco alloy (approximately 72 percent cobalt, 23 percent nickel and certain other elements) which will generate 10,000-hour design data in a vacuum environment (1×10^{-6} torr or less). This material represents a presently available magnetic material with the highest useful application temperature for stressed applications.

A. TASK 1 - OPTIMIZED PRECIPITATION HARDENED MAGNETIC MATERIALS FOR APPLICATION IN THE 1000 TO 1200°F RANGE

1. Summary of Technical Progress

a) Fourteen additional alloys were tested in the screening program - nine alloys of the martensitic and five of the cobalt-base type, bringing the total number tested to date to 107 alloys. The alloys were melted by the levitation melting technique.

b) Dilatometer tests, magnetic saturation measurements, and aging tests, with hardness and coercivity measurements, were conducted. Observations of microstructure were made by means of optical and electron microscopy.

c) Promising alloy compositions within narrow range limits have been determined. For the martensitic type alloys the basic composition is iron; nickel, 10 to 15 weight percent; and cobalt, 20 to 30 weight percent (1 weight percent chromium may replace 2 weight percent nickel, up to a total of 5 weight percent chromium). Additions to the base composition to obtain hardening include tantalum, 3 to 4 weight percent; tungsten, 0 to 2 weight percent; aluminum, 0.5 weight percent; and titanium, 0.5 weight percent.

The cobalt-type base composition is cobalt; nickel, 10 to 15 weight percent; and iron, 5 weight percent. Additions to the base composition to obtain hardening include aluminum, 1.0 to 1.5 weight percent; tantalum, 2 to 4 weight percent; and zirconium, 0.3 weight percent. Six alloys of the martensitic type and six of the cobalt-base type with the above listed composition ranges were melted by the vacuum arc non-consumable tungsten electrode method and have been processed by hot and cold rolling. Mechanical and electrical tests have been started.

2. Discussion

The objective of this program is to find and evaluate an alloy composition which displays high-creep strength at elevated temperature

as well as useful ferromagnetic properties. The target tensile strength for the alloy at 1100°F is 125,000 psi or better. The target stress to produce 0.4 percent creep strain in 1000 hours at 1100°F is 76,000 psi or greater. The 10,000-hour stress target for 0.4 percent total creep strain at 1100°F is 80 to 90 percent of that at 1000 hours. The target magnetic saturation for the developmental alloy is 13,000 gauss or better at 1100°F and a coercive force less than 25 oersteds. A screening program of a variety of alloy compositions, now in progress was the first step in attaining this goal.

The purpose of the screening program is to find a certain region of alloy composition where an optimum combination of high strength and magnetic saturation, low coercivity, and stability of structure during exposure at temperature can be attained. Hardness tests, coercivity measurements and saturation measurements, after a suitable heat treatment, and dilatometer tests were conducted to provide the data for the properties and thermal stability of the structure. Details on the test methods were reported in the first and second quarterly reports.

As an additional step in the screening program, six alloys of the martensitic type and six of the cobalt-base type were prepared in a larger button size of ~ 300 grams. Testing of these alloys shall confirm the results of the screening program, define the suitable range of alloy composition within narrow limits, and extend the measurements of mechanical and magnetic measurements.

a. EXPERIMENTAL PROCEDURE

Martensitic alloys 1-A-53 to 1-A-61 (Table II-1) and the cobalt-base alloys 1-B-42 to 1-B-46 (Table II-2) were studied during this report period. As a result of the work cited in the fourth quarterly report, the combination of Ta + Al + Ti + Si was investigated in alloy 1-A-53. The combinations of Ta + Si, Ta + Al + Ti, and Ta + W, which have exhibited a beneficial influence on the structural stability of Fe-15Ni-25Co, were applied to the Fe-12Ni-25Co base in alloys 1-A-54, 1-A-55, and 1-A-57.

The influence of the combination of Mo + Ti + Al, present in commercial 15 percent nickel maraging steel, was tested with the base Fe-12Ni-25Co (alloy 1-A-56). The combinations of Ta + W + Si, Ta + Si + Al + Ti, and Ta + W + Si + Al + Ti were also applied to the Fe-12Ni-25Co base in alloys 1-A-58, 1-A-59, and 1-A-60 respectively. The combination of Ta + Al + Si was applied to the Fe-5Ni-25Co base in alloy 1-A-61. One-tenth

TABLE II-1. Nominal Composition of Levitation Melted Martensitic Alloys 1-A-53 to 1-A-61

Alloy Number	Nominal Alloy Composition (weight percent)
1-A-53	54.9Fe-15Ni-25Co-3Ta-1Si-0.5Al-0.5Ti-0.1Mn
1-A-54	55.9Fe-12Ni-25Co-5Ta-2Si-0.1Mn
1-A-55	57Fe-12Ni-25Co-5Ta-0.5Ti-0.5Al
1-A-56	57Fe-12Ni-25Co-5Mo-0.5Ti-0.5Al
1-A-57	56Fe-12Ni-25Co-5Ta-2W
1-A-58	55.9Fe-12Ni-25Co-4Ta-2W-1Si-0.1Mn
1-A-59	55.9Fe-12Ni-25Co-3Ta-2W-1Si-0.5Al-0.5Ti-0.1Mn
1-A-60	55.9Fe-12Ni-25Co-4Ta-2Si-0.5Al-0.5Ti-0.1Mn
1-A-61	57.4Fe-5Ni-25Co-5Cr-5Ta-0.5Al-0.1Mn-2Si

TABLE II-2. Nominal Composition of Levitation Melted Cobalt-Base Alloys 1-B-42 to 1-B-46

Alloy Number	Nominal Alloy Composition (weight percent)
1-B-42	70.8Co-15Ni-5Fe-2.2Ti-1.5Al-0.5Zr-5Nb
1-B-43	71Co-15Ni-5Fe-2.2Ti-1.5Al-0.3Zr-5Ta
1-B-44	73Co-15Ni-5Fe-2.2Ti-1.5Al-0.3Zr-3Ta
1-B-45	71.7Co-15Ni-5Fe-1.5Ti-1.5Al-0.3Zr-5Ta
1-B-46	76Co-10Ni-5Fe-2.2Ti-1.5Al-0.3Zr-5Ta

percent manganese was added to all alloys containing silicon to improve the ductility.

Cobalt alloy 1-B-42 was formulated to determine the influence of niobium on a composition based on alloy series 1-B-32 to 1-B-41. Data on this series were reported in the fourth quarterly report. The other cobalt base alloys in the current series were modifications of alloy 1-B-39 (see fourth quarterly report). The effect of a reduction of the added elements on the gain in magnetic saturation and the sacrifice in VHN hardness was determined.

Based on the results obtained in these studies six cobalt alloys and six martensitic alloys (Tables II-3 and II-4) were selected for melting as larger buttons in a subsequent screening step in the program.

The experimental alloys were melted in the form of 20 gram ingots by the levitation melting technique as described in detail in the second quarterly report. Small pieces of the added elements were wrapped in nickel or cobalt foil and inserted into a compaction of pure metal chips to form the alloy during melting. Melting and pouring was accomplished in an argon atmosphere at a reduced pressure.

Specimens for magnetic saturation measurements and dilatometer tests on the martensitic alloys were machined from the tapered, bar-shaped ingots. The magnetic saturation specimens were 1/10 inch in diameter, 1/10 inch high and weighed approximately 1/10 gram. The dilatometer specimens were 1/4 inch in diameter and 1 inch long. Magnetic saturation specimens and 1/4 inch diameter bars were machined from the cobalt alloy ingots.

Detailed description of the saturation measurements and dilatometer tests were presented in the first quarterly report. The Vickers hardness tests and coercivity measurements performed on alloy samples were described in the second quarterly report.

For the aging treatments, the round sample bars were rolled down to 95 mil thick strip. The martensitic specimens were annealed for one hour at 1922°F (1050°C) in a helium-flushed tube furnace, then quenched in oil. Before cold rolling the martensitic alloys were warmed for about 30 seconds at 200°F. Cold roll-

TABLE II-3. Nominal Composition of Vacuum Arc Melted Buttons of Martensitic Alloys 1-A-V-1 to 1-A-V-6

Alloy Number	Nominal Alloy Composition (weight percent)
1-A-V-1	48Fe-15Ni-30Co-2W-4Ta-0.5Al-0.5Ti
1-A-V-2	66Fe-10Ni-20Co-3Ta-0.5Al-0.5Ti
1-A-V-3	57.5Fe-12Ni-25Co-1W-3.5Ta-0.5Al-0.5Ti
1-A-V-4	51Fe-15Ni-30Co-3Ta-0.5Al-0.5Ti
1-A-V-5	49Fe-15Ni-30Co-2W-3Ta-0.5Al-0.5Ti
1-A-V-6	60Fe-5Ni-5Cr-25Co-1W-3Ta-0.5Al-0.5Ti

TABLE II-4. Nominal Composition of Vacuum Arc Melted Buttons of Cobalt-Base Alloys 1-B-V-1 to 1-B-V-6

Alloy Number	Nominal Alloy Composition (weight percent)
1-B-V-1	71.7Co-5Fe-15Ni-1.5Ti-1.5Al-0.3Zr-5Ta
1-B-V-2	80.5Co-5Fe-10Ni-1.2Al-0.3Zr-3Ta
1-B-V-3	76.3Co-5Fe-12Ni-1.0Ti-1.4Al-0.3Zr-4Ta
1-B-V-4	73.5Co-5Fe-15Ni-1.2Al-0.3Zr-5Ta
1-B-V-5	78.2Co-5Fe-10Ni-1.5Al-0.3Zr-5Ta
1-B-V-6	74Co-5Fe-15Ni-1.5Ti-1.2Al-0.3Zr-3Ta

ing was done as described in the second quarterly report. Cold rolling of martensitic alloys 1-A-54 and 1-A-60 was unsuccessful. Both samples broke into pieces. Alloy 1-A-61 developed extensive cracks during rolling. All other martensitic alloys were rolled successfully. The cobalt-base alloys were annealed for one hour at 2012°F (1100°C), then quenched in oil and successfully cold rolled.

After cold rolling, the sheet samples were subjected to a series of heat treatments as reported in the second quarterly report.

A summary of the treatments is included in this discussion. After annealing for 30 minutes at 1832°F (1000°C) in an argon flushed tube furnace, the samples were aged for one hour at temperatures successively increased in steps of 90°F (50°C) to obtain the isochronal curve of property change at different temperatures. After a homogenization treatment which consisted of two anneals and a slight deformation between anneals, an isothermal aging treatment was applied. The martensitic alloys were aged up to 100 hours at 1022°F (550°C). The cobalt-base alloys were aged at 1292°F (700°C). The measurements of property changes such as hardness and coercivity were always made at room temperature, thus interrupting the aging treatment to perform the measurements.

Samples for optical metallography were prepared in the manner described in the second quarterly report. The martensitic alloys were mechanically polished, then etched electrolytically in 10 percent chromic acid. The cobalt-base alloys were etched in a solution of 20 parts HCl, 40 parts HNO_3 and 60 parts glycerin. Electron microscopic studies of alloys 1-A-26, 1-A-27, and 1-A-28 have been completed. Electron transmission micrographs and replicas were taken to study the microstructure and nature of the precipitate phases.

The following methods of sample preparation were used: Extraction replicas were made by first etching the polished surfaces in two percent nital. Then a 500 Å thick layer of carbon was vapor-deposited on the etched surface. The carbon film and the attached particles were released by re-etching in two percent nital solution.

Thin foils, suitable for observation by transmission electron microscopy were prepared in the following way: Random pieces

from each specimen were ground to a thickness of 25 mils on water cooled grit grinding paper. The resulting sheet specimens were then electropolished in a 10 percent solution of perchloric acid in acetic acid at a cell voltage of 30V and a current density of 0.8 A/cm^2 using the Bollman geometry. Electropolishing was continued until the sample attained a uniform thickness of five mils. Small discs, 1/8 inch in diameter, were then punched out on a hollow-ground grid punch. These discs were then inserted in a twin-jet electropolishing unit described by R. C. Glenn and R. O. Schoone (ref. 1). An electrolyte consisting of 810ml acetic acid, 150g chromium oxide and 42ml water, operating at a cell voltage of 100V with a resultant current density of 0.5 A/cm^2, was found optimum for all alloys in this investigation. Electropolishing was continued until the first hole was detected in the specimen. It was then washed in methyl alcohol and mounted in a double-tilting specimen holder for observation in the electron microscope.

The preparation of a deformed and aged sample of alloy 1-A-39 was similar to that used in the preparation of deformed sample of alloy 1-B-15 described in the third quarterly report. The polished samples were etched in a 20 percent solution of H_3PO_4 in water at a current density of 30 mA/cm^2. A 500 Å thick carbon layer was vapor deposited on the etched surface. The sample was etched electrolytically again in the same solution after the carbon film, with adhering precipitate particles, was stripped from the etched surface. The Siemens Elmiscope was used for the electron microscopic examination. An accelerating voltage of 100 kV was used for the transmission of the thin-metal foils and the carbon replicas. A voltage of 50 kV was applied for electron diffraction studies.

In some cases, the electron microprobe was used to obtain a qualitative estimate of the precipitate composition. A scanning ARL electron-probe X-ray micro analyzer was used at an accellerating voltage of 30 kV.

b. PREPARATION OF VACUUM-ARC MELTED BUTTONS

For the next stage of the screening program, 300-gram buttons of alloys 1-A-V-1 through 1-A-V-6 and 1-B-V-1 through 1-B-V-6 were prepared. Buttons were melted in a vacuum arc furnace with nonconsumable tungsten electrodes. Small pieces of the metals and master alloys were placed in copper crucibles. All of the

minor additions were added as master alloys. Table II-5 lists the metal and master alloy suppliers and the supplied material analyses.

The vacuum-arc furnace contained a turntable with six copper molds which were about three inches in diameter. These served simultaneously as crucibles for vacuum-arc melting. The furnace was evacuated to a pressure of less than 1×10^{-4} torr and then back-filled with 99.995 percent pure argon to a pressure of ~450 torr and evacuated again. The furnace was back-filled three times in this manner and evacuated to less than 1×10^{-4} torr. Finally, the furnace was back-filled with helium to a pressure of ~200 torr. The first alloy button was melted in about three minutes. The arc current was approximately 600 amps and the operating voltage was 30 volts. After melting six buttons, the furnace was opened and the buttons were turned upside down. The procudure of evacuating and back-filling was repeated and the buttons were re-melted. In general, the alloy buttons were re-melted twice. In a few cases when the bottom of the button did not appear smooth, the buttons were re-melted a third time. The three-inch diameter by 400 mil thick buttons were then cleaned. The martensitic alloys were heated for 30 minutes at 1922°F (1050°C), then hot rolled in three passes to a thickness of ~150 mils. After each pass the slabs were put into the furnace for 15 minutes. After hot rolling, the slabs were sandblasted, then cold rolled to 65 mil sheet.

Alloy 1-A-V-2 developed a few cracks during cold rolling. All other alloy samples were successfully rolled down.

The cobalt-base alloys were heated to 2012°F (1100°C) and soaked for one hour then hot rolled in three passes to 140 mils. After each pass the slabs were heated in the furnace for 15 minutes. After hot rolling, the slabs were reheated for 15 minutes at 2012°F (1100°C) and cooled in air. The slabs were then sandblasted and cold rolled to 65 mil sheet.

Samples for saturation measurements were machined from the hot-rolled slabs. One inch by 1/4 inch wide samples for hardness tests and coercive force measurements were made from the cold-rolled sheets. The annealing and aging of these samples were performed in the same manner as the levitation melts.

TABLE II-5. Composition of Master Alloys Used in the 300 Gram Button Melts (weight percent)[a]

Material Designation	Supplier	Fe	Co	Ni	Ta	Cr	Ti	W	Al	Si	Mn	Cu	P	C	Other
Electrolytic 99.9 Iron	The Gidden Co.	99.9	0.002	0.005			0.001		0.003	0.001	0.001	0.001	0.003	0.004	S -0.004 V -0.005 Be -0.0005
Electrolytic 99.61 Cobalt	International Nickel Co.	0.0015	99.61	0.35								0.005		0.016	S -0.001 Pb -0.00026
Electrolytic 99.95 Nickel	International Nickel Co.	0.04		99.95						Trace		0.03		Trace	S -Trace
Nickel-Tantalum	Union Carbide Corp.	0.15		48.06	51.56				0.40	0.07	0.01			0.01	Nb -0.08
Low Carbon Ferrochrome	Union Carbide Corp.					72.53				0.23				0.019	
Ferrotitanium	Union Carbide Corp.	30.2[b]					65.97		3.68	0.04				0.05	
UCAR Ferro-tungsten	Union Carbide Corp.	20.0[b]						79.84		0.02	0.05	0.02	<0.01	0.04	P -0.01 Sn -<0.01
Nickel Aluminum	Reading Alloys Inc.	0.47		71.11					27.58	0.41					

(a) Analyses reported by supplier

(b) By Difference

c. RESULTS

(1) Workability

The fact that the alloy 1-A-54 and 1-A-60 broke into pieces during cold rolling indicates that addition of silicon may lead to severe embrittling. Similar behavior of silicon was found in the previous studies.

(2) Dilatometer Tests

The transformation temperatures of alloy samples 1-A-53 to 1-A-61, as determined by dilatometer tests, are shown in Table II-6. One test of each sample was made at a high cooling and heating rate of 90°F/min (50°C/min). Another test was made at a very slow heating rate of 0.9°F/min (0.5°C/min) and a slow cooling rate of 9°F/min (5°C/min). The beginning and end of a noticeable deviation in the slope of the thermal expansion curve is listed in Table II-6 as the beginning and end of the transformation.

All of the martensitic alloys showed that the beginning of transformation into gamma phase during slow heating occurred at a temperature higher than 1202°F (650°C), indicating that sufficient stability of the alpha phase can be expected.

(3) Magnetic Saturation

The results of the saturation measurements on the levitation melted alloys are shown in Tables II-7 and II-8. The values measured at room temperature after annealing and the values measured at room temperature and at 1112°F (600°C) after aging are listed in these tables. All samples of the martensitic alloys were annealed for one hour at 1832°F (1000°C) and aged for one hour at 1112°F (600°C). The cobalt-base alloys were annealed for one hour at 2012°F (1100°C) and aged for one hour at 1292°F (700°C).

The martensitic alloys show values of magnetic saturation greater than 150 emu/g (~15,000 gauss) at 1112°F (600°C) with the exception of alloy 1-A-61. For this alloy, which

TABLE II-6. Transformation Temperature of Martensitic Alloys 1-A-53 to 1-A-61

Alloy Number	Nominal Alloy Composition (weight percent)	Transformation on Heating			
		90°F/Min (°F)	50°C/Min (°C)	3.6°F/Min (°F)	2°C/Min (°C)
1-A-53	54.9Fe-15Ni-25Co-3Ta-1Si-0.5Al-0.5Ti-0.1Mn	1575-1679	857-915	1260-1553	682-845
1-A-54	55.9Fe-12Ni-25Co-5Ta-2Si-0.1Mn	1569-1704	854-929	1310-1605	710-874
1-A-55	57Fe-12Ni-25Co-5Ta-0.5Ti-0.5Al	1596-1677	869-914	1382-1641	750-894
1-A-56	57Fe-12Ni-25Co-5Mo-0.5Ti-0.5Al	1501-1652	816-900	1233-1551	667-844
1-A-57	56Fe-12Ni-25Co-5Ta-2W	1535-1670	835-910	1292-1617	700-881
1-A-58	55.9Fe-12Ni-25Co-4Ta-2W-1Si-0.1Mn	1517-1652	825-900	1242-1620	672-882
1-A-59	55.9Fe-12Ni-25Co-3Ta-2W-1Si-0.5Al-0.5Ti-0.1Mn	1584-1681	862-916	1301-1602	705-872
1-A-60	55.9Fe-12Ni-25Co-4Ta-2Si-0.5Al-0.5Ti-0.1Mn	1542-1670	839-910	1303-1600	706-871
1-A-61	57.4Fe-5Ni-25Co-5Cr-5Ta-0.5Al-0.1Mn-2Si	1564-1695	851-924	1220-1587	660-864
Alloy Number	Nominal Alloy Composition (weight percent)	Transformation on Cooling			
		90°F/Min (°F)	50°C/Min (°C)	9°C/Min (°F)	5°C/Min (°C)
1-A-53	54.9Fe-15Ni-25Co-3Ta-1Si-0.5Al-0.5Ti-0.1Mn	752-491	400-255	777-572	414-300
1-A-54	55.9Fe-12Ni-25Co-5Ta-2Si-0.1Mn	811-631	433-333	900-712	482-378
1-A-55	57Fe-12Ni-25Co-5Ta-0.5Ti-0.5Al	905-684	485-362	963-786	517-419
1-A-56	57Fe-12Ni-25Co-5Mo-0.5Ti-0.5Al	705-419	374-215	730-505	388-263
1-A-57	56Fe-12Ni-25Co-5Ta-2W	815-644	435-340	918-777	492-414
1-A-58	55.9Fe-12Ni-25Co-4Ta-2W-1Si-0.1Mn	809-637	432-336	900-718	482-381
1-A-59	55.9Fe-12Ni-25Co-3Ta-2W-1Si-0.5Al-0.5Ti-0.1Mn	802-585	428-307	871-669	466-354
1-A-60	55.9Fe-12Ni-25Co-4Ta-2Si-0.5Al-0.5Ti-0.1Mn	820-628	438-331	887-709	475-376
1-A-61	57.4Fe-5Ni-25Co-5Cr-5Ta-0.5Al-0.1Mn-2Si	727-549	386-287	799-572	426-300

TABLE II-7. Saturation Magnetic Moment of Martensitic Alloys 1-A-53 to 1-A-61

Alloy Number	Nominal Alloy Composition (weight percent)	SATURATION MAGNETIC MOMENT (emu/g) [a]		
		After Annealing One Hour at 1832°F (1000°C)	After Aging One Hour at 1112°F (600°C)	
		Tested at Room Temperature	Tested at Room Temperature	Tested at 1112°F (600°C)
1-A-53	54.9Fe-15Ni-25Co-3Ta-1Si-0.5Al-0.5Ti-0.1Mn	190	192	157
1-A-54	55.9Fe-12Ni-25Co-5Ta-2Si-0.1Mn	188	192	159
1-A-55	57Fe-12Ni-25Co-5Ta-0.5Ti-0.5Al	196	197	167
1-A-56	57Fe-12Ni-25Co-5Mo-0.5Ti-0.5Al	192	192	160
1-A-57	56Fe-12Ni-25Co-5Ta-2W	195	195	165
1-A-58	55.9Fe-12Ni-25Co-4Ta-2W-1Si-0.1Mn	191	195	161
1-A-59	55.9Fe-12Ni-25Co-3Ta-2W-1Si-0.5Al-0.5Ti-0.1Mn	189	192	160
1-A-60	55.9Fe-12Ni-25Co-4Ta-2Si-0.5Al-0.5Ti-0.1Mn	186	191	158
1-A-61	57.4Fe-5Ni-25Co-5Cr-5Ta-0.5Al-0.1Mn-2Si	172	176	136

(a) To convert the saturation magnetic moment to the approximate induction in gauss, multiply the listed value by 100.

TABLE II-8. Saturation Magnetic Moment of Cobalt Base Alloys 1-B-42 to 1-B-46

Alloy Number	Nominal Alloy Composition (weight percent)	SATURATION MAGNETIC MOMENT (emu/g) [a]		
		After Annealing One Hour at 2012°F (1100°C)	After Aging One Hour at 1292°F (700°C)	
		Tested at Room Temperature	Tested at Room Temperature	Tested at 1112°F (600°C)
1-B-42	70.8Co-15Ni-5Fe-2.2Ti-1.5Al-0.5Zr-5Nb	109	108	82
1-B-43	71Co-15Ni-5Fe-2.2Ti-1.5Al-0.3Zr-5Ta	119	117	90
1-B-44	73Co-15Ni-5Fe-2.2Ti-1.5Al-0.3Zr-3Ta	124	122	95
1-B-45	71.7Co-15Ni-5Fe-1.5Ti-1.5Al-0.3Zr-5Ta	122	122	94
1-B-46	76Co-10Ni-5Fe-2.2Ti-1.5Al-0.3Zr-5Ta	123	122	93

(a) To convert saturation magnetic moment to the approximate induction in gauss, multiply the listed value by 110.

contains chromium and silicon, the magnetic saturation was only 136 emu/g. It may be noted that the addition of silicon reduced the magnetic saturation in other experimental alloys as well.

Cobalt-base alloy 1-B-42 with five weight percent niobium exhibited a substantial reduction in magnetic saturation. The other cobalt alloys (1-B-43 to 1-B-46) with tantalum additions may be compared to alloy 1-B-39 which was reported in the fourth quarterly report (also see Table II-15 of this report for a summary). Reduced amounts of elements such as tantalum, titanium, and nickel produced an increase in magnetic saturation but it was still not equal to that of Nivco alloy.

(4) Aging Tests

The isochronal aging data for the martensitic alloys made by levitation melting are plotted in Figures II-1 and II-2. An alloy (LM10) with Fe-15Ni-25Co-5Ta was included for comparison. This alloy was studied in a previous Westinghouse program. It had been re-melted and treated similar to the martensitic alloy specimens under test on this program. The lowest isochronal aging temperature was 842°F (450°C), the highest 1202°F (650°C). The data obtained during the isothermal aging of these samples at 1022°F (550°C) are shown in Figures II-3 to II-6.

Figures II-7 and II-8 shows the isochronal aging curves of the samples made from the 300 gram vacuum arc-melted martensitic alloys. The isochronal aging was started at 932°F (500°C) and increased to 1202°F (650°C). The 1022°F (550°C) isothermal aging data for these alloys are plotted in Figures II-9, II-10, and II-11. The maximum values of room temperature hardness which were measured during isochronal aging of the martensitic alloys are listed in Tables II-9 and II-10. These tables indicate the aging temperature at which maximum hardness was obtained as well as the associated coercivity value.

All of the martensitic alloys exhibited a very pronounced increase in hardness after isochronal aging. The maximum

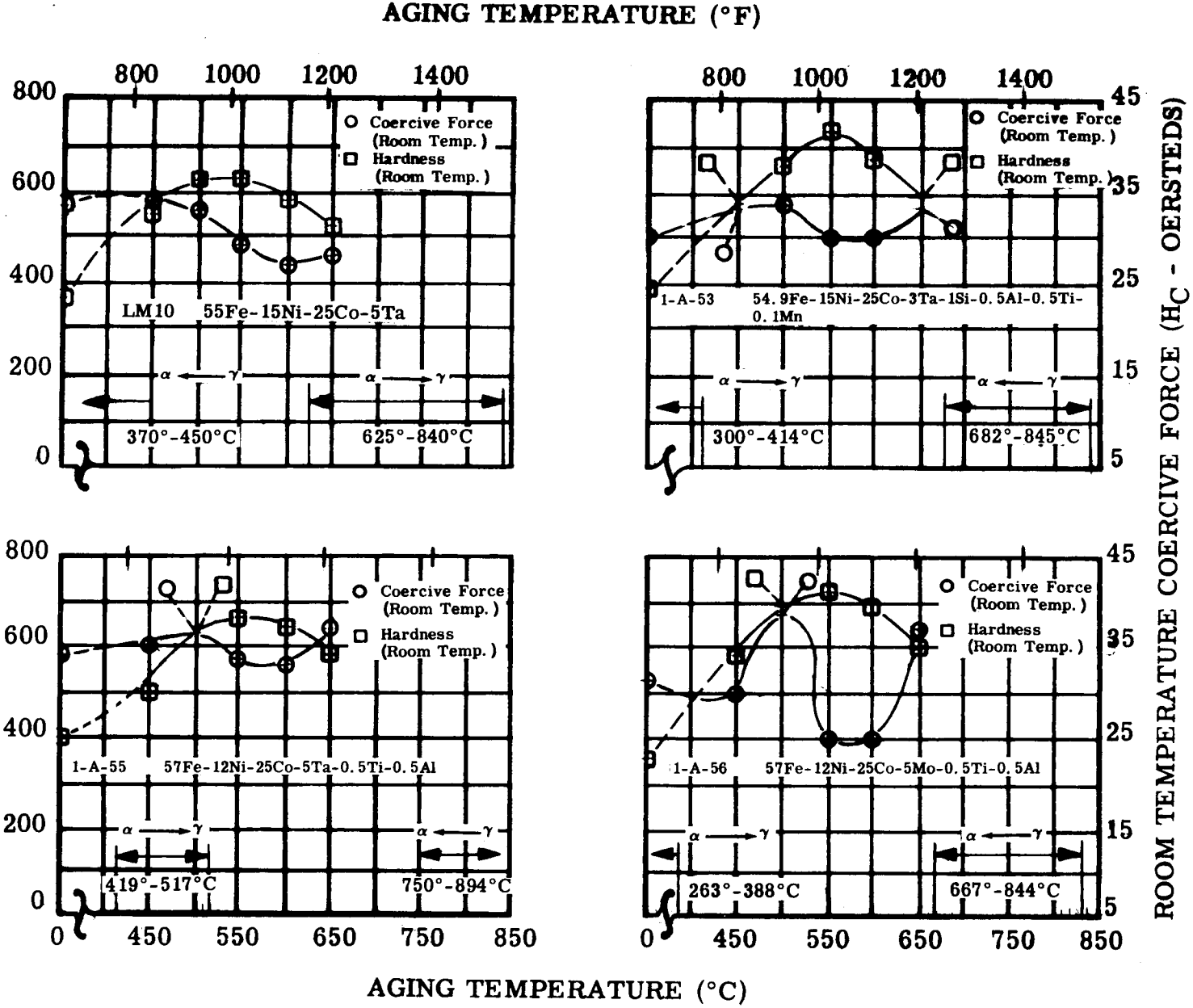

Figure II-1. Hardness and Coercive Force of Alloys LM10, 1-A-53, 1-A-55, and 1-A-56

FIGURE II-1. Hardness and Coercive Force of Alloys LM10, 1-A-53, 1-A-55, and 1-A-56 at Room Temperature After Aging One Hour at Temperature

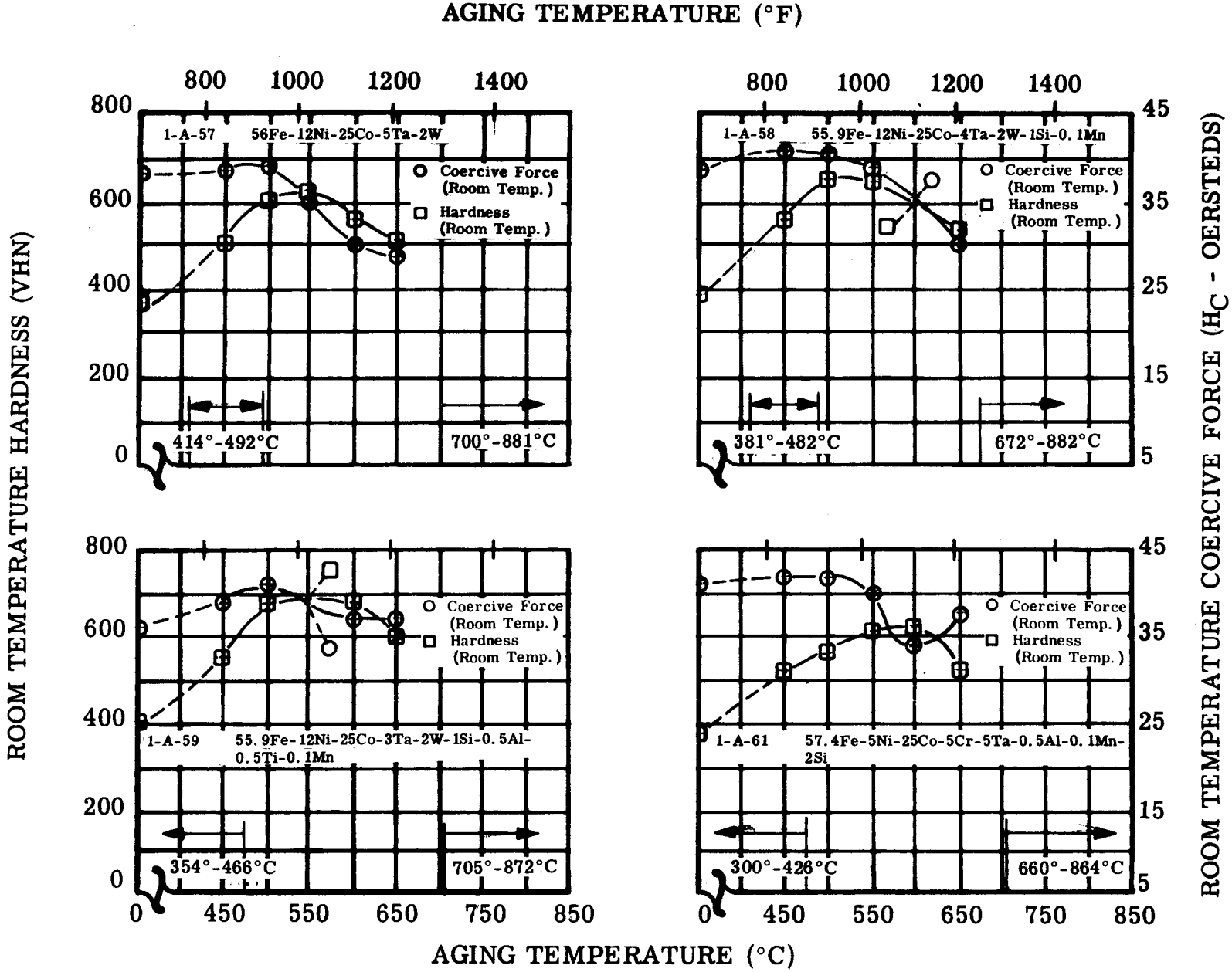

FIGURE II-2. Hardness and Coercive Force of Alloys 1-A-57, 1-A-58, 1-A-59, and 1-A-61 at Room Temperature After Aging One Hour at Temperature

Figure II-2. Hardness and Coercive Force of Alloys 1-A-57, 1-A-58, 1-A-59, and 1-A-61

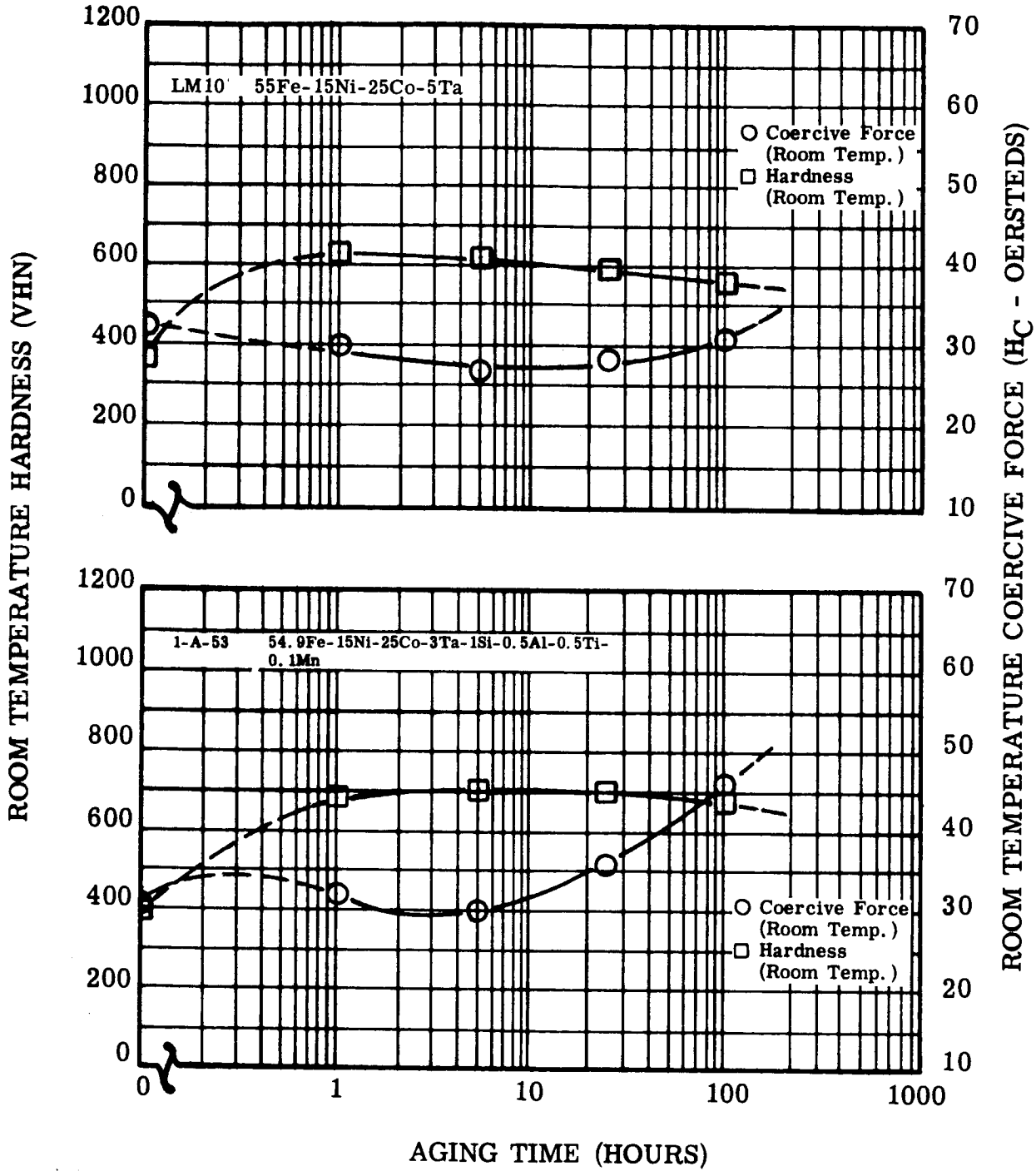

FIGURE II-3. Change in Room Temperature Hardness and Coercive Force of Alloys LM10 and 1-A-53 During Isothermal Aging at 1022°F (550°C)

Figure II-3. Hardness and Coercive Force of Alloys LM10 and 1-A-53 During Isothermal Aging

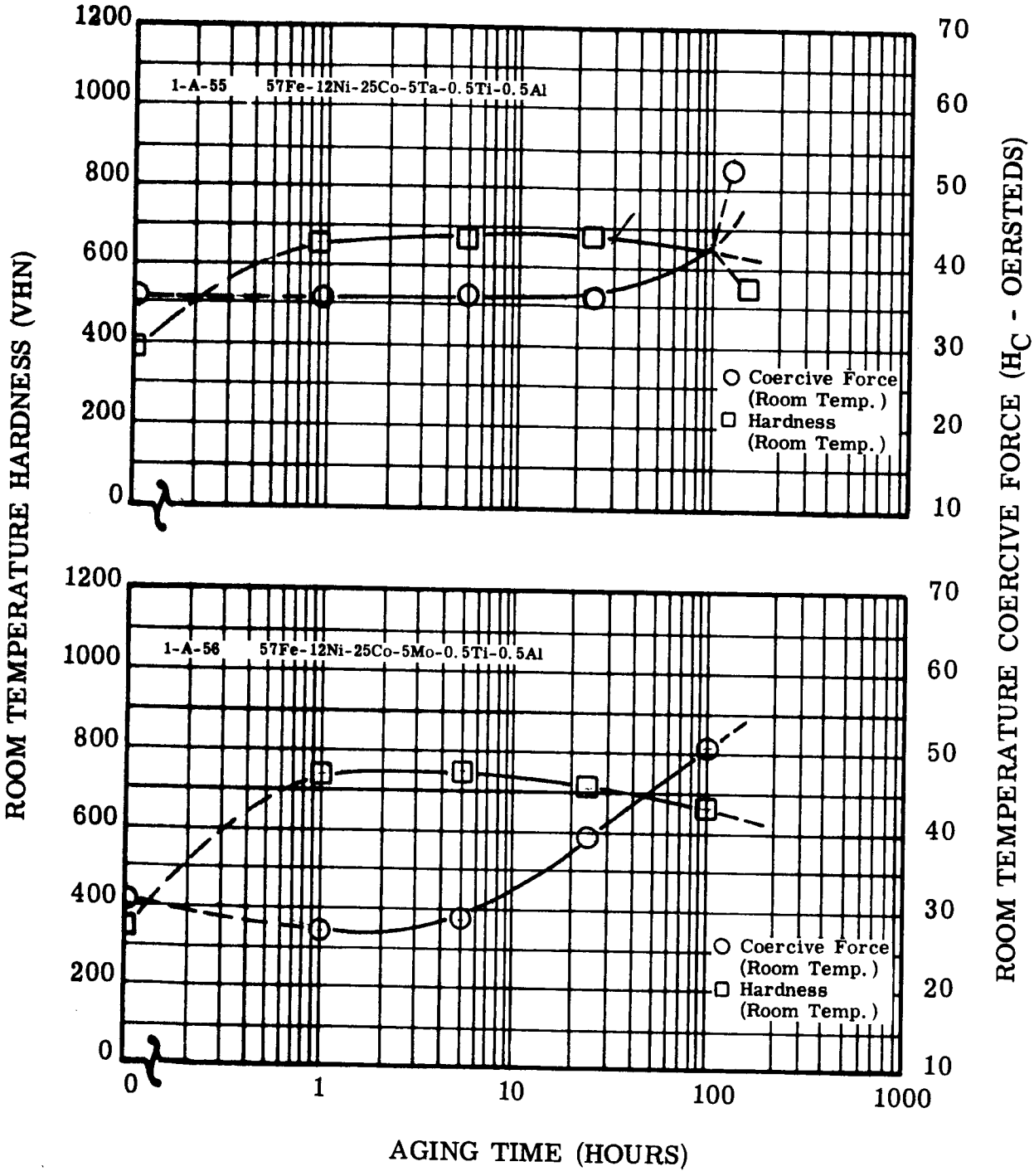

FIGURE II-4. Change in Room Temperature Hardness and Coercive Force of Alloys 1-A-55 and 1-A-56 During Isothermal Aging at 1022°F (550°C)

Figure II-4. Hardness and Coercive Force of Alloys 1-A-55 and 1-A-56 During Isothermal Aging

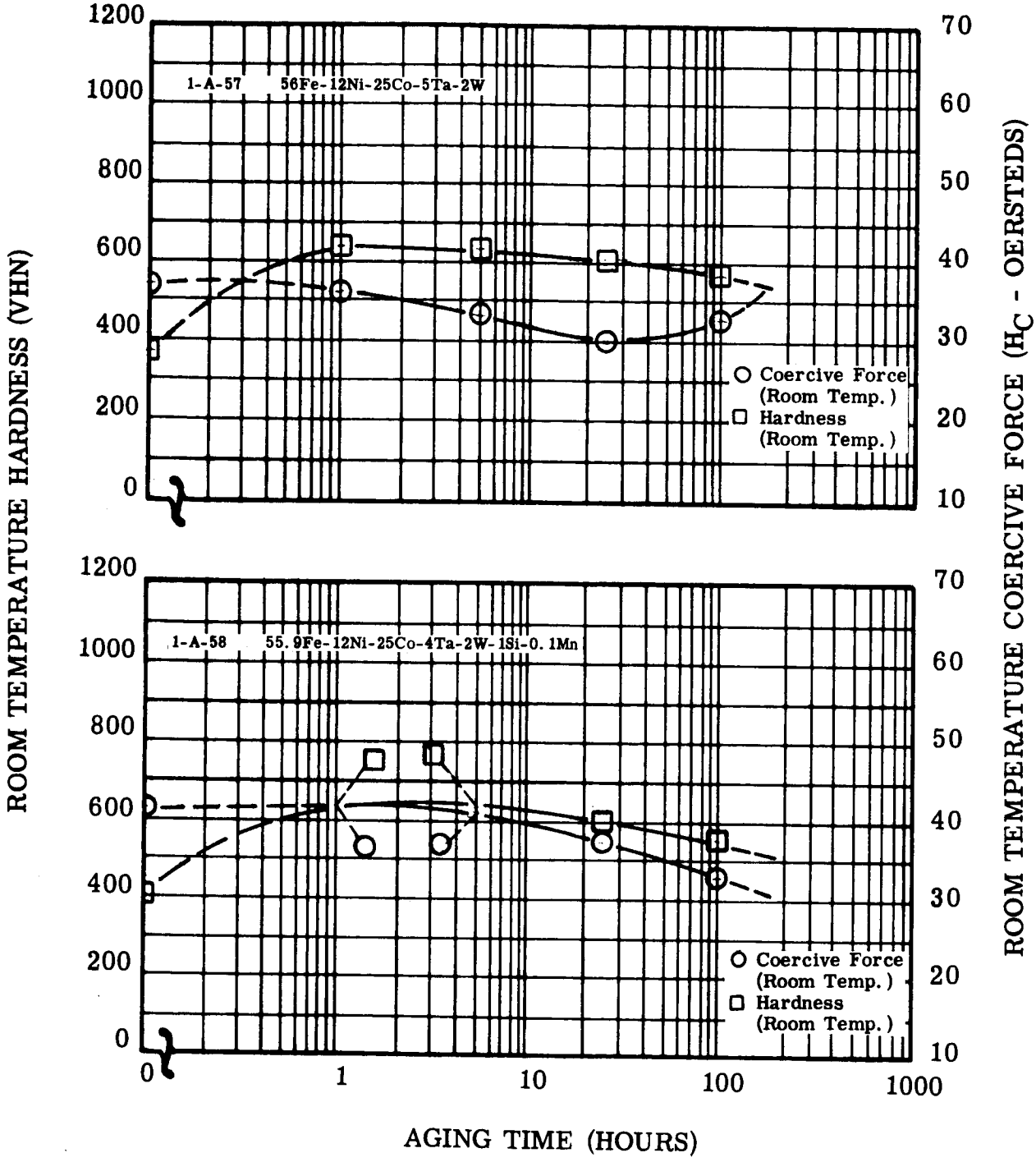

FIGURE II-5. Change in Room Temperature Hardness and Coercive Force of Alloys 1-A-57 and 1-A-58 During Isothermal Aging at 1022°F (550°C)

Figure II-5. Hardness and Coercive Force of Alloys 1-A-57 and 1-A-58 During Isothermal Aging

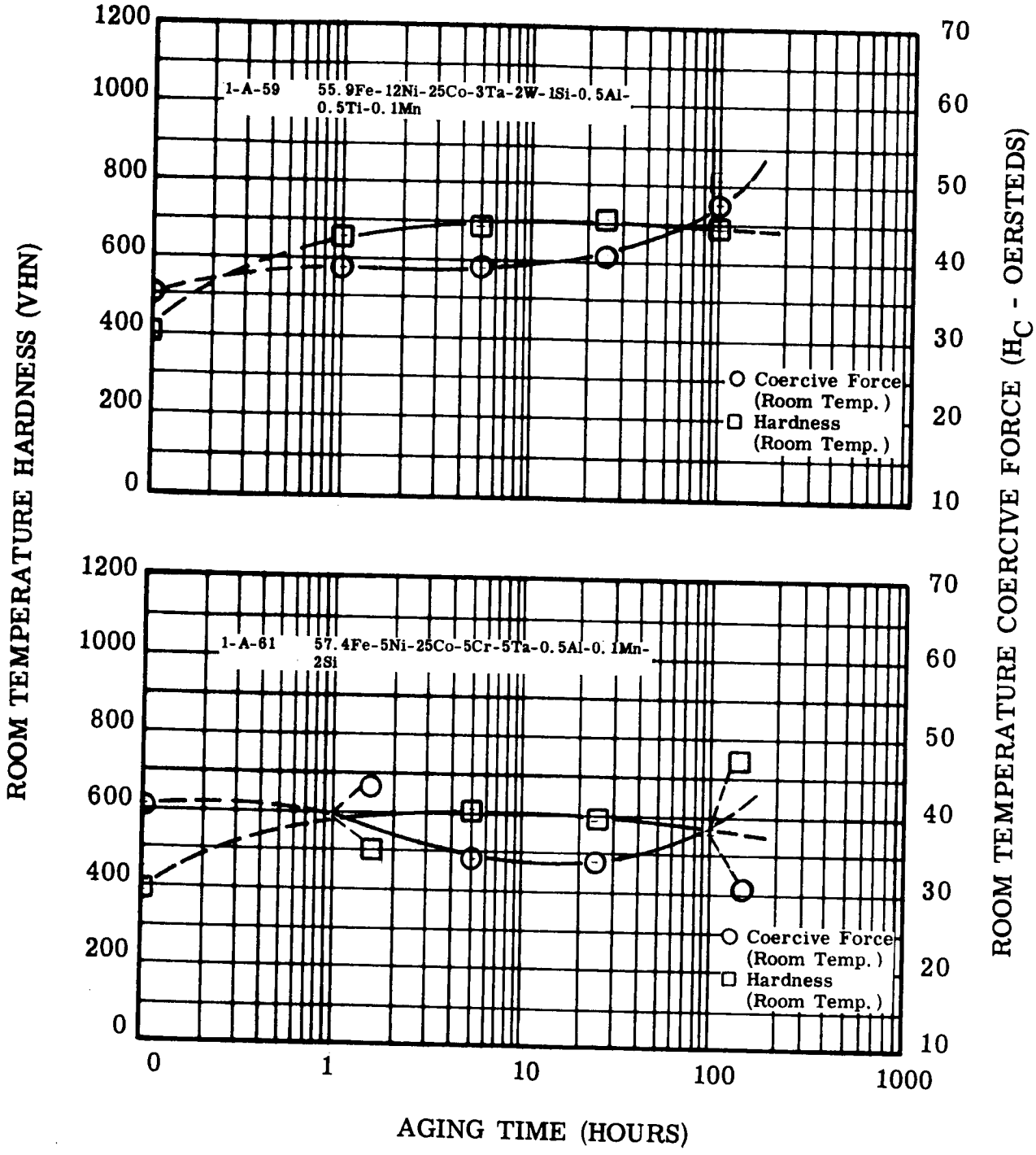

FIGURE II-6. Change in Room Temperature Hardness and Coercive Force of Alloys 1-A-59 and 1-A-61 During Isothermal Aging at 1022°F (550°C)

Figure II-6. Hardness and Coercive Force of Alloys 1-A-59 and 1-A-61 During Isothermal Aging

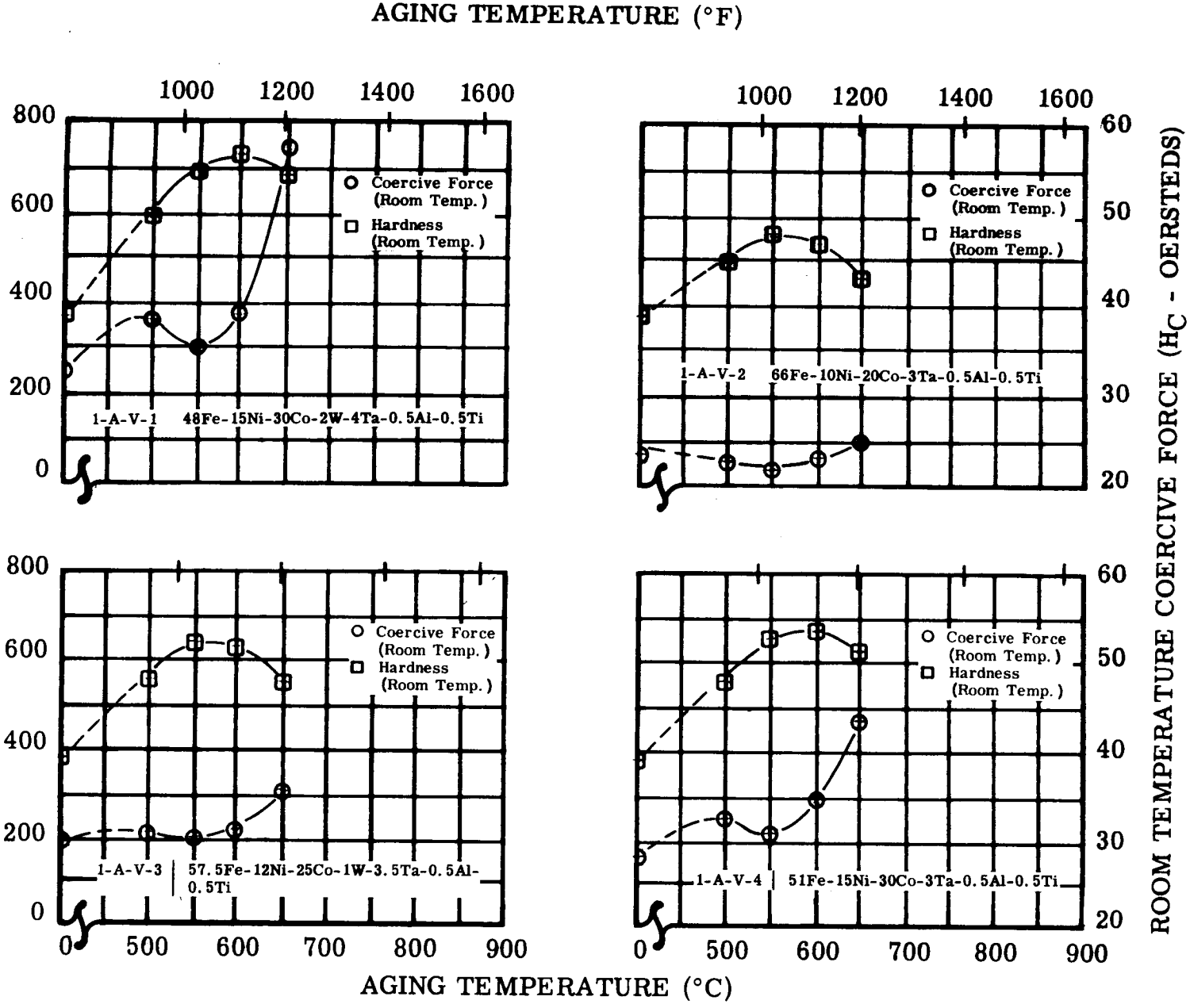

Figure II-7. Hardness and Coercive Force of Alloys 1-A-V-1, 1-A-V-2, 1-A-V-3, and 1-A-V-4

FIGURE II-7. Hardness and Coercive Force of 300 Gram Vacuum Arc Melted Alloys 1-A-V-1, 1-A-V-2, 1-A-V-3, and 1-A-V-4 at Room Temperature After Aging One Hour at Temperature

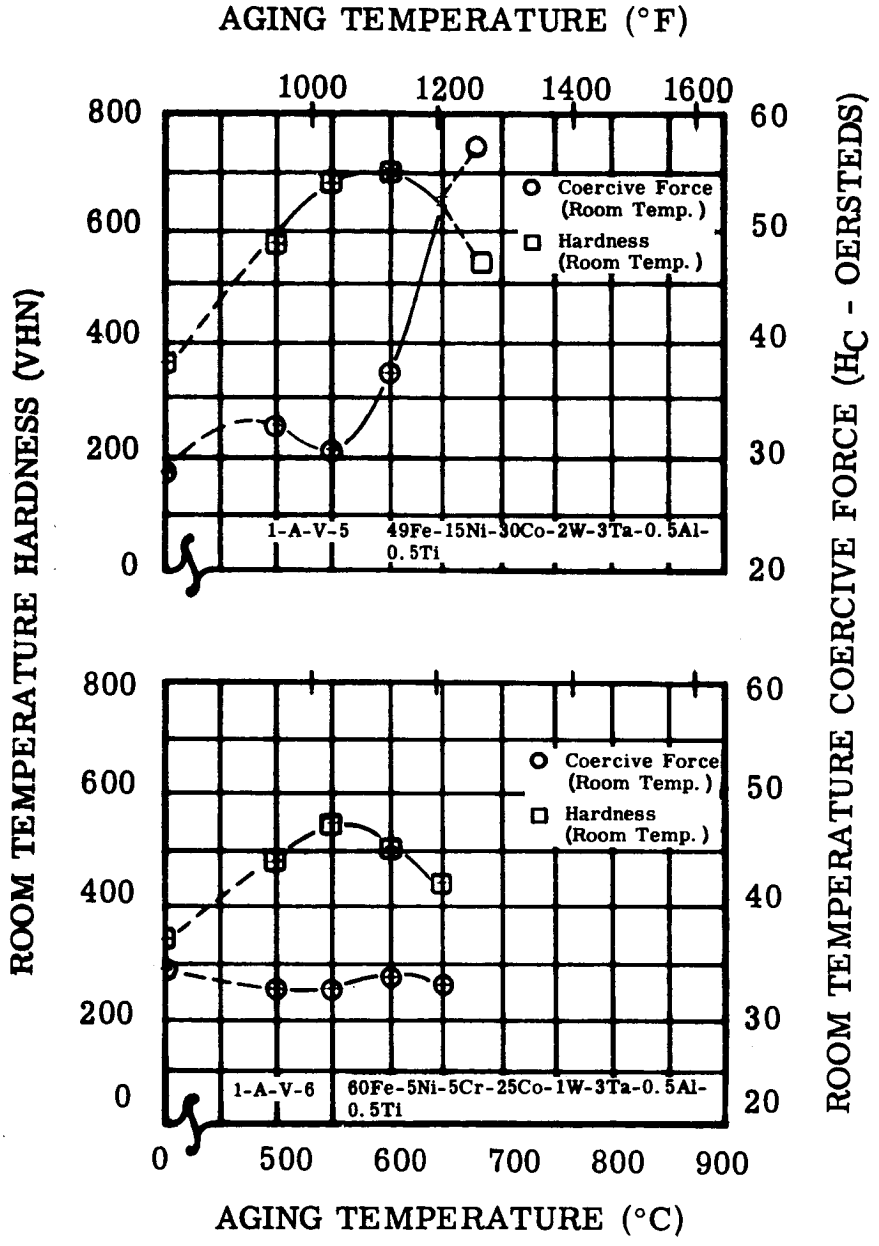

FIGURE II-8. Hardness and Coercive Force of 300 Gram Vacuum Arc Melted Alloys 1-A-V-5 and 1-A-V-6 at Room Temperature After Aging One Hour at Temperature

Figure II-8. Hardness and Coercive Force of Alloys 1-A-V-5 and 1-A-V-6

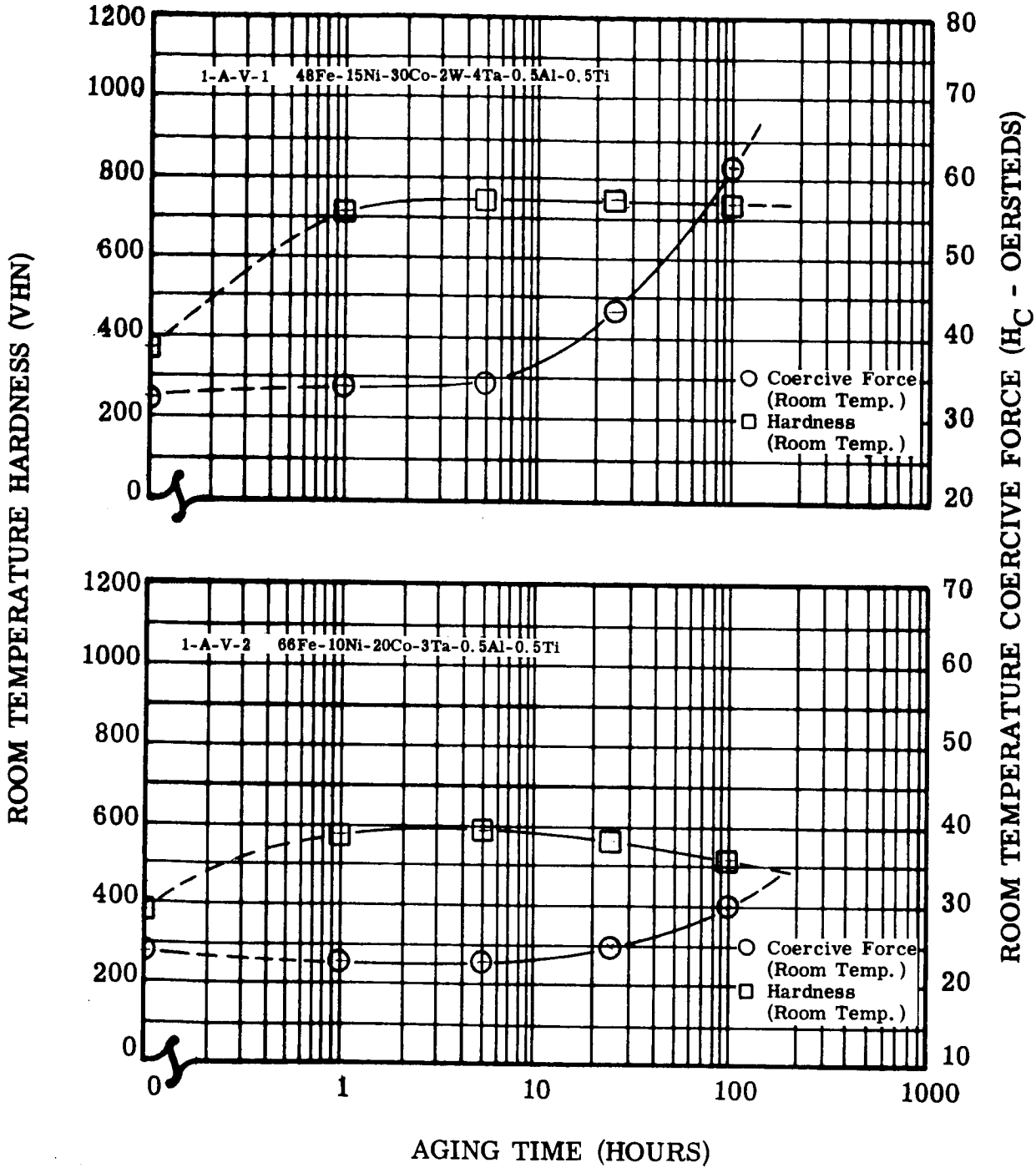

FIGURE II-9. Change in Room Temperature Hardness and Coercive Force of 300 Gram Vacuum Arc Melted Alloys 1-A-V-1 and 1-A-V-2 During Isothermal Aging at 1022°F (550°C)

Figure II-9. Hardness and Coercive Force of Alloys 1-A-V-1 and 1-A-V-2 During Isothermal Aging

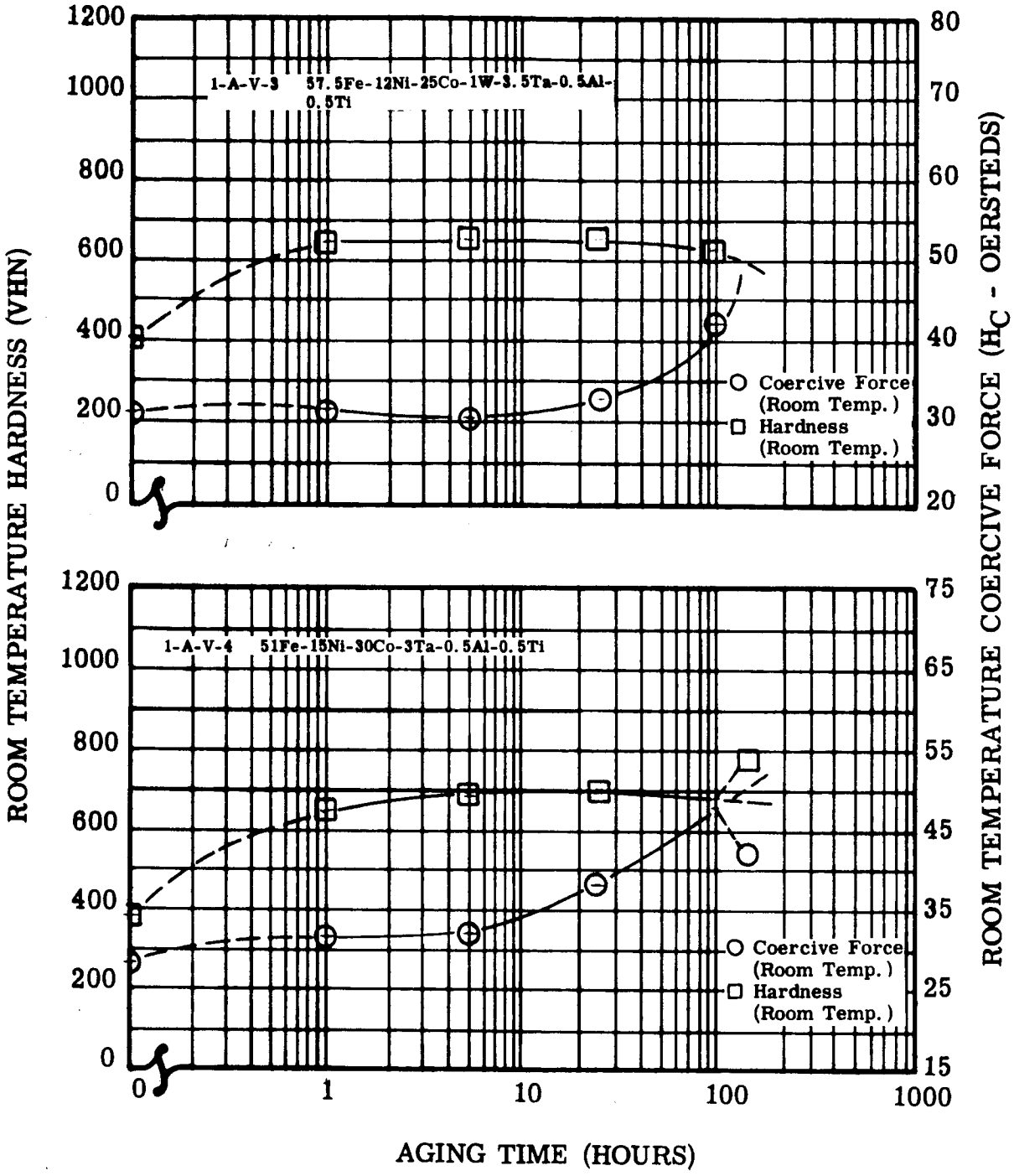

FIGURE II-10. Change in Room Temperature Hardness and Coercive Force of 300 Gram Vacuum Arc Melted Alloys 1-A-V-3 and 1-A-V-4 During Isothermal Aging at 1022°F (550°C)

Figure II-10. Hardness and Coercive Force of Alloys 1-A-V-3 and 1-A-V-4 During Isothermal Aging

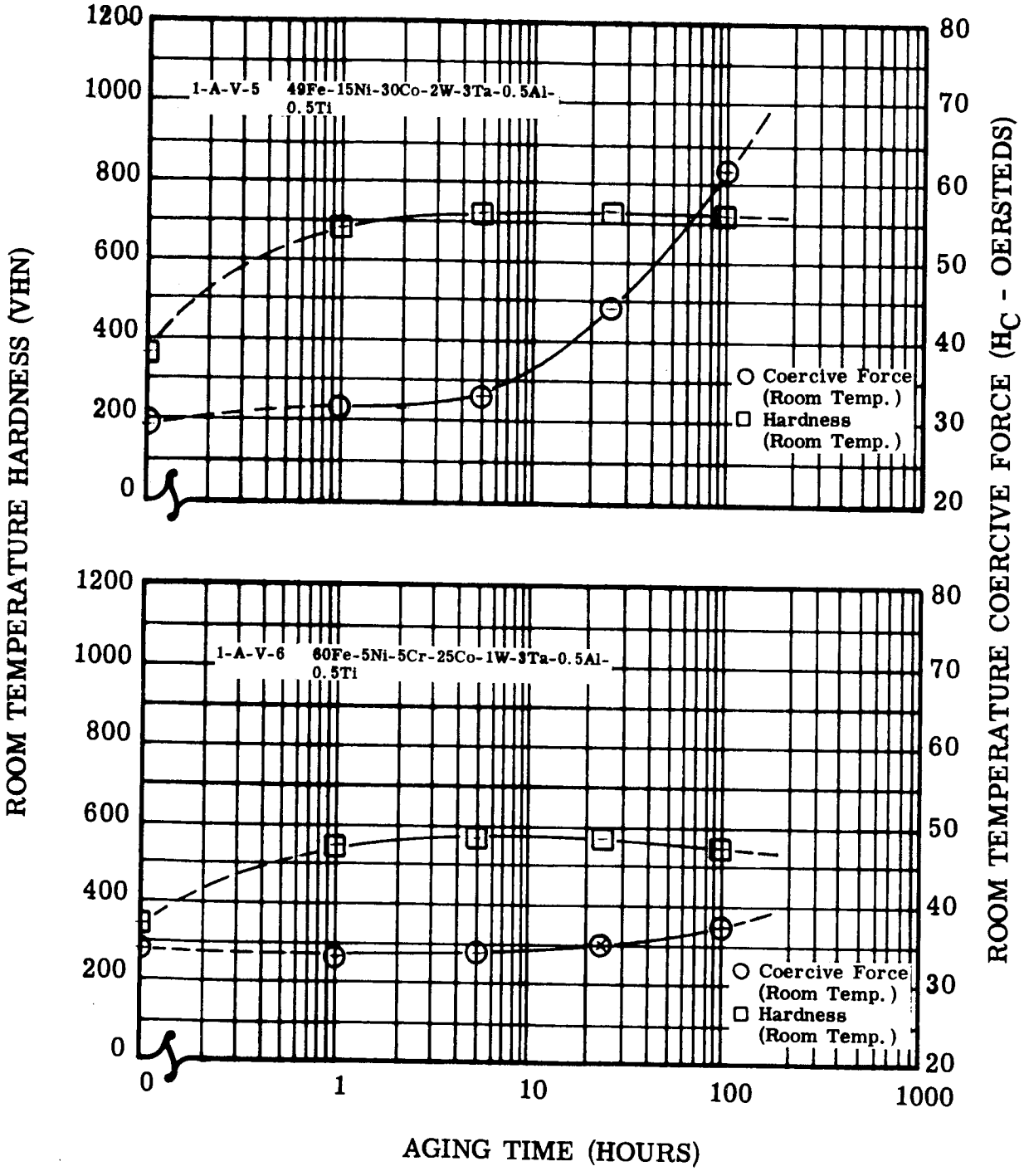

FIGURE II-11. Change in Room Temperature Hardness and Coercive Force of 300 Gram Vacuum Arc Melted Alloys 1-A-V-5 and 1-A-V-6 During Isothermal Aging at 1022°F (550°C)

Figure II-11. Hardness and Coercive Force of Alloys 1-A-V-5 and 1-A-V-6 During Isothermal Aging

TABLE II-9. Maximum Hardness Obtained by the Isochronal Aging of Martensitic Alloys 1-A-53, 1-A-55 to 1-A-59, and 1-A-61[a]

Alloy Number	Nominal Alloy Composition (weight percent)	Aging Temperature at Which Maximum Room Temperature Hardness was Obtained (°F)	(°C)	Total Aging Time[b] (hours)	Maximum Room Temperature Hardness (VHN)	Room Temperature Coercivity at Maximum Hardness (oersteds)
1-A-53	54.9Fe-15Ni-25Co-3Ta-1Si-0.5Al-0.5Ti-0.1Mn	1022	550	3	732	30.0
1-A-55	57Fe-12Ni-25Co-5Ta-0.5Ti-0.5Al	1022	550	3	663	33.5
1-A-56	57Fe-12Ni-25Co-5Mo-0.5Ti-0.5Al	1022	550	3	732	25.0
1-A-57	56Fe-12Ni-25Co-5Ta-2W	1022	550	3	629	35.0
1-A-58	55.9Fe-12Ni-25Co-4Ta-2W-1Si-0.1Mn	1022	550	3	649	39.0
1-A-59	55.9Fe-12Ni-25Co-3Ta-2W-1Si-0.5Al-0.5Ti-0.1Mn	1022	550	3	692	39.0
1-A-61	57.4Fe-5Ni-25Co-5Cr-5Ta-0.5Al-0.1Mn-2Si	1022	550	3	616	40.0

(a) See Figures II-1 and II-2.

(b) Total aging time may be determined by adding one hour aging time for each 90°F (50°C) increment in temperature starting at 842°F (450°C).

TABLE II-10. Maximum Hardness Obtained by the Isochronal Aging of Vacuum Arc Melted Martensitic Alloys 1-A-V-1 to 1-A-V-6[a]

Alloy Number	Nominal Alloy Composition (weight percent)	Aging Temperature at Which Maximum Room Temperature Hardness was Obtained (°F)	(°C)	Total Aging Time[b] (hours)	Maximum Room Temperature Hardness (VHN)	Room Temperature Coercivity at Maximum Hardness (oersteds)
1-A-V-1	48Fe-15Ni-30Co-2W-4Ta-0.5Al-0.5Ti	1112	600	4	732	39
1-A-V-2	66Fe-10Ni-20Co-3Ta-0.5Al-0.5Ti	1022	550	3	570	22
1-A-V-3	57.5Fe-12Ni-25Co-1W-3.5Ta-0.5Al-0.5Ti	1022	550	3	641	30.5
1-A-V-4	51Fe-15Ni-30Co-3Ta-0.5Al-0.5Ti	1112	600	4	670	35
1-A-V-5	49Fe-15Ni-30Co-2W-3Ta-0.5Al-0.5Ti	1112	600	4	704	37
1-A-V-6	60Fe-5Ni-5Cr-25Co-1W-3Ta-0.5Al-0.5Ti	1022	550	3	553	34

(a) See Figures II-7 and II-8.

(b) Total aging time may be determined by adding one hour aging time for each 90°F (50°C) increment in temperature starting at 842°F (450°C).

strength was obtained during isochronal aging at 1022°F (550°C). The results show that the addition of aluminum and titanium to the Fe-12Ni-25Co alloys held the percent decrease in hardness to a low level during isochronal aging at 1022°F (550°C). This had also occurred in the case of similar additions to the Fe-15Ni-25Co alloys which were reported in the fourth quarterly report. However, the coercive force increased to very high levels. It was also demonstrated that the addition of molybdenum instead of tantalum (in the same weight percent) to the Fe-12Ni-25Co base resulted in more overaging than in the Fe-15Ni-25Co base alloys, but led to a higher strength when isothermally aged in a similar manner.

The isochronal curves for the levitation melted cobalt-base alloys are plotted in Figures II-12 and II-13. The lowest aging temperature was 932°F (500°C) and the highest was 1472°F (800°C). A sample of Nivco alloy was tested in a similar manner for comparison. This sample was made from heat 10-NO2V-1099 and was heat treated in the same manner as the experimental cobalt-base alloys before testing. The test data obtained from the isothermal aging tests at 1292°F (700°C) are plotted in Figures II- 14, II-15, and II-16.

The isochronal curves of the vacuum arc melted cobalt-base alloys are plotted in Figure II-17 and II-18. The isochronal temperature range was 1202°F (650°C) to 1472°F (800°C). Isothermal curves for these alloys are shown in Figures II-19, II-20, and II-21. Isothermal aging was performed at 1292°F (700°C). The maximum values of room temperature hardness which were measured during the isochronal aging of the cobalt-base alloys are listed in Tables II-11 and II-12. The tables indicate the temperature at which maximum hardness was obtained and the associated coercivity value.

In the cobalt-base alloys studied, superior values of hardness were obtained during the aging treatment compared to Nivco alloy. After isothermal aging 100 hours at 1292°F (700°C) the hardness values were higher than 400 VHN in all of the alloys studied while in Nivco 300 VHN was obtained by this treatment. In the alloys studied, columbium addition promoted the highest value of hardness. The beneficial

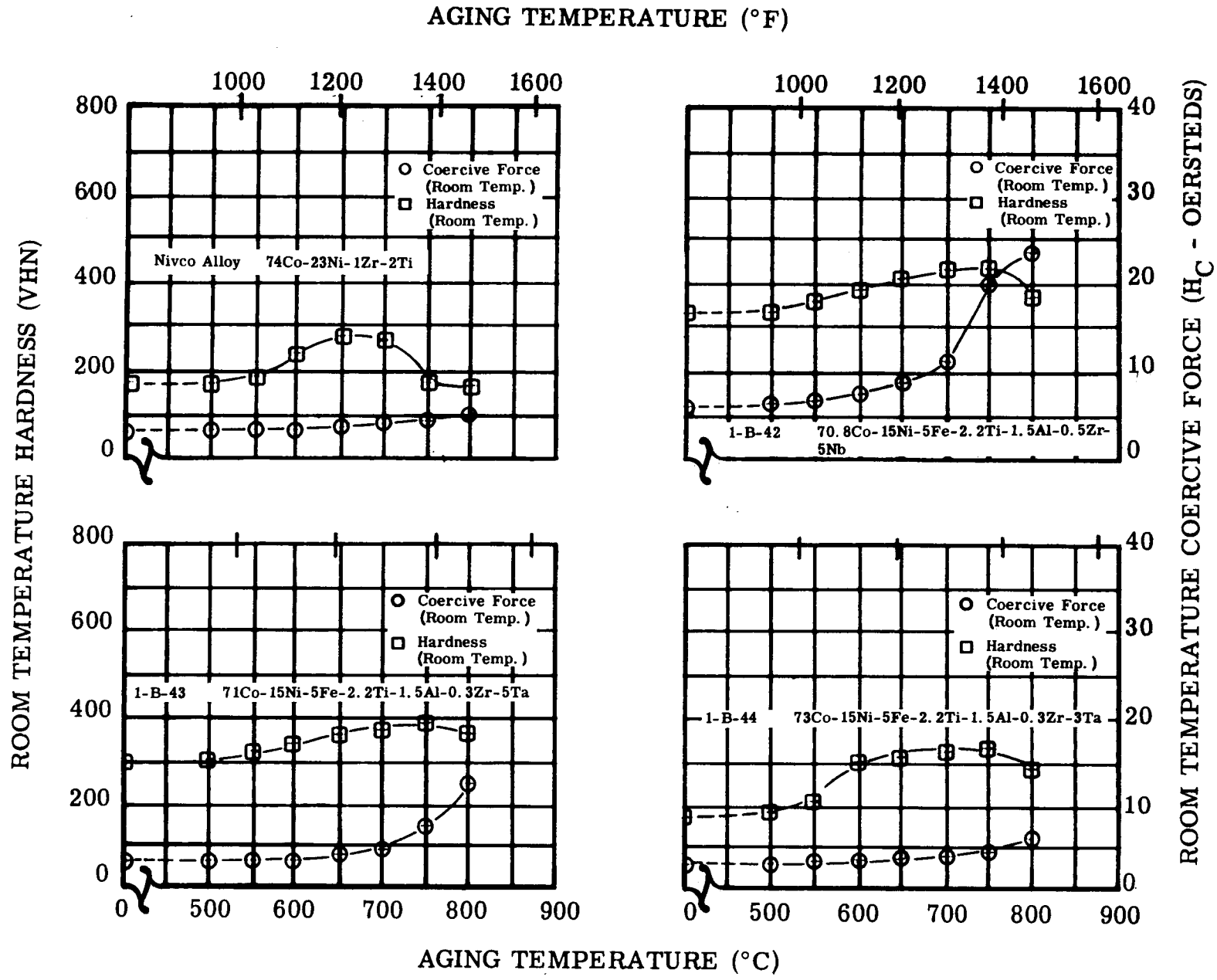

Figure II-12. Hardness and Coercive Force of Nivco, 1-B-52, 1-B-43, and 1-B-44

FIGURE II-12. Hardness and Coercive Force of Nivco, 1-B-42, 1-B-43, and 1-B-44 at Room Temperature After Aging One Hour at Temperature

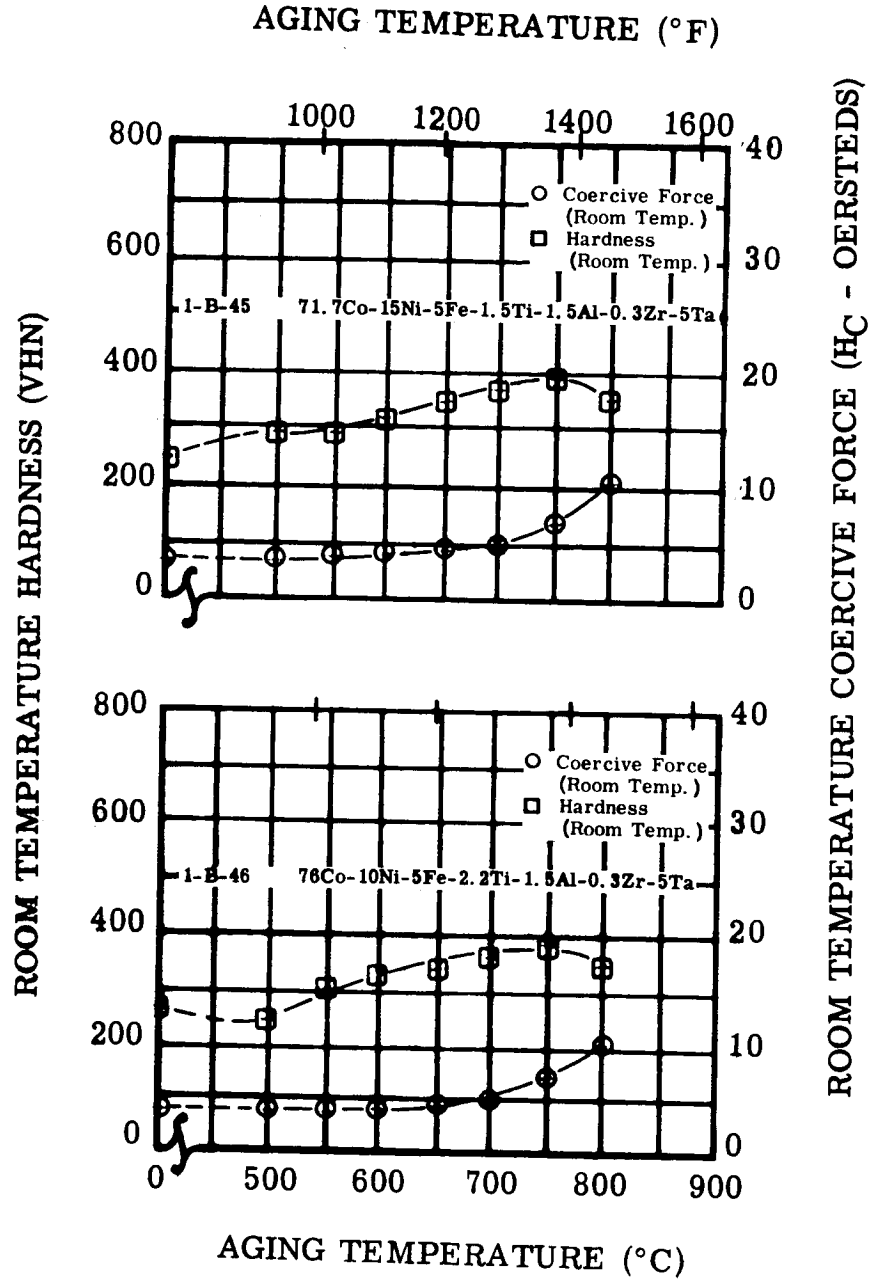

FIGURE II-13. Hardness and Coercive Force of Alloys 1-B-45 and 1-B-46 at Room Temperature After Aging One Hour at Temperature

Figure II-13. Hardness and Coercive Force of Alloys 1-B-45 and 1-B-46

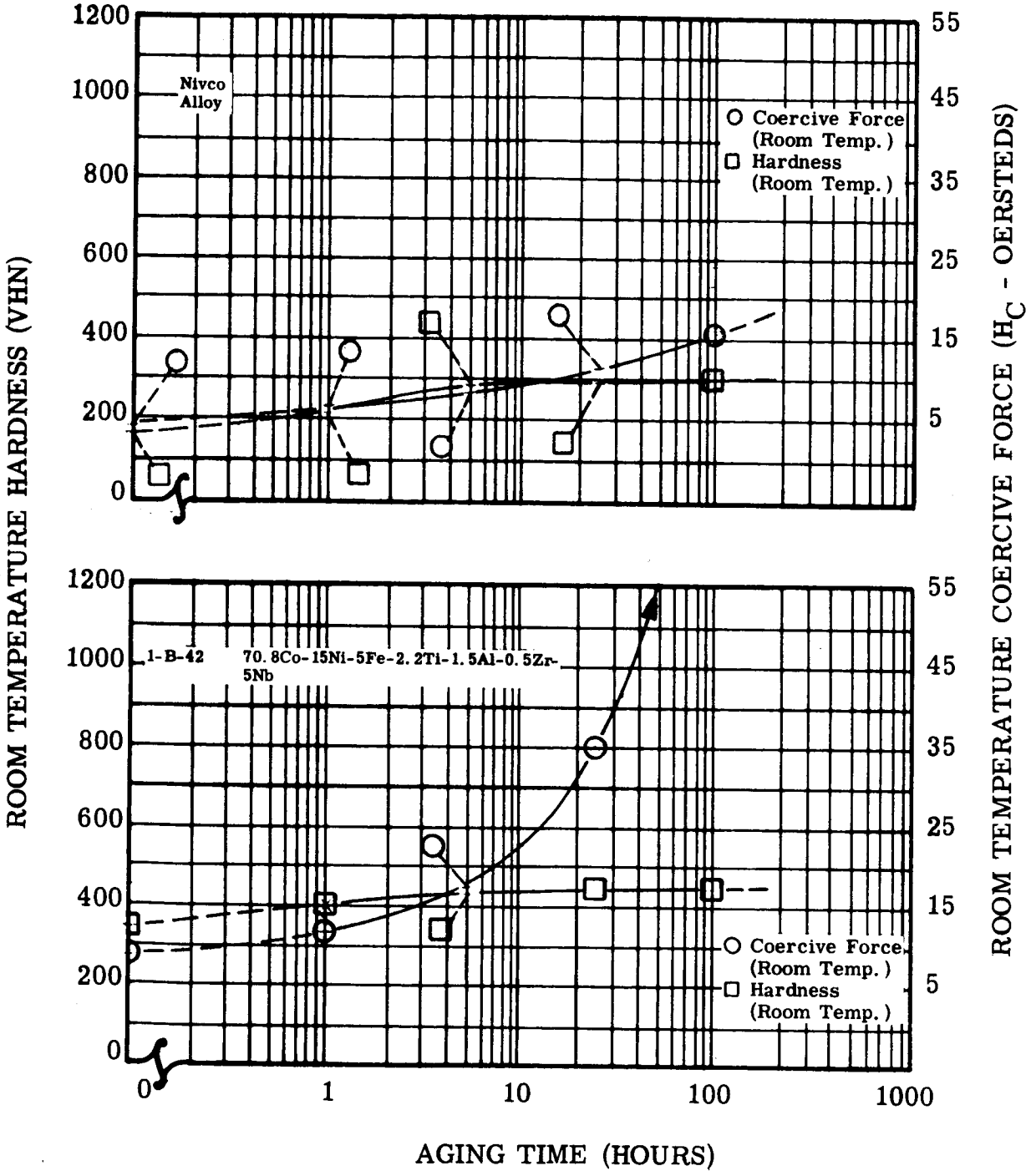

FIGURE II-14. Change in Room Temperature Hardness and Coercive Force of Nivco and 1-B-42 During Isothermal Aging at 1292°F (700°C)

Figure II-14. Hardness and Coercive Force of Nivco and 1-B-42 During Isothermal Aging

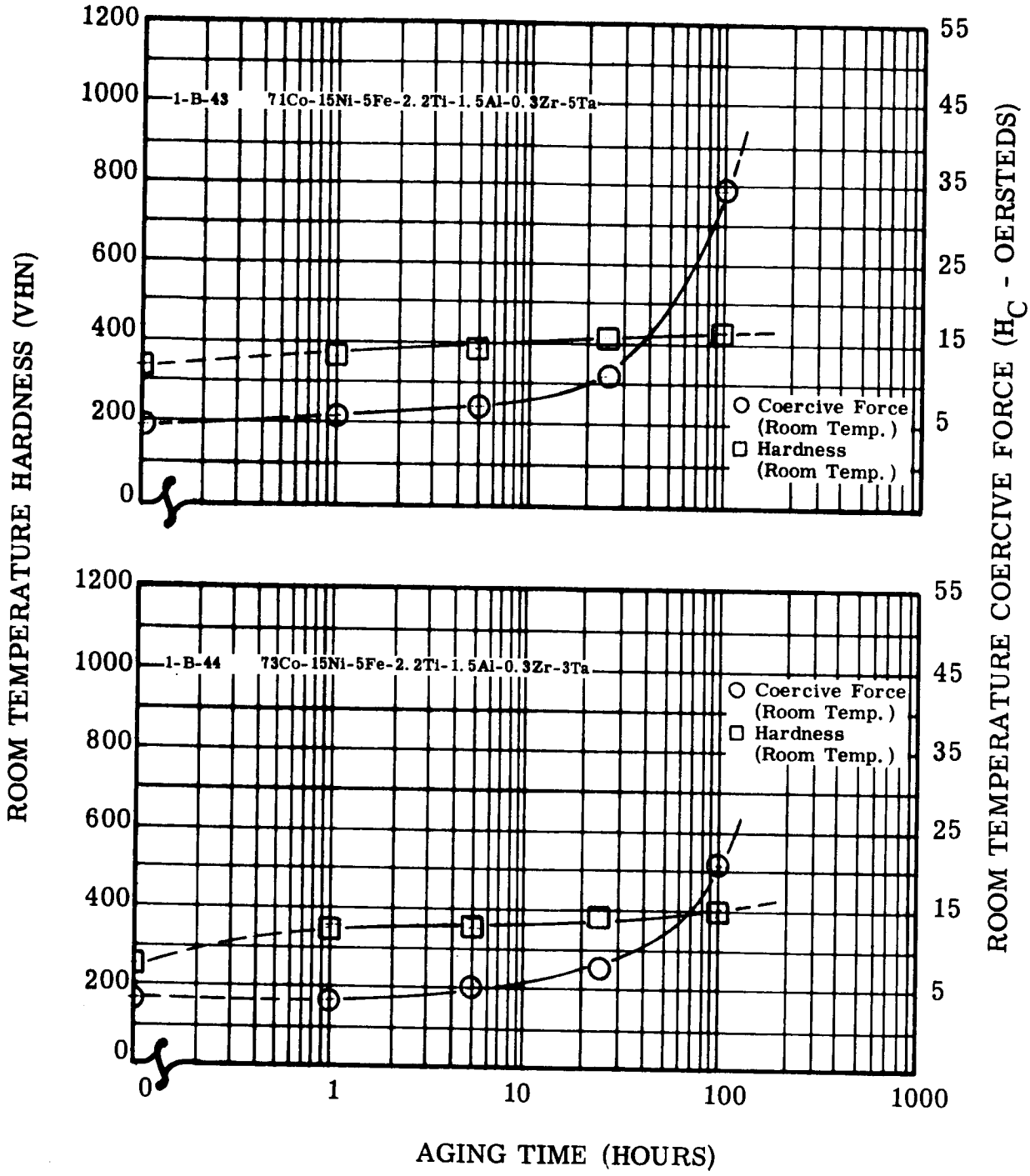

FIGURE II-15. Change in Room Temperature Hardness and Coercive Force of Alloys 1-B-43 and 1-B-44 During Isothermal Aging at 1292°F (700°C)

Figure II-15. Hardness and Coercive Force of Alloys 1-B-43 and 1-B-44 During Isothermal Aging

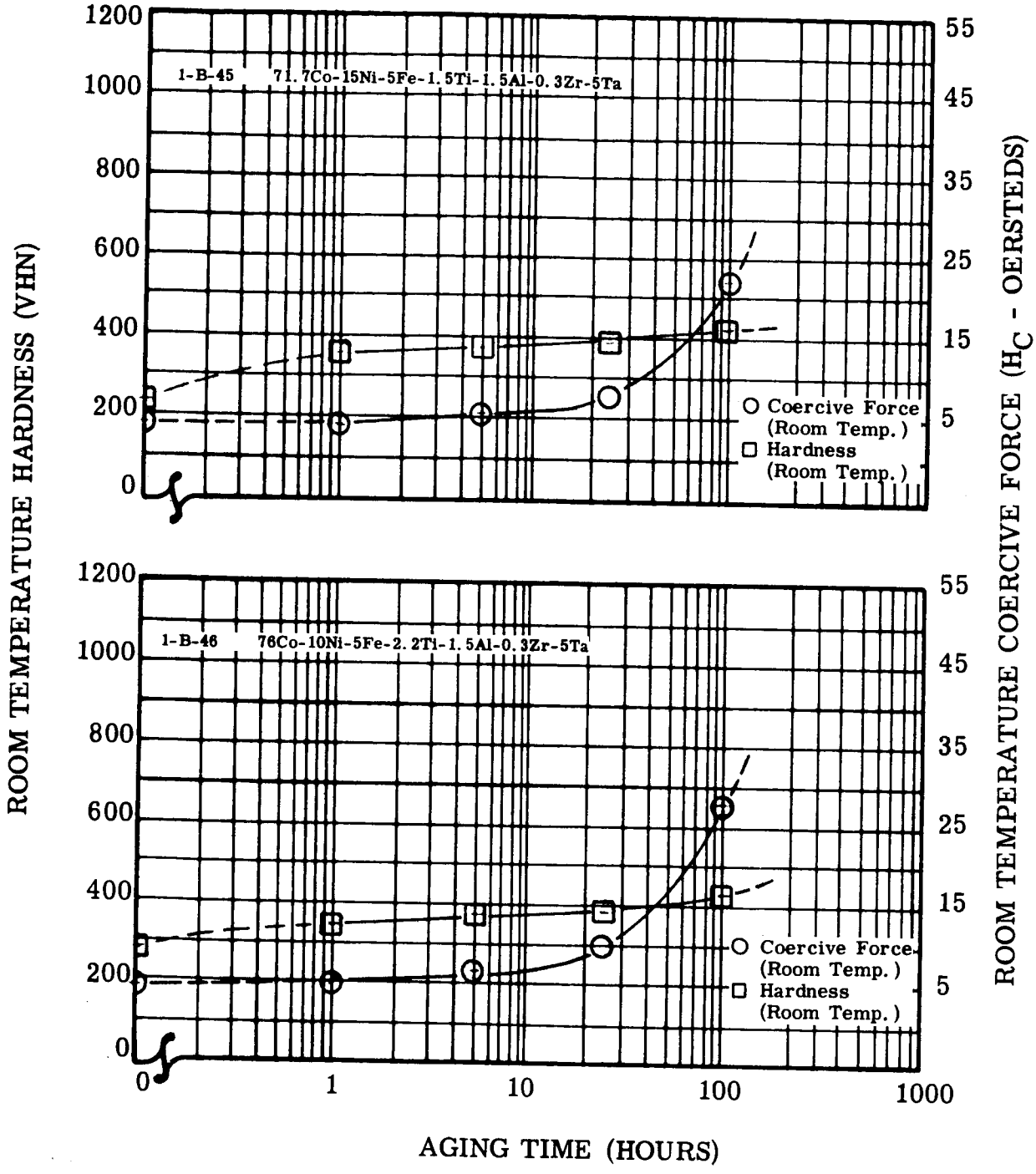

FIGURE II-16. Change in Room Temperature Hardness and Coercive Force of Alloys 1-B-45 and 1-B-46 During Isothermal Aging at 1292°F (700°C)

Figure II-16. Hardness and Coercive Force of Alloys 1-B-45 and 1-B-46 During Isothermal Aging

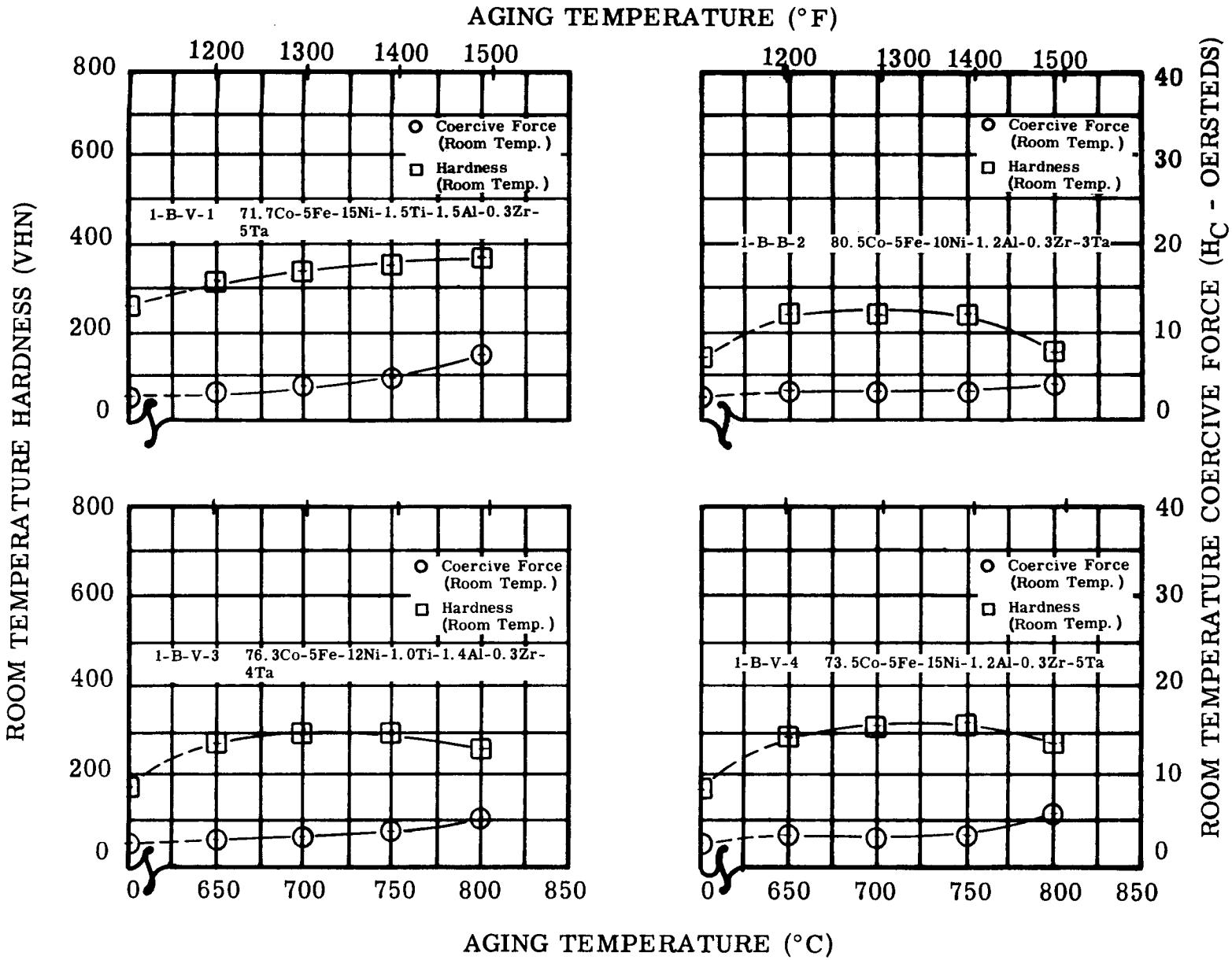

Figure II-17. Hardness and Coercive Force of Alloys 1-B-V-1, 1-B-V-2, 1-B-V-3, and 1-B-V-4

FIGURE II-17. Hardness and Coercive Force of 300 Gram Vacuum Arc Melted Alloys 1-B-V-1, 1-B-V-2, 1-B-V-3, and 1-B-V-4 at Room Temperature After Aging One Hour at Temperature

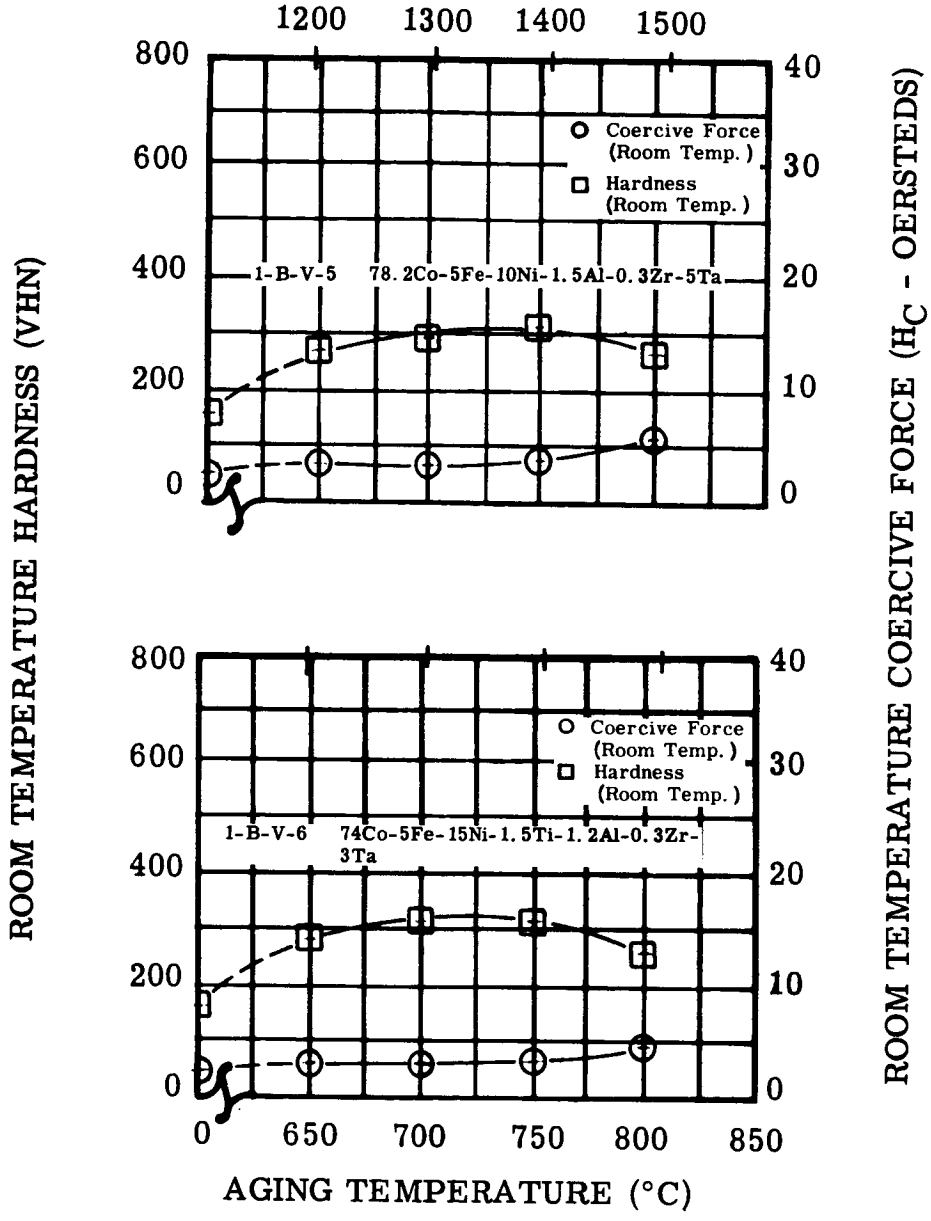

FIGURE II-18. Hardness and Coercive Force of 300 Gram Vacuum Arc Melted Alloys 1-B-V-5 and 1-B-V-6 at Room Temperature After Aging One Hour at Temperature

Figure II-18. Hardness and Coercive Force of Alloys 1-B-V-5 and 1-B-V-6

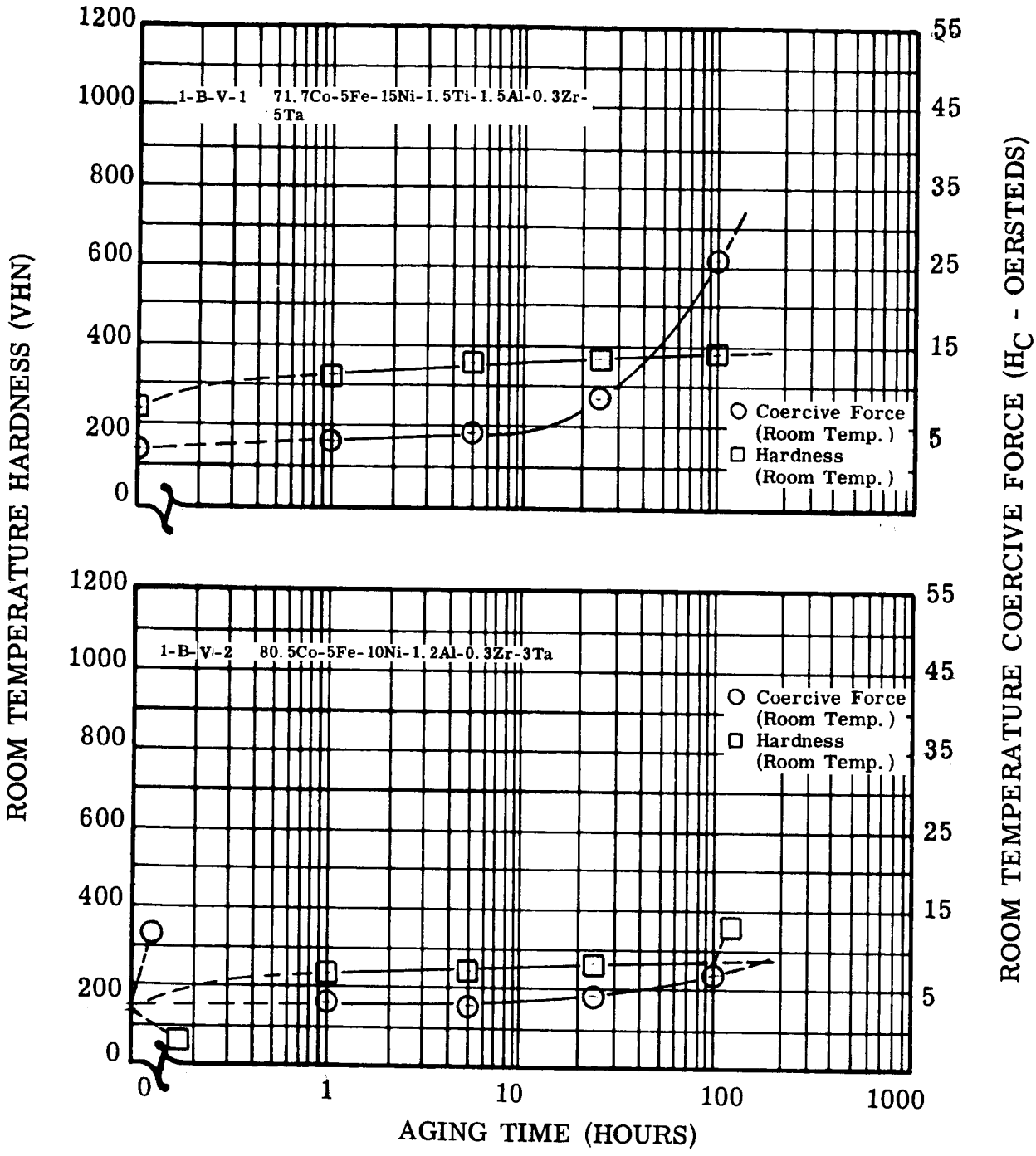

FIGURE II-19. Change in Room Temperature Hardness and Coercive Force of 300 Gram Vacuum Arc Melted Alloys 1-B-V-1 and 1-B-V-2 During Isothermal Aging at 1292°F (700°C)

Figure II-19. Hardness and Coercive Force of Alloys 1-B-V-1 and 1-B-V-2 During Isothermal Aging

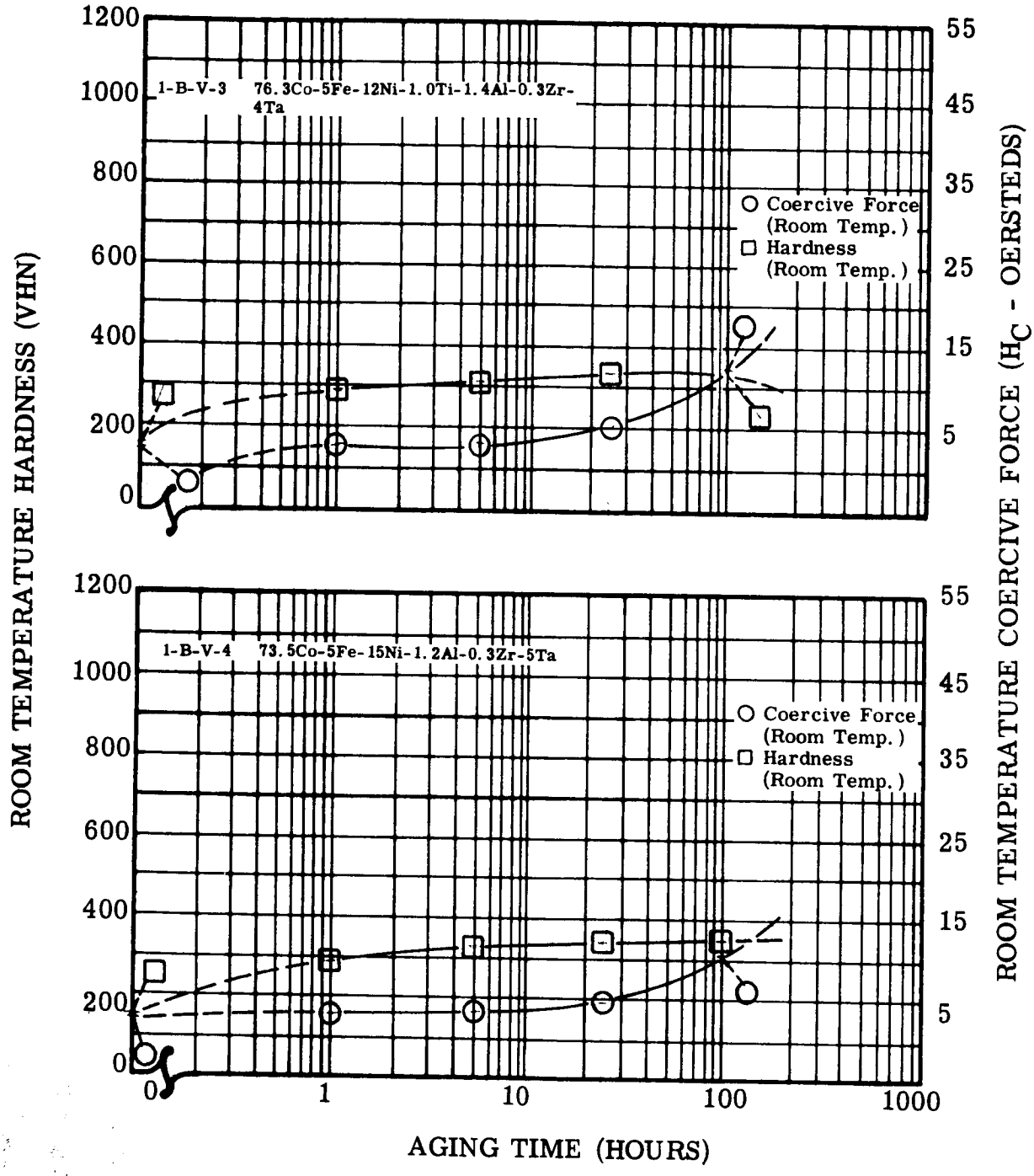

FIGURE II-20. Change in Room Temperature Hardness and Coercive Force of 300 Gram Vacuum Arc Melted Alloys 1-B-V-3 and 1-B-V-4 During Isothermal Aging at 1292°F (700°C)

Figure II-20. Hardness and Coercive Force of Alloys 1-B-V-3 and 1-B-V-4 During Isothermal Aging

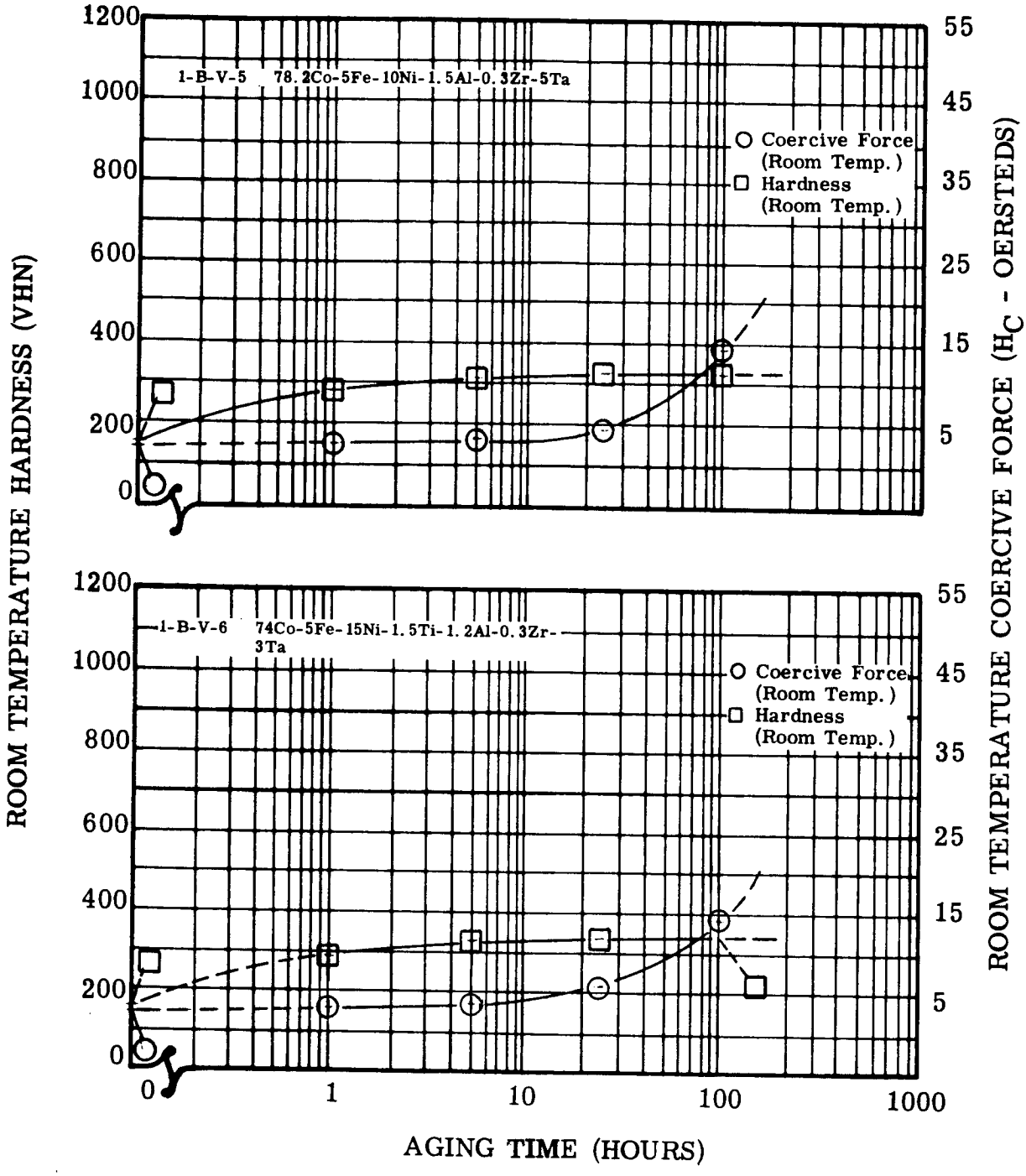

FIGURE II-21. Change in Room Temperature Hardness and Coercive Force of 300 Gram Vacuum Arc Melted Alloys 1-B-V-5 and 1-B-V-6 During Isothermal Aging at 1292°F (700°C)

Figure II-21. Hardness and Coercive Force of Alloys 1-B-V-5 and 1-B-V-6 During Isothermal Aging

TABLE II-11. Maximum Hardness Obtained by the Isochronal Aging of Cobalt Base Alloys 1-B-42 to 1-B-46(a)

Alloy Number	Nominal Alloy Composition (weight percent)	Aging Temperature at Which Maximum Room Temperature Hardness was Obtained (°F)	(°C)	Total Aging Time(b) (hours)	Maximum Room Temperature Hardness (VHN)	Room Temperature Coercivity at Maximum Hardness (oersteds)
1-B-42	70.8Co-15Ni-5Fe-2.2Ti-1.5Al-0.5Zr-5Nb	1382	750	6	433	20.0
1-B-43	71Co-15Ni-5Fe-2.2Ti-1.5Al-0.3Zr-5Ta	1382	750	6	393	7.2
1-B-44	73Co-15Ni-5Fe-2.2Ti-1.5Al-0.3Zr-3Ta	1382	750	6	339	4.9
1-B-45	71.7Co-15Ni-5Fe-1.5Ti-1.5Al-0.3Zr-5Ta	1382	750	6	385	6.8
1-B-46	76Co-10Ni-5Fe-2.2Ti-1.5Al-0.3Zr-5Ta	1382	750	6	380	6.9
For Comparison						
Nivco Alloy	74Co-23Ni-1Zr-2Ti	1202	650	4	272	3.9

(a) See Figures II-12 and II-13.

(b) Total aging time may be determined by adding one hour of aging time for each 90°F (50°C) increment in temperature start at 932°F (500°C).

TABLE II-12. Maximum Hardness Obtained by the Isochronal Aging of Vacuum Arc Melted Cobalt Base Alloys 1-B-V-1 to 1-B-V-6

Alloy Number	Nominal Alloy Composition (weight percent)	Aging Temperature at Which Maximum Room Temperature Hardness was Obtained (°F)	(°C)	Total Aging Time(b) (hours)	Maximum Room Temperature Hardness (VHN)	Room Temperature Coercivity at Maximum Hardness (oersteds)
1-B-V-1	71.7Co-5Fe-15Ni-1.5Ti-1.5Al-0.3Zr-5Ta	1382	750	6	354	4.7
1-B-V-2	80.5Co-5Fe-10Ni-1.2Al-0.3Zr-3Ta	1382	750	6	248	3.1
1-B-V-3	76.3Co-5Fe-12Ni-1.0Ti-1.4Al-0.3Zr-4Ta	1382	750	6	307	3.6
1-B-V-4	73.5Co-5Fe-15Ni-1.2Al-0.3Zr-5Ta	1382	750	6	323	3.6
1-B-V-5	78.2Co-5Fe-10Ni-1.5Al-0.3Zr-5Ta	1382	750	6	303	3.9
1-B-V-6	74Co-5Fe-15Ni-1.5Ti-1.2Al-0.3Zr-3Ta	1382	750	6	313	3.4

(a) See Figures II-17 and II-18.

(b) Total aging time may be determined by adding one hour aging time for each 90°F (50°C) increment in temperature starting at 932°F (500°C).

influence of columbium on age hardening nickel-base superalloys has been recognized (ref. 2). The conclusions that Mitchell drew on the influence of columbium on the precipitation of γ' may also be true in the cobalt-base alloys reported here. On the other hand the very high value of coercive force was obtained after 100 hours at 1292°F (700°C) may indicate particle growth of the precipitate.

Alloy 1-B-43 should reproduce the behavior of alloy 1-B-39 because of the similarity in composition, which differed only in its zirconium content. Similarity of the measured properties was, in fact, obtained except that after aging 100 hours at 1292°F (700°C) the measured values of hardness and coercive force of 1-B-43 were remarkably higher than in the case of alloy 1-B-39. It is doubtful that reducing the amount of zirconium from 0.5 to 0.3 weight percent had caused this effect. The data obtained by isochronal aging show the differences one would expect due to the slight change in composition, but the values measured after aging 100 hours at 1292°F (700°C) do not show these differences as clearly. In the alloy 1-B-46 an even higher value of hardness was obtained than in alloy 1-B-43 after 100 hours at 1292°F (700°C).

(5) Microstructure

Optical micrographs of the martensitic alloys made by levitation melting and aged at 1022°F (550°C) are shown in Figures II-22 to II-29. In the alloys LM10, 1-A-53, 1-A-57, 1-A-58, and 1-A-61 one can recognize a fine precipitate delineating the substructure of the martensite. The precipitate, which is evident in alloys 1-A-55 and 1-A-59, is more or less randomly distributed. A grain boundary precipitate is present in alloy 1-A-56. The microstructure of the isothermally aged martensitic alloy samples appear very similar to that of the alloys shown in the previous reports. The difference in appearance of the structure should be noted in those alloys where molybdenum was added instead of tantalum (alloys 1-A-55 and 1-A-56).

Optical micrographs of the levitation melted cobalt-base

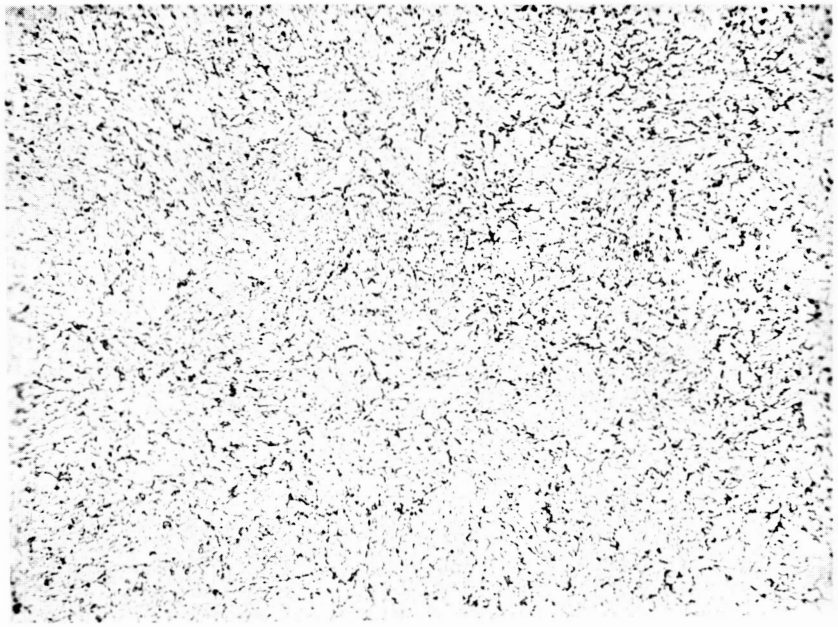

Electrolytically etched in 10 percent chromic acid.

FIGURE II-22. Microstructure of Alloy LM10 (55Fe-15Ni-25Co-5Ta) After 100 Hours Aging at 1022°F (550°C) 500 X

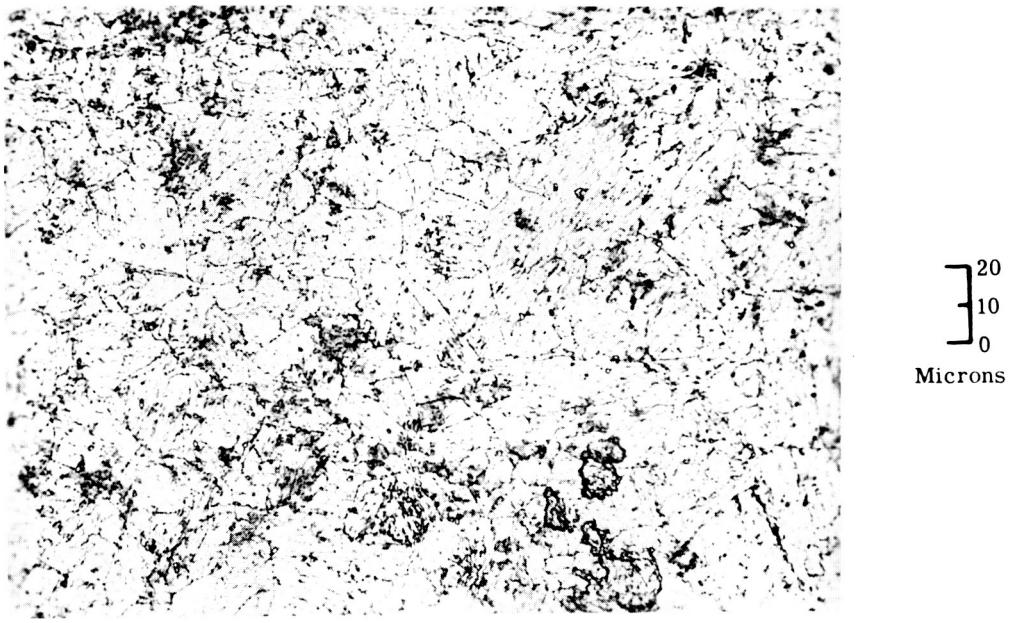

Electrolytically etched in 10 percent chromic acid.

FIGURE II-23. Microstructure of Alloy 1-A-53 (54.9Fe-15Ni-25Co-3Ta-1Si-0.5Al-0.5Ti-0.1Mn) After 100 Hours Aging at 1022°F (550°C) 500X

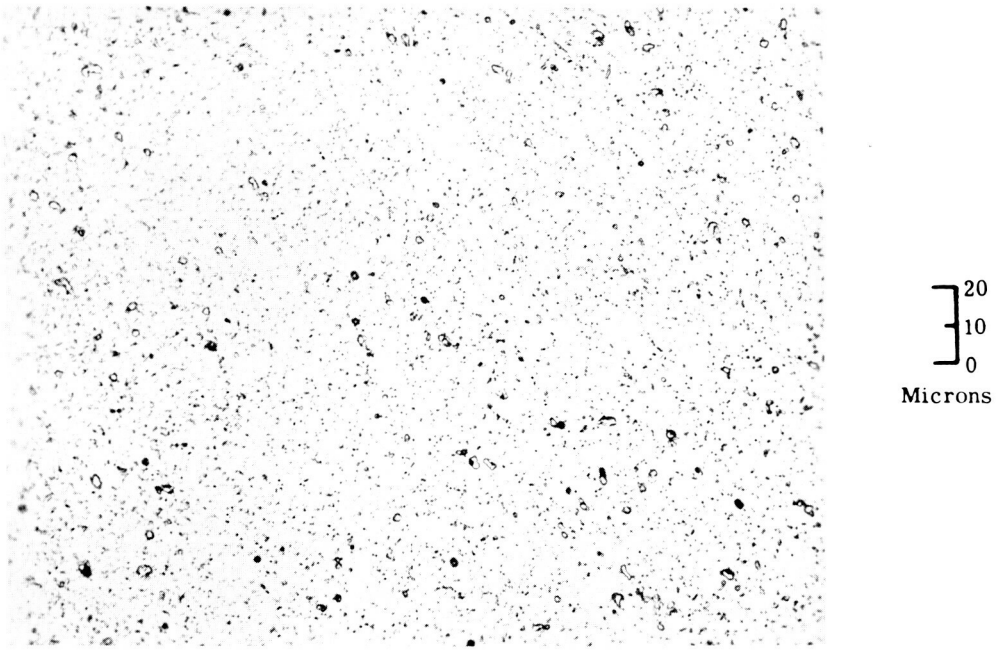

Electrolytically etched in 10 percent chromic acid

FIGURE II-24. Microstructure of Alloy 1-A-55 (57Fe-12Ni-25Co-5Ta-0.5Ti-0.5Al) After 100 Hours Aging at 1022°F (550°C) 500 X

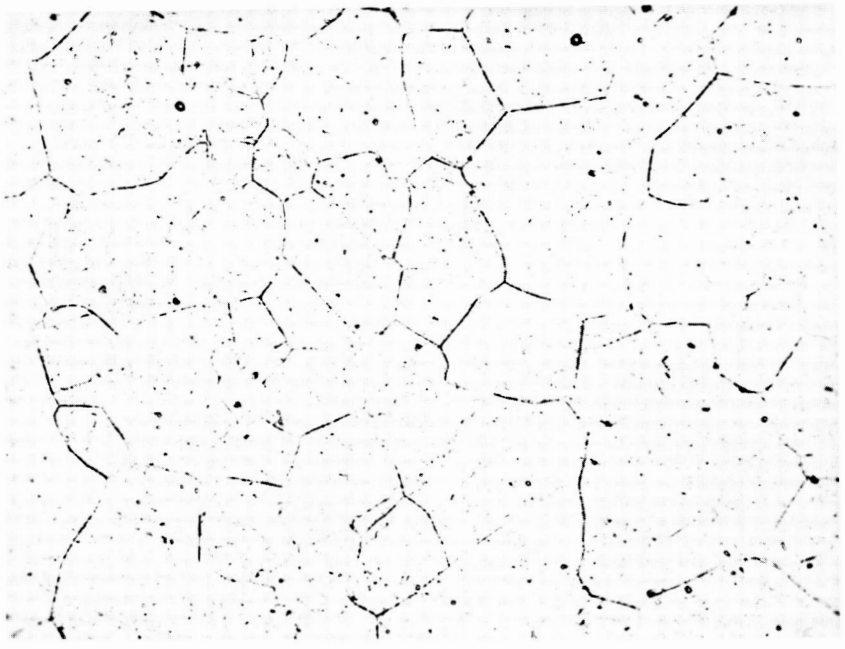

Electrolytically etched in 10 percent chromic acid

FIGURE II-25. Microstructure of Alloy 1-A-56 (57Fe-12Ni-25Co-5Mo-0.5Ti--0.5Al) After 100 Hours Aging at 1022°F (550°C) 500X

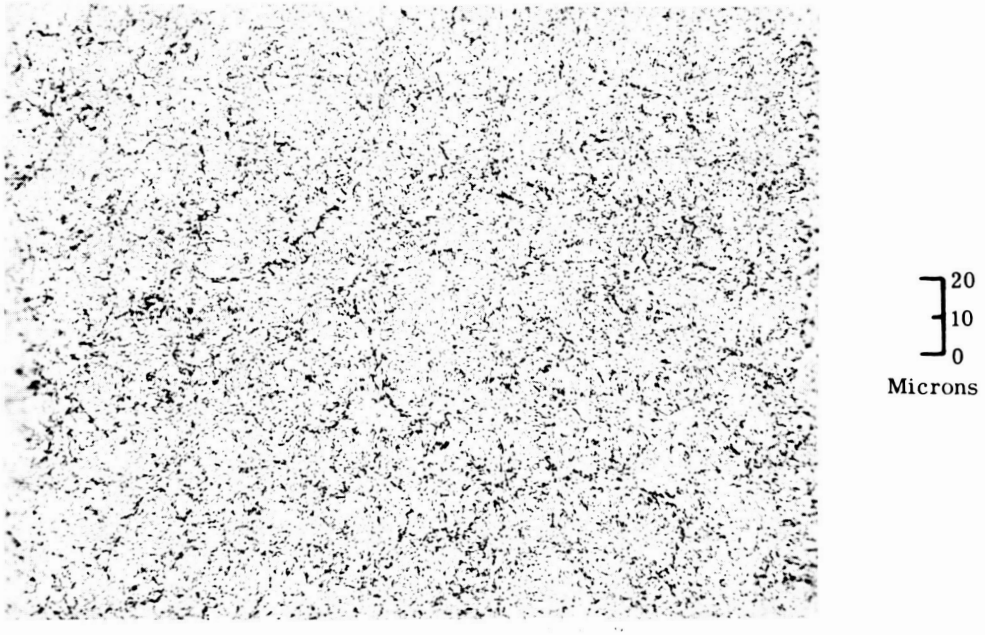

Electrolytically etched in 10 percent chromic acid.

FIGURE II-26. Microstructure of Alloy 1-A-57 (56Fe-12Ni-25Co-5Ta-2W) After 100 Hours Aging at 1022°F (550°C) 500X

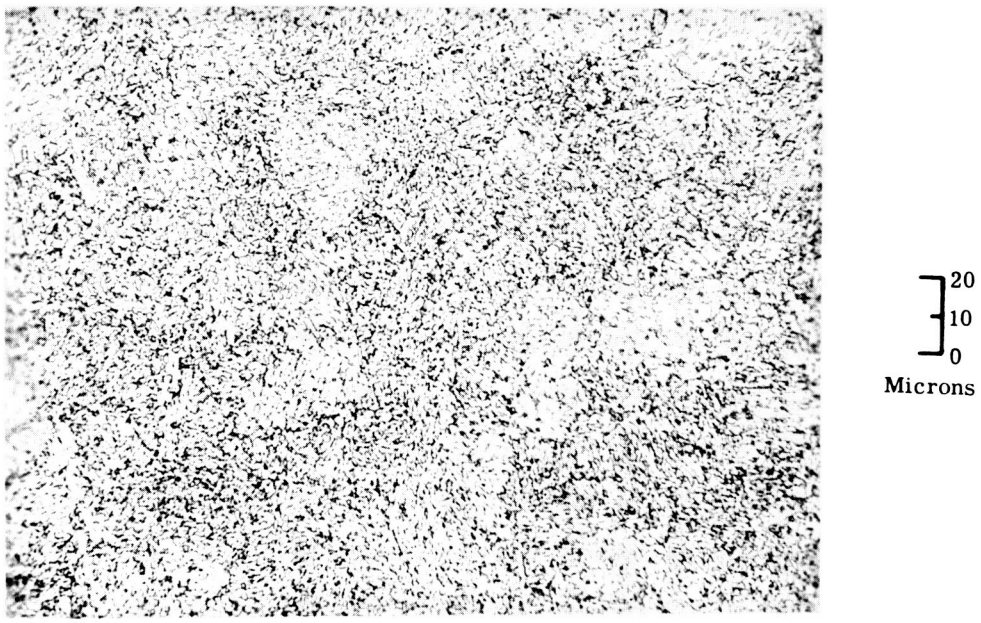

Electrolytically etched in 10 percent chromic acid.

FIGURE II-27. Microstructure of Alloy 1-A-58 (55.9Fe- 12Ni-25Co-4Ta-2W-1Si-0.1Mn) After 100 Hours Aging at 1022°F (550°C) 500X

Electrolytically etched in 10 percent chromic acid.

FIGURE II-28. Microstructure of Alloy 1-A-59 (55.9Fe-12Ni-25Co-3Ta-2W-1Si-0.5Al-0.5Ti-0.1Mn) After 100 Hours Aging at 1022°F (550°C) 500X

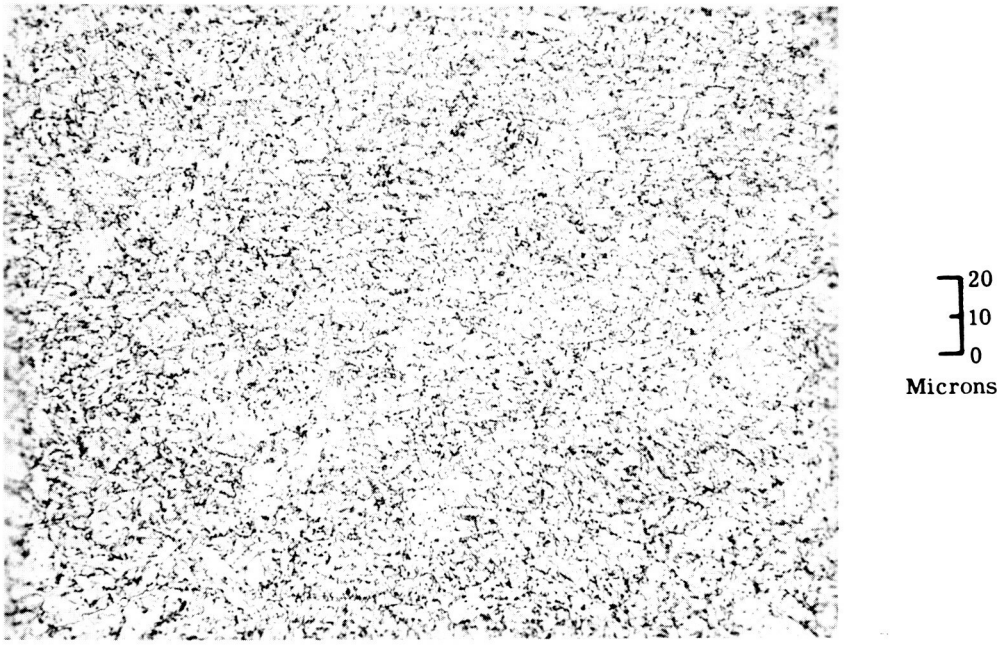

Electrolytically etched in 10 percent chromic acid.

FIGURE II-29. Microstructure of Alloy 1-A-61 (57.4Fe-5Ni-25Co-5Cr-5Ta-0.5Al-0.1Mn-2Si) After 100 Hours Aging at 1022° F (550° C) 500 X

alloys after 100 hours aging at 1292°F (700°C) are shown in Figures II-30 to II-35. Fine second phase particles may be seen in all of the cobalt alloys with the exception of Nivco alloy where the particles are coarse. Grain boundary precipitate is present in all of these alloys. Alloy 1-B-44 has a rather large grain size. With respect to the second phase particles at the grain junctions, this alloy resembles a cast structure which contains segregations. A discontinuous precipitate which covers 10 percent of the matrix has developed in the Nivco alloy. The etching behavior of alloy 1-B-42 containing columbium differed from the other cobalt alloys. The darkening of the grain faces is an indication that the etching solution caused a stronger attack in this alloy. This may indicate presence of fine precipitate particles which are too small to be resolved by the optical microscope. Second phase particles, a few microns in diameter, are present in the alloys, indicating that even 0.3 weight percent zirconium is too high to remain in solid solution after solidification.

Figures II-36 to II-44 show micrographs which were obtained by electron microscopy on the samples 1-A-26 (Fe-12Ni-20Co-1Ti), 1-A-28 (Fe-12Ni-20Co-5Ta), and 1-B-39 (Co-15Ni-5Fe-2.2Ti-1.5Al-0.5Zr-5Ta). Data pertaining to these alloys were presented in detail in the third and fourth quarterly reports. A very fine precipitate is present in alloy 1-A-26 after aging for 100 hours at 1022°F (550°C). The precipitate consists of fine needles with a diameter on the order of 100 Å and a length of 1000 to 2000 Å (see Figures II-36 and II-37). One also observes the presence of very small discs, about 100 to 200 Å in diameter, which may represent needles standing perpendicular to the surface. The orientation of the needles with respect to that of the ground matrix is evident in the transmission micrograph of the alloy 1-A-26 in Figure II-37. Larger particles may be seen at the grain boundaries. Some areas which are free of precipitate are evident in Figure II-36. These areas appear to be particles of a different phase in the transmission micrograph shown in Figure II-37. Phase identification results obtained by electron diffraction are listed in Table II-13 (1-A-26). The diffraction lines of the needle shaped precipitate corresponds closely to the lattice reflections of a Ni_3Ti DO_{24} lattice.

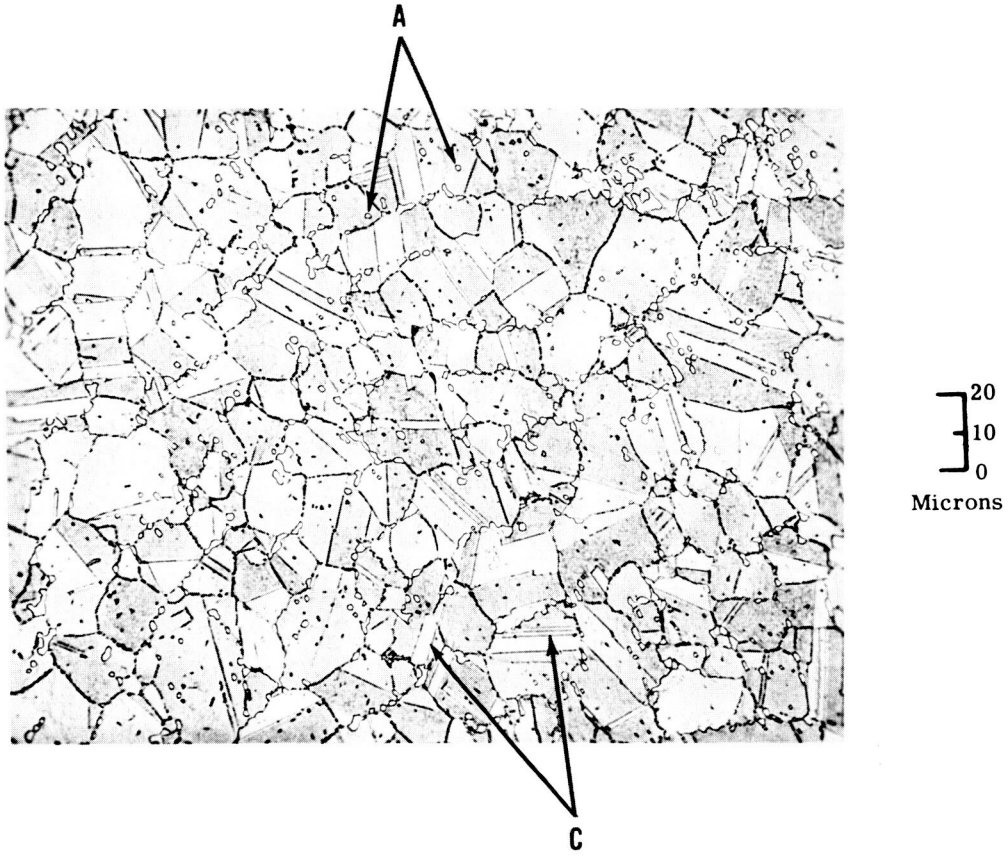

A - Second phase particles
C - Twin boundaries

Etchant: 20 ml HCl, 40 ml HNO_3, 60 ml glycerin

Note: The darkening of grains indicates fine precipitate which is unresolved at 500X

FIGURE II-30. Microstructure of Alloy 1-B-42 (70.8Co-15Ni-5Fe-2.2Ti-1.5Al-0.5Zr-5Nb) After 100 Hours Aging at 1292°F (700°C) 500X

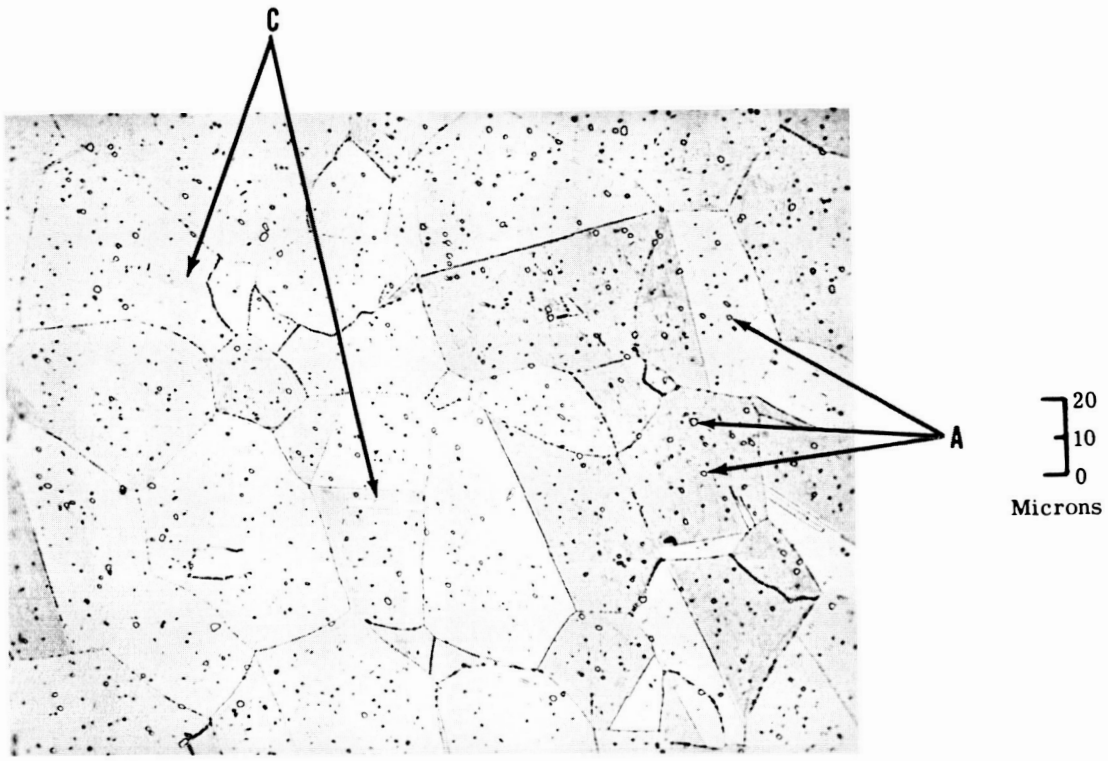

A - Second phase particles
C - Twin boundaries

Etchant: 20 ml HCl, 40 ml HNO_3, 60 ml glycerin

Note: The darkening of grains indicates fine precipitate which is unresolved at 500X

FIGURE II-31. Microstructure of Alloy 1-B-43 (71Co-15Ni-5Fe-2.2Ti-1.5Al-0.3Zr-5Ta) After 100 Hours Aging at 1292°F (700°C) 500X

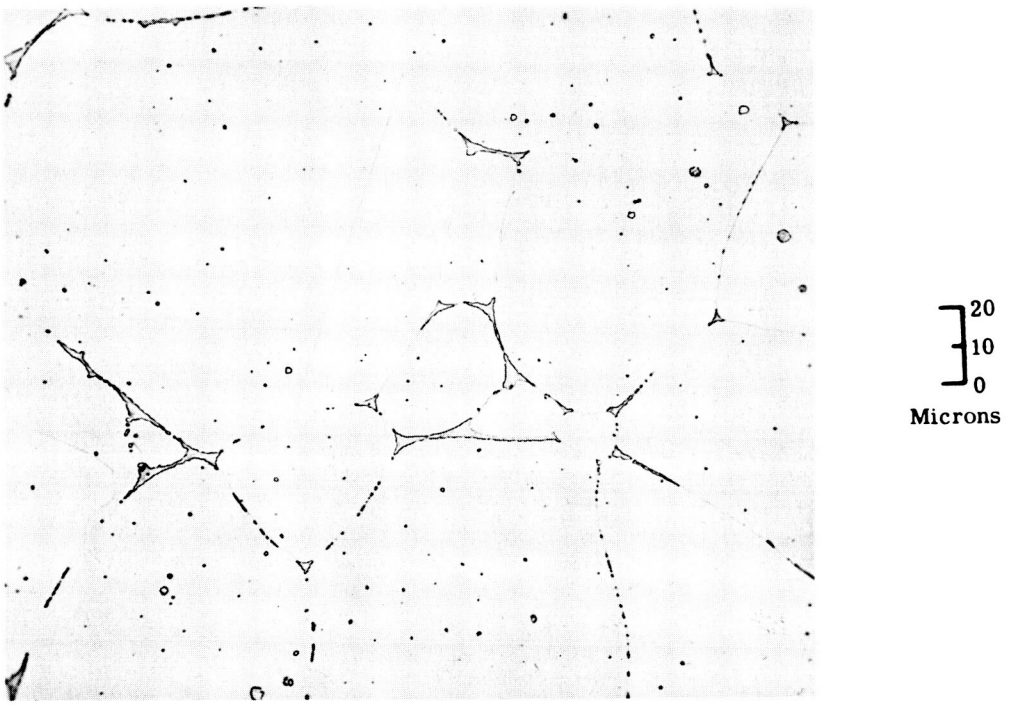

Etchant: 20 ml HCl, 40 ml HNO_3, 60 ml glycerin

FIGURE II-32. Microstructure of Alloy 1-B-44 (73Co-15Ni-5Fe-2.2Ti-1.5Al-0.3Zr-3Ta) After 100 Hours Aging at 1292°F (700°C) 500 X

Etchant: 20 ml HCl, 40 ml HNO_3, 60 ml glycerin

FIGURE II-33. Microstructure of Alloy 1-B-45 (71.7Co-15Ni-5Fe-1.5Ti-1.5Al-0.3Zr-5Ta) After 100 Hours Aging at 1292°F (700°C) 500 X

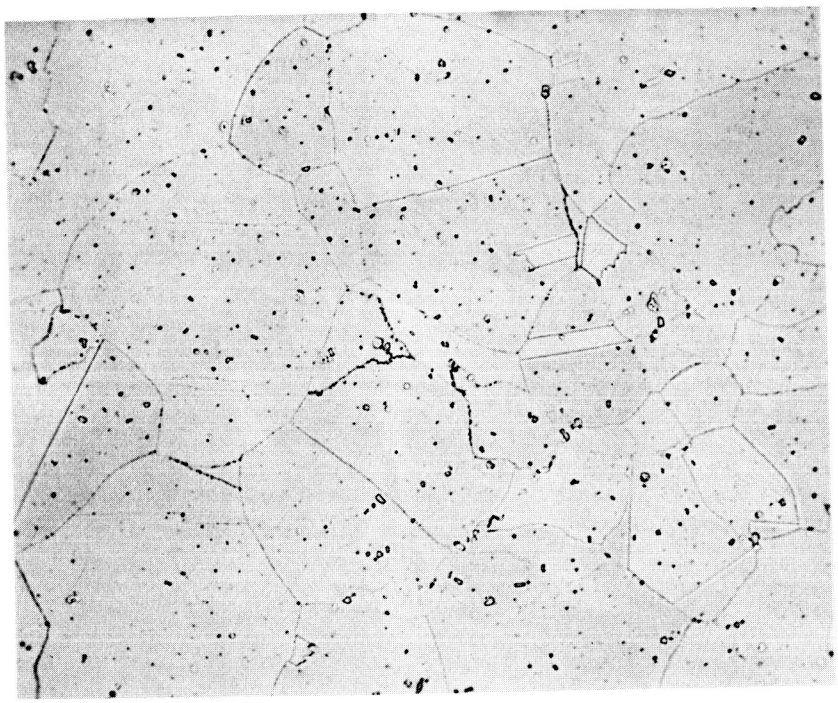

Etchant: 20 ml HCl, 40 ml HNO_3, 60 ml glycerin

FIGURE II-34. Microstructure of Alloy 1-B-46 (76Co-10Ni-5Fe-2.2Ti-1.5Al-0.3Zr-5Ta) After 100 Hours Aging at 1292°F (700°C) 500 X

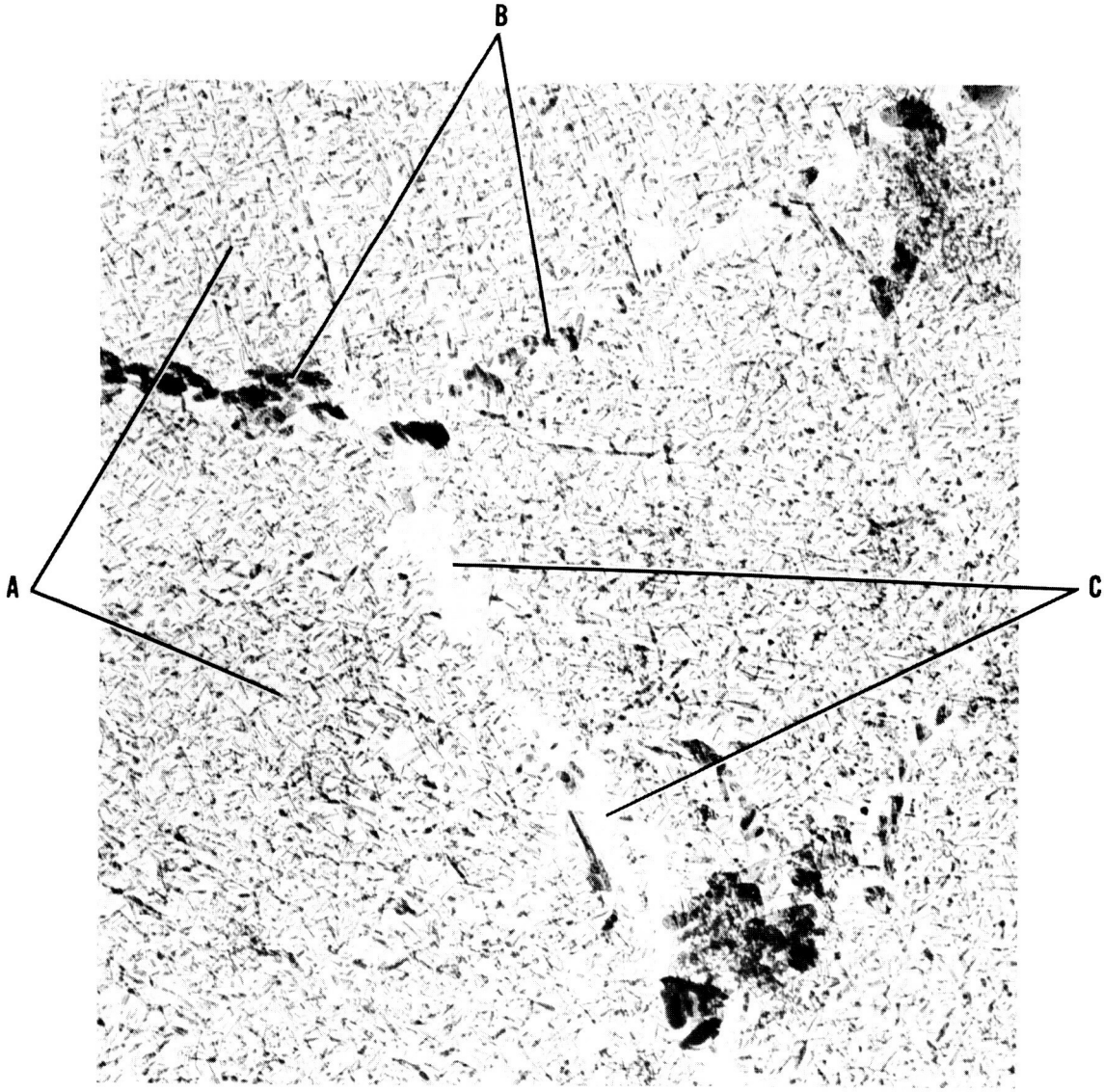

A - Fine needle-like precipitate 100 Å diameter, 1000 to 2000 Å long
B - Grain boundary precipitate
C - Grain boundary free of precipitate

FIGURE II-36. Electron Microscope Replica of Alloy 1-A-26 (67Fe-12Ni-20Co-1Ti) After 100 Hours Aging at 1022°F (550°C) 30,000X

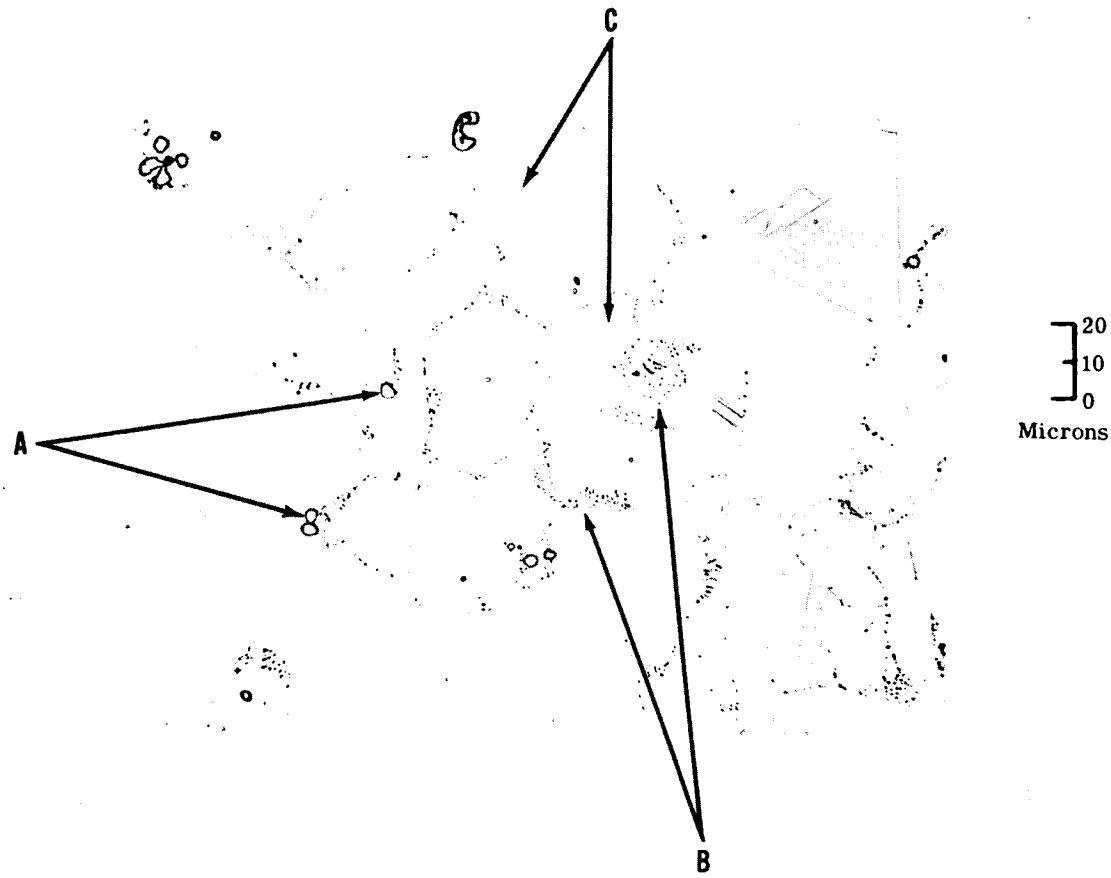

A - Second phase particles
B - Discontinuous precipitate (cellular precipitate at grain boundaries)
C - Twin boundaries

Etchant: 20 ml HCl, 40 ml HNO_3, 60 ml glycerin

Note: The second phase particles are coarser than the ones shown in alloys 1-B-42 to 1-B-46

FIGURE II-35. Microstructure of Nivco Alloy (74Co-23Ni-1Zr-2Ti) After 100 Hours Aging at 1292°F (700°C) 500X

FIGURE II-37. Electron Transmission Micrograph of Alloy 1-A-26 (67Fe-12Ni-20Co-1Ti) After 100 Hours Aging at 1022°F (550°C) 32,000X

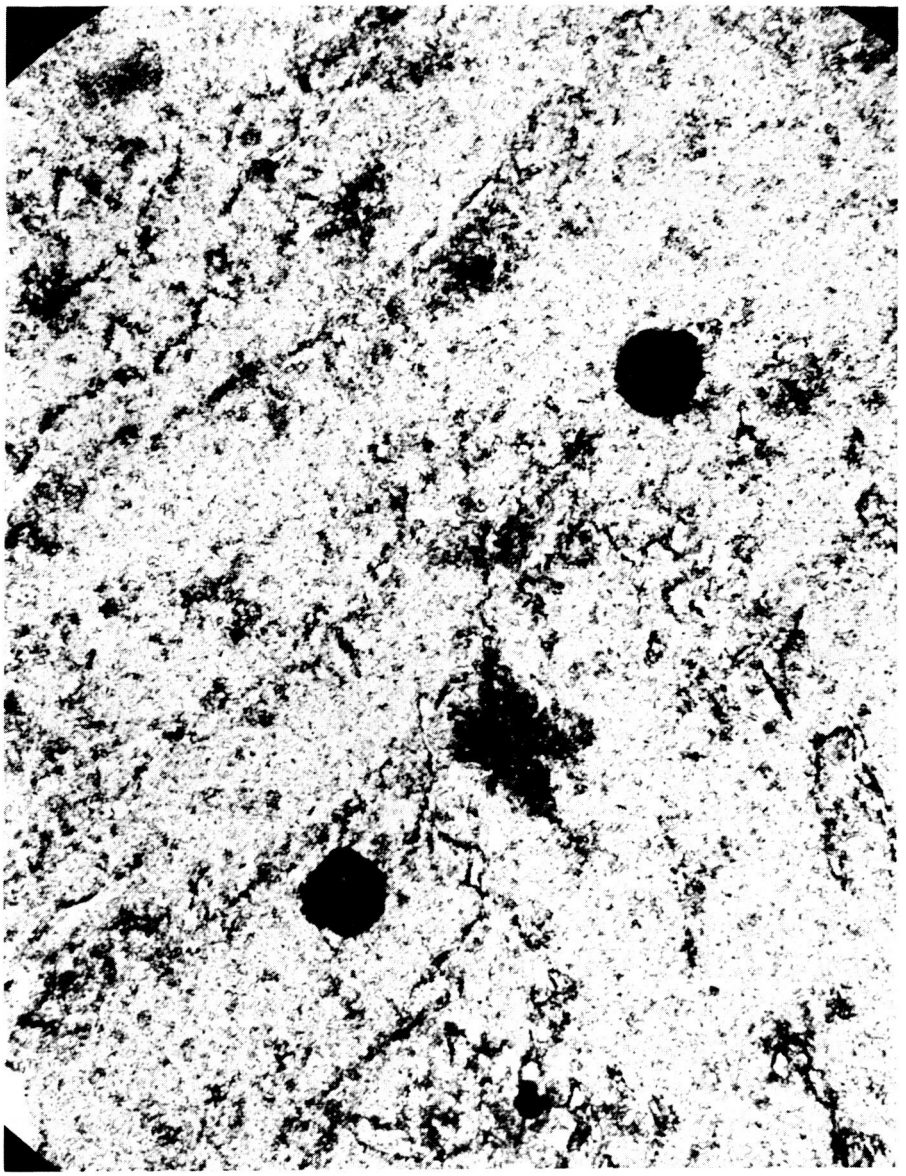

FIGURE II-38. Electron Microscope Replica of Alloy 1-A-27 (63Fe-12Ni-20Co-5Mo) After 100 Hours Aging at 1022°F (550°C) 8000X

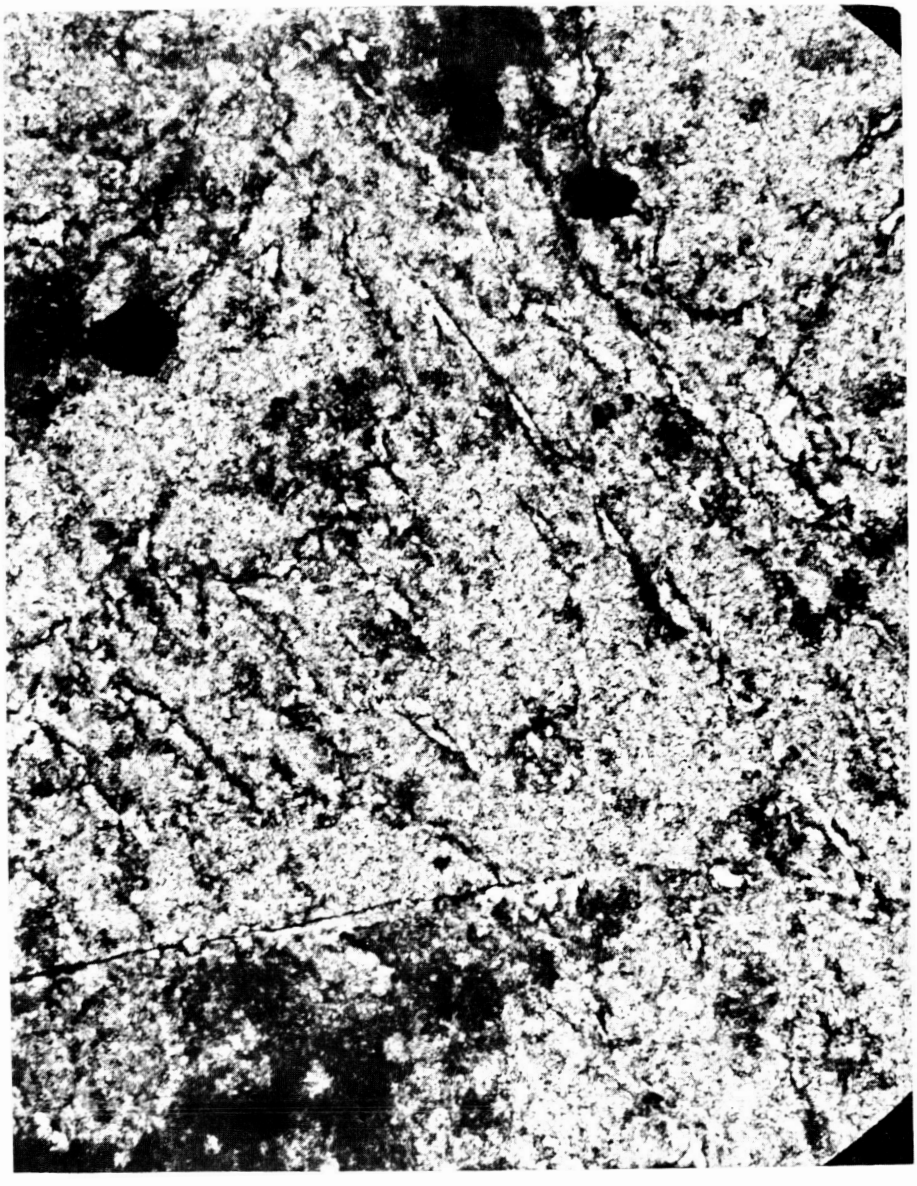

FIGURE II-39. Electron Microscope Replica of Alloy 1-A-27 (63Fe-12Ni-20Co-5Mo) After 100 Hours Aging at 1022°F (550°C) 22,400X

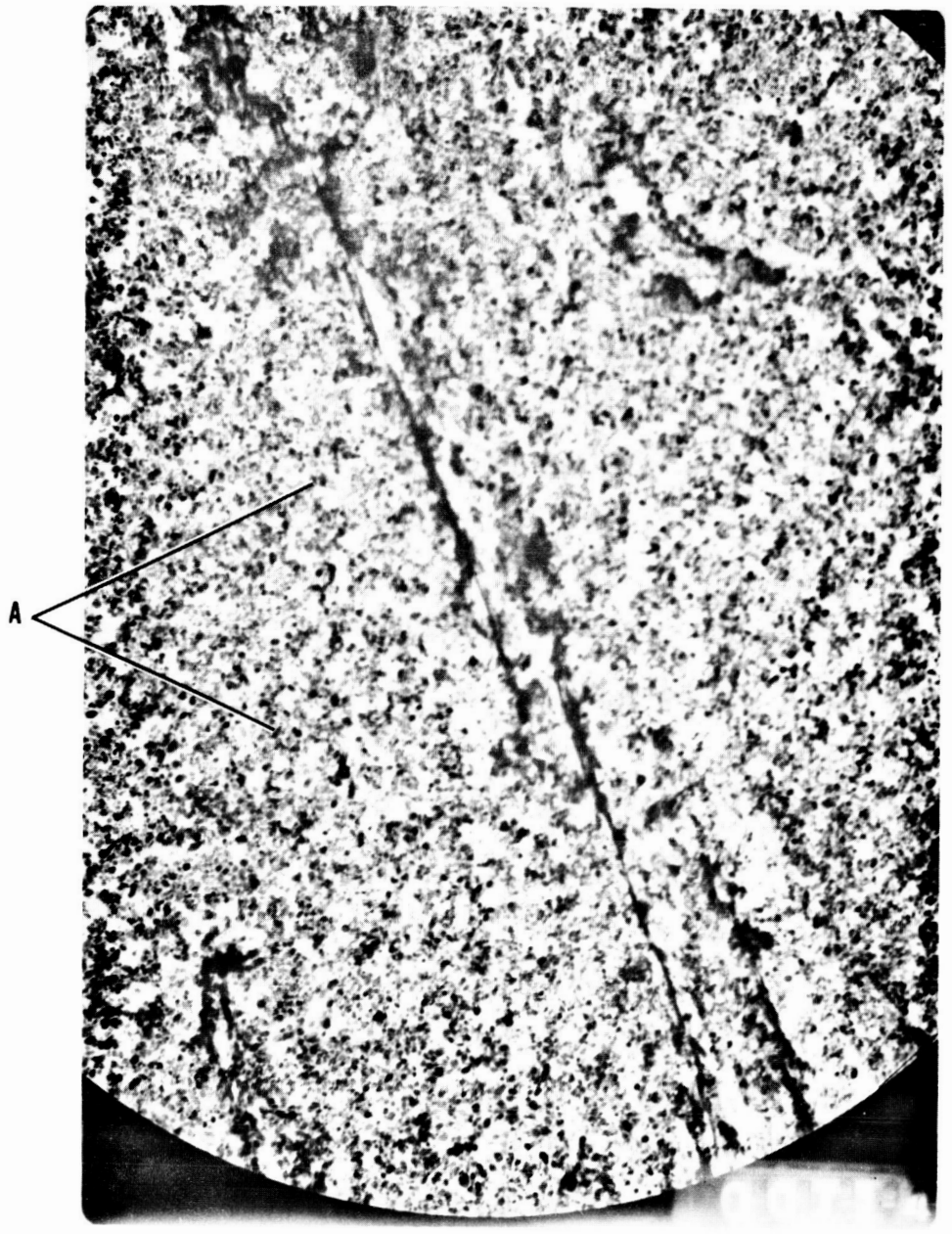

A - Fine precipitate 200 to 1000 Å in diameter

FIGURE II-40. Electron Microscope Replica of Alloy 1-A-27 (63Fe-12Ni-20Co-5Mo) After 100 Hours Aging at 1022°F (550°C) 22,400X

FIGURE II-41. Electron Transmission Micrograph of Alloy 1-A-27 (63Fe-12Ni-20Co-5Mo) After 100 Hours Aging at 1022°F (550°C) 32,000 X

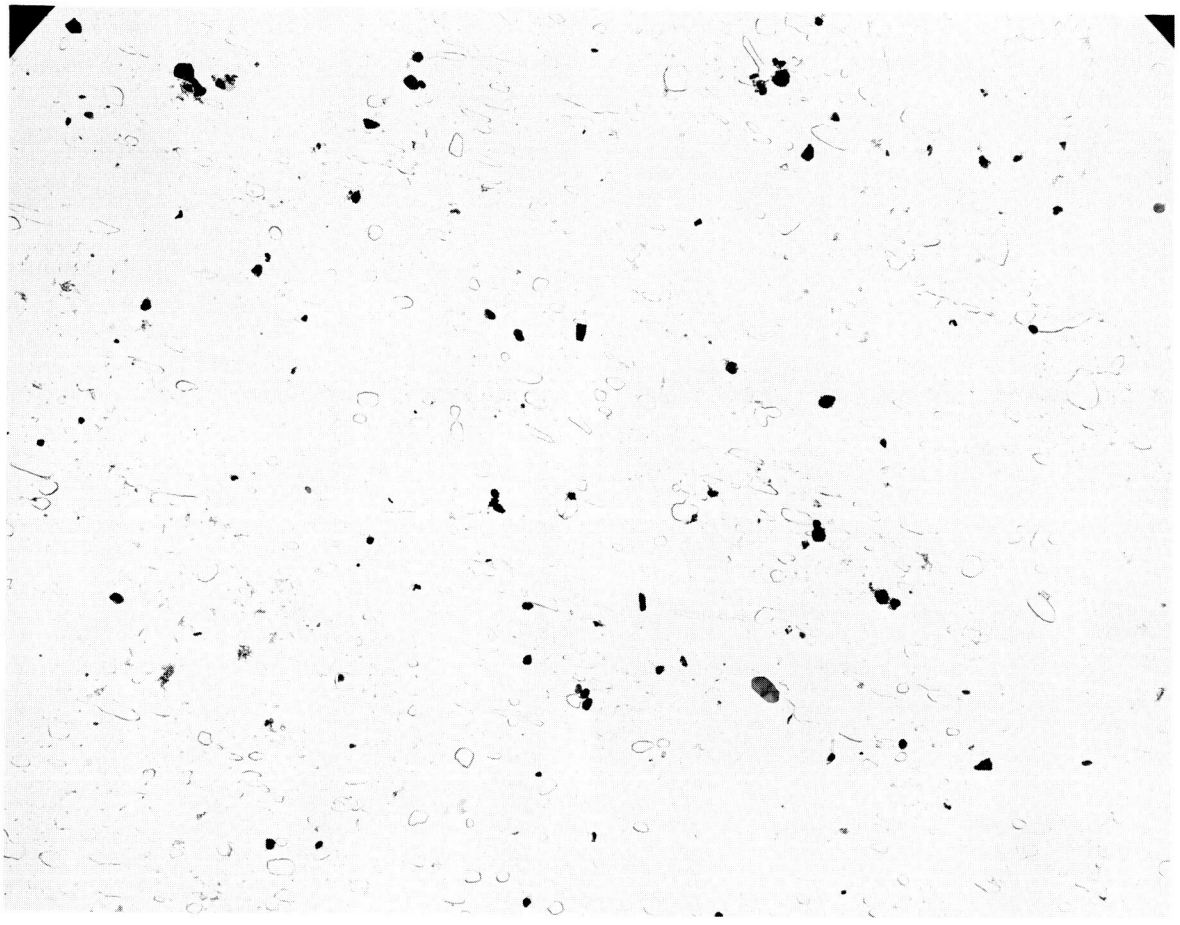

FIGURE II-42. Electron Microscope Replica of Alloy 1-A-28 (66Fe-12Ni-20Co-5Ta) After 100 Hours Aging at 1022°F (550°C) 64,000 X

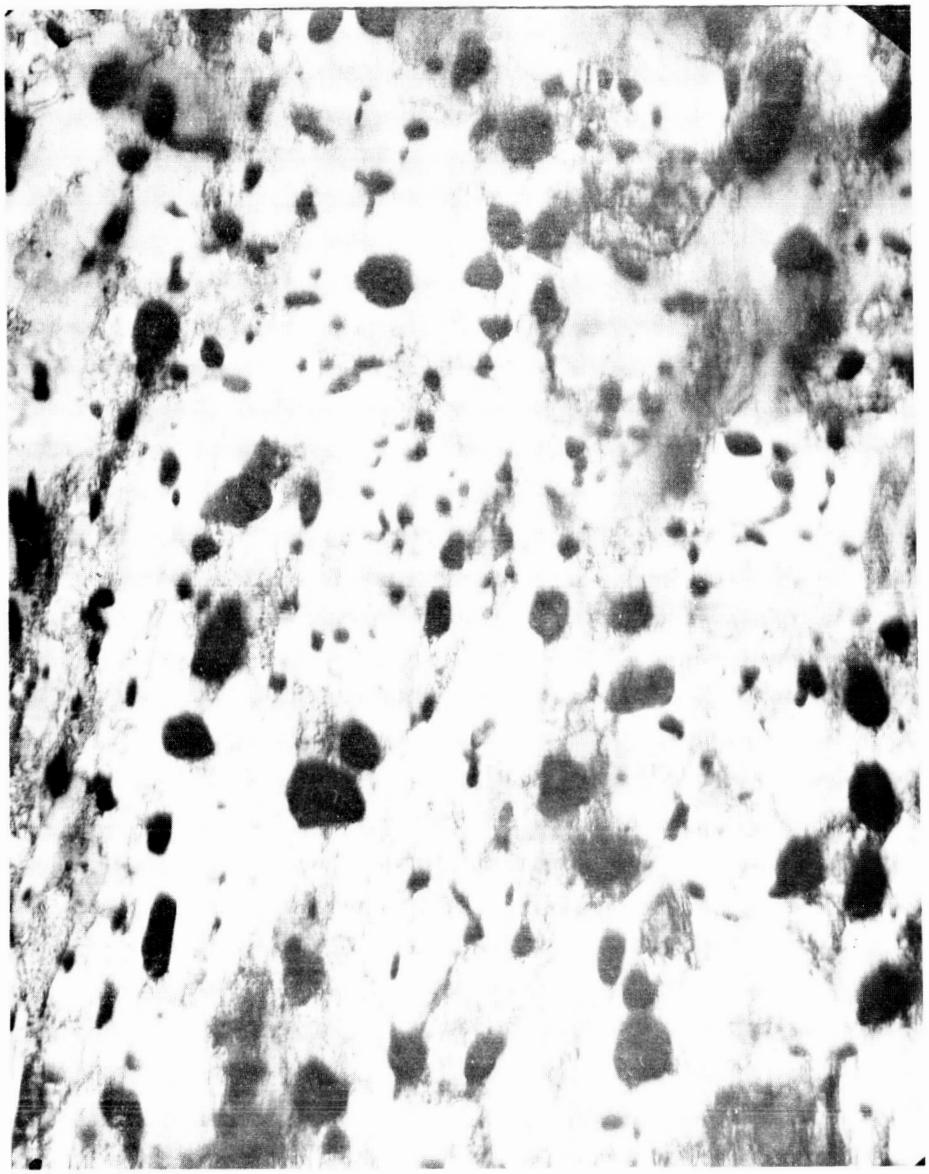

FIGURE II-43. Electron Transmission Micrograph of Alloy 1-A-28 (66Fe-12Ni-20Co-5Ta) After 100 Hours Aging at 1022°F (550°C) 32,000 X

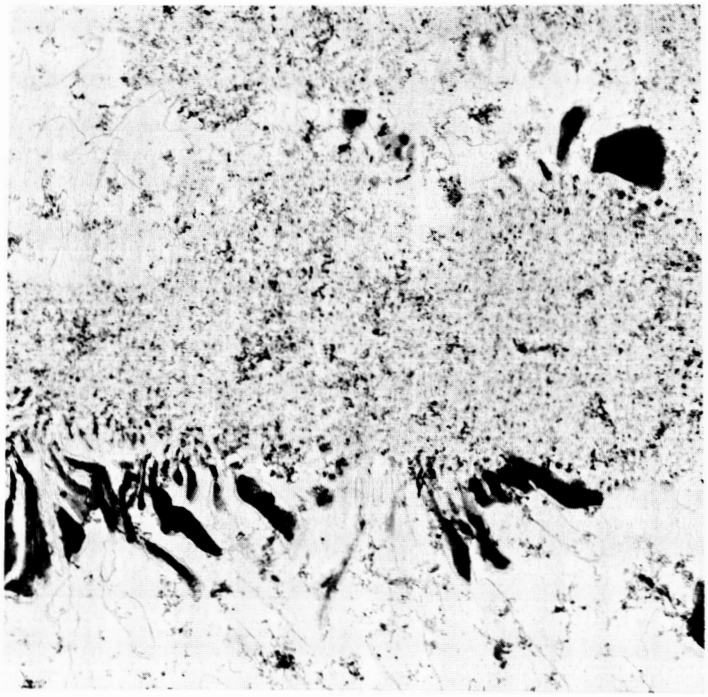

FIGURE II-44. Electron Microscope Replica of Alloy 1-B-39 (70.8Co-15Ni-5Fe-2.2Ti-1.5Al-0.5Zr-5Ta) After 50 Percent Cold Reduction and 100 Hours Aging at 1292°F (700°C) 20,000 X

TABLE II-13. Phases Detected in Alloys 1-A-26, 1-A-27, 1-A-28 After Aging 100 Hours at 1022°F (550°C) and in Alloy 1-B-39 After 50 Percent Deformation and Aging 100 Hours at 1292°F (700°C)

Shape of Phases	Lattice	Probable Identification
1-A-26 (67Fe-12Ni-20Co-1Ti)		
Needles ~100 Å diam ~1000 Å long	hexagonal a_o = 5.1 Å, c = 8.3 Å	Ni_3Ti Do_{24}
Dark globular particles at grain boundaries	cubic a_o = 4.6 Å	Ti(C, N)
Bright particles at boundaries	face centered cubic a_o = 3.6 Å	Austenite A1
1-A-27 (63Fe-12Ni-20Co-5Mo)		
Discs 200 Å diam (some as large as 1000 Å)	tetragonal a_o = 9.2	FeMo $D8_6$
	or	or
Black Stringers 500 Å diam 3 μ long	hexagonal a_o = 4.7, c = 7.7	Fe_2Mo C14
	or both	
Large particles 1 μ diam	cubic a_o = 4.6 Å	Carbonitrides γ'
Large white elongated particles	face centered cubic a_o = 3.6 Å	Austenite A1
1-A-28 (63Fe-12Ni-20Co-5Ta)		
Large particles 0.5 μ diam	hexagonal a_o = 4.8, c = 7.8	Fe_2Ta C14
1-B-39 (70.8Co-15Ni-5Fe-2.2Ti-1.5Al-0.5Zr-5Ta)		
Fine precipitate Larger lamellae	face centered cubic a_o = 3.62	γ similar to Ni_3Al L_2 a_o = 3.561
Coarse particles		
Matrix	face centered cubic a_o = 3.55	
		(The presence of M_6C or $M_{23}C_6$ and M_2C was detected)

The dark globular particles at the boundaries apparently have a cubic lattice. These particles may be tentatively identified as titanium carbonitride. Selected area diffraction of the bright particles at the boundaries show good agreement with reflections from the austenite lattice.

A very dense precipitate of disc-shaped particles with a diameter of 200 to 500 Å is present in alloy 1-A-27 after aging at 1022°F (550°C) for 100 hours (see Figure II-40). In some areas the precipitate particles are as large as 1000 Å in diameter. The presence of a black stringer-like phase is evident, particularly in Figure II-40. These stringers have a diameter of 500 to 1000 Å and many are several microns long. The stringers appear to delineate the substructure of the martensite. Figure II-31 shows bright particles of elongated shapes distributed in rows. Furthermore, very coarse and bulky particles with a diameter of 0.5 μ to 1 μ are present (see Figure II-38). The diffraction lines of the fine precipitate listed in Table II-13 can best be related to the σ phase (Fe-Mo). Because of the similarity of the Laves phase Fe_2Mo with the σ phase one can not clearly distinguish between the two phases and the result can be interpreted as a mixture of both phases. The black stringer phase could not be identified as a separate phase and may therefore be σ phase or Laves phase. Phase identity of the large particles was not established but several diffration spots indicate the presence of a cubic lattice. The bright elongated particles represent austenite. It should be noted that more austenite areas were found in alloy 1-A-27 than in alloy 1-A-26.

Very coarse particles of a second phase are present in alloy 1-A-28 after aging at 1022°F (550°C) for 100 hours (see Figure II-43). The diameter of the smallest particles was about 1000 Å; the mean diameter of the largest particles was about 5000 Å. Only a minor portion of these particles was retained on the replicas. However, a question exists whether these large particles had formed during aging. They might have formed during cooling. This question requires further study. The electron transmission micrograph, seen in Figure II-43, shows that the matrix itself resembles a partially polygonized structure. The diameter of the polygonized network is in the order of 0.2 to 0.5 μ.

In other areas a very dense dislocation structure is present. This observation points to a stablizing effect of submicroscopic precipitation on the dislocation network. The electron diffraction pattern obtained from the larger particles can be best fitted to the hexagonal structure of the Laves phase Fe_2Ta.

The electron microscopy studies reported here have confirmed the concept that maraging is caused by a very fine precipitate which can be resolved only by the electron microscope. In alloy 1-A-26, the Ni_3Ti phase formed in a needle-like shape. This is in agreement with previous results obtained by Reisdorf (ref. 3), Baker (ref. 4), Speich (ref. 5), Miller and Mitchell (ref. 6), and their co-workers. The needles observed on this program were very small even after 100 hours at 1022°F (550°C) indicating that particle growth proceeds at a very slow rate at this temperature. The existence of reverted ausenite has been observed, particularly at grain boundaries. This may be the main reason for overaging which was found in commercial 18 percent nickel maraging steel.

In the alloy 1-A-27 with molybdenum addition, a different precipitate formed. The shape in this case was spherical and the lattice structure points to a Laves phase Fe_2Mo and the sigma phase Fe-Mo. There is some controversy about the nature of precipitate phase containing molybdenum. It has been reported that this phase is Ni_3Mo with a lattice similar to Ni_3Ti (refs. 4 and 5). The existence of molybdenum Laves phase and molybdenum sigma phase has also been reported to be present in commercial maraging steel after prolonged aging (refs. 4 and 6). The results reported here which indicate the presence of a mixture of Fe_2Mo and Fe-Mo sigma phase apply to a state after prolonged aging. The possibility therefore exists that after shorter periods of aging the Ni_3Mo phase is formed as an intermediate phase which then transforms into the equilibrium phase during prolonged aging.

It has been demonstrated previously (see the third quarterly report) that alloy 1-A-27 tends to overage more rapidly than alloys 1-A-26 or 1-A-28. This phenomena may be related to the observation, that the amount of reverted

austenite present in alloy 1-A-27 is greater than in alloys 1-A-26 or 1-A-28. On the other hand, the spherical particles have grown to much larger sizes in some instances, so there is a possibility that particle growth, which occurs in this alloy at a faster rate, is at least partly responsible for overaging at 1022°F (550°C).

The appearance of the microstructure of the alloy 1-A-28 is quite different from that of alloys 1-A-26 and 1-A-27. The presence of larger particles, 0.5 to 1 micron in diameter, which can contribute little to the strengthening, poses two questions. First, the cause of the observed hardening must be determined. Second, the mode of formation of the large particles must be studied. There is a possibility that the large particles had nucleated during cooling after the annealing treatment. The cause of strengthening can be rather fine precipitate at the sites of dislocations, which will dissolve during prolonged aging, thereby causing growth of the larger particles. If this idea is correct, an attempt must be made to eliminate the larger particles being nucleated during a previous treatment before aging.

For the study of the cobalt-base alloys a sample of alloy 1-B-39 was homogenized at 1832°F (1000°C) after the normal aging tests, then cold rolled to a 50 percent reduction in thickness and finally aged for 100 hours at 1022°F (550°C).

The structure was heterogenized to more than 50 percent so that x-ray diffraction of the bulk material as well as electron diffraction and x-ray diffraction of the extracted particles in the replica could be applied. The matrix contains a few rather coarse particles of a second phase which were difficult to identify. Qualitative measurements with the microprobe showed that these coarse particles contain minute quantities of zirconium and tantalum. The precipitate which was present in the form of coarse lamellae or fine particles was identified as the γ' phase with the face centered cubic lattice having a slightly larger lattice constant that the Ni_3Al phase (see Table II-13). A difference in lattice parameter of 2.5 percent was obtained between the parent matrix and the precipitate.

The X-ray and electron microscopic studies of the cobalt-base alloy 1-B-39 produced results similar to those obtained in the studies of the 1-B-15 alloy (see the third quarterly report). Once again γ' forms as the main phase of the precipitate. The addition of tantalum does not influence the lattice constant of the matrix or the precipitate appreciably. A mechanism similar to that advanced by Miller and Mitchell (ref. 6) to describe the strengthening influence of columbium addition on γ' precipitation-hardened nickel-base super alloys applied in the present case. The tantalum content may result in a finer distribution of the particles.

(6) Selection of Alloys for 300 Gram Vacuum Arc Melts

The results of all the screening tests performed during this program are listed in Tables II-14 and II-15. The purpose of the screening test was to find an alloy composition that could be expected to have the required creep strength and magnetic properties. The tests, however, were confined to hardness measurements, coercive force measurements, and magnetic saturation measurements at room temperature and 1112°F (600°C). In the case of the martensitic alloys, transformation temperature was also measured by the dilatometer technique. All of these measurements were readily performed on small samples which could be obtained from 20 to 25 gram levitation melts. The data from the tests were evaluated to determine the most promising compositions.

Martensitic Alloys

In the case of the martensitic alloys the following criteria were used:

a) Transformation should not start at a temperature below the upper limit of the anticipated range of service temperature. Therefore, all of the alloys which showed an A_s temperature during a slow rate of heating (0.9°F/min), which was less than 1202°F (650°C), were eliminated.

b) The magnetic saturation at 1112°F (600°C) should be well in excess of the saturation of

TABLE II-14. Results of Screening Tests on Levitation-Melted Martensitic Alloys

Alloy Number	Nominal Alloy Composition (weight percent)	Transformation Temperature (As)[a] On Heating 0.9°F/Min (°F)	Transformation Temperature (As)[a] On Heating 0.5°C/Min (°C)	Saturation Magnetic Moment at 1112°F (600°C) (emu/g)[b]	Isochronal Tests: Aging Temperature at which Maximum Hardness was Obtained (°F)	Isochronal Tests: Aging Temperature at which Maximum Hardness was Obtained (°C)	Isochronal Tests: Maximum Room Temperature Hardness (VHN_m)	Isochronal Tests: Room Temperature Coercivity at Maximum Hardness (Oe)	Isothermal Tests (After 100 Hours at 1022°F (550°C)): Room Temperature Hardness VHN_{100}	Isothermal Tests (After 100 Hours at 1022°F (550°C)): Room Temperature Coercivity $H_{c_{100}}$ (Oe)	Isothermal Tests (After 100 Hours at 1022°F (550°C)): Δ VHN[d] (%)
For Comparison											
15% Ni Maraging Steel	71.1 Fe-15Ni-8Co-4.5Mo-0.7 Al-0.7Ti	1036	558	130	1022	550	607	17.5	539	60	10
LM10	55 Fe-15Ni-25Co-5Ta	-	-	164	1022	550	632	29	557	32.0	11
1-A-1	55 Fe-15Ni-25Co-5W	1087	586	153	932	500	610	33.5	511	27.5	10
1-A-2	58 Fe-15Ni-25Co-2Nb	1193	645	168	932	500	558	27.4	494	21.0	10
1-A-3	58 Fe-15Ni-25Co-2V	1112	600	158	932	500	390	18.3	363	21.0	10
1-A-4	58 Fe-15Ni-25Co-2Cr	1065	574	150	1022	550	391	20.1	-	-	-
1-A-5	59.5 Fe-15Ni-25Co-0.5Al	1164	629	169	1022	550	412	14.7	351	150	15
1-A-6W	59.5 Fe-15Ni-25Co-0.5Be	-	-	(170)[c]	932	500	717	19.1	451	20.0	22
1-A-7	58 Fe-15Ni-25Co-2Sb	1175	635	163	brittle, no test			-	-	-	-
1-A-8	58 Fe-15Ni-25Co-2Sn	1112	600	166	brittle, no test			-	-	-	-
1-A-9	58 Fe-15Ni-25Co-2Si	1195	646	154	842	450	468	24.2	-	-	-
1-A-10	58 Fe-15Ni-25Co-2Mn	1058	570	151	932	500	482	16.3	-	-	-
1-A-26	67 Fe-12Ni-20Co-1Ti	1317	714	181	1022	550	502	18.0	413	20	11
1-A-27	63 Fe-12Ni-20Co-5Mo	1233	667	161	1022	550	629	26.0	488	20	21
1-A-28	63 Fe-12Ni-20Co-5Ta	1310	710	171	1022	550	541	24	452	23	19
1-A-29	66 Fe-12Ni-20Co-2Nb	1330	721	175	1022	550	538	20.5	425	21	20
1-A-30	66 Fe-12Ni-20Co-2W	1224	662	174	1112	600	354	16	-	-	-
1-A-31	67.5 Fe-12Ni-20Co-0.5Be	1332	722	179	932	500	639	21.5	372	21	22
1-A-32	67.5 Fe-12Ni-20Co-0.5Al	1411	766	177	1022	550	337	11.0	-	-	-
1-A-21	54.5 Fe-15Ni-25Co-0.5Ti-5Mo	1148	620	143	932	500	684	29.3	553	36.7	23
1-A-22	54.5 Fe-15Ni-25Co-0.5Ti-5Ta	1242	672	158	1022	550	682	30.1	598	37.8	10
1-A-23	54.5 Fe-15Ni-25Co-0.5Ti-2Mo-3Ta	1224	662	156	1022	550	664	30.0	577	43.2	11
1-A-24	54 Fe-15Ni-25Co-1Nb-5Ta	1249	676	161	932	500	649	36.0	533	34.1	11
1-A-25	52.5 Fe-15Ni-25Co-0.5Be-5Ta-2Si	1276	691	148	brittle, no test			-	-	-	-
1-A-33	54.5 Fe-15Ni-25Co-0.5Be-5Ta-0.1Mn	1292	700	160	1022	550	810	44.5	673	45.0	19
1-A-34	53.9 Fe-15Ni-25Co-1W-5Ta-0.1Mn	1260	682	156	1022	550	642	31.0	617	32.0	11
1-A-35	54.4 Fe-15Ni-25Co-0.5Al-5Ta-0.1Mn	1272	688	161	1022	550	649	31.0	646	40.5	4
1-A-36	53.9 Fe-15Ni-25Co-0.5Al-0.5Ti-5Ta-0.1Mn	1292	700	156	1022	550	687	34.0	696	46.0	2
1-A-37	53.9 Fe-15Ni-25Co-0.5Al-0.5Ti-2Mo-3Ta-0.1Mn	1256	680	150	1022	550	674	32.0	688	57.0	4

(a) As - beginning of transformation from α into γ during heating at 0.9°F (0.5°C).

(b) To convert saturation magnetic moment to the approximate induction in gauss, multiply the listed value by 100.

(c) Interpolated value.

(d) Δ VHN, the change in hardness during aging at 1022°F (550°C) or $\frac{VHN_1 - VHN_{100}}{VHN_1} \times 100$.

TABLE II-14. Results of Screening Tests on Levitation-Melted Martensitic Alloys - Continued

Alloy Number	Nominal Alloy Composition (weight percent)	Transformation Temperature (As)[a] On Heating 0.9°F/Min (°F)	Transformation Temperature (As)[a] On Heating 0.5°C/Min (°C)	Saturation Magnetic Moment at 1112°F (600°C) (emu/g)[b]	Isochronal Tests: Aging Temperature at which Maximum Hardness was Obtained (°F)	Isochronal Tests: Aging Temperature at which Maximum Hardness was Obtained (°C)	Isochronal Tests: Maximum Room Temperature Hardness (VHN_m)	Isochronal Tests: Room Temperature Coercivity at Maximum Hardness (Oe)	Isothermal Tests (After 100 Hours at 1022°F (550°C)): Room Temperature Hardness VHN_{100}	Isothermal Tests (After 100 Hours at 1022°F (550°C)): Room Temperature Coercivity $H_{c_{100}}$ (Oe)	Isothermal Tests (After 100 Hours at 1022°F (550°C)): Δ VHN[d] (%)
For Comparison											
15% Ni Maraging Steel	71.1Fe-15Ni-8Co-4.5Mo-0.7 Al-0.7Ti	1036	558	130	1022	550	607	17.5	539	60	10
1-A-43	55 Fe-15Ni-25Co-2Mo-3Ta	1222	661	147	1022	550	695	31.0	534	40.0	14
1-A-44	53 Fe-15Ni-25Co-2Cr-5Ta	1112	600	122	1022	550	663	35.0	574	53.0	14
1-A-45	57.5 Fe-15Ni-25Co-2Cr-0.5Be	1069	576	137	842	450	757	39.0	466	33.0	24
1-A-46	56 Fe-15Ni-25Co-2Cr-2Si	1040	560	119	842	450	568	29.5	446	37.0	18
1-A-47	53 Fe-15Ni-25Co-2V-5Ta	1222	661	145	1022	550	677	31.0	607	56.0	10
1-A-48	53 Fe-15Ni-25Co-2Si-5Ta	1265	685	147	1022	550	663	30.5	565	30.0	10
1-A-49	56 Fe-15Ni-25Co-2Si-2W	1218	659	129	932	500	572	30.5	452	26.5	10
1-A-50	57 Fe-15Ni-25Co-1Si-2V	1337	725	133	842	450	546	29.5	450	27.5	10
1-A-51	58 Fe-15Ni-25Co-1Si-1Ti	1308	709	166	932	500	616	29.5	523	23.0	15
1-A-52	56 Fe-15Ni-25Co-2Mo-2W	1175	635	143	932	500	577	30.0	502	25.0	11
1-A-53	54.9 Fe-15Ni-25Co-1Si-3Ta-0.5Al-0.5Ti-0.1Mn	1260	682	157	1022	550	732	30.0	670	46.0	5
1-A-54	55.9 Fe-12Ni-25Co-5Ta-2Si-0.1Mn	1310	710	159	brittle, no test			-	-	-	-
1-A-55	57 Fe-12Ni-25Co-5Ta-0.5Ti-0.5Al	1382	750	167	1022	550	663	33.5	629	43.0	6
1-A-56	57 Fe-12Ni-25Co-5Mo-0.5Ti-0.5Al	1233	667	160	1022	550	732	25.0	660	51.0	13
1-A-57	56 Fe-12Ni-25Co-5Ta-2W	1292	700	165	1022	550	629	35.0	570	33.0	11
1-A-58	55.9 Fe-12Ni-25Co-4Ta-1Si-0.1Mn	1242	672	161	1022	550	649	39.0	557	33.0	13
1-A-59	55.9Fe-12Ni-25Co-3Ta-2W-1Si-0.5Al-0.5Ti-0.1Mn	1301	705	160	1022	550	692	39.0	697	48.5	2.3
1-A-60	55.9 Fe-12Ni-25Co-4Ta-2Si-0.5Al-0.5Ti-0.1Mn	1303	706	158	brittle, no test			-	-	-	-
1-A-38	69.9 Fe-25Co-5Ta-0.1Mn	1740	949	192	1022	550	259	14.0	-	-	-
1-A-41	66 Fe-25Co-5Ta-4Mn	1416	769	174	brittle, no test			-	-	-	-
1-A-40	62 Fe-5Ni-25Co-5Ta-3Mn	1292	700	171	brittle, no test			-	-	-	-
1-A-39	64.9 Fe-5Ni-25Co-5Ta-0.1Mn	1517	825	182	brittle, no test			-	-	-	-
1-A-42	59.9 Fe-5Ni-25Co-5Cr-5Ta-0.1Mn	1222	661	152	1022	550	533	36.0	518	37.0	8
1-A-61	57.4 Fe-5Ni-25Co-5Cr-5Ta-0.5Al-2Si-0.1Mn	1220	660	136	1022	550	616	40.0	571	38.0	7

(a) As - beginning of transformation from α into γ during heating at 0.9°F (0.5°C).

(b) To convert saturation magnetic moment to the approximate induction in gauss, multiply the listed value by 100.

(c) Interpolated value.

(d) Δ VHN, the change in hardness during aging at 1022°F (550°C) or $\frac{VHN_1 - VHN_{100}}{VHN_1} \times 100$

TABLE II-15. Results of Screening Tests on Levitation-Melted Cobalt Base Alloys

			Isochronal Tests				Isothermal Tests (After 100 hours 1292°F (700°C)		
Alloy Number	Nominal Alloy Composition (weight percent)	Saturation Magnetic Moment at 1112°F (600°C) (emu/g)[a]	Aging Temperature at which Maximum Hardness was Obtained (°F)	(°C)	Maximum Room Temperature Hardness (VHN_m)	Room Temperature Coercivity at Maximum Hardness (Oe)	Room Temperature Hardness VHN_{100}	Room Temperature Coercivity H_{c100} (Oe)	Discontinuous Precipitate (Volume Percent)
Nivco Alloy	73.4 Co-23.4Ni-0.3Fe-1.7Ti-0.4Al-0.2Zr-0.3Si-0.3Mn	100	1202	650	272	3.9	303	17.0	10
1-B-13	86 Co-5Ni-5Fe-3Ti-1Al	109	1112	600	218	1.62	220	7	4
1-B-14	81 Co-10Ni-5Fe-3Ti-1Al	106	1292	700	239	2.45	260	8.5	4
1-B-15	76 Co-15Ni-5Fe-3Ti-1Al	102	1292	700	273	3.36	290	10.5	5
1-B-21	76.5 Co-20Ni-2Ti-0.5Al-1Zr	105	1292	700	329	7.65	346	15.1	4
1-B-22	77.3 Co-20Ni-2Ti-0.5Al-0.2Zr	108	1292	700	309	5.00	331	11.0	3
1-B-23	77.5 Co-20Ni-2Ti-0.5Al	102	1202	650	280	3.03	325	10.8	13
1-B-24	76 Co-20Ni-3Ti-1Al	100	1292	700	327	6.41	351	15.2	17
1-B-25	71 Co-20Ni-5Fe-3Ti-1Al	100	1292	700	290	4.3	332	7.8	6
1-B-26	66 Co-20Ni-10Fe-3Ti-1Al	100	1292	700	270	3.3	310	5.0	2
1-B-27	81 Co-15Ni-3Ti-1Al	103	1292	700	310	3.8	335	15.1	9
1-B-28	71 Co-15Ni-10Fe-3Ti-1Al	102	1292	700	258	3.4	289	4.7	1
1-B-29	75.7 Co-15Ni-5Fe-3.8Ti-0.5Al	104	1292	700	303	3.5	340	10.0	5
1-B-30	76.3 Co-15Ni-5Fe-2.2Ti-1.5Al	103	1292	700	239	3.1	269	4.6	1
1-B-31	76.3 Co-15Ni-5Fe-1.4Ti-2.0Al	104	1202	650	209	1.9	221	3.0	0
1-B-32	75.8 Co-15Ni-5Fe-2.2Ti-1.5Al-0.5Zr	103	1292	700	264	3.8	297	8.7	0
1-B-33	70.8 Co-15Ni-5Fe-2.2Ti-1.5Al-0.5Zr-5Cu	93	1202	650	280	4.0	301	17.0	0
1-B-34	70.8 Co-15Ni-5Fe-2.2Ti-1.5Al-0.5Zr-5Mn	65	1112	600	224	2.5	-	-	-
1-B-35	73.8 Co-15Ni-5Fe-2.2Ti-1.5Al-0.5Zr-2Si	79	1112	600	293	5.0	282	29.0	0
1-B-36	75.3 Co-15Ni-5Fe-2.2Ti-1.5Al-0.5Zr-0.5Be	97	1382	750	353	42.0	377	82.0	1
1-B-37	70.8 Co-15Ni-5Fe-2.2Ti-1.5Al-0.5Zr-5Cr	32	1202	650	256	3.0	269	8.4	0
1-B-38	70.8 Co-15Ni-5Fe-2.2Ti-1.5Al-0.5Zr-5W	84	1382	750	328	5.3	378	10.5	1
1-B-39	70.8 Co-15Ni-5Fe-2.2Ti-1.5Al-0.5Zr-5Ta	90	1382	750	383	7.1	420	19.0	0
1-B-40	70.8 Co-15Ni-5Fe-2.2Ti-1.5Al-0.5Zr-5Mo	70	1292	700	330	5.85	389	32.0	0
1-B-41	70.8 Co-15Ni-5Fe-2.2Ti-1.5Al-0.5Zr-5V	62	1202	650	287	3.3	337	38.0	0
1-B-42	70.8 Co-15Ni-5Fe-2.2Ti-1.5Al-0.5Zr-5Nb	82	1382	750	433	20.0	440	93.0	0
1-B-43	71 Co-15Ni-5Fe-2.2Ti-1.5Al-0.3Zr-5Ta	90	1382	750	393	7.2	422	34.0	0
1-B-44	73 Co-15Ni-5Fe-2.2Ti-1.5Al-0.3Zr-3Ta	95	1382	750	339	4.9	402	21.0	0
1-B-45	71.7 Co-15Ni-5Fe-1.5Ti-1.5Al-0.3Zr-5Ta	94	1382	750	385	6.8	420	22.0	0
1-B-46	76 Co-10Ni-5Fe-2.2Ti-1.5Al-0.3Zr-5Ta	93	1382	750	380	6.9	431	28.5	0

(a) To convert saturation magnetic moment to the approximate induction in gauss, multiply the listed value by 110.

the best available material (B_S = 13,000 gauss at 1112°F in H-11 steel and 15 percent nickel maraging steel). Attention was therefore focused only on those alloys in which the measured magnetic moment per gram at 1112°F (600°C) was higher than 150 (equivalent to B_S = 15,000 gauss).

c) Only those alloys which exhibited substantial age hardening were considered. In order to be comparable with commercially available materials such as H-11 steel or 15 percent nickel maraging steel, the hardness measured at room temperature during isochronal or isothermal aging was required to be at least 550 VHN.

d) The values of coercivity associated with these hardness measurements should be relatively low. It is difficult to select a definite limit on the measured room temperature values. The coercive force will decrease at elevated temperatures (ref. 7). Since it is difficult to predict the amount of decrease, an arbitrary room temperature value of H_c = 50 oersteds was selected as the limit which should not be exceeded even after 100 hours aging at 1022°F (550°C).

e) The most important criterion is the stability of the structure. Yet, there is no such stability in its genuine meaning, which would forbid any diffusion controlled process to proceed in measurable times. In all of the alloys tested, age hardening was promoted in the temperature range between the 842 and 1202°F (450 and 650°C). This indicated that the diffusion controlled precipitation - reaction proceeds in measurable times. Therefore, it is desirable to find conditions which establish a certain state of structure defined as dynamically stable. Such a state requires that hardness and strength remain nearly at a constant level during exposure at temperature while some diffusion controlled

processes may continue. Practically all creep resistant alloys make use of such state of structure, stable only in its dynamic sense.

It is common experience that such behavior is related to the temperature at which the maximum hardness is obtained during isochronal aging. The anticipated service temperature may be higher than the temperature at which maximum hardness is attained; however, in those cases one has to anticipate that overaging will occur at prolonged exposure times at temperature.

Therefore, it appears reasonable to focus attention only on those alloys exhibiting a maximum hardness temperature of at least 1022°F (550°C). In addition, the decrease of hardness from the maximum value obtained during the isothermal aging at 1022°F (550°C) to the value obtained after 100 hours should be less than 10 percent.

In applying the listed criteria one notices that the commercially available 15 percent nickel maraging steel does not fulfill or even approach these requirements. The screened alloys 1-A-22, 1-A-35, 1-A-36, 1-A-53, 1-A-55, and 1-A-59 fulfill all of the requirements simultaneously. The alloys LM10, 1-A-23, 1-A-34, 1-A-48, 1-A-57, and 1-A-61 very nearly fulfill the requirements. These results enable us to derive a most suitable alloy composition.

However, some ambiguity still remains regarding the exact amount of added elements to use for the best combination. Furthermore, one should be cautioned in assuming that the nominal weight percent is the actual amount present in the 20 gram ingots. Deviations of 20 percent may be expected based on previous experience with levitation melts. The results of the screening tests obtained from the levitation melts can provide certain ranges of the most suitable composition and it is the purpose of the next step to

narrow the limits of these ranges still further.

The limits of the most suitable nickel content may be defined as 10 to 15 weight percent. The cobalt content may vary between 20 and 30 weight percent. As far as the beneficial additions of Ta, W, Si, Cr, Al, and Ti in the above listed test alloys are concerned, Si may be eliminated, even in advantageous combination with other elements, for the following reasons: silicon addition has an embrittling effect, as noted in many cases. It furthermore reduces the magnetic saturation drastically. In comparing alloy 1-A-53 with 1-A-36, the former did not show improvement in other properties when silicon was added in similar combinations (see Table II-14). Comparing 1-A-48 with LM10 (see Table II-14) shows that the addition of silicon produced only marginal benefits as far as hardness and stability were concerned.

The addition of chromium has a very detrimental effect on stability of the α phase and on the magnetic saturation. Therefore, chromium can only be tolerated as an addition when a substantial reduction in nickel compensates for the detrimental effects of chromium.

The addition of tantalum has proven beneficial in nearly any combination tested. It should be restricted to between 3 and 4 weight percent in combination with aluminum and titanium at ~ 0.5 weight percent. There is some doubt whether an increase in tungsten content to two weight percent will provide enough improvement to compensate its more drastic effect in reducing the transformation temperature and magnetic saturation.

Because of the previously mentioned uncertainties in the actual composition of the levitation melts, it appeared impractical to try to reproduce specific alloy composition of the levitation melts as 300 gram ingots made by vacuum arc melting. It appeared to be more useful to design the alloy compositions for the 300 gram ingots to obtain information about the optimum composition and its limits. Therefore,

six alloys were melted containing variations of composition within the above specified limits. Ni content was between 10 and 15 weight percent; Co, 20 and 30 weight percent (Cr 1 weight percent substituting ~ 2 weight percent Ni); Ta, 3 and 4 weight percent; W, 0 and 2 weight percent. Al and Ti 0.5 weight percent each. The nominal compositions of the alloys are listed in Table II-3. The first five alloys were designed to obtain equations for the properties expressed as independent linear relationships with the weight percent of the components Ni, Ta, W, and Co. It was assumed that within the narrow limits defined, the independent linear relationship is a justified approximation. The common rule for such a procedure was followed in placing the composition of the experimental alloys at the range limit except for one alloy. The composition of the latter corresponds to the mid range quantity of each component. However, nickel was reduced to five weight percent while introducing five weight percent chromium as in alloy 1-A-61.

The results (Table II-10) obtained to date from the 300 gram vacuum arc melted ingots indicate that this approach was successful and has placed the results in agreement with the properties anticipated on the basis of results obtained on the levitation melts.

Cobalt-Base Alloys

A comparison of the data obtained from the screening tests of the cobalt-base alloys, listed in Table II-15, with those from the screening tests of the martensitic iron-base alloys showed that hardness values and values of magnetic saturation of the cobalt-base alloys were substantially lower. However, the temperature at which the maximum hardness was obtained was much higher; in some instances even 1382°F (750°C), which indicates that the permissible service temperature in this type of alloy may be 270°F higher than the martensitic alloys. Under these circumstances it appeared fruitful to study this system further in spite of the inferior values of magnetic saturation and hard-

ness compared to the martensitic alloys.

If a superficial comparison of hardness and magnetic saturation values obtained in the experimental alloys is made with those of the final commercial Nivco alloy, one might conclude that no substantial improvement was obtained in the experimental alloys. The value of magnetic saturation induction of Nivco alloy at 1112°F (600°C) was B_S = 11,000 gauss (σ = 100 emu/g).

The hardness value in the final heat treated condition was about 320 to 340 VHN. No experimental alloys attained hardness and saturation values which were simultaneously larger than these values for Nivco alloy.

However, such a comparison neglects two important facts. First, the hardness in the Nivco alloy material is obtained by a rather tedious heat treatment and can in no way be compared to hardness values obtained by the rather simple aging treatment applied during this study. Therefore, a sample of Nivco alloy was heat treated according to the aging routine used throughout the present program. In this case the hardness obtained in Nivco alloy reached only 300 VHN after the isothermal aging of 100 hours at 1292°F (700°C). Secondly, one should not neglect the fact that Nivco alloy contains about 15 percent discontinuous precipitate after its final heat treatment. Such discontinuous precipitate contributes to the measured value of hardness and short time tensile strength (refs. 8 and 9). It is, however, detrimental to the creep strength and may even lead to premature failure (ref. 10).

A requirement was established during the development of the screening program. No discontinuous precipitate was tolerated after isothermal aging for 100 hours at 1292°F (700°C). A simple comparison of the hardness of an alloy having no discontinuous precipitate to a Nivco alloy sample with 10 or 15 percent discontinuous precipitate is therefore meaningless. However, the creep strength of an alloy with the same or even

better hardness with no discontinuous precipitate may be far superior to the creep strength obtained in Nivco alloy provided that the other parameters are similar.

A further improvement of some of the experimental alloys is indicated by the temperature at which the maximum hardness was obtained during the isochronal aging. A temperature of 1202°F (650°C) was obtained for the Nivco alloy sample. In some of the experimental alloys this temperature was as high as 1382°F (750°C). Using this temperature parameter as the criterion, alloy selection was confined to 1-B-36, 1-B-38, 1-B-39, and 1-B-42 to 1-B-46.

These alloys exhibited high hardness values. However, the magnetic saturation values at 1112°F (600°C) were less than that of Nivco alloy. The coercive force values measured in alloys 1-B-36 and 1-B-42 after isothermal aging at 1292°F (700°C) were high. The data indicates that the addition of Ta + Ti + Al to the cobalt-base alloys were the most beneficial. It is interesting to note that a combination of the same elements produced the best results in the martensitic alloys. This result warrants more careful analysis. A more detailed analysis of this observation follows.

The addition of 2.2Ti + 1.5Al + 0.3 to 0.5 Zr (nominal weight percent) to the cobalt-base alloys was the most effective for providing high-hardness without discontinuous precipitate. The further addition of 0.5Be, 5W, 5Ta, or 5Nb increased maximum hardness and temperature during isochronal aging and also increased the hardness after isothermal aging for 100 hours 1292°F (700°C). The increments in hardness, together with the associated increment in coercive force and decrement in magnetic saturation with reference to alloy 1-B-32 are listed in Table II-16. In order to learn which of the additions increase hardness with the least reduction of magnetic saturation and with the least increase of coercive force, the ratios of the increments are also listed in this table. The highest ratio of hardness increment to saturation decrement was obtained for

TABLE II-16. Increments and Decrements of Properties of Alloy 1-B-36, 1-B-38, 1-B-39, 1-B-42, and 1-B-44 to 1-B-46

Alloy Number	Change In Composition (Δ Comp. in nominal weight percent)	Change in Saturation (Δ σ)	Effect of Isochronal Aging One Hour at 1382°F(750°C)				Effect of Isothermal Aging 100 Hours at 1292°F(700°C)			
			Change in Hardness After Aging 1 Hour (ΔH_1)	Change in Coercive Force After Aging 1 Hour (ΔH_{c1})	$\frac{\Delta H_1}{\Delta \sigma}$	$\frac{\Delta H_1}{\Delta H_{c1}}$	Change in Hardness After Aging 100 Hours (ΔH_{100})	Change in Coercive Force After Aging 100 Hours (ΔH_{c100})	$\frac{\Delta H_{100}}{\Delta \sigma}$	$\frac{\Delta H_{100}}{\Delta H_{c100}}$
Changes in Reference to Alloy 1-B-32 (75.8Co-15Ni-Fe-2.2Ti-1.5Al-0.5Zr)										
1-B-36	+0.5Be	- 6	+ 89	+38.2	14.8	2.33	80	73.3	13.3	1.1
1-B-38	+5W	-19	+ 64	+ 1.5	3.4	42.8	81	1.8	3.4	45
1-B-39	+5Ta	-13	+119	+ 3.3	9.1	36.0	123	10.3	9.5	12
1-B-42	+5Nb	-21	+169	+16.2	8.1	10.5	143	84.3	6.9	1.7
Changes in Reference to Alloy 1-B-43 (71Co-15Ni-5Fe-2.2Ti-1.5Al-0.3Zr-5Ta)										
1-B-44	-2Ta	+ 5	- 54	- 2.3	10.8	23	-20	-13	4	1.5
1-B-45	-0.7Ti	+ 4	- 8	- 0.4	2	20	- 2	-12	0.5	0.17
1-B-46	-5Ni	+ 3	- 13	- 0.3	4.3	43	+ 9	- 5.5	3	1.63

the beryllium addition. Tantalum showed the next highest ratio and the tungsten addition was the lowest. The highest ratio of hardness increment to coercive force increment was obtained for the tungsten addition; tantalum was next and beryllium was by far the lowest. The tantalum addition, therefore, is the best choice. These ratio values definitely depend on the amount of the alloying additions. For this reason extrapolation of this type of preference must be made with caution if an appreciable change is made in the amount of the alloying addition.

The 1-B-39 alloy remains too low in magnetic saturation - about 10 percent lower than Nivco alloy, while its hardness values appear quite high. The results obtained from alloys 1-B-43 to 1-B-46 should show which element might be reduced to give the largest increase in magnetic saturation associated with the smallest sacrifice in hardness. These results were analyzed in a manner similar to that described above for alloys 1-B-36, 1-B-38, 1-B-39, and 1-B-42. The increments and decrements for alloys 1-B-44 to 1-B-46 with reference to alloy 1-B-43 and the various ratios are listed in Table II-16. In this case the reduction which produces the lowest value in ratios were required. It was shown that the reduction of the titanium content increased the saturation with the smallest sacrifice in strength.

With these results the alloy compositions for the 300 gram button melts could be chosen. As mentioned above some uncertainties existed concerning the actual amount of alloy composition of the levitation melts, and secondly some adjustment of composition appeared desirable to obtain an even better balance of magnetic saturation and hardness than obtained in alloy 1-B-45. Therefore, the six alloys for the larger melts were chosen to cover a range of composition with the composition of 1-B-45 as upper limit. From these compositions equations were obtained to define the linear relationship between properties and the weight percent additions of Ni, Al, Ti, and Ta while keeping Fe fixed at five

weight percent and Zr at 0.3 weight percent nominal addition. The limits listed below were chosen on the assumption that within these narrow limits the independent linear relationship was a justified approximation. Furthermore, the previous results indicated that this range is sufficient to vary the saturation by more than 20 percent: nickel, 10 to 15 weight percent; titanium, 0 to 15 weight percent; aluminum, 1.2 to 1.5 weight percent; and tantalum, 3 to 5 weight percent. Again the values of additions in the alloys correspond with the limits of variation except for one alloy which has a composition corresponding to the center of the ranges of variation. The nominal composition of the vacuum arc melted cobalt-base alloys are listed in Table II-4.

The hardness and coercive force (Table II-11) results obtained from these 300 gram button vacuum arc melts to date indicate that the alloys were chosen successfully.

3. Program for the Next Quarter

a) The tests on the 300 gram vacuum arc melted alloys will be completed. Testing will include tensile tests of flat specimens at room temperature and at 1112°F (600°C). Hardness tests and coercive force measurements will be performed at elevated temperatures.

b) Initiate the melting of 15-pound melts for final anlaysis.

B. TASK 2 - INVESTIGATION FOR RAISING THE ALPHA TO GAMMA TRANSFORMATION TEMPERATURE IN COBALT-IRON ALLOYS

Work on this task is complete and will be reported in the Final Topical Report.

C. TASK 3 - DISPERSION-STRENGTHENED MAGNETIC MATERIALS FOR APPLICATION IN THE 1200° to 1600°F RANGE

1. Summary of Technical Progress

a) The extrusion of canned powder compacts at 2000°F in a conventional hydraulic press representing 19 dispersion-strengthened compositions has been completed. Included are eleven cobalt-base and eight iron-27 percent cobalt-base systems. Extrusions of eight prealloyed atomized powders, four internally oxidized powders, and seven composite powders were made. Evaluation of microstructures and determination of magnetic and tensile properties in the hot-extruded condition at room temperature, 1200° and 1600°F, has been nearly completed.

b) The Dynapak extrusion of three canned powder compacts at 1600°F representing three prealloyed powder compositions was completed and determination of properties are underway.

c) Evaluation of microstructure and determination of magnetic and tensile properties were completed on three cobalt-base rods dispersion-strengthened with thoria particles that were purchased from two suppliers. Two of these rods (Co + 10 v/o ThO_2 and Co + 2 v/o ThO_2) were tested in the hot-extruded condition (conventional hydraulic press) while one rod (Co + 2 v/o ThO_2) was tested after an 85 percent cold reduction by swaging.

d) The program goal of a coercive force of less than 25 oersteds at 1200° to 1600°F has been achieved in all compositions tested to date.

e) The dispersion-strengthened iron-cobalt alloys had a higher value of saturation magnetization than the cobalt-base alloys for a given volume percent of non-magnetic, dispersed phase, as expected. Analysis of the data showed that a value of 12 kilogauss minimum, for example, could be maintained with cobalt-base alloys containing as much as 20 v/o dispersoid at 1200°F and 7 v/o at 1600°F. In the case of the iron-27 percent cobalt-base materials, the dispersoid content could

be much higher and still maintain 12 kilogauss (43 v/o at 1200°F and 22 v/o at 1600°F). Higher values of B_S than 12 kilogauss were desirable, of course, and were achieved with smaller volume percents of dispersoid.

f) Large amounts of dispersed phase (32 v/o maximum) were present in some base metal-dispersoid systems, and yet satisfactory values of tensile elongation were maintained at room temperature, 1200° and 1600°F. In other systems, low values of elongation resulted with only 2 to 10 v/o dispersoid. Other factors besides volume percent of dispersoid, such as uniformity of distribution, effective particle size, and interparticle spacing, had their usual important effects on ductility.

g) The composition in the hot-extruded condition with the highest strength at 1200° to 1600°F tested to date was Co + 1.1 w/o B + 4.4 w/o Cb made from prealloyed atomized powder. Its tensile strength at 1600°F was 41,100 psi, 0.2 percent offset yield strength 22,600 psi, and elongation in 4D was 66 percent. The material was dispersion strengthened by 27 v/o of tau ($Cr_{23}C_6$ structure) ternary boride compound. It had saturation magnetization values of 10.9 kilogauss at 1200°F and 8.6 kilogauss at 1600°F. The coercive force values at those temperatures were 10.3 and 4.6 oersteds, respectively.

2. Discussion

The purpose of this project is to develop a dispersion-strengthened, magnetically soft material for use in the 1200° to 1600°F temperature range for rotor applications. As an initial and tentative goal, the material should have the following properties at some temperature between 1200° and 1600°F, preferably at 1600°F:

Saturation Magnetization, B_S -- 12,000 gauss minimum
Coercive Force, H_C -- 25 oersteds maximum
Creep strain in 10,000 hours at 10,000 psi -- 0.4 percent maximum

In pursuit of this goal, dispersion-strengthened cobalt-base and 27 percent cobalt-iron-base extrusions were made from (1) prealloyed atomized powders containing boride compound particles, (2) internally oxidized powders containing alumina or beryllia, and (3) composite powders containing both a metal phase and a refractory oxide phase (alumina or thoria)

within each powder particle. Also, dispersion-strengthened cobalt-base extrusions containing thoria were purchased from two suppliers. The work done so far is part of the initial evaluation phase of the project which includes determination of saturation magnetization, coercive force, and tensile properties at room temperature and in the 1200° to 1600°F range on hot-extruded compositions. Later on, the intermediate and final evaluation phases of this project will be conducted on the best candidate compositional systems developed in this first phase. Changes in powder processing conditions and application of secondary working treatments to extruded material will be made on a selective basis.

a. PREALLOYED ATOMIZED POWDERS

A chemical analysis was performed on an extrusion made from prealloyed atomized powder No. 13, Fe + 24.8% Co + 1.1% B + 3.2% Zr, obtained from the Hoeganaes Sponge Iron Corporation. The results are presented in Table II-17 and compared with the analysis of the powder reported by the powder supplier. It may be seen that there is good agreement between the analyses of the powder and extrusion for all major elements. However, the oxygen content of this extrusion was unexpectedly high.

An x-ray powder diffraction investigation conducted on the original minus 325 mesh fraction of powder No. 13 as received from the supplier showed that some of the zirconium alloying element was already present as ZrO_2, while the rest was in a complex boride compound (containing boron, zirconium, cobalt, and probably iron) having the $Cr_{23}C_6$ type of crystal structure (refs. 11 to 13). Diffraction patterns of the extrusion made from the powder revealed that the complex boride compound was no longer present, but that $(Fe, Co)_2B$ and ZrO_2 were the final dispersed phases.

In view of the oxidation of zirconium, it was decided to investigate the following additional prealloyed atomized powders (minus 325 mesh) by x-ray diffration in order to determine if some of these other alloying elements were present as oxides or nitrides in the original powders:

TABLE II-17. Comparison of Chemical Analysis of Powder and Extrusion

Element	Intended Composition (percent by weight)	Analysis (percent by weight)	
		Prealloyed[a] Atomized Powder No. 13	Extrusion[b] from Atomized Powder No. 13
Mn	0.50 max.	0.11	0.30
Si	0.25 max.	0.22	0.23
C	0.020 max.	0.023	0.048
S	0.025 max.	0.011	0.007
P	0.015 max.	< 0.005	0.005
Ni	0.70 max.	0.12	0.09
Cr	--	0.064	0.026
Co	25.6 + 1.5	24.75	24.4
Fe	69.2 ± 2.0	69.73	69.5
B	1.0 ± 0.2	1.1	1.33
Ti	--	--	0.03[c]
Zr	4.2 ± 0.8	3.24	3.40
O	--	--	0.185
N	--	--	0.066
Al	--	--	0.2[c]
Cu	--	--	0.2[c]
Ca	--	--	< 0.01[c]
Mg	--	--	< 0.01[c]
Be	--	--	< 0.001[c]

Note: (a) Analysis reported by powder supplier.
(b) Analysis made by Westinghouse.
(c) Emission spectrographic semi-quantitative analysis.

Atomized Powder No.	Nominal Composition (weight percent)	Powder Supplier
5	Co + 1.1B + 4.4Cb	Hoeganaes Sponge Iron Corp.
9(a)	Co + 1.3Be	Domtar Chemicals Ltd.
16	Fe + 25.9Co + 4.0Ce	Domtar Chemicals Ltd.
17(a)	Fe + 26.3Co + 2.7Al	Hoeganaes Sponge Iron Corp.
18(a)	Fe + 26.6Co + 1.4Be	Domtar Chemicals Ltd.

(a) Used for internal oxidation treatment to be described in later section.

The diffraction patterns of the preceding atomized powders did not reveal the presence of any oxides or nitrides, and it was concluded that the alloying elements were either in solid solution or in the form of intermetallic compounds. The presence of ZrO_2 in atomized powder No. 13 and the extruded form indicated that such a composition, probably with higher zirconium content, should be considered for a ZrO_2 dispersion-strengthened product.

It should be noted that all prealloyed atomized powders obtained for this program from both suppliers were made by essentially the same process. The molten metal stream was broken up into discrete particles which were solidified and cooled very rapidly by water jets in a large tank filled with nitrogen.

b. INTERNALLY OXIDIZED POWDERS

Internal oxidation treatments were applied to the following four prealloyed atomized powders to obtain approximately 10 v/o dispersed alumina or beryllia in the matrix:

Atomized Powder No.	Nominal Composition (weight percent)
8	Co + 2.5Al
9	Co + 1.3Be
17	Fe + 26.3Co + 2.7Al
18	Fe + 26.6Co + 1.4Be

The Inconel 600 retort and globar furnace used for internal oxidation treatment of the powders, and the subsequent hydrogen reduction of cobalt and iron oxides back to metal were described in the

second and third quarterly reports. The flange on the retort pan was machined flat by milling and then polished. A 1/16-inch thick nickel gasket was interposed between the retort pan and lid, which was drawn tight by bolts at two-inch intervals.

The 99.5 percent purity oxygen (water-pumped) used for internal oxidation was dried by passing through a Drierite drying apparatus. The hydrogen used for reduction and the argon used for pre-purge and post-purge of the retort flowed from their cylinders through two Deoxo Hydrogen Catalytic Purifiers (Model 10-50) attached in parallel and thence through a Drierite drying apparatus. The gas inlet line to the retort was 1/4-inch outside diameter by 0.035-inch wall Inconel 600 tubing running outside the retort to the back where the gas entered through two inlet ports. The outlet line on the front of the retort was 3/8-inch outside diameter by 0.035-inch wall tubing of Inconel 600 which ran to a Lectrodryer Dew Point Indicator containing dry ice in acetone in the cup. Copper tubing from the outlet of the dew point cup carried the hydrogen to burn-off. After passing through the Deoxo Purifier and Drierite, the dew points of the hydrogen and argon were measured at less than -90°F.

The treatment used in the preliminary internal oxidation trials involved first heating the minus 325 mesh powders to 1830°F and holding for two hours in purified and dried hydrogen flowing at 7 SCFH (5 retort volume changes per hour) in order to reduce cobalt and iron oxides that might be present back to metal, and to put the aluminum and beryllium additions in solid solution prior to internal oxidation. After holding an additional 1/2-hour at 1830°F while the hydrogen atmosphere was replaced by purified and dried argon, dried oxygen was slowly introduced over a 1/2-hour period until a complete oxygen atmosphere flowing at 5 SCFH was obtained. The powder was exposed for an additional six hours at 1830°F to to the flowing oxygen while spread out to a depth varying from 5/8 to 1/16-inch in flat, 99 percent alumina trays (Coors AD99) 150 mm long by 65 mm wide by 19 mm high. The trays were located inside two Alundum D-shaped muffles of 3-inch inside height by 6-inch inside width by 20-inch length by 3/8-inch wall thickness (Norton Company No. 46230, Mixture RA-4139, fused 98.8% alumina, 36% apparent porosity). The powder was cooled to room temperature under argon flowing at 5 SCFH.

Cross-sections of both the oxidized powder cake, and the cake after hydrogen reduction at 1220°F for 38 hours were examined under the microscope. The alumina and beryllia particles resulting from this treatment varied from coarse (micron size range) at the top of the 5/8-inch thick cake to fine (submicron size range) at the bottom of the cross-section.

On the basis of these preliminary tests, it was decided to internally oxidize new samples of the same minus 325 mesh powders spread out in trays to a uniform depth of 1/8 inch using a two hour instead of the previous six hour holding time at 1830°F in oxygen flowing at 7 SCFH. Otherwise, the internal oxidation procedure and equipment were the same as in the preliminary trials. Each powder sample was oxidized separately while spread out in 12 alumina trays to a depth of 1/8 inch. The powder charge weights were 1050 grams each of the Co-base powders (Nos. 8 and 9), and 950 grams each of the 27 percent Co-Fe powders (Nos. 17 and 18). This procedure resulted in the formation of a relatively uniform size of dispersed alumina and beryllia particles (mainly submicron) from top to bottom of the cross-section of the cake. Therefore, the powders oxidized in this manner appeared to be satisfactory for processing into extrusions.

The oxidized cake was broken up into 1/8-inch pieces in a stainless steel tray, high speed blender, and, where necessary, Pitchford Pica Blender-Mill Model No. 3800, (Pitchford Manufacturing Co., Pittsburgh, Pa.) using stainless steel containers and hardened steel balls. The oxidized powder was screened through 65 mesh before hydrogen reduction.

Six Alundum tubes 2-inch inside diameter by 3/8-inch thick wall by 2-1/2 inches long of 99.8% alumina with 36% apparent porosity (Norton Co. RA-4139) were fitted inside six 99% alumina trays and filled with oxidized powder to a height of approximately 1-1/2 inches. The trays were placed inside two Alundum D-shaped muffles described previously to keep solid contaminants from falling into the powder, and loaded into an Inconel 600 retort. Each oxidized powder composition was given hydrogen reduction treatments separately.

The purpose of containing the powder in 2-inch diameter tubes was to provide a cylindrical shape of the proper diameter suitable for

an extrusion billet in case the powder particles strongly bonded together and formed a dense, ductile, metallic cake during hydrogen reduction which would not lend itself to compaction to size by the normal isostatic pressing procedure.

Hydrogen reduction of the cobalt and iron oxides consisted of heating to 1200°F and holding for approximately 18 hours with a 6 to 1 ratio of argon and hydrogen mixture flowing at 7 SCFH through the retort. Then the temperature was raised to 1800°F and held for approximately 11 hours. The 6 to 1 argon-hydrogen mixture flowing at a minimum of 7 SCFH was maintained during heating from 1220°F to 1800°F, and during the furst 3 hours (approximately) at 1800°F. For the remaining 8 hours at 1800°F purified and dried hydrogen was used, and flowed through the retort at a minimum of 7 SCFH. Furnace cooling to room temperature was performed under hydrogen. The argon-hydrogen mixture was used initially, rather than pure hydrogen, because substantial amounts of moisture were being carried from the retort.

Upon removal from the retort, the reduced powders were in the form of soft cakes approximately 1-3/4-inch diameter. The six cakes of each composition were stacked on top of each other in a rubber bag and isostatically pressed under 50,000 psi for one minute. Isostatic pressing procedure was described in the third quarterly report.

The green compacts were sintered in purified and dried hydrogen for two hours at 1800°F in the manner described in the third quarterly report.

The bake-out of sintered billets and mild steel cans (2-inch inside diameter by 2.25-inch outside diameter) for two hours at 1220°F in the 10^{-5} torr range, hermetic sealing of billets in can by electron beam welding, preheating of billets for one hour at 2000°F prior to extrusion, and the standard hydraulic extrusion practice used in this program were all described in detail in the fourth quarterly report. These procedures were continued and applied to the internally oxidized powders.

The microstructure, magnetic properties, and tensile properties of extrusions are described in a later section.

c. COMPOSITE POWDERS

The extrusion to rod of all seven composite powders containing 10 v/o alumina or thoria was completed. The microstructure, magnetic properties, and tensile properties are discussed in a later section.

d. SUPPLIER EXTRUSIONS OF DISPERSION-STRENGTHENED COBALT

The examination of the microstructures, and determination of magnetic and tensile properties were completed. The results are given in a later section.

e. PROCESSING OF POWDERS INTO EXTRUSIONS

The third and fourth quarterly reports contained descriptions of the procedures used in making extrusions from sintered powder compacts in a hydraulic press and the methods applied to evaluate extrusion quality and microstructure. These procedures and methods have been continued and were used to make and evaluate additional extrusion. Specimens for test purposes were taken from locations near the front of extrusions found to be of good quality and representative of the material.

During the past quarter, sintered compacts of the following three atomized powders (minus 325 mesh) were extruded to rod in a Dynapak 1220C Machine.

Atomized Powder Number	Composition (weight percent)	Sintered Compact Density (percent of theoretical)	Billet Size	
			Diameter (inches)	Length (inches)
4	Co+1.3B+3.4Zr	60	1.6	3-15/16
13	Fe+24.8Vo+1.1B+3.2Zr	66	1.6	3-11/16
14	Fe+25.8Co+0.9B+4.1Cb	68	1.6	3-5/16

The purpose of this work was to investigate the effect of lower processing temperatures, 1600°F maximum, and high extrusion speed on the magnetic and tensile properties. These same compositions had been extruded earlier in a hydraulic press with a

2000°F billet temperature at a speed of 43 feet per minute. The extrusion ratios were 11 to 1 for conventional extrusion and 6 to 1 for the Dynapak.

The powders for the billets extruded in the Dynapak Machine were processed into compacts in the same manner as described in earlier reports, except that the compact sintering temperature was 1600°F (for two hours) instead of 1800°F. The compacts were canned in mild steel and hermetically sealed by electron beam welding prior to extrusion. The billet was preheated to 1600°F in an induction coil under argon and held at temperature approximately 15 minutes. (The billet preheat for hydraulic extrusion was one hour at 2000°F.) Rod with an overall diameter of 0.763 inch and an alloy core diameter of 0.656 inch was produced.

f. TESTING OF EXTRUSIONS

(1) Microstructure

The methods used to study and evaluate the microstructure of extrusions were described in the fourth quarterly report. These studies have continued and the results to date are summarized in Table II-18 for material made by the conventional, hydraulic extrusion process. Dynapak extrusions are not included.

The cobalt-base and iron-cobalt-base extrusions made from prealloyed atomized powders containing boron, titanium, zirconium, columbium, and tantalum had the greatest amount of dispersed phase, 20 to 32 percent by volume. The average dispersoid particle size ranged around one micron. The particles were evenly distributed throughout the matrix.

As mentioned earlier, a x-ray diffraction investigation of the original minus 325 mesh atomized powders was performed on two compositions containing borides: No. 5, Co + 1.1% B + 4.4% Cb and No. 13, Fe + 24.8% Co + 1.1% B + 3.2% Zr. The former contained the face centered cubic form of cobalt, (lattice parameter 3.553 angstroms) and the Co-Cb-B ternary boride compound having the cubic $Cr_{23}C_6$ structure (D_{84} structure type). The ternary boride belonged to the family

TABLE II-18. Microstructure of Extrusions, Preliminary Measurements

Powder or Extrusion No.	Nominal Composition (weight percent)	Amount of Dispersed Phase (percent by volume)	Average Size of Dispersed Particles(g) (microns)	Average Interparticle Spacing (microns)	Degree of Recrystallization (percent)	Average Grain Size (Approx.) (microns)	Amount of Porosity (percent)
a. Prealloyed Atomized Powders (Extruded)							
3	Co+1.3B+1.6Ti	32	1.5	3.2	(d)	5	2
4	Co+1.3B+3.4Zr	26	0.95	2.7	(d)	5	2
5	Co+1.1B+4.4Cb	27	0.75	2.0	(d)	5	2
6	Co+1.2B+7.7Ta	27	0.73	2.0	(d)	5	2
12	Fe+26.5Co+0.9B+1.8Ti	20	1.6	6.4	Complete(e)	20	2
13	Fe+24.8Co+1.1B+3.2Zr	20	0.90	3.6	Complete(e)	20	2
14	Fe+25.8Co+0.9B+4.1Cb	20	0.77	3.1	Complete(e)	20	2
15	Fe+24.1Co+1.0B+7.0Ta	21	0.74	2.8	Complete(e)	20	2
b. Internally Oxidized Powders (Extruded)							
8	Co+4.7Al_2O_3	9.8	0.3(f)	2.8	(d)	4	2
9	Co+3.6BeO	8.3	0.3(f)	3.3	(d)	4	2
17	Fe+25.6Co+5.1Al_2O_3	8.4	1.0(f)	10.9	Complete(e)	25	2
18	Fe+26.0Co+3.9BeO	9.6	0.3(f)	2.8	Complete(e)	10	2
c. Composite Powders (Extruded)							
3	Co+11.2ThO_2(0.01-0.06μ), Sherritt Gordon	10	0.1(f)	0.9	(d)	4	2
11	Fe+23.7Co+12.1ThO_2(0.01-0.06μ), Vitro Labs	10	1.1(f)	9.9	Complete(e)	30	2
1	Co+4.75Al_2O_3(0.01-0.06μ), Chas. Pfizer	10	0.2(f)	1.8	(d)	5	2
2	Co+4.75Al_2O_3(0.1-0.6μ), Chas. Pfizer	10	0.6(f)	5.4	(d)	12	2
3	Co+11.2ThO_2(0.01-0.06μ), Chas. Pfizer	10	0.2(f)	1.8	(d)	7	2
4	Co+11.2ThO_2(0.1-0.6μ), Chas. Pfizer	10	0.3(f)	2.7	(d)	5	2
11	Fe+23.7Co+12.1ThO_2(0.01-0.06μ), Chas. Pfizer	10	0.3(f)	2.7	Complete(e)	10	2
d. Supplier Extrusions of Dispersion-Strengthened Cobalt							
3(b)	Co+10.4ThO_2(0.01-0.06μ ThO_2)	9.3	0.1(f)	1.0	(d)	2	2
9(c)	Co+2.0ThO_2(0.01-0.06μ ThO_2)	1.8	0.1(f)	5.5	(d)	5	0-1
9(a)(c)	Co+2.0ThO_2(0.01-0.06μ ThO_2)	1.8	0.1(f)	5.5	(d)	-	0-1

Note:

(a) Given 85 percent cold reduction by swaging after hot extrusion. All other material in hot extruded condition.
(b) Extrusion supplied by New England Materials Laboratory, Inc., Medford, Massachusetts.
(c) Extrusion supplied by Curtiss-Wright Corp., Metals Processing Division, Buffalo, New York.
(d) Cobalt undergoes phase transformation at 783°F from cubic to hexagonal structure on cooling. These materials were partially transformed and contained a mixture of hexagonal and cubic cobalt at room temperature.
(e) Iron-cobalt matrix undergoes phase transformation at approximately 1771°F from face centered cubic to body centered cubic on cooling.
(f) Estimated value from observations under light microscope and on photomicrographs. Could not be measured with light microscope.
(g) No evidence of lack of bonding between the dispersed phase and the matrix was found.

of ternary borides called tau and represented by $T_{23-m}M_mB_n$, where T is Co, and M is one of the following: Ti, Zr, Cb, or Ta (refs. 11 to 13). The other powder was revealed to contain the body centered cubic matrix expected of iron-base materials (lattice parameter 2.866 angstroms) apparently with very little, if any, other elements in solid solution. Also, the presence of the complex boride, tau, having the $Cr_{23}C_6$ structure, and ZrO_2 were detected. This evidence indicated that some oxidation of the zirconium alloying element occurred during the manufacture of the original powder by the atomizing process.

Additional work was performed to establish the identity of the constituents present in extrusions made from these two powder compositions. Extraction replicas were obtained from as-extruded rod and used for electron micrographs, and electron and x-ray diffraction studies. Furthermore, filings obtained from the rods were used to obtain x-ray diffraction powder patterns. Figure II-45 shows a photomicrograph and Figure II-46 an electron micrograph of the Co + 1.1% B + 4.4% Cb extrusion. The larger, clear constituent particles were identified by diffraction studies to be the tau ternary boride, while the small amount of finer constituent particles remained unidentified. The larger, clear particles in Figures II-47 and II-48 were found to be $(Fe, Co)_2B$ with a tetragonal structure, while the smaller, dark particles were ZrO_2 having a monoclinic structure. No tau ternary boride was detected in the Fe + 24.8% Co + 1.1% B + 3.2% Zr extrusion. This indicated that either the zirconium present in the tau ternary boride in the original atomized powder had continued to react with oxygen during processing of the powder into an extrusion, forming more ZrO_2, and leaving the iron, cobalt and boron to form $(Fe, Co)_2B$ constituent particles or the tau boride was a non-equilibrium phase in this alloy which decomposed during thermal treatments applied during subsequent processing.

All of the Fe-Co-base extrusions in Table II-18 were in the recrystallized condition and tended to have a coarser grain size than the Co-base. In the latter case, the matrix examined at room temperature in the as-extruded condition consisted of a mixture of hexagonal and cubic cobalt of fine grain size.

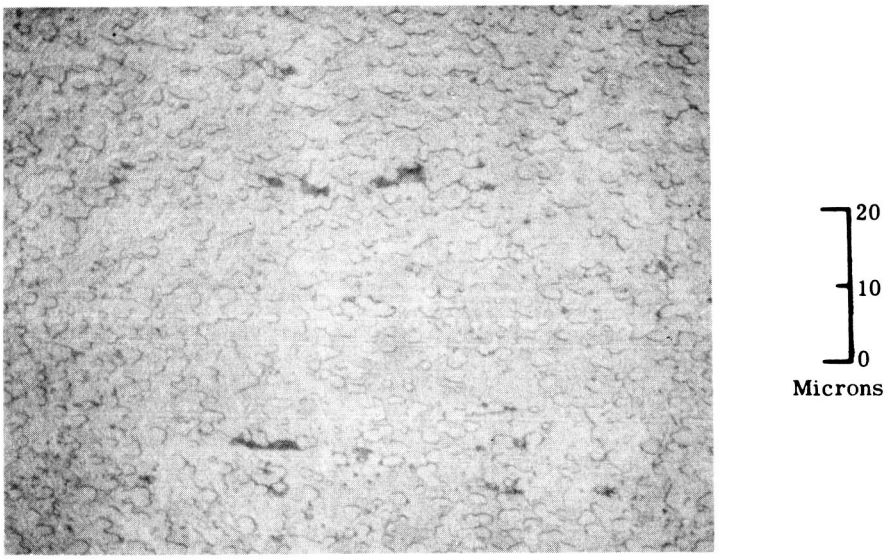

FIGURE II-45. Photomicrograph of As-Extruded Atomized Powder No. 5 Co + 1.1%B + 4.4%Cb, Showing Larger Particles of Tau Ternary Boride (Light) and Other Finer Particles (Dark) Dispersed in Cobalt Matrix, Longitudinal Section Near Front of Extrusion, 1000X, Etched in Acetic-Nitric-Hydrochloric-Water (1:1:4:1 Ratio)

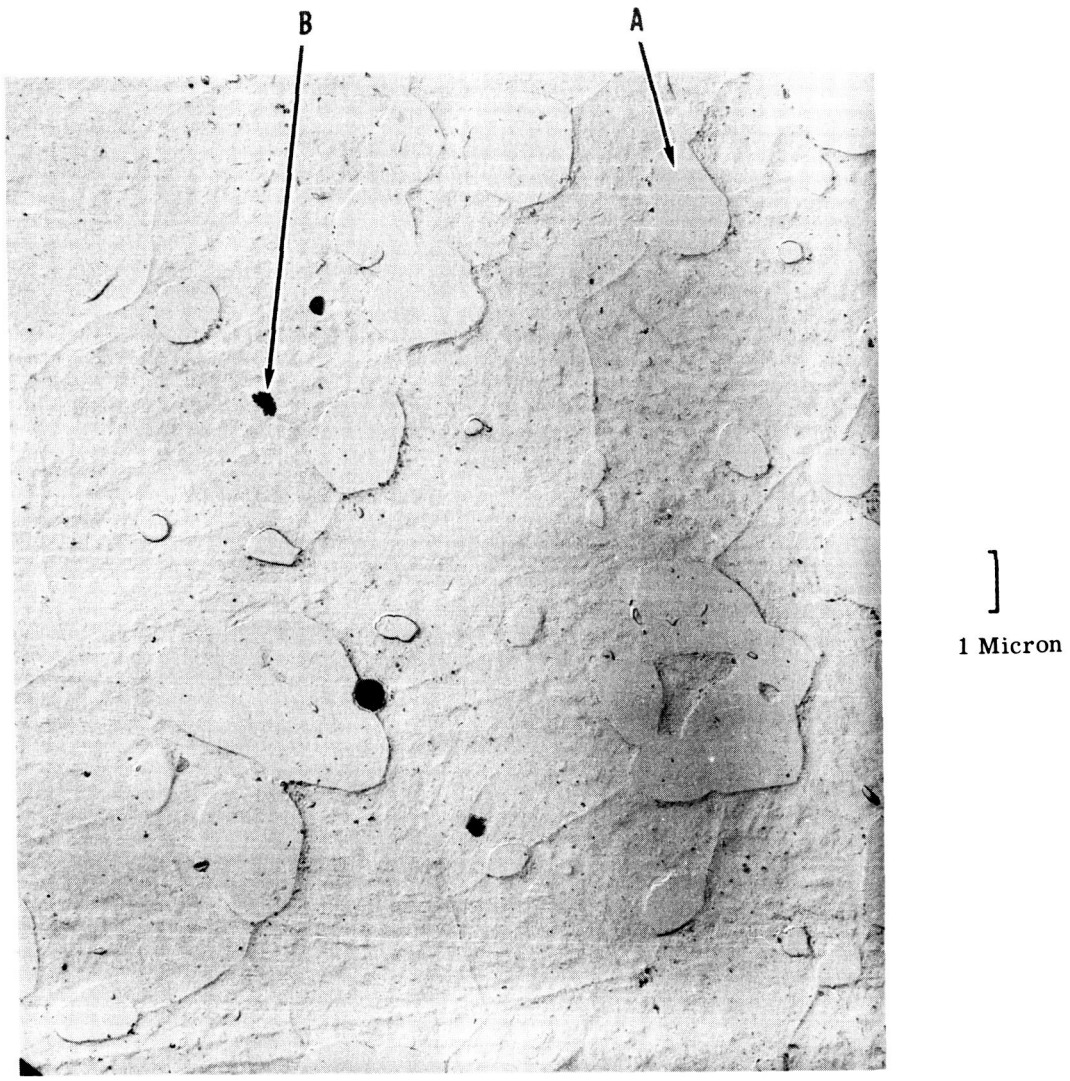

FIGURE II-46. Electron Micrograph of Replica of As-Extruded Atomized Powder No. 5, Co + 1.1%B + 4.4%Cb, Showing Larger Particles of Tau Ternary Boride (A) and Finer Particles of Another Phase (B), 7500X, Rod Etched in Carapella's Reagent.

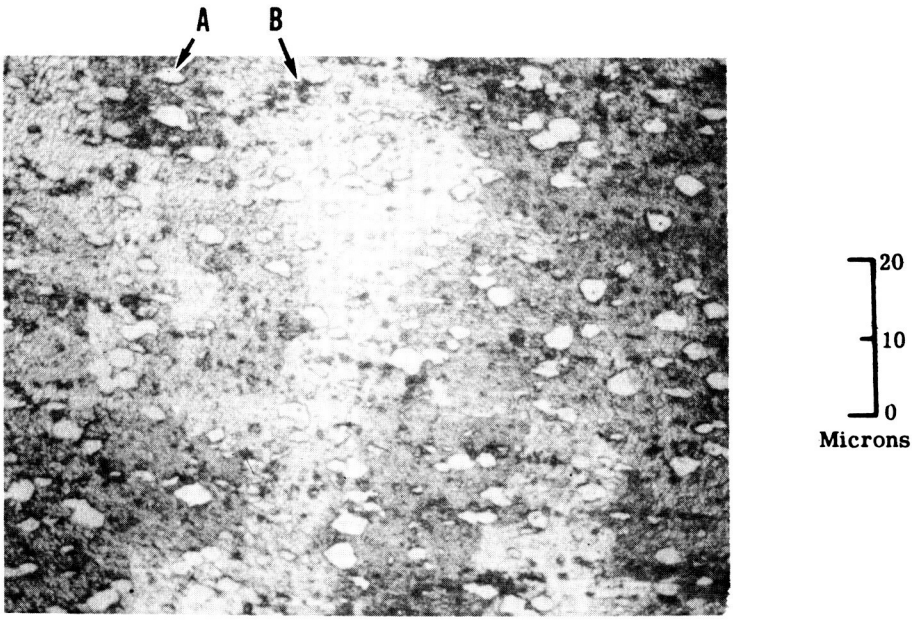

FIGURE II-47. Photomicrograph of As-Extruded Atomized Powder No. 13, Fe + 24.8%Co + 1.1%B + 3.2%Zr, Showing Larger Particles of (Fe, Co)$_2$B (A-Light) and Finer Particles (B-Dark) of ZrO_2 Dispersed in Recrystallized Matrix, Longitudinal Section Near Front of Extrusion, 1000X, Etched in Acetic-Nitric-Hydrochloric-Water (1:1:4:1 Ratio)

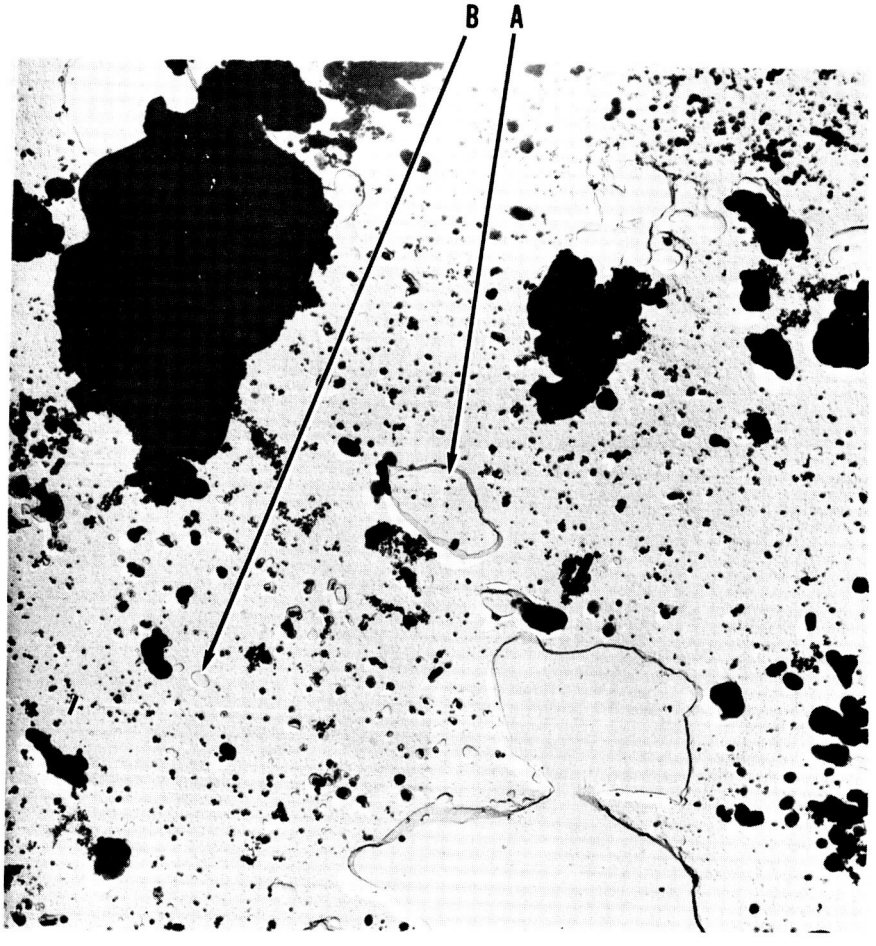

FIGURE II-48. Electron Micrograph of Extraction Replica of As-Extruded Rod, Atomized Powder No. 13, Fe + 24.8%Co + 1.1%B + 3.2% Zr, Showing Larger Particles (A) of $(Fe, Co)_2B$ and Finer Particles (B) of ZrO_2, 12,000X, Rod Etched in Carapella's Reagent.

(2) Magnetic Properties

In general, magnetic properties of materials may be divided into two classes: structure insensitive and structure sensitive. The primary or structure insensitive properties include saturation magnetization, Curie temperature, crystalline anisotropy and magnetostriction. These are dependent on atomic structure and chemical compostion of the material. The properties which are considered to be secondary and influenced by the microstructure and internal condition of the material are coercive force, permeability, residual magnetization, and hysteresis loss.

A "soft" magnetic material can be magnetized to saturation, and then demagnetized by the application of rather weak magnetic fields. The ideal soft magnetic material for a power application would have high permeability, high saturation and residual magnetizations, low coercive force, high electrical resistivity, low losses, high degree of preferred grain orientation, and low crystal anisotropy and magnetostrictive constants.

Since the coercive force is the strength of reverse field which has to be applied to demagnetize a previously magnetized sample, it is an excellent indicator of the "softness" of a magnetic material.

The saturation magnetization of dispersion-strengthened alloys might be expected to decrease in proportion to the amount of non-magnetic, insoluble dispersed phase added.

(a) Coercive Force

The coercive force values of all compositions tested were less than 25 oersteds at 1200° to 1600°F and, therefore, met the tentative program goal in that respect, Table II-19. For each composition, whether cobalt-base or iron-cobalt-base, the coercive force decreased as the temperature increased. This was more striking for the cobalt-base extrusions which contained a mixture of hexagonal and face centered cubic forms of cobalt in the matrix at room temperature. Hexagonal

TABLE II-19. DC Magnetic Properties of Hot Extruded Rod

Powder or Extrusion No.	Nominal Composition (weight percent)	Coercive Force, H_c (oersteds)					
		At Room Temperature					
		As Recvd.	After Testing at 1200-1600°F	At 1200°F	At 1400°F	At 1500°F	At 1600°F
a. Prealloyed Atomized Powders (Extruded)							
3	Co+1.3B+1.6Ti	25.0	27.0	6.3	4.8	4.0	3.3
4	Co+1.3B+3.4Zr	48.0	53.0	9.2	7.1	5.8	4.7
5	Co+1.1B+4.4Cb	47.0	45.5	10.3	8.0	5.9	4.6
6	Co+1.2B+7.7Ta	41.0	45.0	11.6	9.4	8.4	6.3
12	Fe+26.5Co+0.9B+1.8Ti	12.8	12.1	5.5	4.1	3.4	2.3
13	Fe+24.8Co+1.1B+3.2Zr	18.8	17.6	8.4	6.4	4.9	3.6
14	Fe+25.8Co+0.9B+4.1Cb	19.6	19.0	8.7	6.8	5.3	3.7
15	Fe+24.1Co+1.0B+7.0Ta	21.0	19.0	10.4	8.6	6.2	4.4
b. Internally Oxidized Powders (Extruded)							
8	Co+4.7Al_2O_3	44.5	42.4	9.7	8.0	7.1	6.1
9	Co+3.6BeO	56.0	52.2	9.0	6.4	5.2	4.4
17	Fe+25.6Co+5.1Al_2O_3	19.6	12.4	-	-	-	-
18	Fe+26.0Co+3.9BeO	21.0	15.3	9.3	4.9	3.7	2.7
c. Composite Powders (Extruded)							
3	Co+11.2ThO_2 (0.01-0.06μ), Sherritt Gordon	60.0	58.5	21.5	16.8	15.1	13.0
11	Fe+23.7Co+12.1ThO_2 (0.01-0.06μ), Vitro Labs	13.9	9.4	-	-	-	-
1	Co+4.75 Al_2O_3 (0.01-0.06μ), Chas. Pfizer	85.0	82.0	10.0	7.9	6.8	5.9
2	Co+4.75Al_2O_3 (0.1-0.6μ), Chas. Pfizer	79.0	78.0	9.0	7.7	6.8	5.5
3	Co+11.2ThO_2 (0.01-0.06μ), Chas. Pfizer	76.5	76.0	12.4	10.3	9.0	8.2
4	Co+11.2ThO_2 (0.1-0.6μ), Chas. Pfizer	76.9	73.0	10.5	8.8	7.8	6.4
11	Fe 23.7Co+12.1ThO_2 (0.01-0.06μ) Chas. Pfizer	19.6	19.2	9.0	6.5	5.3	4.4
d. Supplier Extrusions of Dispersion-Strengthened Cobalt							
3(d)	Co+10.4ThO_2 (0.01-0.06μ ThO_2)	49.0	49.0	19.4	16.7	14.8	13.4
9(e)	Co+2.0ThO_2 (0.01-0.06μThO_2)	68.0	62.0	8.4	7.3	6.1	5.3
9(a)(e)	Co+2.0ThO_2 (0.01-0.06μThO_2)	114.0	71.0	9.3	7.1	5.7	4.8
e. Comparison Alloy							
	Nivco[f]	11.9	9.3	6.8	5.5	3.9	2.3

Note:

(a) Given 85 percent cold reduction by swaging after hot extrusion. All other mate
(b) Based on measurements of weight in air and water (ASTM Method B 311-58) and
(c) Measured values are presumably 5 percent too low because it was not possible t
(d) Extrusion supplied by New England Materials Laboratory, Inc., Medford, Mass
(e) Extrusion supplied by Curtiss-Wright Corp., Metals Processing Division, Buff
(f) Forged and heat treated 5/8 inch diameter rod.

Magnetic Saturation										
Saturation Magnetic Moment, σ (emu/gram)					Approximate Saturation Magnetization, B_s (kilogauss)					Room Temp. Density of Material[b] (g/cc)
At Room Temp.	At 1200°F	At 1400°F	At 1500°F	At 1600°F	At Room Temp.	At 1200°F	At 1400°F	At 1500°F	At 1600°F	
132[c]	95.7	89.2	83.5	77.4	13.7[c]	9.9	9.3	8.7	8.0	8.26
132[c]	99.9	92.6	86.9	80.6	14.0[c]	10.6	9.8	9.2	8.5	8.43
127[c]	101.2	93.6	87.7	79.8	13.7[c]	10.9	10.1	9.5	8.6	8.58
134[c]	95.3	87.5	82.8	78.8	14.8[c]	10.6	9.7	9.2	8.7	8.81
216	179	156	144	129	20.9	17.3	15.1	13.9	12.5	7.70
212	175	152	142	127	20.9	17.2	15.0	14.0	12.5	7.84
211	165	152	140	127	20.8	16.3	15.0	13.8	12.5	7.86
200	159	145	135	121	20.5	16.2	14.9	13.8	12.4	8.15
152[c]	133	122	118	108	15.6[c]	13.7	12.6	12.1	11.1	8.19
153[c]	137	127	121	112	15.5[c]	13.9	12.9	12.3	11.4	8.10
-	-	-	-	-	-	-	-	-	-	7.40
222	191	179	172	152	20.4	17.5	16.4	15.8	14.0	7.31
144[c]	124	116	109	102	15.9[c]	13.7	12.8	12.1	11.2	8.79
-	-	-	-	-	-	-	-	-	-	7.99
149[c]	134	125	118	111	15.3[c]	13.8	12.9	12.1	11.4	8.19
152[c]	134	124	118	112	15.7[c]	13.8	12.8	12.1	11.5	8.18
142[c]	126	117	110	102	15.7[c]	13.9	12.9	12.1	11.2	8.78
142[c]	125	116	100	102	15.7[c]	13.8	12.8	12.0	11.2	8.79
201	172	161	152	137	20.2	17.3	16.2	15.3	13.7	7.99
144[c]	125	116	110	103	15.7[c]	13.6	12.6	12.0	11.2	8.66
155[c]	137	127	119	112	17.2[c]	15.2	14.1	13.2	12.4	8.82
155[c]	138	128	121	112	17.2[c]	15.3	14.2	13.5	12.5	8.85
124	100	75.0	61.7	40.0	13.4	10.8	8.1	6.7	4.3	8.61

ial in hot extruded condition.
measurements of weight and dimensions of machined rod specimens.
o saturate the specimens at room temperature.
achusetts.
lo, New York.

cobalt has high crystal anisotropy and magnetostriction constants relative to the cubic form, and the result is a high coercive force. The transformation of cubic cobalt to hexagonal as the extrusion cooled to room temperature would be expected to induce residual, internal stresses in the matrix and lead to a high coercive force, considering the high magnetostriction of the hexagonal phase. At 1200°F and 1600°F the hexagonal phase was gone and only the cubic form remained. Both anisotropy and magnetostriction constants were much lower at 1200°F and 1600°F, and the coercive force of the cobalt-base materials was sharply reduced relative to room temperature.

The iron-cobalt-base materials, of course, retained the body centered cubic matrix at all testing temperatures. Since the magnetostriction of iron is low even at room temperature and further decreases at 1200° to 1600°F, internal stresses, if present, would have little effect on coercive force in comparison with their effect on cobalt. The crystal anisotropy constant of iron, therefore, would be left as a major factor to interact with the microstructure and influence coercive force.

The effect of the amount of dispersed phase on the coercive force of cobalt-base extrusions at room temperature and 1200°F is illustrated in Figure II-49. At 1200° to 1600°F, where cobalt has the cubic form, the coercive force increased as the amount of dispersoid increased. However, it should be pointed out that the rate of increase was less for dispersoids of coarser particle size, Figure II-49. At room temperature hexagonal cobalt is the stable form. However, a mixture of hexagonal and face centered cubic existed because the transformation was incomplete. The coercive force at room temperature tended to decrease with increasing amounts of dispersed phase. This was due to a simultaneous decrease in the relative amount of hexagonal cobalt present.

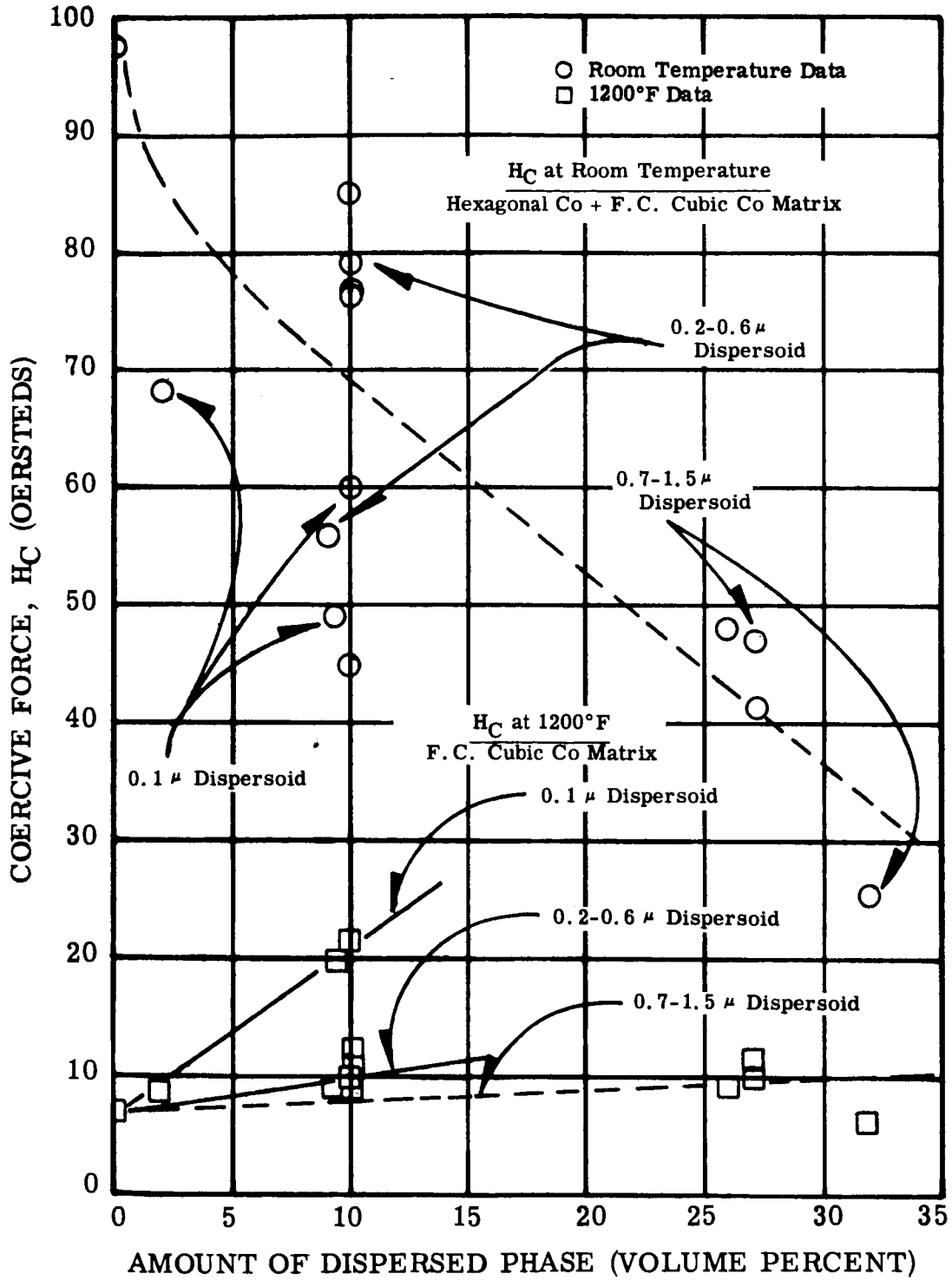

FIGURE II-49. Effect of Amount of Dispersed Phase of Three Different Particle Sizes (Approximate Values) in Cobalt As-Extruded Rod on the Coercive Force at Room Temperature and 1200°F

Figure II-49. Coercive Force of Cobalt-Base Material Containing Different Sizes and Amounts of Dispersoid

For the iron-cobalt-base materials with the body centered cubic matrix, the coercive force at all temperatures increased with increasing volume percent of dispersed phase and decreasing particle size, Figure II-50.

(b) Saturation Magnetization

The values of saturation magnetic moment, σ_s, in emu per gram and saturation magnetization, B_s, in gauss for the various compositions are listed in Table II-19. The B_s values were calculated from the equation: $B_s = 4\pi\delta\sigma$, where δ is the density of the material in grams per cubic cm, and should be considered approximate, because the density at room temperature was used to calculate elevated temperature values of B_s as well. In the case of the cobalt-base alloys, the saturation values measured at room temperature were approximately five percent low because it was not possible to completely saturate the specimens containing hexagonal cobalt with the mean applied field of 11,500 oersteds.

The dilution effect on saturation magnetization by the amount of dispersoid present in the matrix is illustrated for cobalt-base alloys in Figure II-51. The decrease in B_s with increasing volume fraction of dispersed phase was linear at all temperatures, but the absolute values of B_s for the dispersion-strengthened materials tended to be slightly lower than predicted from a straight dilution basis. Some of this may be due to slight inaccuracies in the density values used. The relationship between B_s and volume percent dispersoid was similar for dispersion-strengthened iron-cobalt alloys. These data show that the B_s values at any temperature for dispersion-strengthened compositions can be predicted quite accurately from a knowledge of the volume percent dispersoid present.

If it proves necessary to maintain the current tentative program goal of B_s = 12 kilogauss minimum at 1200° to 1600°F, it will also be necessary to restrict the amount of dispersoidadded to the approximate values

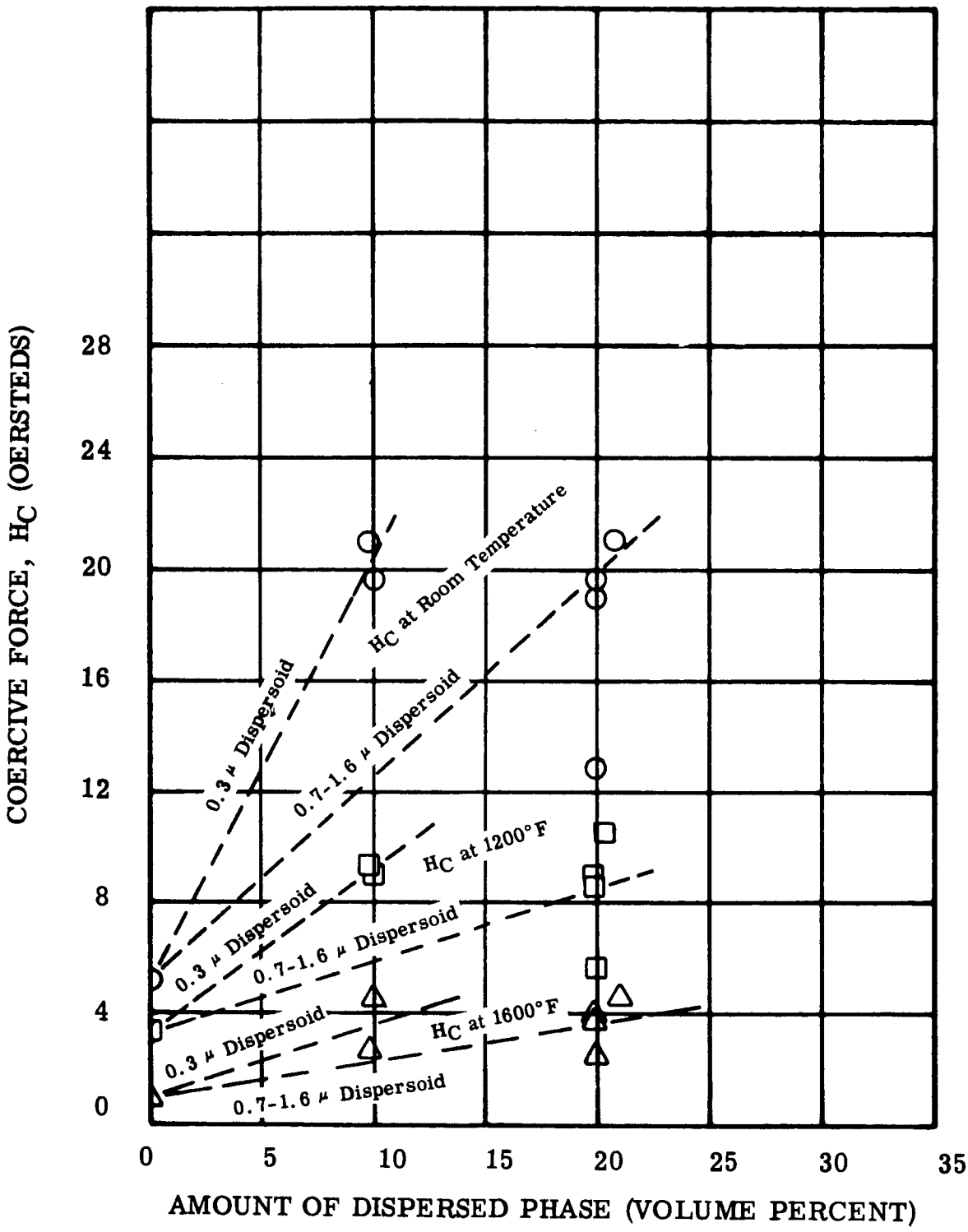

FIGURE II-50. Effect of Amount of Dispersed Phase of Two Different Particle Sizes (Approximate Values) in Iron + 27 w/o Cobalt As-Extruded Rod on the Coercive Force at Room Temperature, 1200°F, and 1600°F

Figure II-50. Coercive Force of Iron+27 w/o Co Base Material Containing Different Sizes and Amounts of Dispersoid

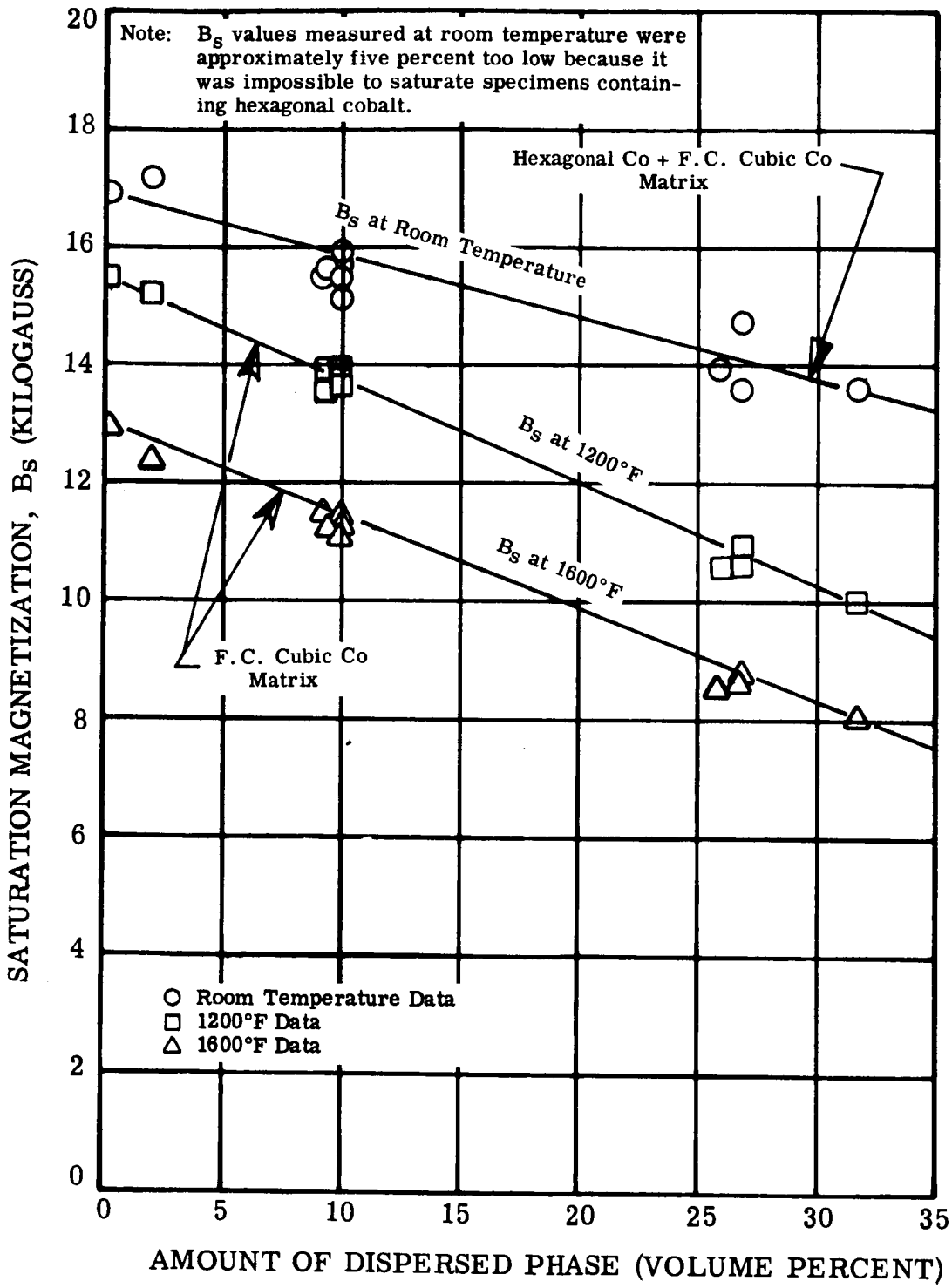

FIGURE II-51. Effect of Amount of Dispersed Phase in Cobalt As-Extruded Rod on the Saturation Magnetization at Room Temperature, 1200°F, and 1600°F

Figure II-51. Saturation Magnetization of Cobalt-Base Material Containing Different Amounts of Dispersoid

listed below. Of course there are other considerations, such as maintaining sufficient ductility and avoiding notch sensitivity, which must be allowed for in establishing finalized B_S minimum values.

Temperature (°F)	Approximate Maximum Amount of Dispered Phase (v/o) Permitted to Maintain a Saturation Magnetization of 12 Kilogauss	
	In Co-Base	In 27% Co-Fe-Base
1200	20	43
1400	15	37
1500	10	31
1600	7	22

For reaching higher levels of saturation magnetization, the Fe-Co-base materials appeared more attractive than the Co-base for future development. All of the Fe-Co-base materials in Table II-19 met the current program goal of B_S = 12 kilogauss minimum at 1200° to 1600°F, while some of the cobalt-base alloys did not.

Since saturation is a structure insensitive property, the values of B_S were not influenced by the particle size of the dispersed phase.

(3) Tensile Properties

The tensile properties of as-extruded rod at room and elevated test temperatures are listed in Table II-20. The rough machined tensile specimens for elevated temperature tests on all experimental compositions were aged 100 hours in vacuum (pressure less than 1 x 10^{-5} torr) before testing at 1 x 10^{-5} torr. The properties of Nivco alloy and DuPont's TD Nickel are given at the bottom of Table II-20 for comparison. The tensile data for Nivco alloy 5/8 inch diameter forged and heat treated bar were obtained on specimens of the same size as for the experimental compositions. The data for TD Nickel bar were obtained from reference 14 (secondary worked after hot extrusion).

TABLE II-20. Tensile Properties of Hot Extruded R

Powder or Extrusion No.	Nominal Composition (weight percent)	At Room Temperature			
		Ultimate Strength (1000 psi)	0.2% Offset Yield Strength (1000 psi)	Elongation in 4D (percent)	Reduction in Area (percent)
a. Prealloyed Atomized Powders (Extruded)					
3	Co+1.3B+1.6Ti	123.1	117.0	6.0	2.1
4	Co+1.3B+3.4Zr	162.4	144.3	1.0	0.7
5	Co+1.1B+4.4Cb	172.8	116.2	10.0	4.1
6	Co+1.2B+7.7Ta	175.6	136.1	9.8	8.4
12	Fe+26.5Co+0.9B+1.8Ti	132.1	87.8	7.0	6.3
13	Fe+24.8Co+1.1B+3.2Zr	147.1	88.9	10.0	11.8
14	Fe+25.8Co+0.9B+4.1Cb	146.5	101.5	10.0	9.1
15	Fe+24.1Co+1.0B+7.0Ta	129.0	79.3	8.0	7.8
b. Internally Oxidized Powders (Extruded)					
8	Co+4.7Al_2O_3	111.5	106.2	0.5(d)	2.1(d)
9	Co+3.6BeO	117.7	99.3	5.0	4.1
17	Fe+25.6Co+5.1Al_2O_3	-	-	-	-
18	Fe+26.0Co+3.9BeO	113.9	92.6	15.0	11.1
c. Composite Powders (Extruded)					
3	Co+11.2ThO_2 (0.01-0.06 μ), Sherritt Gordon	85.8(e)	(c)	0.0	0.0
11	Fe+23.7Co+12.1ThO_2 (0.01-0.06 μ) Vitro Labs	-	-	-	-
1	Co+4.75Al_2O_3(0.01-0.06 μ), Chas. Pfizer	102.4	93.5	1.0	1.8
2	Co+4.75Al_2O_3(0.1-0.6 μ), Chas. Pfizer	-	-	-	-
3	Co+11.2ThO_2(0.01-0.06 μ), Chas. Pfizer	109.6	106.3	3.0	1.5
4	Co+11.2ThO_2(0.1-0.6 μ), Chas. Pfizer	-	-	-	-
11	Fe+23.7Co+12.1ThO_2(0.01-0.06 μ), Chas. Pfizer	118.3	87.4	6.0	4.9
d. Supplier Extrusions of Dispersion-Strengthened Cobalt					
3	Co+10.4ThO_2(0.01-0.06 μ ThO_2)	129.4	97.3	0.2	0.0
9	Co+2.0ThO_2(0.01-0.06 μ ThO_2)	120.5	82.5	3.5	10.6
9(b)	Co+2.0ThO_2(0.01-0.06 μ ThO_2)	104.6	80.8	1.3	3.8
e. Comparison Materials					
	Nivco 5/8 in. dia. Forged and Heat Treated Bar	175.4	116.6	37	23.5
	TD Nickel 1-1/4 in. dia. Bar(f)	90	80	25	80

Note:
(a) Specimens aged 100 hours in vacuum (pressure of 1 x 10^{-5} torr or less
(b) Cold reduction in area of 85 percent by swaging after hot extrusion. A
(c) Failed before reaching 0.2% offset.
(d) Broke outside gage length.
(e) Broke in threads.
(f) Secondary worked condition.

od

At 1200°F[a]				At 1600°F[a]			
Ultimate Strength (1000 psi)	0.2% Offset Yield Strength (1000 psi)	Elongation in 4D (percent)	Reduction in Area (percent)	Ultimate Strength (1000 psi)	0.2% Offset Yield Strength (1000 psi)	Elongation in 4D (percent)	Reduction in Area (percent)
51.2	26.4	27.0	24.6	20.7	6.3	42.0	30.0
75.7	38.9	20.0	24.2	30.3	10.1	52.0	51.1
80.3	41.9	23.0	26.9	41.1	22.6	66.0	61.0
73.6	42.0	24.0	24.8	34.1	12.1	64.0	57.7
56.4	27.6	50.0	52.5	17.5	8.5	86.0	70.0
62.1	31.5	40.0	44.0	18.5	10.0	82.0	69.5
67.2	31.5	34.0	34.2	17.7	7.3	48.0	69.5
62.8	31.5	34.0	27.7	16.6	8.4	76.0	57.7
38.0	30.4	17.0	14.9	20.9	11.7	15.0	11.2
32.5	20.7	78.0	39.6	13.3	7.0	28.0	27.2
-	-	-	-	-	-	-	-
47.7	30.5	24.0	21.1	11.6	3.7	36.0	22.9
25.7	25.6	4.0[d]	0.0[d]	12.9	(c)	0.0[d]	0.0[d]
-	-	-	-	-	-	-	-
28.5	21.6	4.0[d]	7.4[d]	15.2	10.9	1.0	1.3
28.5	21.4	15.0	10.0	7.6	7.0	1.5	0.6
30.1	24.4	8.0	3.5	20.4	15.9	3.0	1.8
27.5	20.7	1.0	2.1	12.6	11.9	2.0	0.6
34.6	22.0	4.0[d]	14.3[d]	20.3	12.2	38.0	26.9
25.1	18.3	4.0	2.1	8.4	(c)	2.0[d]	-[d]
25.8	13.8	30.0	23.6	14.5	6.7	23	16.3
30.5	19.4	7.0	5.4	15.5	9.9	4.0[d]	0.2[d]
97.1	74.3	30.0	51.5	24.9	9.5	124	93.4
38	33	14	29	26	22	10	19

) at the elevated tensile test temperature before testing, except for TD Nickel.
ll other materials tested in hot extruded condition.

The cobalt-base alloys with boron additions made from prealloyed atomized powder Nos. 3 to 6, containing 26 to 32 v/o dispersed phase, and the iron-cobalt-base alloys made from atomized powder Nos. 12 to 15, containing 20 and 21 v/o dispersoid, tended to have the highest strength at room temperature in comparison with the other compositions made by other methods and containing lesser amounts of dispersoid.

At 1200°F the same alloys, Nos. 3 to 6 and 12 to 15, tended to retain their strength advantage, although these strength levels were approached or exceeded by some of the extrusions of internally oxidized and composite powders. The tensile elongation and reduction of area values were high for extrusions of prealloyed atomized powders. This was related to the rather coarse average particle size (0.73 to 1.6 microns) and large average interparticle spacing (2.0 to 6.4 microns) of the dispersed phase, Table II-18.

The tensile tests at 1600°F revealed the Co + 1.1% B + 4.4% Cb alloy extruded from prealloyed atomized powder No. 5 to have the highest ultimate strength (41,100 psi) and highest yield strength (22,600 psi) combined with high elongation (66%) and reduction in area (61%).

The tensile and yield strengths of four extrusions of prealloyed atomized powders may be compared with those of Nivco alloy and TD Nickel at various temperatures in Figures II-52 and II-53.

The extrusions of powders made by other methods containing dispersions of thoria and alumina tended to have lower values of elongation and reduction in area at all test temperatures than the prealloyed atomized powder products. In this respect, the oxide strengthened extrusions behaved more like conventional dispersion-strengthened material. Fracture of the test specimens occurred in some instances before reaching the yield strength at 0.2% offset, and the measured elongation was approximately zero. Some of these materials would be expected to be notch sensitive.

The effect of increasing the amount of dispersoid on the yield strength of extrusion at 1200°F and 1600°F is illustrated in

Figure II-52. Ultimate Tensile Strength at Various Test Temperatures of Dispersion-Strengthened Materials

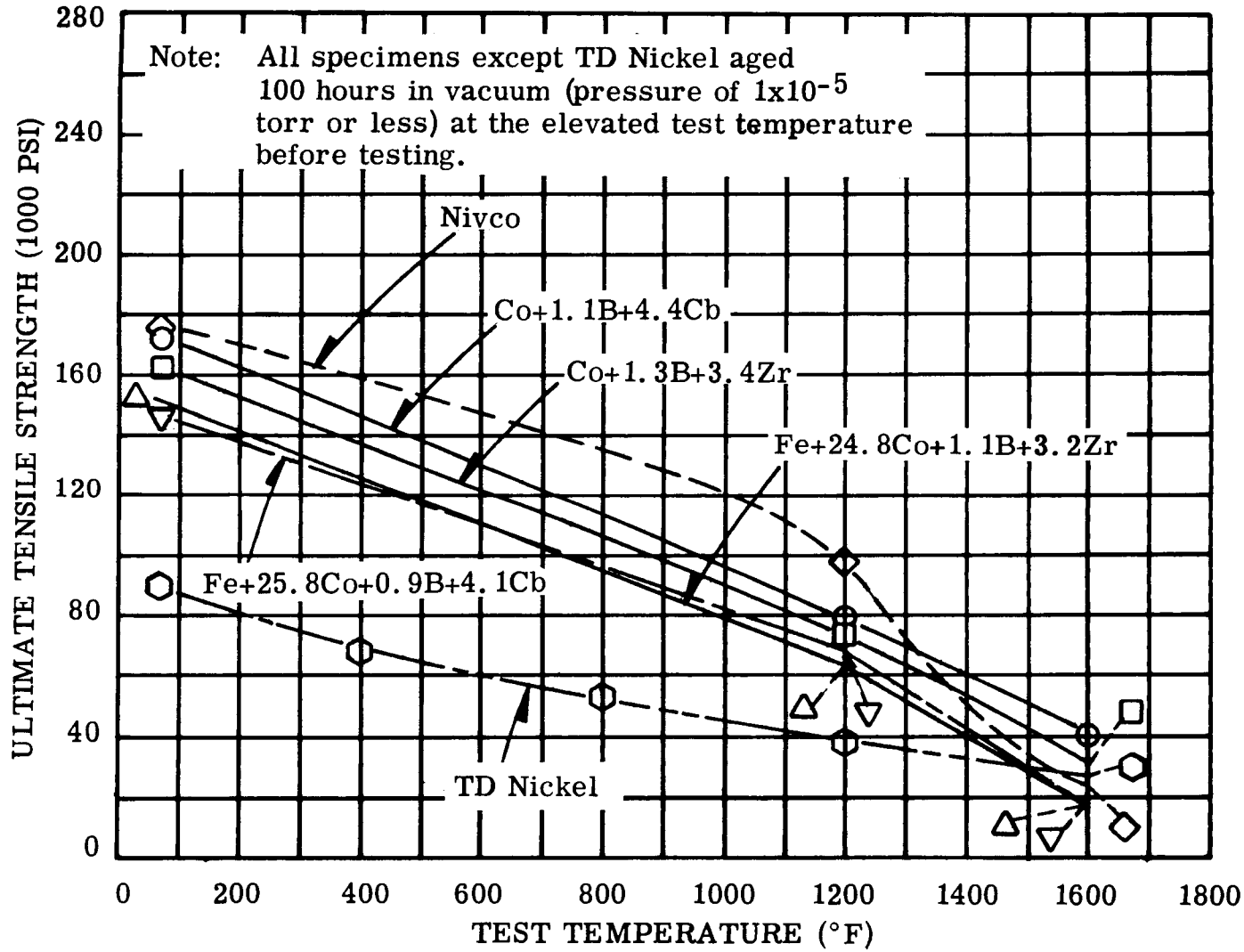

FIGURE II-52. Ultimate Tensile Strength at Various Test Temperatures of As-Extruded Rod of Prealloyed Atomized Powders Compared with Nivco Forged Bar and TD Nickel Bar (Secondary Worked After Hot Extrusion)

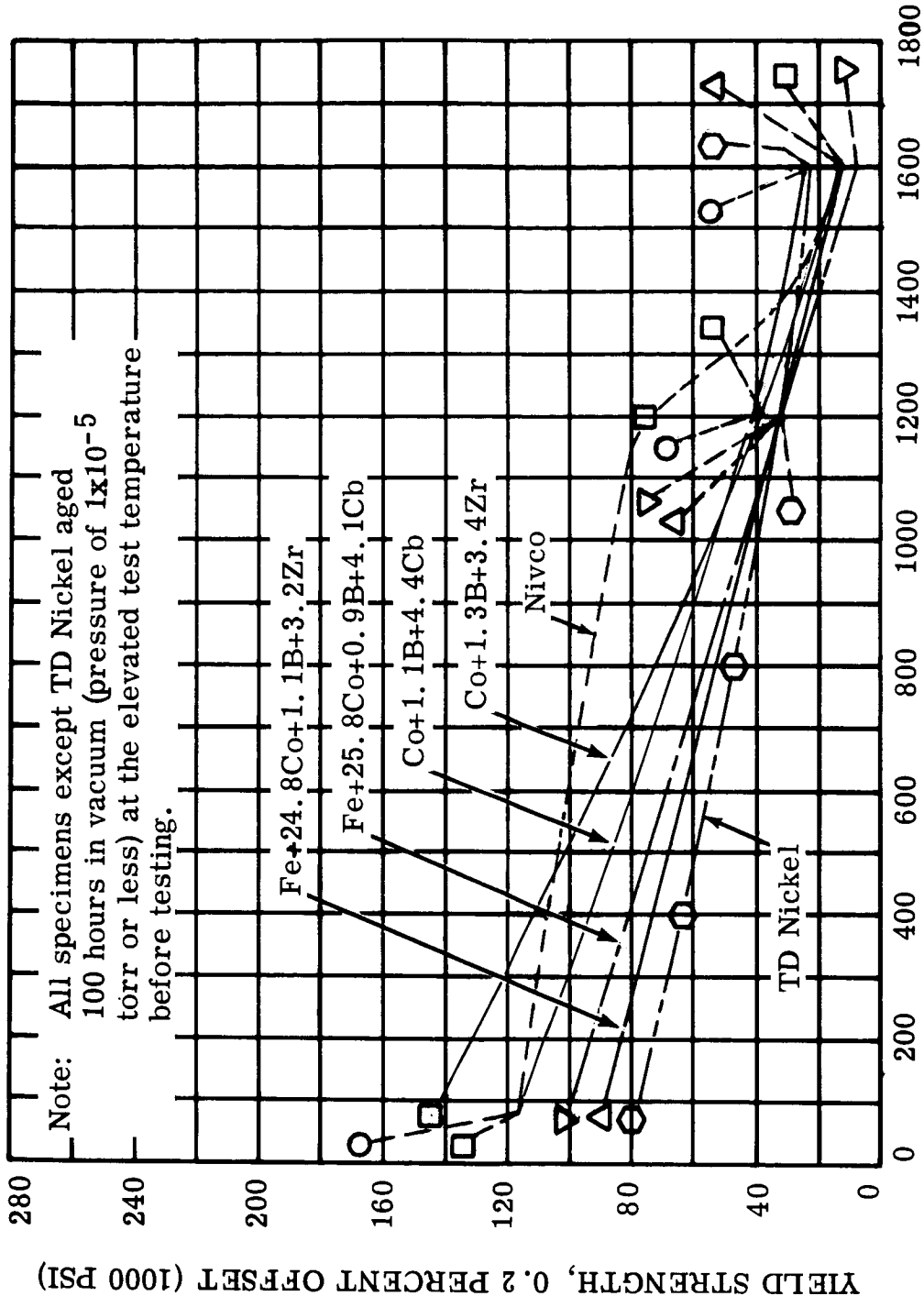

FIGURE II-53. Yield Strength at Various Test Temperatures of As-Extruded Rod of Prealloyed Atomized Powders Compared with Nivco Forged Bar and TD Nickel Bar (Secondary Worked After Hot Extrusion)

Figure II-53. Yield Strength at Various Test Temperatures of Dispersion Strengthened Materials

Figure II-54. There was a general tendency for strength to increase with increasing volume percent of dispersed phase. (In this type of plot the influence of the size of the dispersed particles and their interparticle spacing have been neglected.)

Decreasing the average distance between dispersed particles in the matrix tended to raise the yield strengths of extrusions at 1200°F and 1600°F, as shown in Figure II-55. This decrease in average interparticle spacing was achieved by decreasing the particle size for a given volume percent of dispersoid, or by increasing the volume percent dispersoid while holding the particle size constant.

3. Program for the Next Quarter

a) Magnetic and tensile testing will be completed on extrusions made to date.

b) The correlation of dispersoid parameters measured on the microstructure with magnetic and tensile properties will be finished.

c) Recommendations concerning compositions and processing conditions for materials for the intermediate evaluation phase of this program will be developed. Purchase requisitions for new materials will be written.

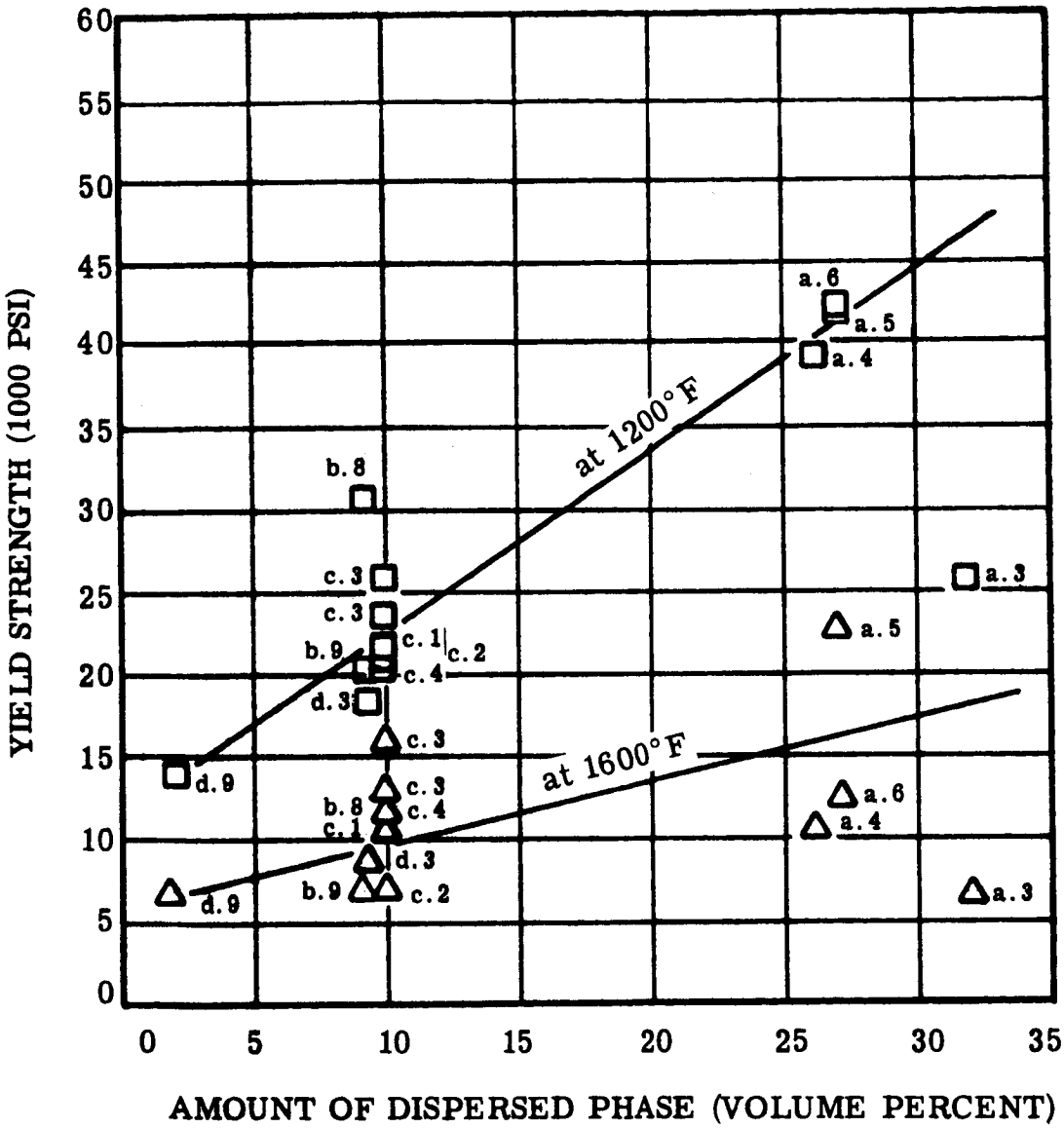

FIGURE II-54. Effect of Amount of Dispersed Phase in Cobalt As-Extruded Rod on the Yield Strength at 1200°F and 1600°F

Note: Data points for the various compositions are identified by Powder or Extrusion numbers listed in Tables II-18 and II-20.

Figure II-54. Yield Strength of Cobalt-Base Material Containing Different Amounts of Dispersoid

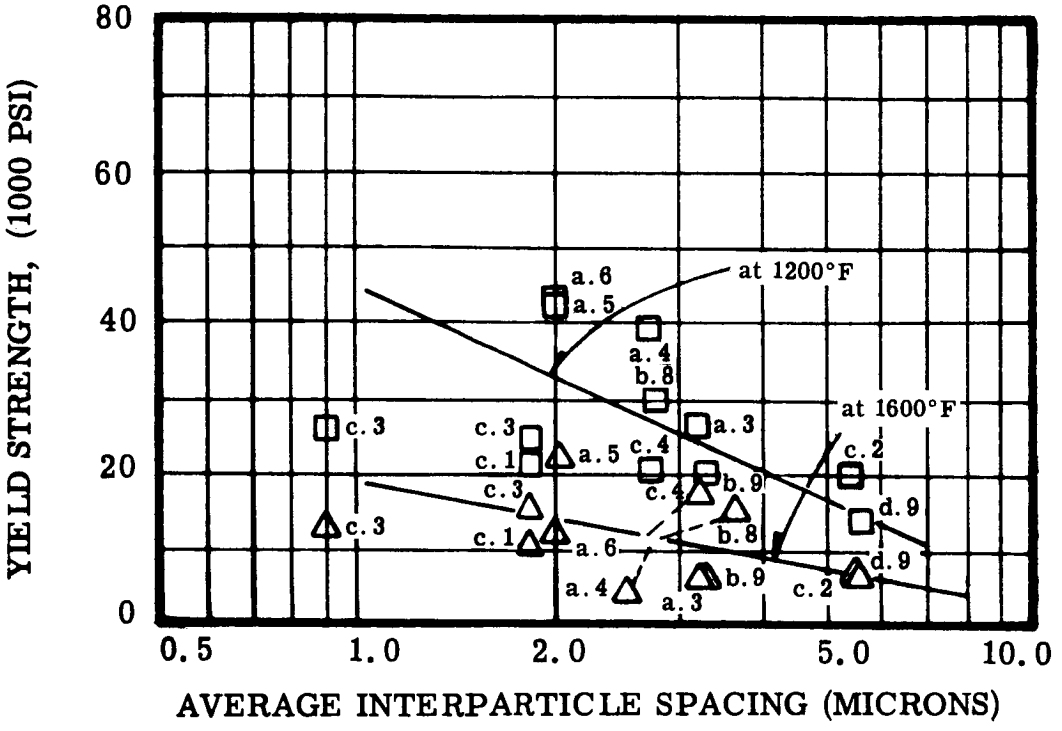

FIGURE II-55. Effect of Distance Between Dispersed Particles (Approximate Values) in Cobalt As-Extruded Rod on Yield Strength at 1200°F and 1600°F

Note: Data points for the various compositions are identified by Powder or Extrusion numbers listed in Tables II-18 and II-20.

Figure II-55. Yield Strength of Cobalt-Base Material Containing Different Interparticle Spacings

D. TASK 4 - CREEP TESTING

1. Summary of Technical Progress

a) Specimen number one from heat 10-NO2V-1099 was removed from test at 3021 hours after reaching 2.4 percent extension. This sample had been on test at 50,000 psi and 1100°F. The test was terminated at the start of third stage creep.

b) Specimen number two has accumulated 4122 hours on test at 37,500 psi and 1100°F. Creep strain amounts to 0.44 percent. Capsule pressure is 2.6×10^{-9} torr.

c) Specimen number three was placed on test at 1150°F and 30,000 psi. Creep strain amounts to 0.78 percent after 1096 hours. Test pressure is 5.1×10^{-9} torr.

d) Specimen number four has accumulated 664 hours at 50,000 psi and 1050°F. Present pressure is 6.8×10^{-9} torr. Creep strain is 0.24 percent.

e) The fifth specimen from heat 10-NO2V-1099 is on test at 1150°F and 25,000 psi. Test pressure is 1.8×10^{-8} torr after 595 hours. Creep strain at this time is 0.39 percent.

f) The chemical analyses of Nivco heats AC 232 and 10-NO2V-1099 were completed.

2. Discussion

Long-term creep data are needed on high-strength rotor materials suitable for electrical alternators. Nivco alloy is presently the highest temperature rotor material available. Five thousand hour tests are planned at temperatures to 1150°F at pressures below 10^{-6} torr to complement short-time data run on NAS 3-4162.

Strain time plots for the five specimens are shown in Figures II-56 to II-58. Capsule pressures for various test times are noted on the plots. The creep rate for the third specimen (1150°F, 30,000 psi) was higher than had been anticipated and another specimen was set up at 25,000 psi and 1150°F.

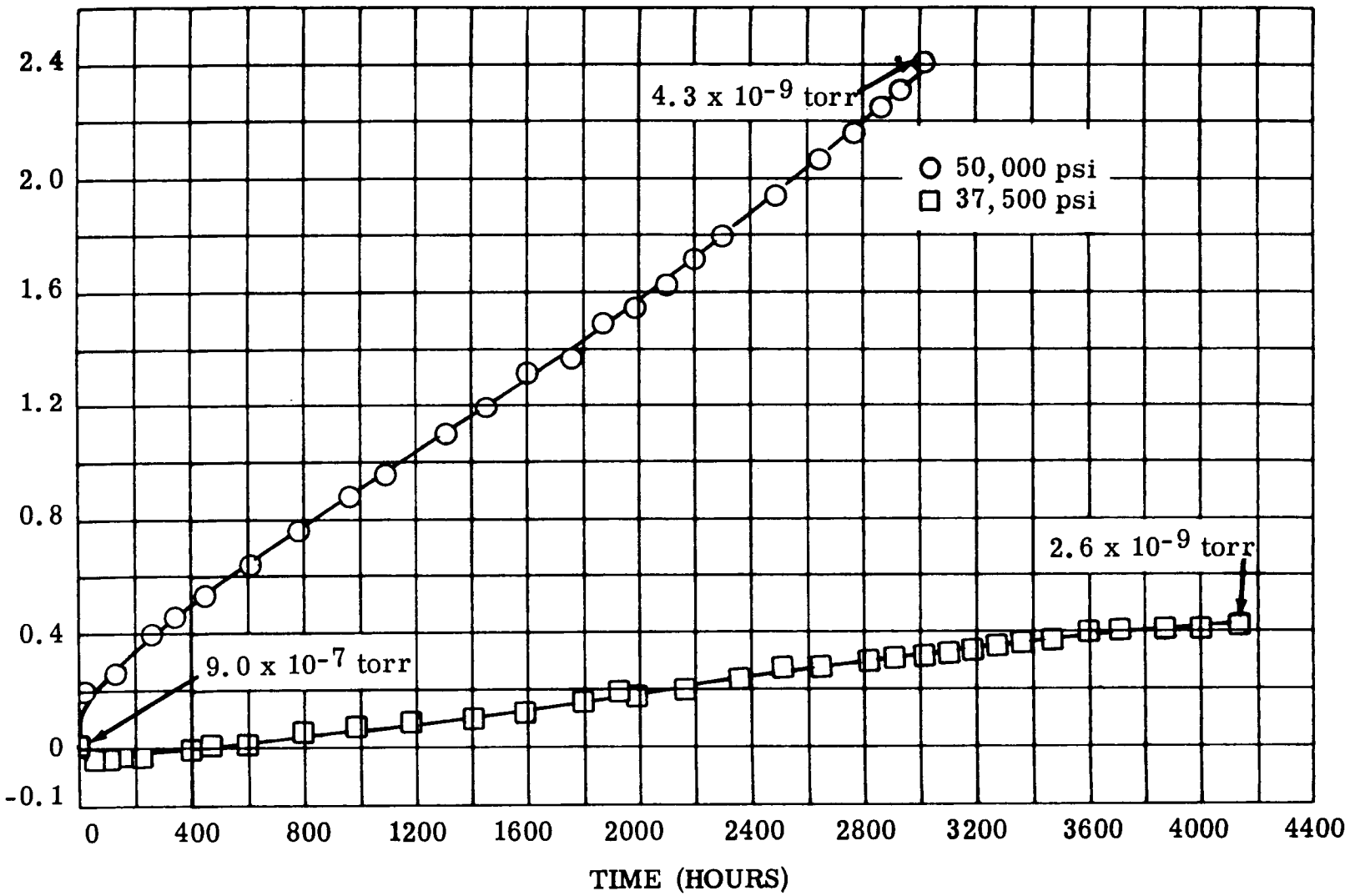

FIGURE II-56. Creep, Nivco Heat No. 10-NO2V-1099, Tested in Vacuum at 1100°F and 50,000 psi and 37,500 psi

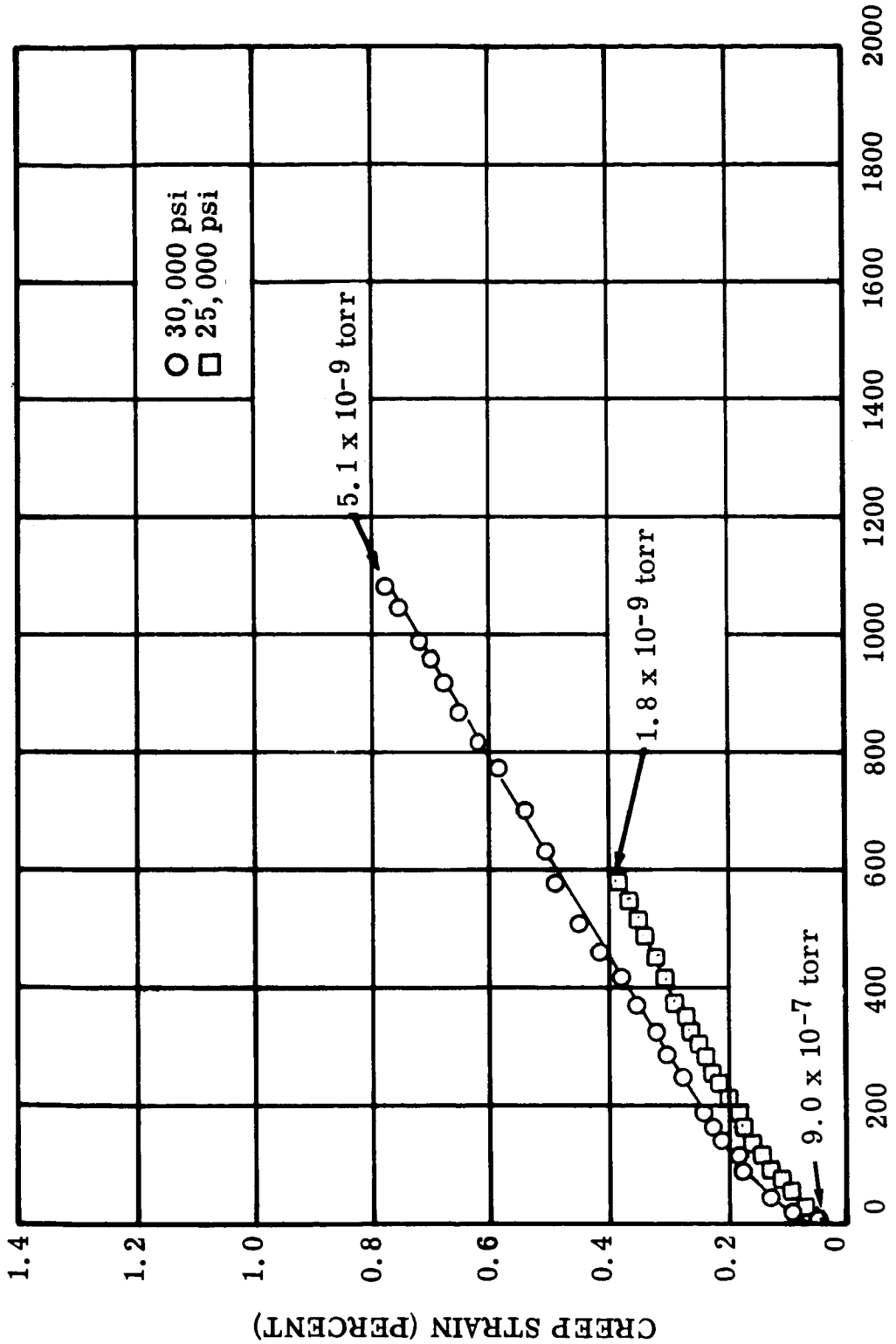

FIGURE II-57. Creep, Nivco Heat 10-NO2V-1099, Tested in Vacuum at 1150°F and 30,000 psi and 25,000 psi

Figure II-57. Creep - Nivco Bar, 1150°F

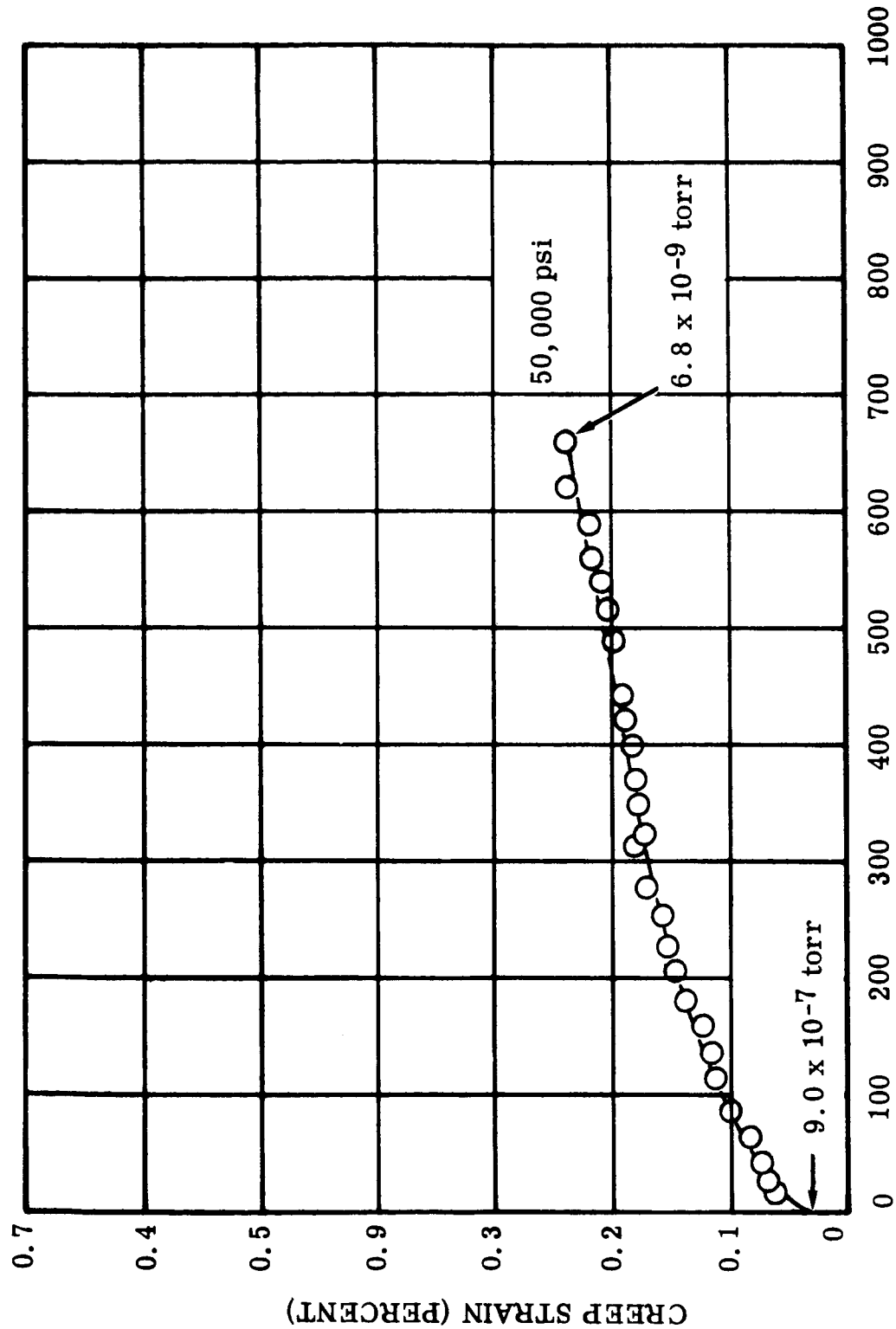

FIGURE II-58. Creep, Nivco Heat 10-NO2V-1099, Tested in Vacuum at 1050°F and 50, 000 psi

Figure II-58. Creep - Nivco Bar, 1050°F

The dates for the completion of 5000 hours testing on each specimen from heat 10-NO2V-1099 are shown below:

Specimen No.	Completion Date
1	Terminated at 3021 hours
2	April 4, 1966
3	August 10, 1966
4	September 1, 1966
5	September 4, 1966

The results of chemical analyses made on Nivco alloy heats AC 232 and 10-NO2V-1099 are listed in Table II-21. The analyses reflect changes in composition which have been made in production Nivco alloy over the past 24 months. The only test run on heat AC 232 was terminated early in the program by a low-strain failure of the test sample. Examination of the failed sample revealed a very large grain size in the material which required that a new heat of alloy be obtained for creep test. The chemical analyses were made for comparison purposes. Note particularly the low oxygen content of both heats of material.

TABLE II-21. Chemical Analysis of Nivco Alloy Heats AC 232 and 10-NO2V-1099

Element	Heat AC 232 (weight percent)	Heat 10-NO2V-1099 (weight percent)
Ni	23.50	23.40
Co	71.70	72.40
Si	0.14	0.27
Mn	0.31	0.26
Al	0.27	0.39
Ti	2.06	1.75
Zr	0.95	0.26
C	<0.0010	0.0038
O	0.0016	0.0009

Specimen number three required 27 hours to reach test temperature while specimens four and five required 75 and 50 hours respectively to reach temperature without exceeding a pressure of 10^{-5} torr. All four capsule sputter ion pumps show currents equivalent to pressures on the 10^{-9} scale, as shown on Figures II-52, II-53, and II-54. The standard ionization gages were valved out of each pump-capsule system when the pressure reached the 10^{-8} scale.

3. Program for the Next Quarter

The four specimens presently on test will be continued.

SECTION III

PROGRAM II - HIGH TEMPERATURE CAPACITOR FEASIBILITY

This program will study the feasibility of building a lightweight capacitor suitable for operation up to 1100°F. It will utilize high-purity dielectric materials and specialized fabrication methods. The ultimate application is in lightweight, high-temperature, power conditioning-equipment suitable for space application.

A. SUMMARY OF TECHNICAL PROGRESS

1) A number of pyrolytic boron nitride wafers have been prepared using improved techniques and a satisfactory method of polishing 0.4 to 1 mil thick wafers was developed.

2) Sheet resistivities of platinum and rhodium thin film electrodes were directly measured and calculated from thickness measurements (interferometer). It was demonstrated that the lower bulk resistivity of rhodium compared to platinum results in a two fold decrease in sheet resistivity for equal thickness films in a range from about 1000 to 4000 Å.

3) A satisfactory correlation between a two probe resistance measurement and film thickness was found. This approach permits a rapid determination of electrode thickness and thickness variations to be made. It has also shown that a capacitor wafer with a mat or "as lapped" surface finish must have an electrode about twice as thick compared to a polished wafer electrode to achieve equivalent sheet resistivities.

4) Sputtering parameters were found to be reproducible from batch to batch. It appears feasible, therefore, to achieve controlled and predictable electrode thickness and to derive the electrode thickness from the measured target current and total sputtering time.

5) A total of seven rectangular pyrolytic boron nitride capacitors (0.46 to 1 mil wafer thickness) were made and evaluated individually and in multi-layer stacks. These capacitors have 50 percent greater areas than the tabbed circular capacitors and, to date, no clear cut data has been obtained to demonstrate a superiority of one geometry over the other.

6) A five wafer multi-layer capacitor consisting of polished tabbed wafers with pure platinum and pure rhodium electrodes and with compensating electrode thickness to achieve equivalent sheet resistivities was evaluated in detail. Capacitance, Tan δ and d-c resistance was measured from room temperature to 1100°F in vacuum and the properties of each wafer was determined individually.

B. DISCUSSION

1. Introduction

The overall objective of this program is to determine feasibility of fabricating high-temperature capacitors which are compact, lightweight, and suitable for operation in static power conditioning apparatus for space applications. A group of specific capacitor capabilities has been established as program objectives. These include:

a) Volume Parameter (μF·volts/in^3): 50 to 150

b) Dissipation Factor (Tan δ) at 1100°F: 0.005 to 0.02 maximum (60 cps to 50 kc/sec)

c) Capacitance change: ± 5% (room temperature to 1100°F)

Feasibility can be demonstrated if these goals are achieved and the capacitor will be capable of operating in the 800 to 1100°F temperature range without supplemental cooling. Furthermore, a high temperature capacitor meeting these requirements will be competitive in terms of size, weight, and electrical properties with more conventional capacitors designed for much lower operating temperatures.

Four quarterly reports have been issued on this program with detailed discussions of the results. The following summarizes these results:

a) Fixturing and methods have been developed for slicing,

lapping, and polishing thin wafers of pyrolytic boron nitride (Boralloy), polycrystalline Al_2O_3 (Lucalox and hot pressed Linde A), single crystal sapphire, and hot pressed polycrystalline BeO. Pyrolytic boron nitride has been successfully made into wafers one inch square with thicknesses as thin as 0.5 mils (12 microns). The minimum thickness that can be reliably achieved with the other materials is in the range from three to five mils (75 to 125 microns).

b) Electrical data (Capacitance, Tan δ , d-c resistance) was obtained over the temperature range from room temperature to 1100°F in vacuum for each of these thin wafer materials and the d-c breakdown strength was measured at room temperature and 1100°F for several different materials. Test capacitors were prepared with sputtered high-purity platinum alloy electrodes using a Plasma-Vac sputtering system.

c) The electrical data has been analyzed and compared for each candidate material. The results show that pyrolytic boron nitride will be the most promising high-temperature capacitor material. Typical measured values obtained for a pyrolytic boron nitride capacitor with 1 mil thick dielectric are:

1) Tan δ at 1100°F: 0.0009 (1 kc/sec)

2) Capacitance change from room temperature to 1100°F: -1.5%

3) DC Electric Strength: Room Temperature - 10 000 volts/mil, 1100°F - 6000 to 7000 volts/mil

The above indicates that the program objectives can be met and possibly exceeded by a substantial margin using this material. In addition, a "figure of merit" was determined for each candidate material in order to assign a quantitative number to relative fabricabilities combined with electrical properties. The selection of pyrolytic boron nitride for a high-temperature capacitor was clearly indicated by this type of comparison.

d) A prototype multi-layered capacitor was fabricated with 1 mil thick pyrolytic boron nitride and "wrap around" sputtered electrodes to achieve parallel electrical interconnection in a three wafer stacked configuration. Design feasibility has been demonstrated based on 1100°F electrical data in vacuum.

This report includes discussions of the most recent improvements made in preparing thin (0.4 to 1.0 mil) wafers of pyrolytic boron nitride, methods used to measure the thickness and sheet resistivities of thin film sputtered electrodes, process controls that can be achieved by sputtering, an evaluation of rectangular vs. circular capacitor wafer geometries, and the results and analysis of the data obtained for a five wafer multi-layer capacitor.

2. Wafer Preparation

All wafers (1 inch x 1 inch x ~ 0.008 inch) used during this phase of the program were prepared by making slits from 1/8 to 1/4-inch deep along one edge of pyrolytic boron nitride blocks 1/8 or 1/4-inch thick. The slits were made with a rubber bonded silicon carbide wheel 0.006 inch thick mounted on a precision wafering machine (Micromesh Mfg. Co.). Best results were obtained without any water coolant, a feed rate of 0.1 inch per minute and a wheel speed of 4000 rpm. Seven slits were made in a 1/8-inch thick block approximately 0.008-inch apart. Wafers were cleaved from the block with a single edged razor blade as described in the second quarterly report.

A yield of eight wafers was expected from a 1/8-inch thick block but generally the first two wafers cleaved did not part parallel to the major block surfaces and would break out before reaching an opposite edge. The remaining six or seven wafers were satisfactory except for a thickness variation of from 0.005 to 0.010-inch measured across the surface. These difficulties may be related to the layered structure of pyrolytic boron nitride with respect to the major surfaces of the block. Further investigation of the effect is planned. It is also planned to gang seven cut off wheels together with six to eight mil spacers to determine the feasibility of making multiple slits.

The preparation of thin wafers (0.5 to 1 mil thick) from cleaved pieces has been modified somewhat from the procedure described in the fourth quarterly report. Wafers are reduced to two mil thicknesses by the methods previously detailed. However, the final thickness reduction

to the one mil range is presently achieved by lapping each wafer between a fixed and floating glass plate using five micron alumina abrasive and water. Wafers about two mils thick are simply laid on a large fixed glass plate with a small amount of abrasive slurry and covered with a 3 x 3 inch square glass plate. The smaller plate is moved by hand in a figure 8 motion and periodically removed for thickness measurements (micrometer). One inch square wafers have been lapped to thicknesses in the range from 0.4 to 1 mil with good yields (about 80%).

A new approach has been developed for polishing one mil wafers based on an extention of the lapping techniques described above. The motion mechanics are the same except that 0.3 micron Linde A abrasive is used and the surface of the fixed and moving plates (three inch diameter steel disk, one inch thick) are covered with Pre K (Geoscience Intr. Co.) polishing paper. Wafers that have been thoroughly cleaned to remove the five micron alumina abrasive are laid between the fixed and moving plate. The cover plate is rapidly moved by hand which effectively polishes both surfaces of the wafer simultaneously in about two to three minutes. The major advantages of this approach is a high degree of wafer flatness and an overall simplification of the polishing process compared to wax bonding wafers to a holding plate. It is also felt that the elimination of organic materials (wax) during these final stages of wafer preparation facilitates the subsequent cleaning process and greatly minimizes the possibility of residual organic or carbon particles remaining on the wafers after cleaning.

Several additional steps have been added to the final cleaning process described in previous reports in the following sequence:

a) After the wafers are cleaned as outlined in the third quarterly report, they are heated in air (platinum crucible) to 600 to 700°C (1112 to 1292°F) for 20 minutes.

b) Cooled wafers are soaked in hot 60 to 70°C (140 to 156°F) concentrated HF for about 10 minutes.

c) Rinse in flowing deionized water for 10 minutes followed by three clean rinses in methyl alcohol and three clean rinses in acetone.

d) Before loading into sputtering masks the wafers are given a final cleaning in vapors of isopropl alcohol and then dried at 150°C (302°F).

3. Process Control of Sputtered Electrodes

a. PURE PLATINUM AND RHODIUM THIN FILM ELECTRODES

A series of preliminary tests were made on pure platinum and rhodium films sputtered onto 2 x 2 and 3 x 3 inch glass squares (Corning 7059) and film thickness was measured by several different methods. The sputtering conditions are shown in Table III-1 for a total argon pressure of approximately one micron. Measurements were made on the sputtered films as follows:

1) Film resistance was measured by diamond scribing electrically isolated strips with length to width ratios of about 15. The strip resistance was measured using a constant current source (battery) and the voltage drop was determined across a known length with an electrometer. The sheet resistivity in ohms/square was calculated from the length to width ratio.

2) Film thickness was measured with a multiple beam microinterferometer attachment to a Unitron Series N Metallograph. This device uses a cadmium light filter and generates interference fringes with a separation of $\frac{\lambda}{2}$ ($\lambda = 0.644\ \mu$).

3) The overall film thickness was measured for the platinum film using before and after weight determinations and calculating the thickness from the substrate area and density of platinum.

4) A two point probe (0.1 inch spacing) connected to an ohmmeter was lightly pressed on the film surfaces and the measured probe resistance was correlated with the sheet resistances determined by 1) and 2) above. The results obtained were as follows:

Platinum (99.95%)

a) Strip Resistance Measurement - 0.430 ohms/square sheet resistivity equivalent to a 2560 Å thick film based on a bulk resistivity value of 10.8×10^{-6} ohm-cm at room temperature.

TABLE III-1 Sputtering Data Used to Derive Electrode Thickness for Tabbed Wafers (5 Wafer Multi-Layer Capacitor No. 2)

Substrate	Target Material (Electrode)	Target Size Spacing 1-1/4"	Sputtering Voltage (VDC)	Total Target Area (cm^2)	Target Current (average)	Target mA/cm^2 (average)	Total Sputtering Time (min)	Specific Rate $\left(\frac{mA}{cm^2 \cdot min}\right)$	Measured Film[(a)] Thickness (Å)	Measured Deposition Rate (Å/min)	Derived Deposition Rate (Å/min)	Derived Film Thickness (Å)
#1 Tabbed (Polished)	Pt	Two 3"x3" Sheets	900	116	105mA	0.905	41	0.022	--	--	91.8	3760
#2 Tabbed (Polished)	Pt	Two 3"x3" Sheets	900	116	105mA	0.905	41	0.022	--	--	91.8	3760
#3 Tabbed (Polished)	Pt	Two 3"x3" Sheets	900	116	105mA	0.905	41	0.022	--	--	91.8	3760
#4 Tabbed (Polished)	Rh	One 3"x3" Sheet	900	58	50mA	0.863	25 ea. side	0.0345	--	--	100	2500
#5 Tabbed (Polished)	Rh	One 3"x3" Sheet	900	58	50mA	0.863	25 ea. side	0.0345	--	--	100	2500
STANDARD 3"x3" glass Square-Corning 7059	Rh	One 3"x3" Sheet	900	58	25mA	0.430	60	0.00717	1270	21	--	--
STANDARD 2"x2" glass Square-Corning 7059	Pt	One 3"x3" Sheet	900	58	40mA	0.690	60	0.0115	2890	48	--	--

(a) Measured film thickness is average of multiple beam interferometer measurement and thickness determined from strip resistance.

(b) Nominal argon pressure - 1 μ.

b) Interferometer measurement - 3200 Å

c) Weight determination - 5540 Å

Rhodium (99.9%)

a) Strip resistance measurement - 0.387 ohms/square sheet resistivity equivalent to 1290 Å thick film based on a bulk resistivity value of 4.98×10^{-6} ohm-cm.

b) Interferometer - 1250 Å

These data show that lower ohms/square values can be obtained with rhodium films that are about 1/2 as thick as platinum. This is in general agreement with the differences in bulk resistivity. Values (ref. 1) for the bulk resistivity of rhodium and platinum at 930°F (14.6×10^{-6} ohm-cm and 27.9×10^{-6} ohm-cm respectively) show that the resistance of platinum is about two times greater than rhodium. For the same thickness electrodes, therefore, rhodium films should make the least contribution to measured capacitor losses over the temperature range from room temperature to 1100°F.

The variation in the thickness of the platinum film over the entire area of the 2 x 2 inch substrate was estimated by using the two probe method outlined above. Figure III-1 shows a plot of measured probe resistance vs. ohms/square. The curve was plotted from the ohms/square values obtained by measuring strip resistances. This curve is not precise but it does give an approximate value of film thickness or sheet resistivity from measured probe resistances. This permits very rapid and simple tests to be made particularly for comparative purposes. On this basis the platinum film thickness varied from about 3600 Å to 2700 Å. The maximum thickness was recorded at the lower edge of the substrate. The target used was 3 x 3 inches square and the target to substrate distance was 1-1/4 inches. A larger target area in relation to the substrate area would be one way to minimize thickness variations.

The two probe method was also used to determine the effect of surface finish vs. effective sheet resistivity. Several measurements have shown that the sheet resistivity is reduced by a factor

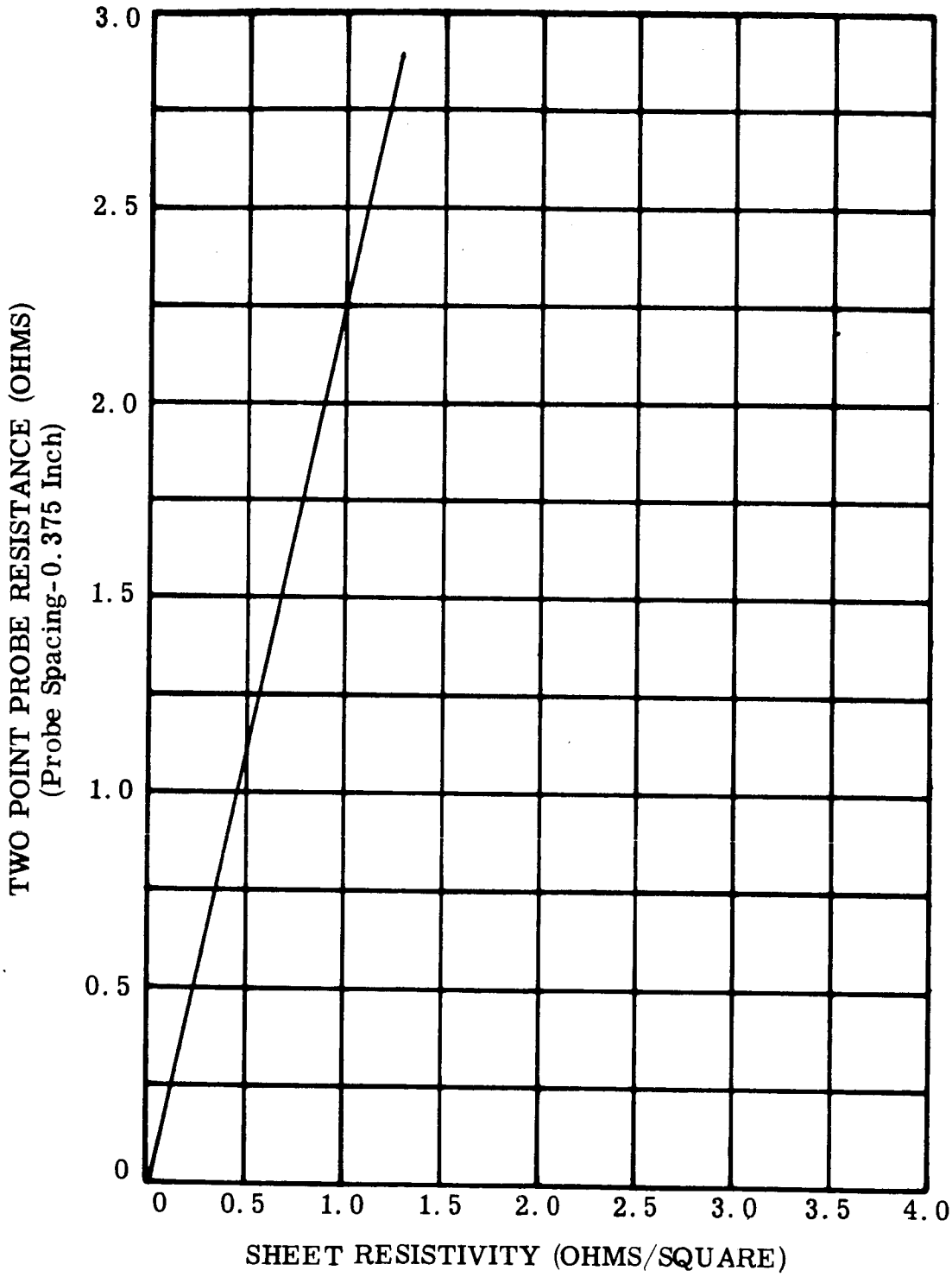

FIGURE III-1. Two Point Probe Resistance vs. Sheet Resistivity

Figure III-1. Two Point Probe Resistance vs. Sheet Resistivity

of about 2.3 on a matte substrate surface vs. a polished surface. For example, wafer No. 2 in Table III-2 has a derived electrode thickness (Rhodium) of 3900 Å. The measured probe resistance is 0.7 ohms which, according to Figure III-1, corresponds to a sheet resistivity of 0.3 ohms/square or an effective film thickness of only 1660 Å. By comparison, the probe resistance measured on wafer No. 4 (Table III-2) was 0.5 ohms which corresponds to a sheet resistivity of about 0.2 ohms/square (2500 Å film thickness). This wafer has polished surfaces and as shown in Table III-2 has a derived film thickness of 2500 Å. These derived film thicknesses were calculated from "sputtering rates" indicating that the overall correlation is satisfactory and that film thickness can, in fact, be determined from sputtering parameters.

Table III-1 shows how the electrode thickness of five tabbed wafers was determined from the sputtering data. The basis for these calculations are the sputtering conditions (sputtering voltage, target area, target current and sputtering times) recorded during the deposition of rhodium and platinum films on the 3 x 3 and 2 x 2 glass substrates. The thicknesses of these films measured with an interferometer and calculated from strip resistance measurements was averaged and a deposition rate of 21 Å/min for rhodium and 48 Å/min for platinum determined. These values are shown in Table III-1 together with values for the target current per unit area and time (ma/cm^2-min). Similar data were obtained during the sputtering of tabbed wafers and assuming a linear relationship, a derived "sputtering rate" (Å/min)was obtained which multiplied by the total sputtering time gives the derived film thickness shown in Table III-1 for tabbed wafers 1 through 5.

4. Rectangular vs. Circular Capacitor Geometries

The previous quarterly report showed the results of electrical measurements on a stacked three wafer capacitor consisting of tabbed 0.750 inch diameter wafers (matte surface finish). Although the results were satisfactory it was felt that lower a-c losses (particularly at frequencies greater than 1 kc/sec might be obtained with a rectangular wafer geometry because of the increased contact area between interconnecting electrodes. Figure III-2 shows the wafer dimensions, electrode dimensions and the interconnection overlap. A photograph of the actual capacitor wafers together with several tabbed 0.750 inch diameter wafers is shown in Figure III-3.

TABLE III-2. Rectangular Wafer Capacitors and Electrical Data for Individual Capacitors and Multi-Layer (Stacked) Units

Wafer No.	Surface Finish	Sputtered Electrode Material	Derived Electrode Thickness (Ref. Table III-1)	Electrode Area (in^2)	Average Wafer Thickness (Calculated)	Capacitance (pF) and Tan δ at Room Temperature				Comments
						1 kc/sec		10 kc/sec		
						Capacitance	Tan δ	Capacitance	Tan δ	
1	Matte	Rh	3900 Å	0.562	0.88 mils	486.4	0.00075	485.9	0.00075	Wafer flatness is good
2	Matte	Rh	3900 Å	0.562	1.0 mils	432.3	0.00068	431.8	0.00061	Wafer ripped during handling
3	Matte	Rh	3900 Å	0.562	0.94 mils	454.9	0.00093	454.3	0.00089	Wafer flatness is good
Unit No. 1	Measured capacitance and Tan δ of matte wafers No. 1, No. 2, and No. 3 stacked					1377.2	0.0008	1375.7	0.00092	Measurements in room ambient
4	Polished	Rh	3200 Å	0.562	0.60 mils	715.3	0.0016	714.2	0.00087	Wafer has tendency to curl
5	Polished	Rh	3200 Å	0.562	0.68 mils	632.2	0.00109	631.4	0.00082	Same
6	Polished	Rh	3200 Å	0.562	0.78 mils	550.8	0.00086	550.3	0.00063	Same
Unit No. 2	Measured capacitance and Tan δ of polished wafers No. 4, No. 5, and No. 6 stacked					1903.9	0.00099	1901.7	0.00076	Measurements in room ambient
Unit No. 3	Measured capacitance and Tan δ of polished and matte wafers No. 1, No. 3, No. 4, No. 5, and No. 6 stacked					2889.2	0.00072	2886.3	0.00070	Measurements in vacuum (100 microns)

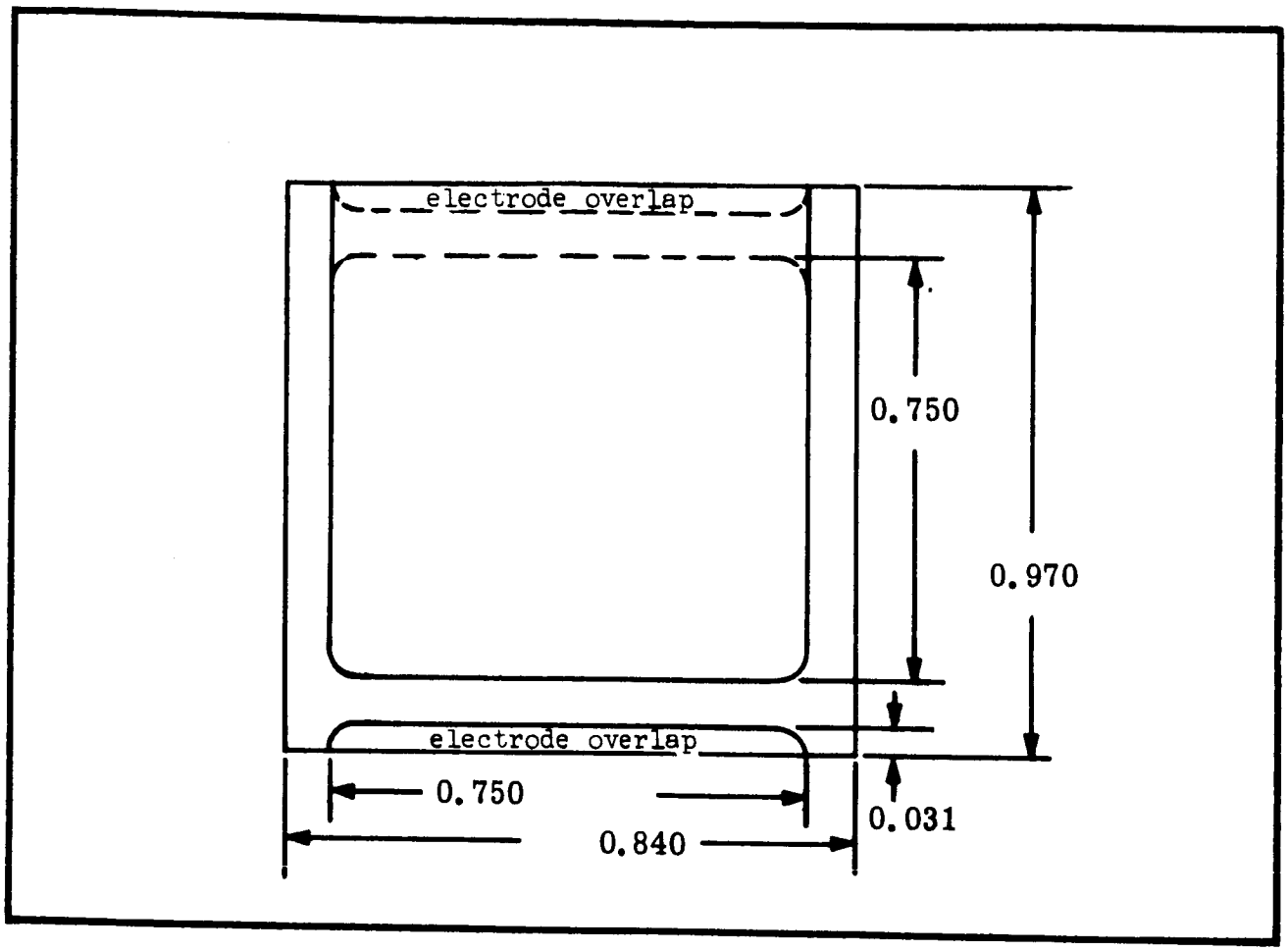

Note: Drawn to Approximate Scale 4 : 1

0.500 Inch

FIGURE III-2. Dimensions of Rectangular Capacitor Wafers and Electrodes

Figure III-2. Dimensions of Rectangular Capacitor Wafer

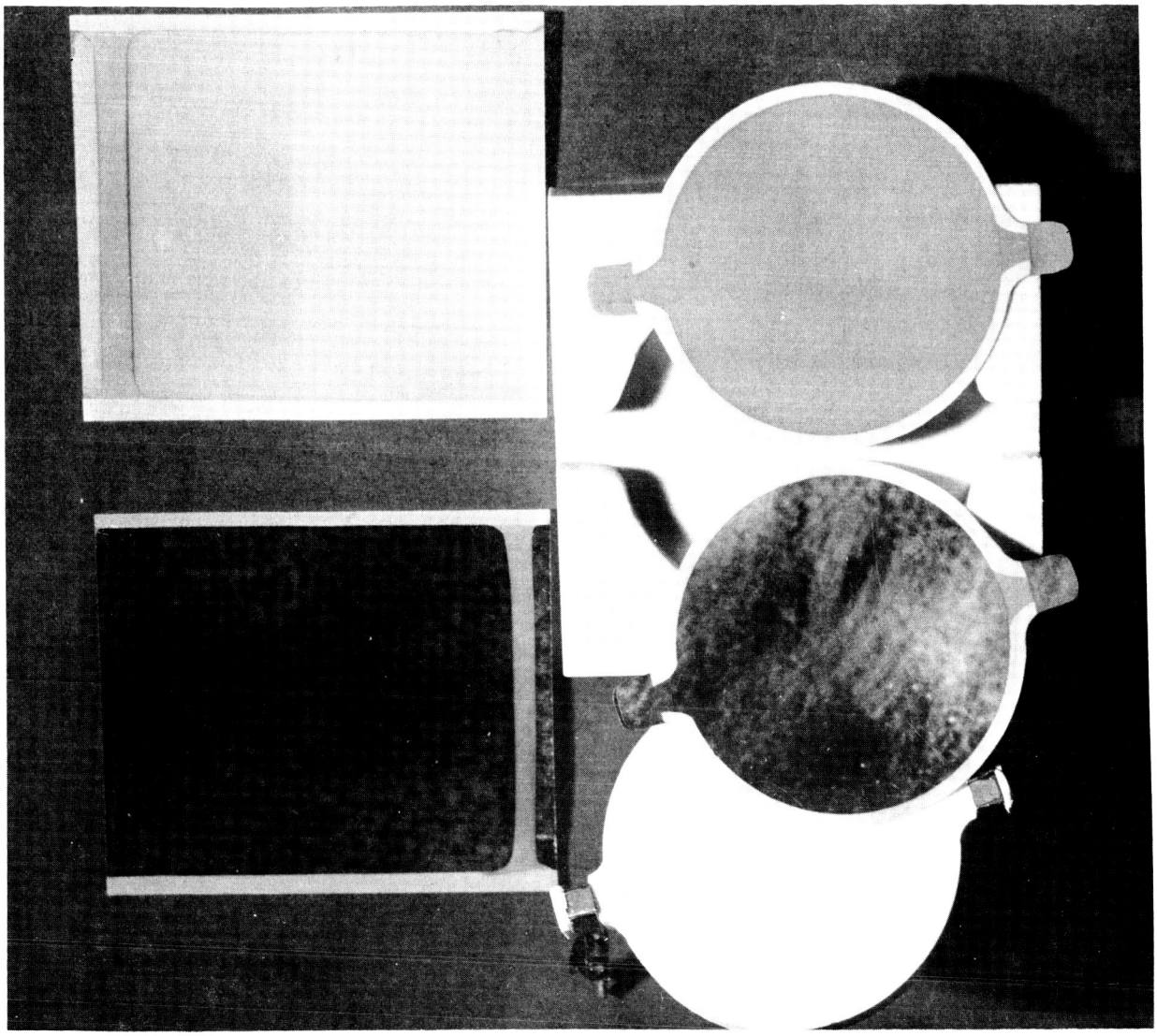

FIGURE III-3. Photograph of Rectangular Capacitor Wafers and Tabbed 0.750 Inch Diameter Wafers

A total of 10 rectangular capacitors have been made. Electrical measurements made at room temperature on individual capacitors and various stacked combinations are shown in Table III-2. All wafers shown have rhodium electrodes with derived electrode thicknesses in the range from 2500 Å to 3900 Å. The average wafer thickness (calculated from measured capacitance) ranged from 0.47 to 1.0 mils. In general, it appears that there is no significant differences in measured tan δ values for a five stack rectangular capacitor vs. a five stack tabbed circular capacitor. (Compare data in Tables III-2 and III-3.) In addition, the tan δ values at 1 and 10 kc/sec shown in Table III-2 for the rectangular capacitors are somewhat higher than the values measured for the tabbed circular capacitors shown in Table III-3. The reason for this is not clear although it may be related to the larger area of the rectangular units and the increased probability that more thin spots in the dielectric are covered by the electrodes. There does appear to be a linear relationship between dielectric thickness and tan δ which will be discussed in the next section.

Under the comments column in Table III-2 it is noted that the polished wafers with sputtered electrodes have a tendancy to curl particularly at the edges where the electrode overlap occurs. The overall flatness of wafers with matte surfaces; however, is much improved.

Data has been obtained that indicates the surface finish of rectangular wafers might have a greater effect on measured tan δ values at frequencies higher than 1 kc/sec compared to the differences in geometry and interconnection area. For example, Table III-2 shows tan δ values at 1 and 10 kc/sec for a three wafer stacked capacitor consisting of all wafers with matte surface finished (wafers No. 1, No. 2, and No. 3). Also shown are the tan δ values for a three wafer stacked capacitor consisting of all wafers with polished surfaces. In the latter case, (Unit No. 2, Table III-2) tan δ decreases from 0.00099 at 1 kc/sec to 0.00076 at 10 kc/sec whereas with matte wafers, (Unit No. 1, Table III-2) tan δ increases at 10 kc/sec indicating higher contact resistance.

These measurements were made with a 200 gram weight on top of the stack and in room ambient conditions. Table III-2 also shows tan δ values for a five wafer stack consisting of a mix of matte and polished wafers (wafer Nos. 1, 3, 4, 5, and 6) but measured in vacuum (100 microns) and at higher clamping pressures. In this case tan δ is about the same at 1 kc/sec and 10 kc/sec. The results would indicate

TABLE III-3. Characteristics of Individual Tabbed Wafers Used in 5 Wafer Multi-Layer Capacitor No. 2 and Calculated Volume Parameter $\frac{\mu F \cdot Volts}{in^3}$

Wafer No. (all polished surface)	Sputtered Electrodes				Capacitance & Tan δ at Room Temp.				Calculated Wafer Thickness $T=\frac{KA}{445C}$	Wafer Area (Including Tabs) (in^2)	Wafer Volume (in^3)	$\frac{\mu F \cdot Volts}{in^3}$ (a)
					1 kc/sec		10 kc/sec					
	Material	Sheet Resistivity (ohms/square)	Derived Thickness (Å)	Area (in^2)	C (pF)	Tan δ	C (pF)	Tan δ				
1	Rh 99.9%	0.2	2500	0.364	343.177	0.000418	342.924	0.00037	0.81 mils ($8.1x10^{-4}$ in)	0.457	$3.7x10^{-4}$	
2	Rh 99.9%	0.2	2500	0.364	398.50	0.00052	398.034	0.00047	0.72 mils ($7.2x10^{-4}$ in)	0.457	$3.3x10^{-4}$	
Wafer 1 and 2 Stacked					741.969	0.000488	741.499	0.00052				
3	Pt 99.99%	0.29	3760	0.364	657.277	0.000786	656.627	0.00072	0.42 mils ($4.2x10^{-4}$ in)	0.457	$1.9x10^{-4}$	
4	Pt 99.99%	0.29	3760	0.364	454.581	0.000605	454.234	0.00054	0.61 mils ($6.1x10^{-4}$ in)	0.457	$2.8x10^{-4}$	
5	Pt 99.99%	0.29	3760	0.364	566.687	0.00108	565.901	0.00105	0.49 mils ($4.9x10^{-4}$ in)	0.457	$2.2x10^{-4}$	
Wafers 3, 4, and 5 Stacked	(Measured values)				1680.74	0.000764	1678.98	0.00078		·		
Total 5 Wafers Stacked	(Measured values)				2434.59	0.000646	2432.42	0.00067	3.05 mils ($3.05x10^{-3}$ in)		$1.4x10^{-3}$	870

(a) The $\frac{\mu F \cdot Volts}{in^3}$ value for the 5 wafer capacitor was calculated using the measured capacitance (2.434×10^{-3} μF), an assumed DC voltage (500V) and the total volume (1.4×10^{-3} in^3).

that the contact resistance was lowered in vacuum and/or by higher clamping pressure.

To summarize, it appears that additional data will have to be accumulated on rectangular and round tabbed capacitors stacked in multiple to show a clear cut preference for one geometry over the other. At present, the rectangular wafers are more difficult to work with and have not shown as good overall electrical properties as the capacitor wafers with a round geometry.

5. Analysis of Five Wafer Tabbed Multi-Layer Capacitor No. 2

Room Temperature Data

Table III-3 was prepared to show a complete breakdown of the characteristics of each individual capacitor in the five stack unit. Electrical data on this unit was obtained from room temperature to 1100°F in vacuum and these results are discussed in the next section. However, several important observations can be made with the aid of Table III-3 and the room temperature electrical data.

For example, the $\mu F/in^3$ value calculated for this unit is 1.74. If it is assumed that the capacitor can be rated at 500 V d-c, then a μF volt/in^3 product of 870 is obtained. This value is better than eight times the minimum value established as a program objective.

Table III-2 also shows the calculated average wafer thickness for each wafer. Thicknesses vary from 0.42 mils to 0.81 mils. Figure III-4 shows a plot of tan δ vs. thickness. For wafers one through four, the relationship is linear with a significant decrease in tan δ with increase in wafer thickness. Tan δ for wafer No. 5 does not lie on the straight line. The value of tan δ for this wafer is abnormally high by comparison and the tan δ vs. thickness relationship obtained for the other four wafers and could indicate that wafer No. 5 contains thin spots or defects. It appears that the type of relationships shown in Figure III-4 will be a valuable aid in the selection of individual wafers for multi-layer units. It is planned to obtain and evaluate additional data of this type as more capacitors are made.

Room Temperature to 1100°F Data (at $< 3 \times 10^{-7}$ torr)

The five wafers shown in Table III-3 were stacked in the pyrolytic boron nitride fixture described in the fourth quarterly report and

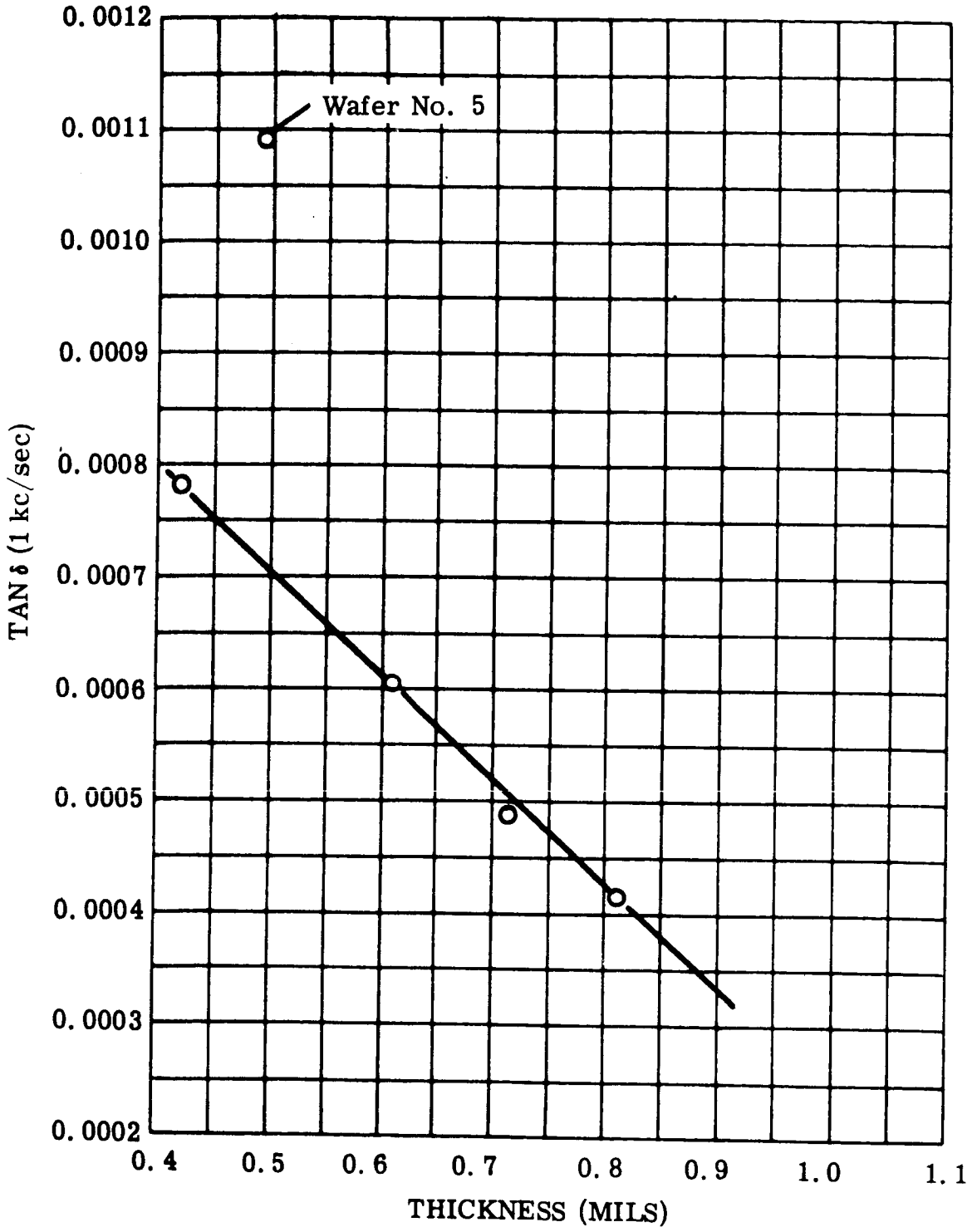

FIGURE III-4. Tan δ vs. Thickness for Pyrolytic Boron Nitride Wafers That Are Used in 5 Wafer Multi-Layer Capacitor No. 2

Figure III-4. Tan δ vs. Thickness for Pyrolytic Boron Nitride Capacitor Wafers

capacitance, tan δ and d-c resistance was measured in vacuum ($< 3 \times 10^{-7}$ torr) to 1100°F. Figures III-5 and III-6 show the complete capacitance and tan δ envelopes vs. temperature for seven different frequencies from 50 cps to 50 kc/sec. In general, there appears to be an overall decrease in tan δ at all temperatures up to 1100°F compared to the three stack unit discussed in the fourth quarterly report. This is probably the result of increased electrode thicknesses and the use of polished wafers. The combined effect would be to decrease the series resistance and therefore tan δ.

Figure III-7 shows tan δ vs. temperature for one selected frequency (1 kc/sec) during heating and cooling. It is evident that compared to sapphire and BeO capacitors (Figures III-1 and III-2, fourth quarterly report) very little dielectric after-working or hysteresis occurred.

A number of d-c resistance measurements were made during heating and cooling to and from 1100°F. These data are shown plotted as RC products (megohms x microfarads) vs. temperature in Figure III-8. Also shown in Figure III-8 are a number of single points quoted by G. Dummer (ref. 2) for Teflon (350°F), mica (670°F), mylar (300°F) and vitreous enamel (200°F) capacitors. It is clearly shown that the pyrolytic boron nitride capacitor has several orders of magnitude better RC values over a very wide temperature range.

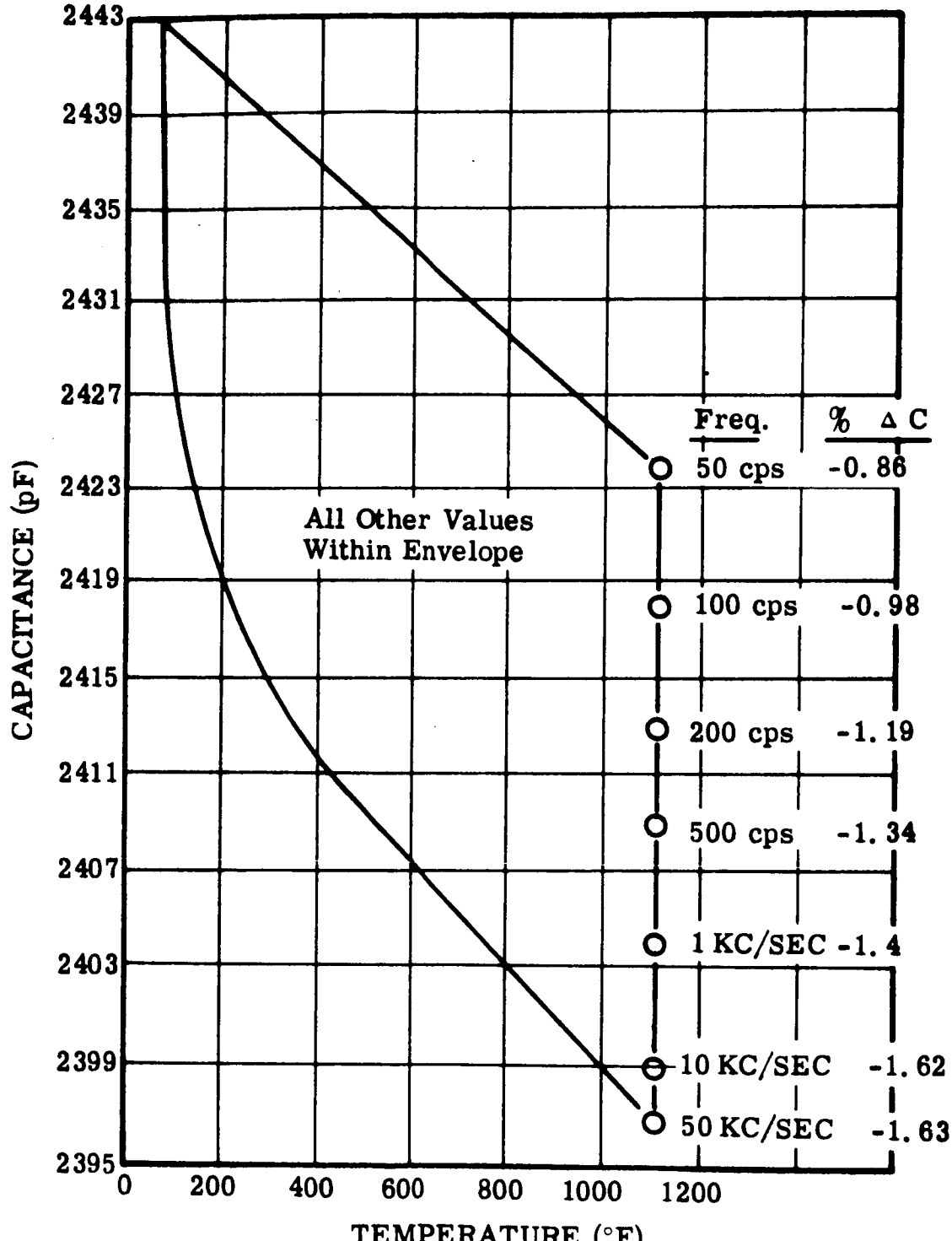

FIGURE III-5. Capacitance vs. Temperature Envelope Including Seven Different Frequencies from 50 cps to 50 kc/sec for a 5 Wafer Pyrolytic Boron Nitride Multi-Layer Capacitor (Measured in Vacuum at $< 3 \times 10^{-7}$ torr)

Figure III-5. Capacitance vs. Temperature at Several Different Frequencies

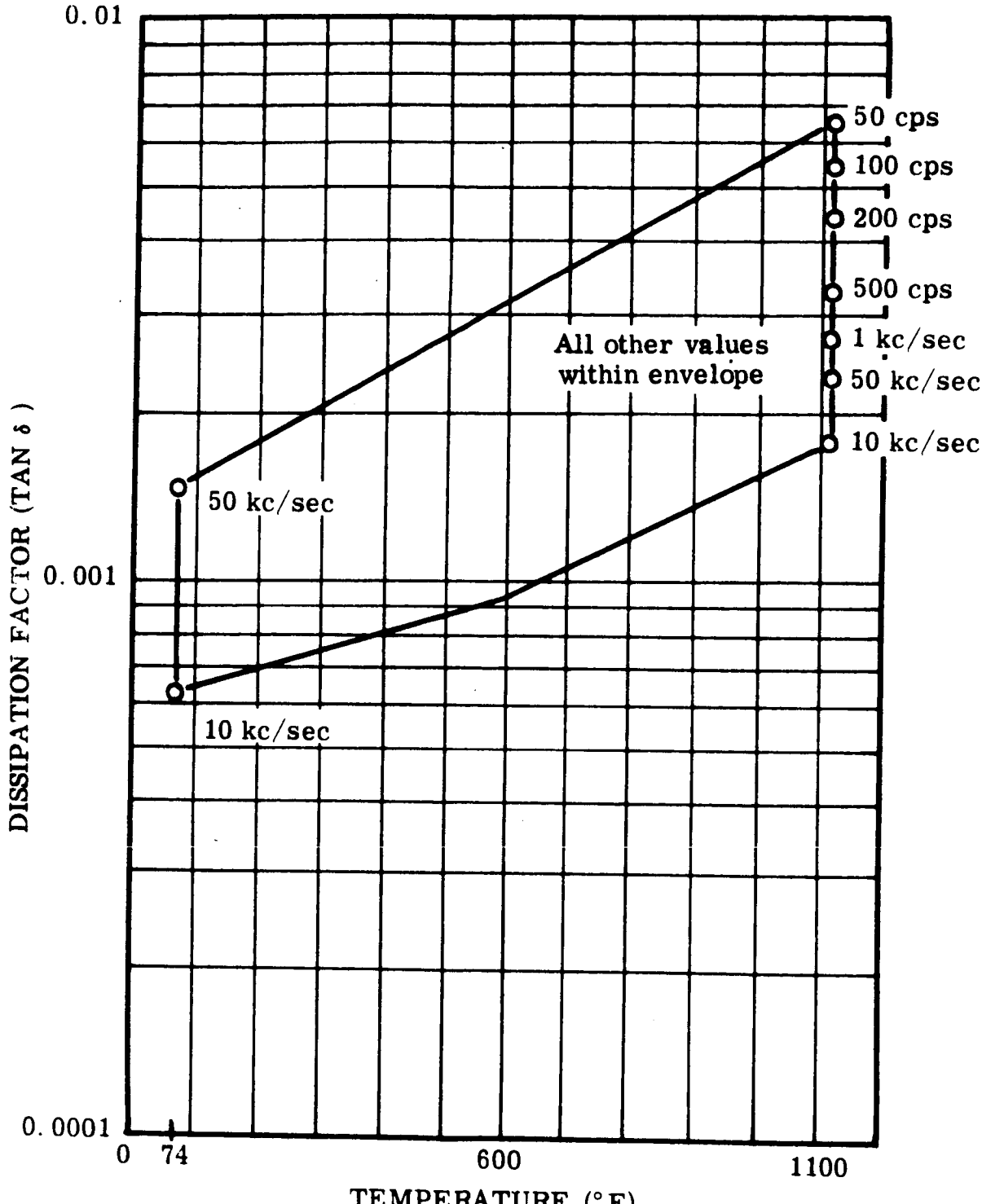

FIGURE III-6. Dissipation Factor (Tan δ) vs. Temperature Envelope Including Seven Different Frequencies from 50 cps to 50 kc/sec for a 5 Wafer Pyrolytic Boron Nitride Multi-Layer Capacitor No. 2 (Measured at $< 3 \times 10^{-7}$ torr)

Figure III-6. Tan δ vs. Temperature at Several Different Frequencies

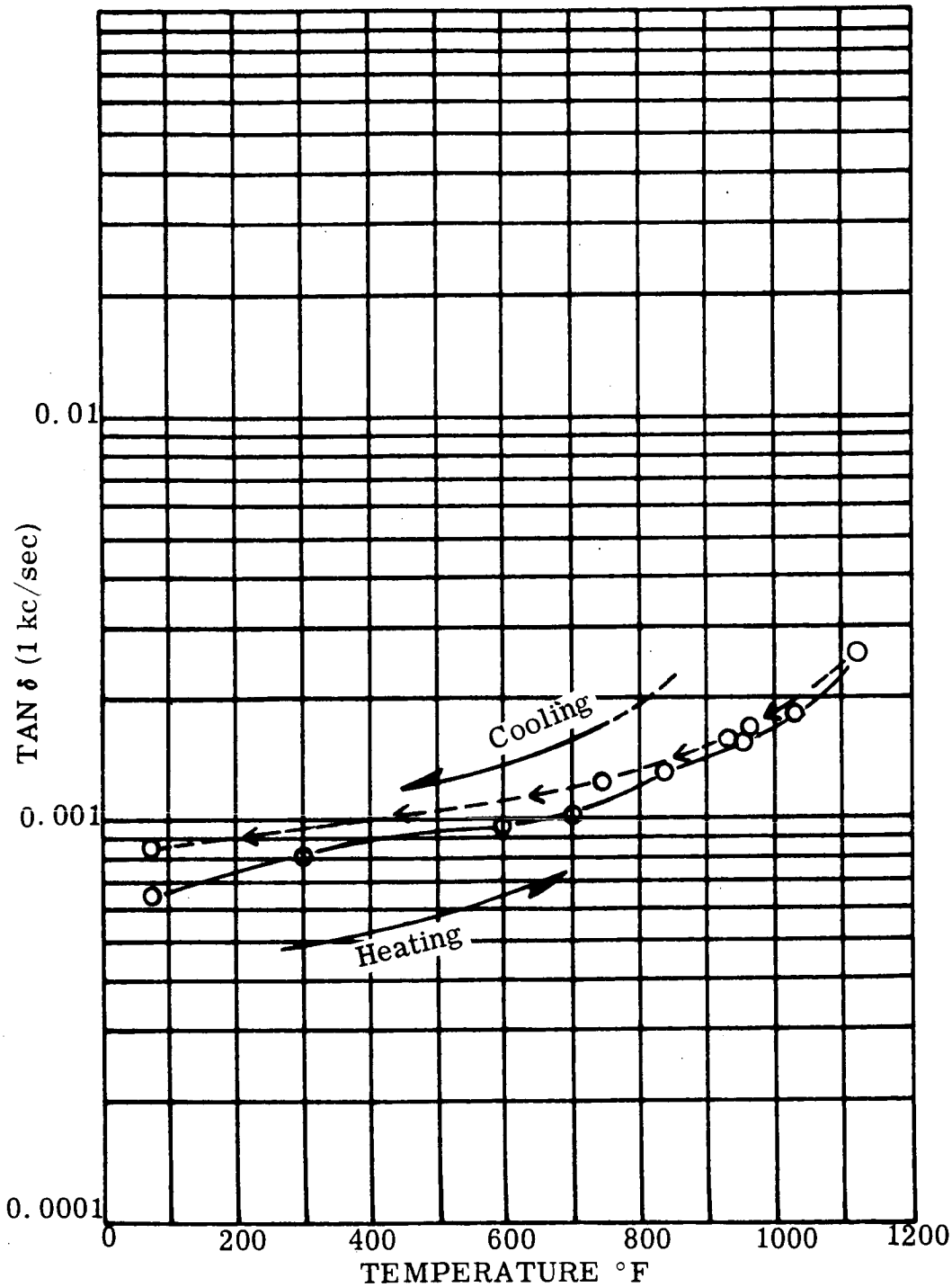

FIGURE III-7. Tan δ vs. Temperature Measured During Heating and Cooling to Room Temperature for 5 Wafer Multi-Layer Capacitor No. 2

Figure III-7. Tan δ vs. Temperature During Heating and Cooling

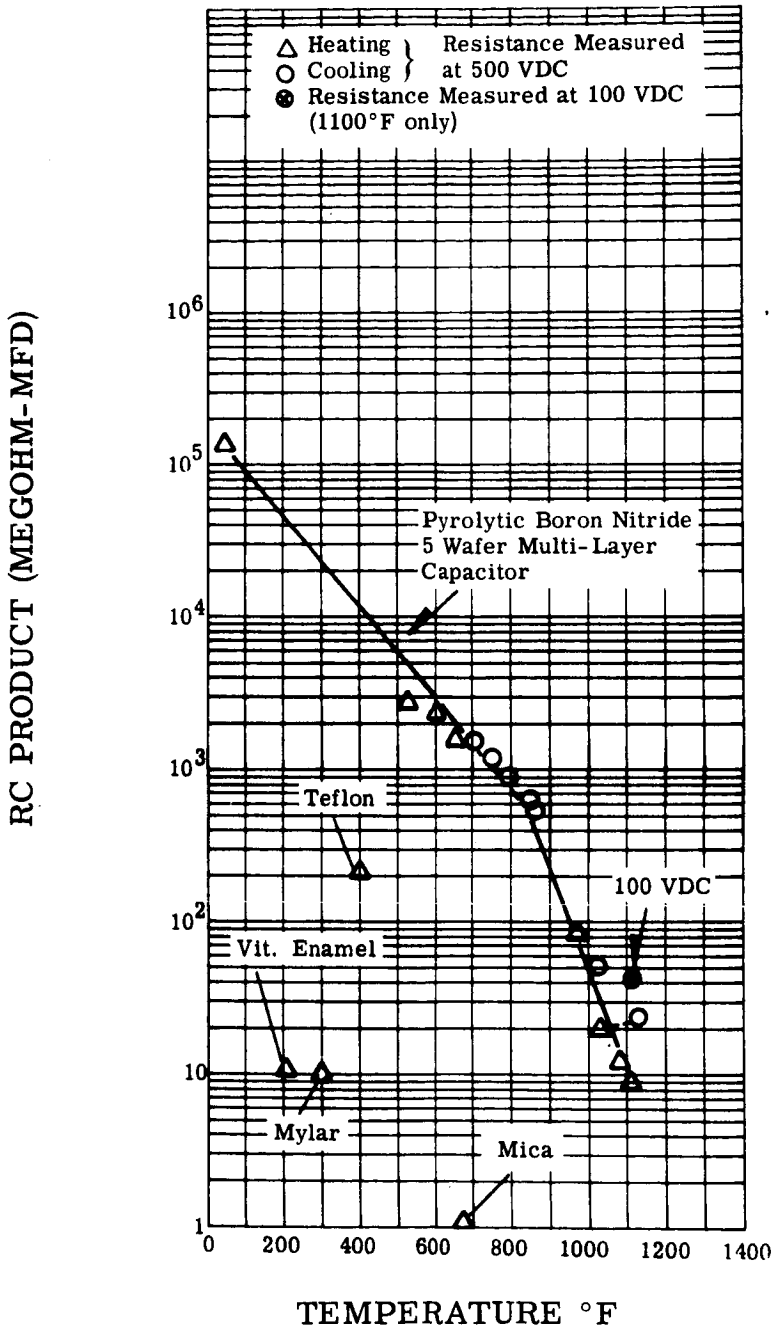

FIGURE III-8. RC Product (Megohm-Microfard) vs. Temperature Pyrolytic Boron Nitride 5 Wafer Multi-Layer Capacitor Measured at 500 VDC at Pressures less than 3×10^{-7} torr

Figure III-8. RC Product vs. Temperature at 500 VDC

C. PROGRAM FOR THE NEXT QUARTER

1) Preparation and electrical evaluation of pyrolytic boron nitride wafers for multi-layer capacitors will be completed.

2) A 250 hour life test will be started on a multi-layer capacitor containing at least five stacked wafers.

SECTION IV

PROGRAM III - BORE SEAL DEVELOPMENT AND COMBINED MATERIAL INVESTIGATIONS UNDER A SPACE-SIMULATED ENVIRONMENT

The bore seal effort under Task 1 will evaluate promising ceramic-metal sealing systems in potassium and lithium vapor at temperatures to 1600°F for 2000 hours. Elevated temperature seal strength and vacuum tightness will be determined. A four-inch diameter bore seal loaded with potassium will be incorporated in a stator design and evaluated in a 5000-hour endurance test at temperature and in a high-vacuum environment. This test will confirm compatibility data determined on smaller geometries.

Two five-thousand hour tests will be run under Task 2 on a stator which typifies the construction of an inductor alternator or a motor. The first will be run between 800 and 1100°F temperature. The second test will be run with a bore seal at temperatures between 1100 to 1600°F. All will be tested at a high-vacuum (less than 10^{-8} torr) under electric and magnetic stresses.

A transformer and two solenoids under Tasks 3 and 4 will be similarly tested under high vacuum and at elevated temperature. The purpose will be to evaluate the combined effects of electric and magnetic stresses, and high vacuum on combinations of materials suitable for application to advanced space electric power systems. One solenoid test will be under d-c excitation and the other under intermittent excitation so the effects of an invariant electric stress can be investigated.

The design features incorporated into the stator, transformer and bore seal were defined in detail in Appendixes A, B, and C of the first quarterly report.

A. TASK 1 - BORE SEAL DEVELOPMENT

1. Summary of Technical Progress

a) The 1600°F, 500 hour potassium exposure test of high-purity beryllia and yttria ceramic specimens and brazed ceramic-to-metal assemblies was completed. Welded columbium-1% zirconium test capsules containing the specimens were maintained at a pressure of less than 1×10^{-8} torr during the 1600°F test to minimize oxygen contamination of the capsule.

b) Mercury amalgamation analyses of potassium loaded into columbium-1% zirconium purity test capsules at the same time as the corrosion test capsules indicated that oxygen content was less than 10 parts per million.

c) Bend strength tests on the brazed assemblies show that active-metal braze alloy No. 9 (60Zr-25V-15Cb) retained high strength (average value 15,250 psi after potassium exposure). In addition all leak-test assemblies remained vacuum tight.

d) The yttria ceramic shows essentially no degradation in strength after potassium exposure at 1600°F for 500 hours. The beryllia ceramic (80 ppm SiO_2) showed a slight (7%) degradation in strength, but a beryllia ceramic with higher silica (150 ppm) showed a 25 percent reduction in strength.

e) Two vacuum-tight active-metal brazed seals have been made using two inch diameter beryllia tubes and columbium-1% zirconium metal members.

2. Discussion

a. ALKALI METAL LOADING AND TESTING FACILITY

The capsule corrosion tests carried out on this program maintained a potassium purity of less than 10 parts per million of oxygen in the sealed capsule. This objective was accomplished by the following:

1) A capsule fabrication and alkali metal handling facility which is suitable for either inert-gas or vacuum operation has been constructed. The chamber is capable of

maintaining a vacuum of 1×10^{-6} torr or an inert atmosphere containing less than 1 ppm water and 1 ppm oxygen. The alkali metal is hot trapped and delivered into the loading chamber through a clean, vacuum outgassed, transfer line.

2) A dual chamber, ion pumped, life test station capable of achieving a vacuum of less than 1×10^{-8} torr, at temperature has been built to carry out the 1000°F and 1600°F capsule corrosion tests.

b. BORE SEAL MATERIALS

(1) Metal Member

Columbium-1% zirconium alloy has been used both as a capsule material and as a metal member in the ceramic-to-metal test assemblies on this program and on NAS3-4162. The oxygen level of all refractory metals used was below 300 ppm. Reliable, vacuum-tight, potassium resistant welds can be made by either tungsten inert-gas or electron-beam welding techniques, as indicated by satisfactory vacuum tightness being maintained during the 500 hour life tests at 1600°F. Test capsules for the current program were welded by the electron-beam welding methods. Metallurgical cross-sections of joints annealed at 2200°F for one hour and subsequently life tested show good joint integrity. Reliable ceramic-to-metal seals can also be fabricated with columbium-1% zirconium.

D-43 columbium alloy (Cb-10W-1Zr-0.1C) and T-111 tantalum alloy (Ta-8W-2Hf) have also proven satisfactory in the fabrication of ceramic-to-metal seals (ref. 2).

(2) Ceramic Materials

High-purity alumina and beryllia ceramics were selected previously on the basis of their thermodynamic stability. Sapphire ($\sim$ 100% single crystal alumina supplied by Linde), Lucalox (99.7% Al_2O_3 supplied by G.E.), and Thermalox 998 (99.8% BeO supplied by Brush Beryllium) were found to retain their intrinsic strength and resist attack by potassium during 500 hour exposure tests at 1600°F (ref. 2).

Since actual bore-seal ceramics are required to operate for long periods, 2000-hour alkali-metal exposure tests will be carried out on this program.

Additional ceramic bodies have been tested for use in the event that the above materials prove unsatisfactory. High-purity yttria and Thermalox 998 beryllia both manufactured under special processes to limit the content of SiO_2, and other thermodynamically unstable species, were ordered from Coors Procelain Company and Brush Beryllium Company respectively in the form of modulus-of-rupture bars and small cylinders. The composition of the yttria was reported in the third quarterly report. It was quite pure with 40 ppm silica reported in the vendor's analysis (Coors). The "low-silica" beryllia material received from Brush Beryllium was rejected because of high-silica content (> 200 ppm) and has not yet been replaced.

A 500-hour, 1600°F potassium exposure test of ceramics on this program has been completed. The mechanical test results are shown in Table IV-1. It is clear that Y_2O_3 of the obtained purity is not attacked by 500 hours of potassium vapor exposure at 1600°F. It is also evident that 150 ppm silicon in the beryllia degrades it significantly.

The importance of developing a reliable source for low-silica material is becoming evident. The ability to accurately measure the silica content in this range in fired bodies is also critical, since conventional spectrographic methods or neutron activation are not sufficiently calibrated.

A ceramic outgassing study was programmed using 99.7% alumina, 99.8% beryllia and single crystal alumina. Results showed the standard treatments given to ceramics in the course of seal fabrication including detergent cleaning, wet-hydrogen-nitrogen firing at 2497°F (1425°C), and vacuum brazing above 1832°F (1000°C), reduce absorbed and adsorbed oxygen in the ceramic sufficiently to give a low-level of oxygen. Complete results were reported in the fourth quarterly report.

3. Ceramic-to-Metal Joining

Two ceramic-to-metal joining techniques have been considered on the bore seal programs: active-metal brazing and conventional brazing to

TABLE IV-1. Effect of 500 Hours Exposure to Potassium Vapor at 1600°F on Room Temperature Flexural Strength of Selected Ceramics

Ceramic Body	Key	Room Temperature Flexural Strength[a] Unexposed Control Specimens (psi)	Room Temperature Flexural Strength[a] Control Specimens After 1600°F, 500 hrs, Vacuum only (psi)	Room Temperature Flexural Strength[a] Exposed Specimens After 1600°F, 500 hrs in Potassium Vapor (psi)
Yttria[b] (99.99% Y_2O_3)	$\bar{x}$	16 825	16 600	18 600
	s	4 260	2 890	3 440
	n	4	5	4
Thermalox 998 99.8% BeO (Batch No. 2 150 ppm Si)	$\bar{x}$	19 820	21 100	15 850
	s	1 420	1 410	224
	n	5	5	4

Key $\bar{x}$ - arithmetic mean
s - standard deviation
n - number of specimens tested

Notes:

(a) Strength determinations were made by four point loading on 0.1 inch x 0.1 inch x 1 inch modulus-of-rupture specimens. Load was applied at the rate of 0.1 inch per minute.
(b) For analysis see Table IV-4 in third quarterly report.

metallized ceramics. Other techniques which were investigated with less emphasis are also described here.

Most metals do not wet ceramics. Metals possessing high free energies of oxide formation ($-\Delta F_f$) as a class can wet and join ceramics to other metals.

A reaction $M + CeO_x \longrightarrow MO_X + Ce$ (Ce = ceramic; M = metal) occurs. Because of this reaction they are termed "active metals". Since the suitable metals Ti, Cb, Zr, Hf, Y, V, all have high-melting points, they are alloyed with each other and with other metals such as Ni, Cu, Be, Ag in order to reduce reactivity with the ceramic and metal members and reduce brazing temperature in order to avoid warping of large structures.

a. METALLIZING AND THIN FILM COATING OF CERAMICS

The non-metallic portion of standard metallizings which are applied to silica-free ceramic (ceramics < 0.1% Si) contain silica, for example; Mo-CaO-Al_2O_3-SiO_2; W-MnO-SiO_2. On the previous program (ref. 2), silica-free metallizing paints (< 0.5% Si) were developed. For example, ceramics metallized with W-CaO-Al_2O_3 were brazed with copper or with nickel-base braze alloys. Results indicated that a 3272°F (1800°C) metallizing sintering temperature would be required to produce sufficiently adherent metallized layers with these metallizing paints. Since this temperature is above the sag temperature of the ceramics in question, the approach was abandoned.

Good bonds exhibiting high strength in tension may be made to the ceramic using evaporated, thin (1 to 10μ) layers of molybdenum. The shear strength of the joint proved to be low (refs. 2 and 3). Thus, only ductile braze alloys and metal members with similar expansion characteristics should be used with this technique. If possible, the joint should be maintained in compression. In order to eliminate erosion of the thin film by braze alloys such as nickel or refractory metal alloys, a barrier layer must be used (ref. 2). The Chemical Vapor Deposition technique (CVD) is presently being utilized to provide a barrier layer (Cb-1Zr) for the molybdenum-metallized ceramic surface.

It was demonstrated on the previous program (ref. 2) that a molybdenum evaporated layer promoted better wetting of the

ceramic by the active metal braze alloy. This wetting technique was applied on the current program. In addition, work was programmed utilizing Mo, MoO_3 and Mo-Li_2O metallizing paints as a possible substitute for the vaporization procedure. The paint-metallized ceramics were brazed into assemblies with several active-metal brazes including 75 Zr-19 Cb-6 Be. Results using conventional pigment-to-vehicle ratios gave a 90 percent vacuum-tight yield and a 50 to 100 percent increase in strength. Reduction of the pigment-to-vehicle ratio produced a thinner metallized layer but reduced the vacuum-tight yield. Photomicrographs of these metallized-brazed assemblies are shown in Figure IV-1. Excessive intermetallic formation between zirconium and molybdenum may be responsible for the low vacuum-tight yields produced by the thinner metallizing paints. The wetting layer used on this program thus continues to be an evaporated molybdenum layer 1 to 3 microns thick.

b. ACTIVE-METAL BRAZING

The major effort on this program has been in the area of active-metal brazing, with or without wetting layers on the ceramics and with or without post brazing heat treatments. The braze system must meet the following requirements:

(1) Resistance of the braze alloy to potassium vapor and liquid at 1600°F.

(2) Intrinsic stability in a vacuum of 1×10^{-9} torr at 1600°F.

(3) High brazed strength, which is promoted by a ductile matrix and a ductile layer next to the ceramic.

(4) The potassium must not attack or alloy with the metal member or the ceramic member. It must not attack the reaction products formed at the interfaces during brazing.

Although empirical rules can act as a guide, no theory is available which can predict the actual resistance of metals to potassium (reference 4). In general, the refractory metals, Groups IV, V and VI, of the Periodic Table, include the most suitable corrosion resistant materials. However, other materials if tied up as

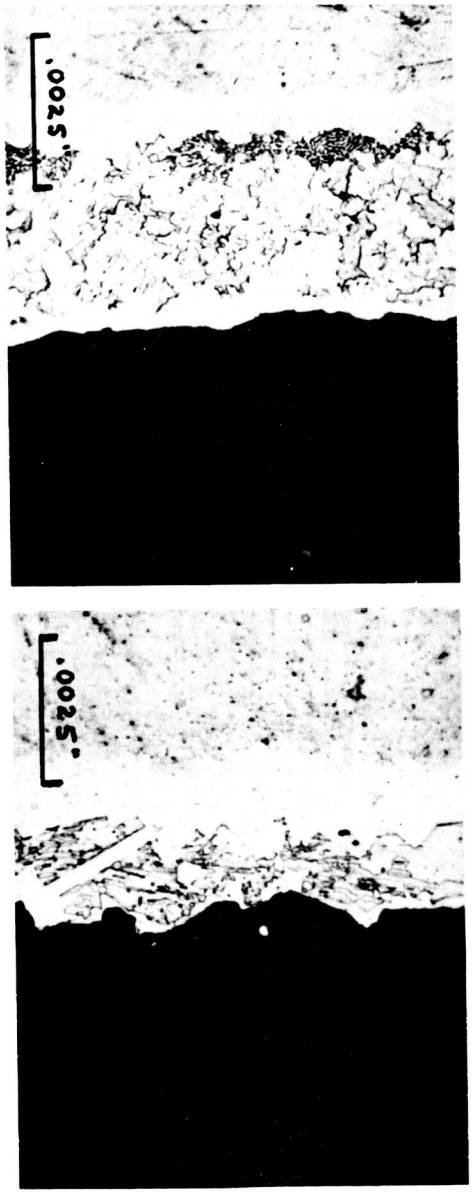

Etchant: 30 ml lactic acid, 10 ml HNO_3, 10 ml HF

Note: In the top photomicrograph the ceramic was metallized with a molybdenum metal paint. In the bottom the same metallizing was reduced in thickness to 1/5 that of the top sample by dilution of the metallizing paint with lacquer.

FIGURE IV-1. Photomicrographs of Alloy 75Zr-19Cb-6Be Brazed Under Standard Conditions Between Cb-1Zr Columbium Alloy and Ei3-3W Alumina (400X Before Photo Reduction)

stable intermetallics, e.g. $CbBe_2$, offer promise. It would be expected that the more refractory the intermetallic, the more resistance it would be to corrosion. For example, $CbBe_2$ (MP = 3812°F) would be superior to $CbBe_{12}$ (MP = 3002°F). Conversely if two refractory metals form a low melting or unstable intermetallic, for example ZrV_2 (MP = 2372°F), it would be expected to have a lower corrosion resistance than the parent metals.

The atomic radii of the elements, Table I V-2, can aid in predicting solid solubility. According to the Hume-Rothery rules, if less than a 15 percent difference in radii exists, complete solid solubility will be possible. However, this rule is of no help with regard to predicting kinetics, i.e., their liquid solubility rates in alkali metals.

In general, the higher the melting point of the metal and the lower the melting point of the alkali metal, the less will be the liquid solubility. One can readily see that lithium may enter the refractory metal lattice by solid solution processes, thus its mode of attack on oxygen present in the alloy can be through the crystal lattice, as well as along its grain boundaries.

The oxygen level of the braze alloy must be low, in order that the alkali metal does not react with the oxygen and leave a porous weakened metal. This criterion is not as critical if the oxygen is tied up by a getter-metal alloy addition to form a very stable oxide such as ZrO_2, Y_2O_3 or BeO. In this case, the braze will be stable until all of the getter has reacted. Table I V-3 lists typical oxygen and nitrogen contents of the braze metals used on this program.

The conditions for the elevated temperature stability must be considered independently. Under some test conditions oxygen and nitrogen will be present on the side of the braze exposed to vacuum. It is important to choose braze alloys which exhibit a low diffusion rate with respect to oxygen and which have built-in getters to absorb the oxygen. Since most alloys do not tie up the oxygen unless they are annealed at high temperatures, it may be necessary to periodically increase the braze joint to a high temperature as is done in the post-weld annealing of columbium-1% zirconium.

The ideal mechanical condition for a joint is that it be ductile, but adequately strong to resist the stresses imposed on it. The

TABLE IV-2. Atomic Radii and Melting Points of Braze Alloy Constituents Compared to the Alkali Metals

Element	Melting Point[a] °F	°C	Atomic Radii[b] (angstrom units - Å)
Yttrium	2748	1509	1.80
Zirconium	3366	1852	1.60
Columbium	4474±18	2468±10	1.46
Titanium	3035±18	1668±10	1.47
Molybdenum	4730	2610	1.39
Tungsten	6170	3410	1.39
Vanadium	3450±50	1900±25	1.34
Beryllium	2332	1277	1.12
Cesium	83.6	28.7	2.67
Potassium	146.7	63.7	2.35
Sodium	208.1	97.8	1.90
Lithium	357	180.5	1.55

(a) Metals Handbook, 8th Edition, 1961

(b) Hume-Rothery, W., The Structure of Metals and Alloys. The Institute of Metals, London, 1947

TABLE IV-3. Interstitial Content of Selected Braze Materials in Button, Powder and Foil Form

Material	Form	Oxygen (ppm)	Nitrogen (ppm)
Be (a)	--	2500 (b)	200
Th (a)	--	600	60
Ti (a)	--	180	20
Y (a)	--	2000-4000	100
Zr (a)	--	0-360	6-36
V (a)	--	784	270
56Zr-28V-16Ti	Melted button (c)	580	100
	Powder (c)	620	120
	Foil (c)	1700	1000
75Zr-6Be-19Cb	Melted Button	520	97
	Powder	960	98
65V-35Cb	Melted Button	900	260
	Powder	990	260
50Ti-30Zr-20V	Powder	710	(f)
	Foil	2600	(f)
40Zr-30Ti-30V	Powder	(f)	(f)
	Foil	1300	(f)
V (d)	Foil	1600	320
Zr (e)	Foil	850	25

(a) - Typical analyses supplied by Battelle Memorial Institute on raw materials used in preparation of active alloy braze materials which they supplied.
(b) - as BeO
(c) - The powder and foil were from a different melt than the button.
(d) - Foil supplied by Battelle.
(e) - Foil supplied by Wah Chang.
(f) - Not determined

All analyses except those materials marked (a) were made by Westinghouse R & D Center. Oxygen by vacuum fusion; nitrogen by modified Kjeldahl.

ceramic is brittle; therefore, nucleation of a hard brittle phase (e. g. an intermetallic) next to the ceramic is undesirable. An ideal situation is for any hard phase in the braze to be of small crystal size and to be surrounded by a ductile matrix phase. A lamellar phase separation system should be avoided.

Different ceramic substrates can introduce different phase distributions. In the case of the 75 Zr-19Cb-6Be braze, a matrix phase (see Figure IV-2) is noted immediately adjacent to the beryllia substrate, but in the case of an alumina substrate a harder, aluminum-containing solid solution phase is noted.

Phase changes can be expected to occur in braze alloys maintained at 1600°F and above, but the precipitation or growth of hard, non-ductile phases is undesirable if mechanical joint integrity is to be maintained. Typical hardness of intermetallics in the Cb-Be system are shown in Table IV-4, (reference 5).

One of the considerations in the selection of brazing alloys is the melting point. Phase diagrams for many binary metal systems of interest on this program are available. The lowest temperature in each listed system is shown in Table IV-5. Figure IV-3 (reference 6) gives a condensed version of the ternary-transition metal systems as predicted from the known binaries. Few complete ternary systems have been completely studied. In general, however, melting points can be estimated from a consideration of the binaries. Appreciable lowering of the melting point cannot be expected by combining binary compositions showing complete solid solution. However, by combining a eutectic with a solid solution series or with another eutectic, a further lowering of the melting point can be expected to occur.

Neither $ZrBe_2$ or ZrV_2 are very stable. They will both decompose below their melting points (2372°F and 2462°F respectively). Therefore, braze alloys based on these systems can be expected to exhibit preferential potassium attack via the intermetallic eutectic ground mass phase. This has been observed to occur for ZrV_2 after attack by potassium at 1742°F (950°C)(reference 7). Conversely, YBe_{13} is a much more stable intermetallic. Its melting point at 3488°F (1920°C) is much higher than Y, 2732°F (1500°C), or Be, 2349°F (1287°C). Therefore braze alloy systems based on this system would be expected to show good corrosion resistance.

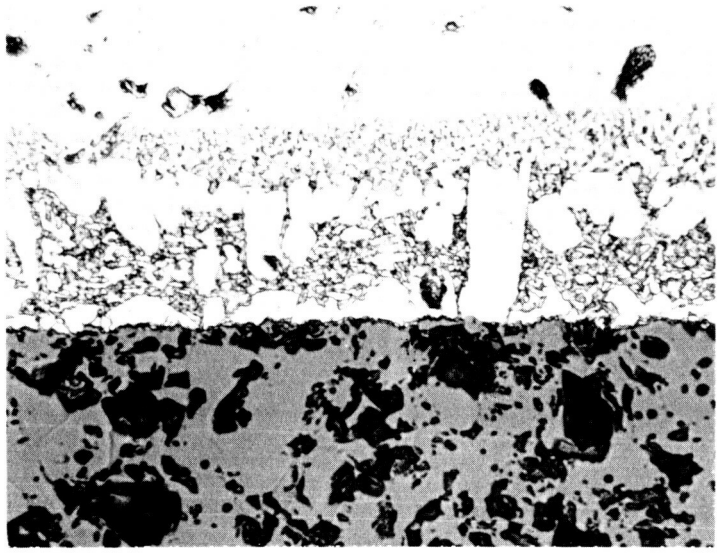

Etchant: 30 ml lactic acid, 10 ml HNO_3, 10 ml HF

FIGURE IV-2. Photomicrograph of Alloy 75Zr-19Cb-6Be Brazement Between Cb-1Zr and Thermalox 998 BeO After 500 Hour Exposure to Potassium Vapor at 1000°F. 400X

TABLE IV-4. Hardness and Structure of Compounds in the Columbium-Beryllium System (reference 5)

Phase Designation	Microhardness[a] k/mm^2	Structure
Cb	200	Body centered cubic
Eutectic	1079	-
Cb Be_2	-	hexagonal
Cb Be_5	1580	-
Eutectic	-	-
Cb Be_8	1430	Rhombic
Eutectic	950	-
Cb Be_{12}	1200	Body centered tetragonal
Eutectic	260	-
Be	-	hexagonal close packed

(a) Knoop or Vickers not specified

TABLE IV-5. Phase Relations in Binary Systems of Interest for Brazing Alloys

Binary System	Lowest Melt		Phase Composition	Remarks
	Temperature (°C)	Additive (weight percent)		
Cb-Be	1260	95	$CbBe_{12}$-Be	Eutectic
Cb-Mo	2468(Mo)	-	Cb-Mo	Isomorphous
Cb-Ti	1720	-	Ti	Pure Ti $\beta \rightarrow \alpha$ (870°C $\longrightarrow$ 600°C)
Cb-Th	1435	92	Cb-Th	Simple Eutectic
Cb-V	1810	65	Cb-V	β-solid solution (s. s.)
Cb-W	2468(Cb)	-	Cb-W	Isomorphous
Cb-Y	1470	94	Cb-Y	Eutectic
Cb-Zr	1800	70	Cb-Zr	β-s. s., eutectoid (below 1000°C)
Ti-Be	950	3-10	Ti-Be_3Ti_4	Eutectic
Ti-Mo	1668(Ti)	-	Ti-Mo	Isomorphous with β-Ti
Ti-Th	1190	87.5	Th-Ti	Eutectic
Ti-V	1620	30	Ti-V	β-s. s. $\longrightarrow \alpha$ (882°C $\longrightarrow$)
Ti-W	1668(Ti)	-	β-Ti	Peritectic (@ 1880°C ~ 52% W)
Ti-Y	1385	88	Ti-Y	Eutectic $\beta \longrightarrow \alpha$ (870°C)
Ti-Zr	1600	50	Ti-Zr	β-s. s. $\longrightarrow \alpha$ (870°C $\longrightarrow$ 500°C)
Zr-Be	970	6	Zr-$ZrBe_2$	Eutectic, $ZrBe_2$ peritectic
Zr-Mo	1520	31	Zr-$ZrMo_2$	Eutectic, $ZrMo_2$ peritectic
Zr-Th	1350	54	Zr-Th	Minimum
Zr-V	1230	30	Zr-ZrV_2	Eutectic, ZrV_2 peritectic
Zr-W	1630	80	Zr-ZrW_2	Eutectic, ZrW_2 peritectic
Zr-Y	1385	56	Zr-Y	Eutectic
V-Be	1600	15	V-VBe_2	Eutectic
V-Mo	1860	-	V-Mo	Isomorphous
V-Th	1400	85	V-Th	Eutectic
V-W	1630	20	V-W	Eutectic
V-Y	1455	93	V-Y	Simple eutectic
Y-Be	1070	6	Y-YBe_{13}	Eutectic; YBe_{13} (M. P. 1920°C)
Y-H_f	1425	13	Y-H_f	Eutectic

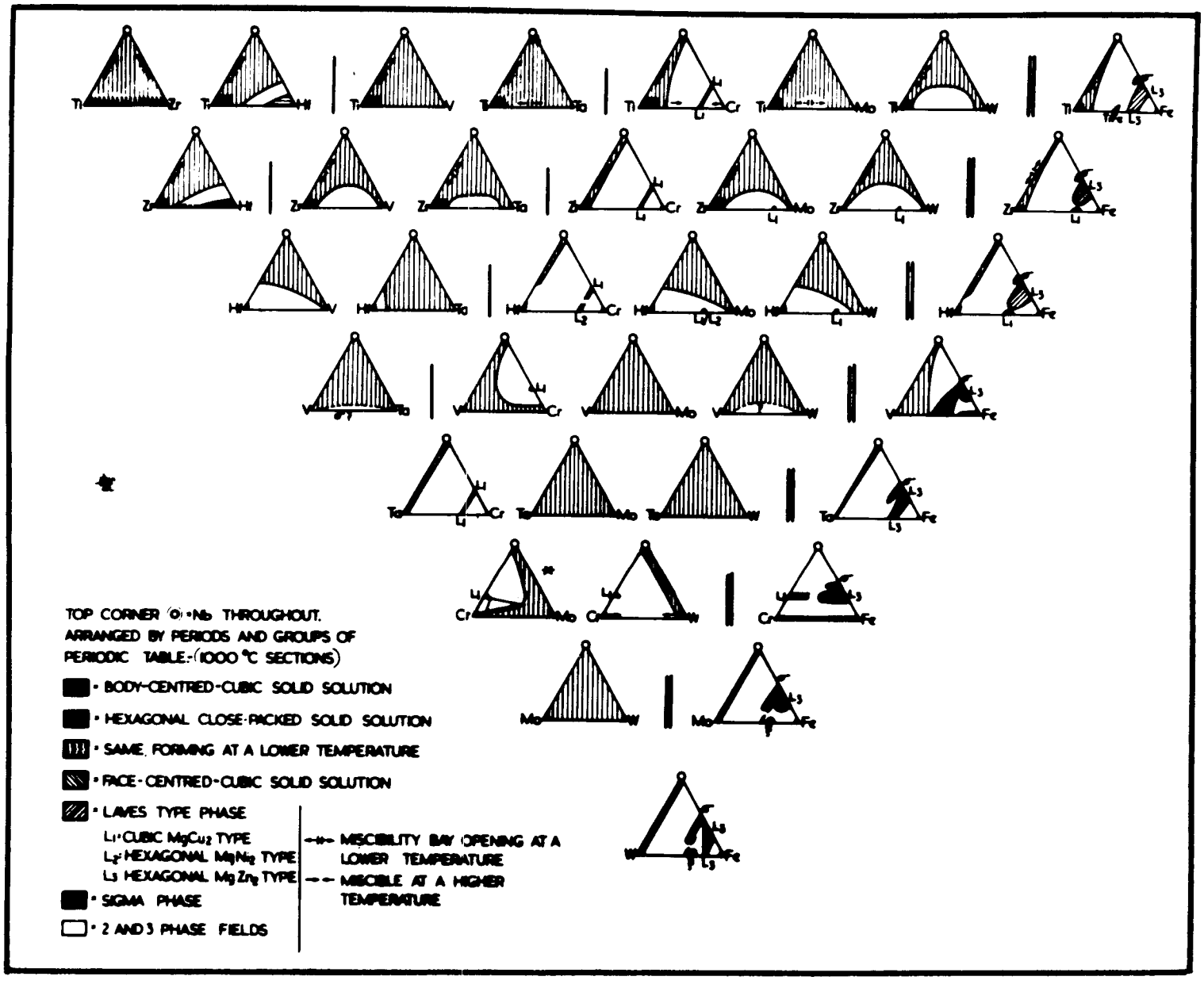

FIGURE IV-3. Ternary Columbium Base-Transition Metal Systems as Predicted From Known Binaries (H. J. Goldschmidt, "Phase Constitutions of Transition Metal Systems". J. of the Less-Common Metals, Vol 2, No. 2-4 April/ August 1960, pp 138-153)

Table IV-6 shows the braze alloy system selected for the previous program (ref. 2). In addition, the systems in Table IV-7, were also selected for consideration. These selections are not exhaustive but were based on the considerations discussed in the foregoing section. The higher melting alloys shown in Table IV-7 generally were not vacuum tight when brazed to alumina substrates but were vacuum tight when brazed to beryllia substrates.

The oxygen and nitrogen levels in the pure metals and powdered braze alloys are shown in Table IV-3. Considerable effort was made to obtain the foil form of both the pure metals and the active metal braze alloys which would minimize oxygen pick-up during the braze operation. The oxygen pick-up during sheathed-pack foil rolling attempts is illustrated in the data presented in this table (also see the second quarterly report). The oxygen content of alloy foils exceeded 0.1%. On the basis of these results, foil work was discontinued because of the excessive work that appeared necessary to develop foils of the desired brazing alloys. Therefore, braze alloys in the form of powder were used.

A thorough evaluation of three braze alloy systems (75Zr-19Cb-6Be; 48Ti-48Zr-4Be; and 56Zr-28V-16Ti) which were previously tested, is reported in the following sections. The alloy, 75Zr-19Cb-6Be, with a brazing temperature of 1985°F (1085°C) is discussed first.

Braze Alloy 75Zr-19Cb-6Be

The low melting point of this alloy is based on the formation of $ZrBe_2$ and $CbBe_{12}$ intermetallics with a cubic β - solid solution of the phase Cb-Zr-3Be. If cooled from 1832° to 1112°F (1000° to 600°C), under equilibrium conditions, the β- solid solution phase will precipitate all of the Be as $ZrBe_2$ and decompose to β- Cb and Rhombohedral β - Zr. Subsequently an eutectoid mixture of β - Cb and hexagonal α -Zr (1112°F) will precipitate. It is highly unlikely that equilibrium conditions will be maintained during cooling from the brazing temperature.

TABLE IV-6. Active Metal Brazing Alloys Selected for Investigation on NAS3-4162 Experimentally Established Brazing Temperatures for Cb-1Zr to 99.8 BeO

Nominal Alloy (weight percent)	Brazing Schedule[a]			
	10 min. hold temp.[b] (°F)	(°C)	Brazing temperature (°F)	(°C)
75Zr-19Cb-6Be	1805	985	1985	1085
68Ti-28V-4Be	1832	1000	2372	1300
56Zr-28V-16Ti	2102	1150	2372	1300
48Ti-48Zr-4Be	1742	950	2030	1110
46Ti-46Zr-4Be-4V	1652	900	1832	1000
50Zr-30V-20Cb	2102	1150	2516	1380
65V-35Cb	-	-	3398	1870
70Ti-30V	-	-	3002	1650
60Zr-25V-15Cb	2192	1200	2436	1330
50Zr-30Ti-20V	2282	1250	2732	1500
40Zr-30Ti-30V		-	2336	1280
45Ti-35V-30Zr	2282	1250	2804	1540
50Ti-30Zr-20V		-	2597	1425
62Ti-30V-8Si	2192	1200	2480	1360

(a) Revised Jan. 1966 to the current schedules. Actual brazing temperatures reported in text may differ.

(b) Active metal brazing is done by raising the vacuum furnace temperature gradually to the temperature shown in the left column for a specific alloy. The pressure in the furnace is maintained at 10^{-5} torr or less during the cycle. This temperature is held for ten minutes, then raised rapidly to the brazing temperature shown. The power is turned off after five minutes at the brazing temperature.

TABLE IV-7. Additional Alloys Selected with Leak Test Data from Preliminary Brazing Runs

Nominal Alloy Composition (weight percent)	Brazing Temperature (°F)	(°C)	Leak Test
75Zr-19Cb-6Be-Mo[a]	1985	1085	Vacuum tight[c]
48Zr-48Ti-4Be-Cb[b]	1940	1060	Vacuum tight[c]
56Zr-28V-16Ti-Cb[b]	2282	1250	Vacuum tight[c]
54Y-46Zr(MP=1385°C)	2552	1400	Leaker
Y-6Cb(MP=1470°C)	2552	1400	Leaker
Y-6Be(MP=1070°C)	-	-	Not Investigated
68Ti-28V-4Be-Mo[a]	2372	1300	Not Investigated
46Zr-46Ti-4V-4Be-Mo[a]	1832	1000	Not Investigated
60Zr-25V-15Cb-Mo[a]	2372	1300	Not Investigated

(a) Mo thin film metallizing used

(b) Obtained from diffusion bonding; columbium thin film metallizing used

(c) Indicates helium leak rate of $< 1 \times 10^{-9}$ torr liter/sec

It can be expected that this system will display a variable microstructure due to the normal variations in brazing conditions, ceramic substrate and metal member composition and post braze reheating treatments. Typical microstructures of the as-brazed 1600°F vacuum exposed and 1600°F potassium-exposed brazements are shown in Figure IV-4. Only minor differences existed between the various brazement microstructures on the beryllia and alumina substrates in the as-brazed condition and after 500 hour 1000°F exposures (see Figure IV-2). This applies to the beryllia samples brazed to columbium D-43 alloy as well. They all displayed a microstructure consisting of a crystalline phase growing from the metal interface, Phase I; and a pearlite laminar eutectic groundmass, Phase II. The 1600°F vacuum exposed and potassium exposed sample showed a marked difference in microstructure, exhibiting no laminar phase.

Figure IV-5 shows the results of a microprobe traverse across the braze area depicted in Figure IV-4. The crystalline phase consisted of a solid solution series of (Cb-1Zr) - (75Cb-22Zr-3Be) and a eutectic intermetallic-solid solution ground mass of composition 24Cb-65Zr-11Be.

The associated micro-hardness data is given in Table IV-8. The solid solution series shows the expected increase in hardness as zirconium diffuses into the Cb-1%Zr metal member and as the platelets growing from the metal interface increase in zirconium and beryllium content. The initial drop in hardness after the 1000°F exposure and further drop after the 1600°F exposures is due to precipitation of the Be phase from the solid solution. The eutectic groundmass is fairly soft. In the 1600°F exposed samples, the eutectic has been altered and hardened by the formation of additional intermetallics from the co-precipitated 75Cb-22Zr-3Be eutectic phase. The ceramic-braze interface shows an additional hardened continuous phase in the case of alumina (Figure IV-2) but not in the case of beryllia (Figure IV-4).

This braze (75Zr-19Cb-6Be) did not resist exposure in potassium at 1600°F with 99.7% alumina or 99.8% beryllia ceramic members. In the case of the alumina, the ceramic-braze interface disintegrated. While the beryllia system was intact, it failed at less than 1000 psi indicating that extensive attack of the beryllia intermetallic phases had occurred. At 1000°F such attack did not occur in potassium, either with alumina or beryllia ceramic mem-

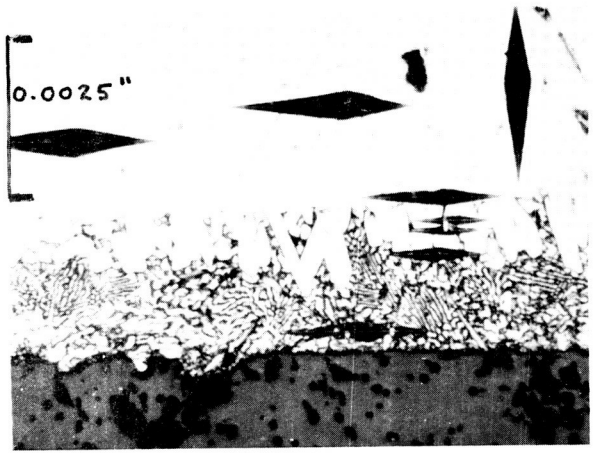

(a)

Cb-1Zr

Braze
75Zr-19Cb-6Be

Thermalox 998
BeO

(b)

Thermalox 998
BeO

Braze
75Zr-19Cb-6Be

Cb-1Zr

Braze
75Zr-19Cb-6Be

Void

(c)

Cb-1Zr

Braze
75Zr-19Cb-6Be

Thermalox 998
BeO

Etchant: 30 ml lactic acid, 10 ml HNO_3, 10 ml HF

Note: Samples shown are the samples used for the microhardness and microprobe analyses described in the accompanying text. (a) as brazed, (b) vacuum exposed 500 hours at 1600°F, (c) potassium exposed 500 hours at 1600°F.

FIGURE IV-4. Photomicrographs of Alloy 75Zr-19Cb-6Be Brazements Between Cb-1Zr and Thermalox 998 (BeO) (400X Before Photo Reduction)

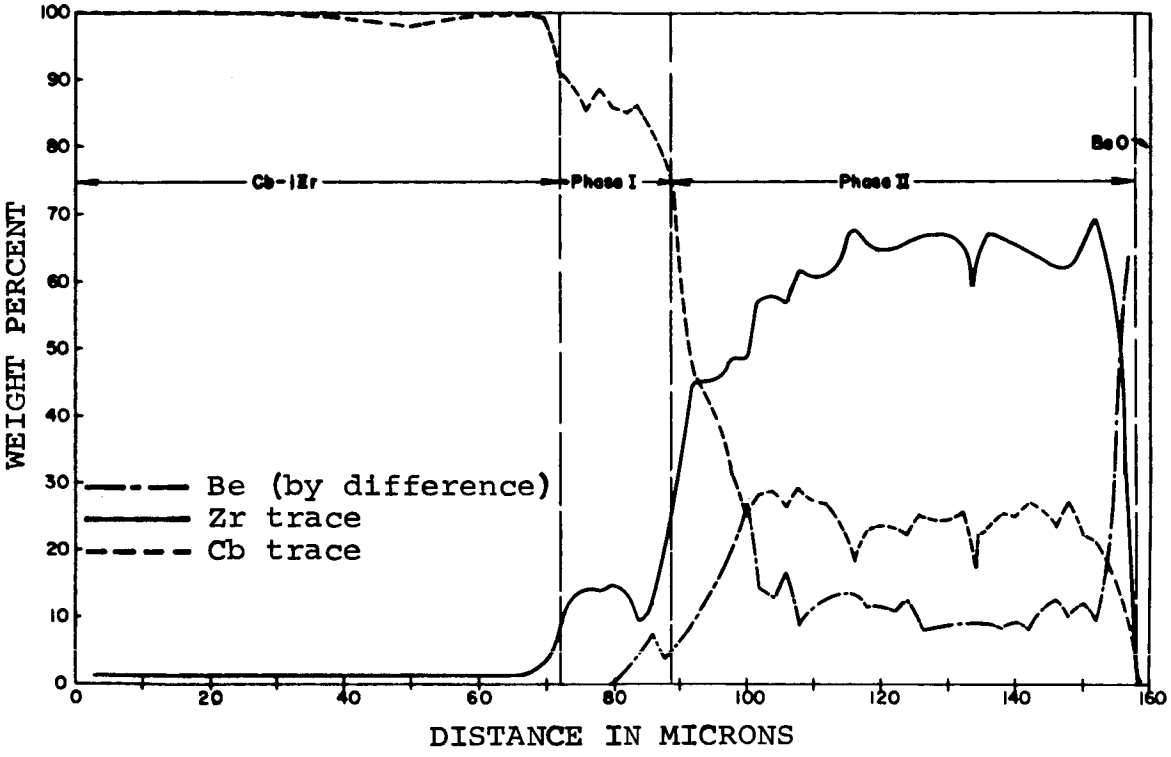

Sample was in the as-brazed condition

FIGURE IV-5. Plot of Electron Microprobe Scan Across Alloy 75Zr-19Cb-6Be Braze Between Cb-1Zr and Thermalox 998 (BeO)

TABLE IV-8. Microhardness Test Results on Five Assemblies of 99.8 Percent Beryllia Joined to Cb-1Zr Alloy with Braze 75Zr-19Cb-6Be

Phase Designation	Knoop Hardness (50g load)				
	Sample 1 As brazed	Sample 2 Vacuum Exposed[a]	Sample 3 Potassium Exposed[a]	Sample 4 As brazed	Sample 5 Potassium Exposed[b]
Cb-1Zr	150	120	151[d], 137	150	157
Interface	350	300	260[d], 319	211	384
Crystal phase	1040	750	813[d], 785	1052	914
Eutectic	284-312	(c)	(c)	497	400, 600
Interface	284-312	820	974[d], 846	463	1138
Ceramic (BeO)	1140				

(a) 1600°F for 500 hours
(b) 1000°F for 500 hours (Ei-3-3)
(c) Not Determined, too small an area
(d) 15g load, otherwise 50g load used

bers brazed to Cb-1Zr alloy or D-43 columbium alloy metal members, but degradation did occur in sodium-potassium eutectic with an alumina member. In all cases preferential attack occurs at the ceramic-braze interface, due to the higher stress level existing in this area and to the presence of unstable oxide species. Based on the poor 1600°F exposure test results there will be no further work with this braze composition.

Braze Alloy 48Ti-48Zr-4Be

In braze alloy 48Ti-48Zr-4Be with a brazing temperature of 1940°F (1060°C), the low braze temperature is a result of the liquation of Ti_3Be_4, $ZrBe_2$, and $CbBe_{12}$ intermetallics with a solid solution phase consisting of β-(Cb-Zr-Ti)-(3Be). As this braze cools under equilibrium conditions, the beryllium precipitates as an intermetallic phase and the refractory members go through various $\alpha \longrightarrow \beta$ phase changes which terminate as β-Cb, α-Ti-Zr solid solution and α-Zr.

As noted earlier, minor changes in the brazing cycle, substrate composition, and post-braze exposures can alter the microstructure of this brazement. Typical microstructures after major processing variations are shown in Figure IV-6. The solid solution phase can be seen extending from the metal member and from the beryllia interface. The laminar pearlite eutectic phase occupies the center of the brazement. Considerable alteration of this eutectic phase has occurred after heat treatment at 1600°F experienced during exposure testing. The 1000°F exposed samples showed only minor changes in the structure of the eutectic phase.

The microprobe data obtained from this beryllia - (48Ti-48Zr-4Be) - Cb-1Zr system (Figure IV-7) shows that the solid solution series extends from Cb-1Zr to 45Ti-25Zr-27Cb-3Be to 35Ti-40Zr-25Cb-$<$ 1Be while the eutectic region is of the composition 32Ti-45Zr-14Cb-9Be. The microprobe trace across the area shown in Figure IV-6(d) shows additional beryllium (by deduction) in the phase next to the beryllia ceramic, but this could be due to secondary fluorescence from the ceramic itself.

The micro-hardness data in Table IV-9 shows that in general the structure is more ductile than that of the 75Zr-19Cb-6Be structure. In particular, the solid solution phase is much softer.

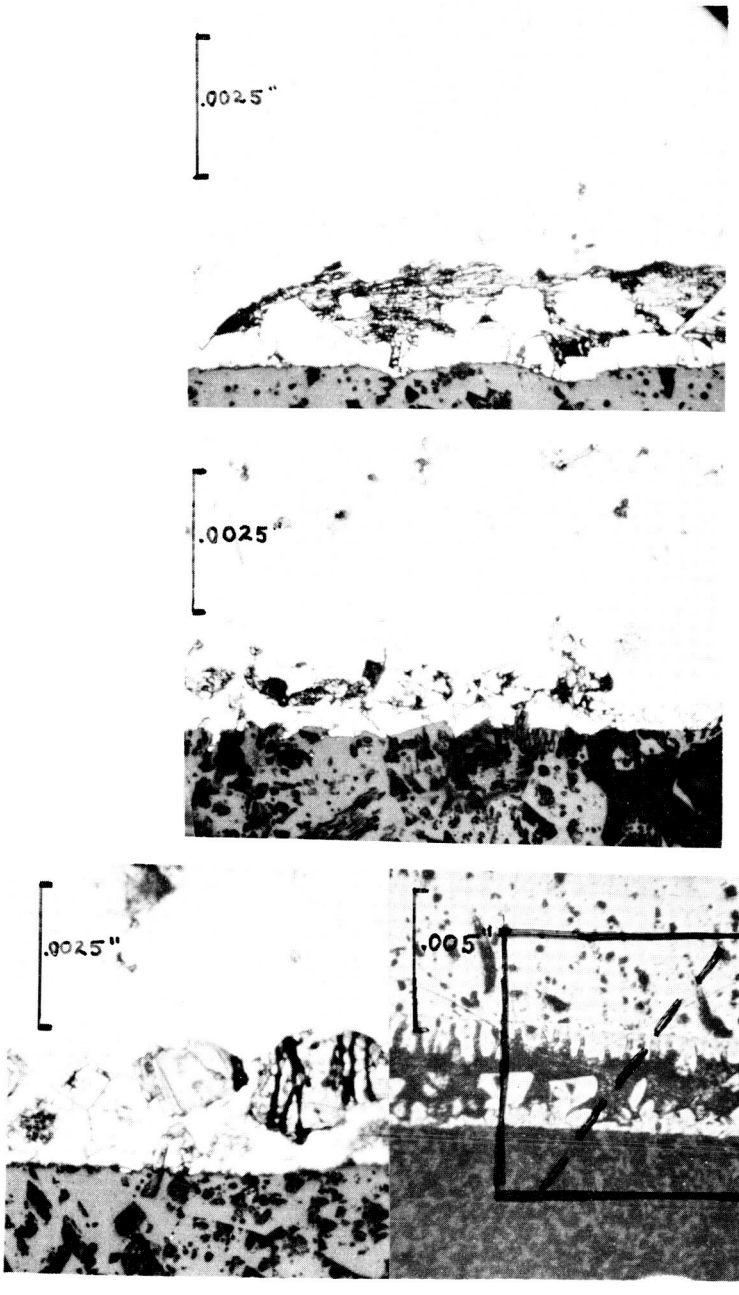

Etchant: 30 ml lactic acid, 10 ml HNO_3, 10 ml HF

Note: Samples shown are the samples used for microhardness and microprobe analyses described in the accompanying text. (a) as brazed, (b) vacuum exposed 500 hours at 1600°F, (c) potassium exposed 500 hours at 1600°F; (d) as for (c), dotted line shows path of microprobe trace.

FIGURE IV-6. Photomicrographs of alloy 48Zr-48Ti-4Be Brazements Between Cb-1Zr and Thermalox 998 (BeO) (abc400X, d200X Before Photo Reduction)

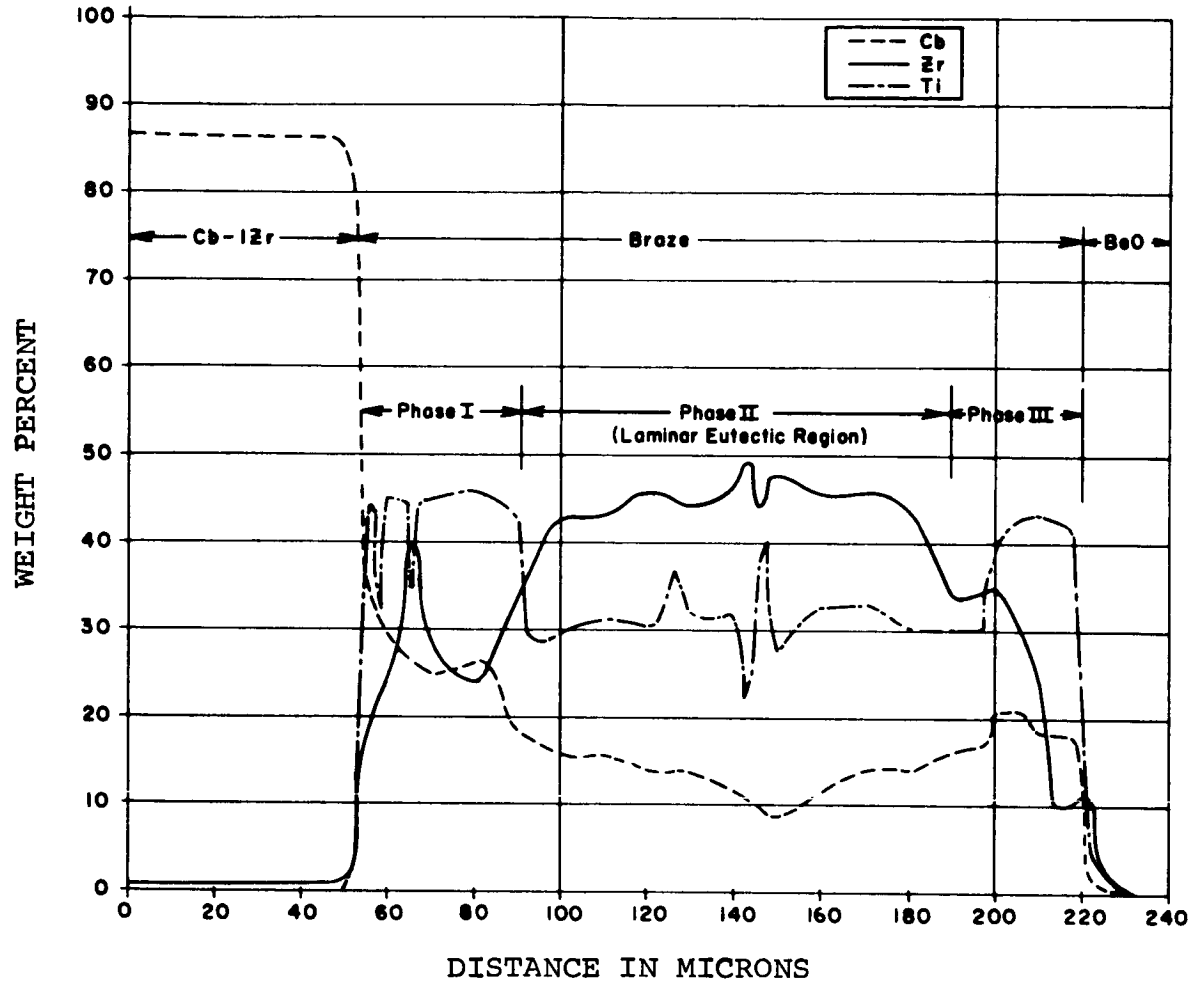

Sample was K exposed for 500 hours at 1600°F

FIGURE IV-7. Plot of Electron Microprobe Scan Across Alloy 48Zr-48Ti-4Be Braze Between Cb-1Zr and Thermalox 998 (BeO)

TABLE IV-9. Microhardness Test Results on 99.8 Percent Beryllia to Cb-1Zr Alloy Assemblies Brazed with 48Ti-48Zr-4Be

Phase Designation	Knoop Hardness (50g load)		
	Sample 1 As brazed	Sample 2 Vacuum Exposed[a]	Sample 3 Potassium Exposed[a]
Cb-1Zr	120	152	148
Interface	314	465	463
Crystal	411	433	425
Eutectic or	512	>445[b]	-
black crystal phase	-	-	1344
Interface crystal	726	456	425
Ceramic (BeO)	1140		

(a) 1600°F, 500 hours

(b) very small area

The potassium exposed sample contains a hard black crystal phase not present in the other cases. Its composition was not determined. It is most certainly an intermetallic phase with a hardness greater than that of the ceramic. A summary of results obtained with the 48Ti-48Zr-4Be alloy follows:

(1) Alumina assemblies brazed to Cb-1Zr with the 48Zr-48Ti-4Be alloy disintegrated in potassium vapor at 1600°F.

(2) Degradation (36% in flexural strength) of beryllia to Cb-1Zr assemblies was noted when tested in potassium at 1600°F.

(3) At 1000°F in potassium this braze alloy degraded (31% in flexural strength) on a beryllia member when brazed to columbium D-43 alloy metal member.

(4) The 48Zr-48Ti-4Be alloy underwent more severe degradation (74% in flexural strength) on an alumina member in 1000°F potassium.

(5) The strength degradation with sodium-potassium eutectic at 1000°F on an alumina member was 55 percent.

With the exception of (1) the first braze assembly noted above, the strength results show that the braze joint was still serviceable. The samples were vacuum tight after alkali metal exposure at 1000°F. No vacuum leak checks were made on the 1600°F specimens as they broke during removal from the capsules.

The behavior of this braze warranted further consideration for a longer exposure test. It appears that the beryllium intermetallic phases in this case are more resistant to potassium attack. Initially there is less beryllium present in the alloy. In general, also, there is considerably less beryllium present in the lamellar eutectic after the post braze treatment. No distinct area of potassium attack could be detected in the degraded braze samples.

Braze Alloy 56Zr-28V-16Ti

In the third braze alloy (56Zr-28V-16Ti) with a brazing temperature of 2273°F (1245°C), the lowering of the melting point is due to the formation of an eutectic melt between ZrV_2 and a solid solution phase of β(Zr-V-Ti). Solution of the Cb-1Zr metal member produces a quaternary high-temperature solid solution of β(Cb-Zr-V-Ti). (A complex intermetallic substitutional series (Zr, Cb, Ti)V_2 will also exist rather than the simple ZrV_2 phase.) If this braze is allowed to cool under equilibrium conditions, $\beta \longrightarrow \alpha$ changes will occur and a β-(Cb-Ti-V) and α (Zr-Ti-V-Cb) phase will finally precipitate from the high temperature β solid solution phase. The complex α (Zr-Ti-V-Cb) intermetallic phase can segregate into a β(Cb-Ti-V) solid solution phase and a ZrV_2 intermetallic phase. Sufficient possibilities therefore exist for a variety of microstructures to occur. At least two main phases, both possessing sub-phases will occur. The exact microstructure will depend on the various nucleation conditions imposed by brazing variations, substrates and post braze treatments.

This braze system was too active to join successfully to alumina but good brazements were made to beryllia. Figure IV-8 shows the microstructure of the BeO(56Zr-28V-16Ti)-Cb-1Zr system, after the major post-braze exposure conditions. The results of the microprobe examination, (Figure IV-9) show that definite compositional areas exist in this sample. These are presented in Tables IV-10 and IV-11. It appears that no pure intermetallic phase of composition M-V_2 exists. The composition of the braze had been considerably modified by the solution of the Cb-1Zr member.

The microhardness data in Table IV-12 shows that both hard and soft phases exist in this microstructure. Phase II consists of the soft solid solution members. The soft phases are predominantly columbium and are probably a β-solid solution. The hard phase (I) contains quenched intermetallic phases which precipitate primarily during the 500 hour exposure at 1600°F since rapid cooling from the braze temperature can rule out initial ZrV_2 precipitation.

The beryllia brazed sample underwent only marginal degradation in 1600°F potassium. Its resistance to lithium was also satisfactory at 1000°F. Attack proceeding via the ZrV_2 phase must be

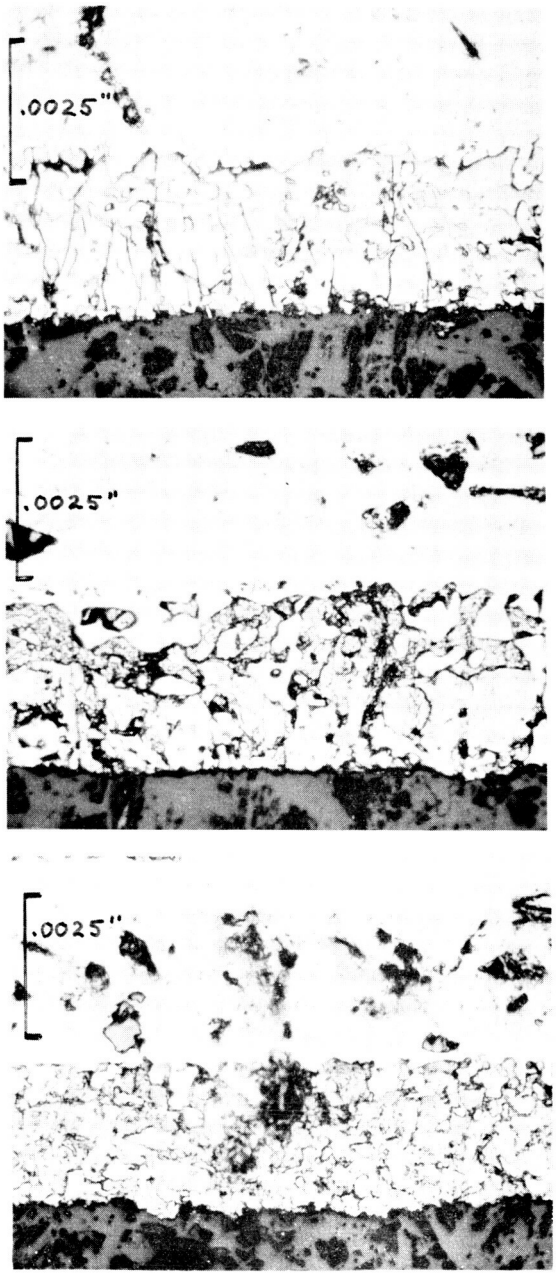

Cb-1Zr (a)

Braze
56Zr-28V-16Ti

Thermalox 998
BeO

Cb-1Zr (b)

Braze
56Zr-28V-16Ti

Thermalox 998
BeO

Cb-1Zr (c)

Braze
56Zr-28V-16Ti

Thermalox 998
BeO

Etchant: 30 ml lactic acid, 10 ml HNO_3, 10 ml HF

Note: Samples shown are the samples used for the microhardness and microprobe analyses described in the accompanying text. (a) as brazed, (b) vacuum exposed for 500 hours at 1600°F, (c) potassium exposed 500 hours at 1600°F.

FIGURE IV-8. Photomicrographs of Alloy 56Zr-28V-16Ti Brazements Between Cb-1Zr and Thermalox 998 (BeO) (400X Before Photo Reduction)

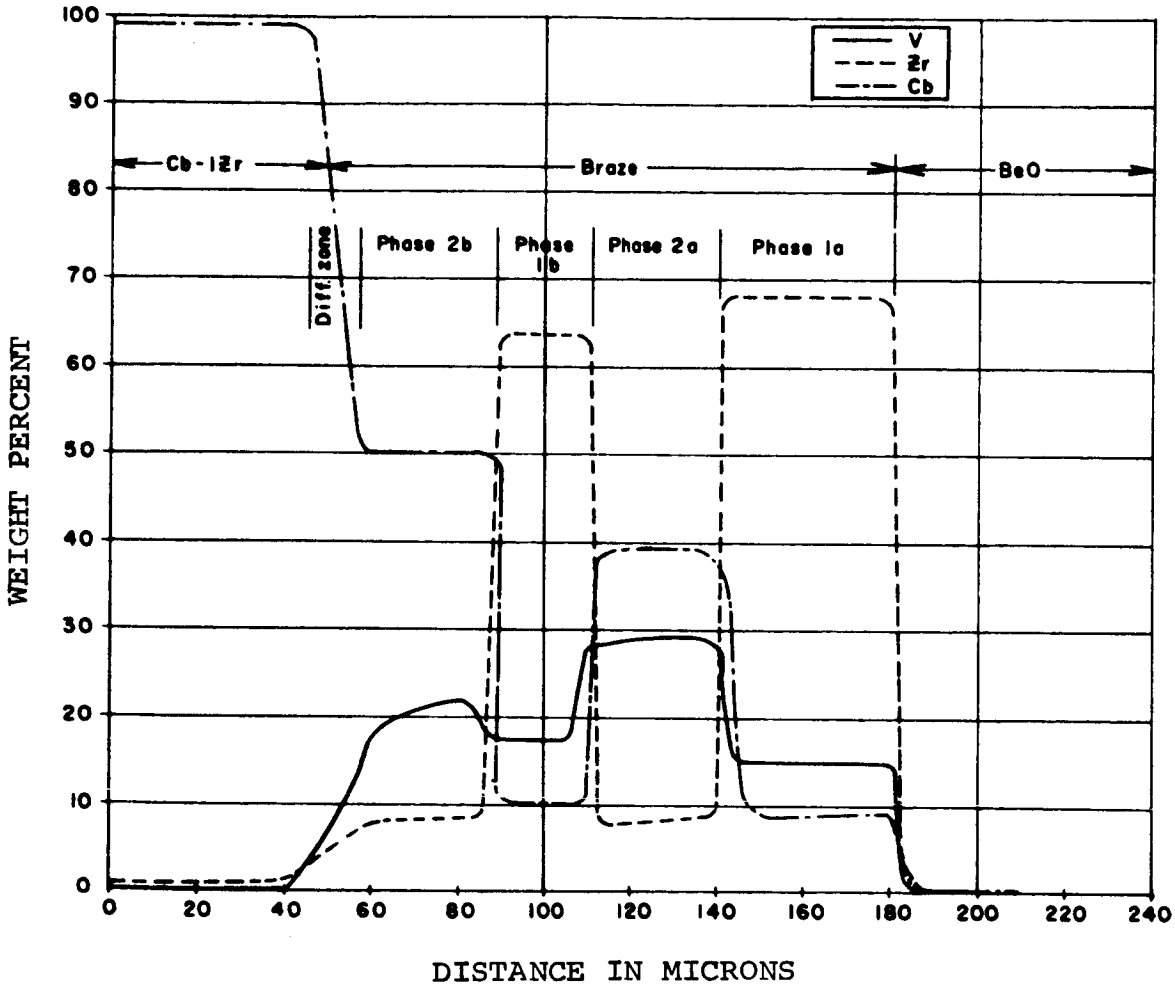

Sample was Potassium Exposed for 500 hours at 1600°F, no potassium defected by microprobe, limit of defectability 230 ppm.

FIGURE IV-9. Plot of Electron Microprobe Scan Across Alloy 56Zr-28V-16Ti Braze Between Cb-1Zr and Thermalox 998 (BeO)

TABLE IV-10. Composition of Various Phases of the Brazement of 56Zr-28V-16Ti to Cb-1Zr and Beryllia Ceramic Expressed in Weight Percent

Phase Designation (a)	Composition (weight percent)			
	Ti	V	Zr	Cb
2B	20	22	8	50
1B	7	18	64	11
2A	26	28	8	38
1A	8	15	68	9

(a) For braze zone see Figure IV-9.

TABLE IV-11. Composition of Various Phases of the Brazement of 56Zr-28V-16Ti to Cb-1Zr and Beryllia Ceramic Expressed in Atomic Percent

Phase Designation (a)	Composition (atomic percent)			
	Ti	V	Zr	Cb
1A + 1B	13	23	57	7
2B	28.4	29.2	6	36.4
2A	35	35	5.1	25

(a) For braze zone see Figure IV-9.

TABLE IV-12. Microhardness Test Results on 56Zr-28V-16Ti Alloy Brazed to Cb-1Zr and 99.8 Percent Beryllia

Phase Designation[a]	Knoop Hardness (50g load)		
	Sample 1 As brazed	Sample 2 Vacuum Exposed[b]	Sample 3 Potassium Exposed[b]
Cb-1Zr	113	139	160
Interface 2B	357	364	450
Brown phase 1A + 1B	-	1235	780-900
White phase 2A	407	211	(c)
Interface phase	1140-1300	-	-
Ceramic (BeO)	1140	-	-

(a) For Phase area and compositions, see Figure IV-9 and Tables IV-10 and IV-11
(b) 1600°F, 500 hours
(c) Too small in unit size to determine

relatively slow as compared to the attack experienced in the beryllium-containing-alloy systems. The completely refractory metal braze alloy systems will definitely be considered further. The possibility of complete suppression of the ZrV_2 phase by additional Cb-1Zr solution in the braze and further diffusion of V into the Cb-1Zr metal phase is explored later.

The three systems evaluated above can be ranked according to potassium exposure resistance as follows:

Best - 56Zr-28V-16Ti

Intermediate - 48Zr-48Ti-4Be

Poor - 75Zr-19Cb-6Be

The principle discussed earlier with regard to potassium corrosion via the low melting or unstable intermetallic phase agree well with the data already presented and offer a method of predicting braze joint stability. The ductile-brittle phase microstructure conditions, although not as predictable, also determine the integrity of the bond. As noted, improvements in braze behavior may be expected if the intermetallic phases can be diluted by refractory metal additions or by prolonged braze treatments which permit additional columbium solution from the metal member. The analysis of these three systems aided in the modification of braze alloys and selection of additional braze alloys for joining ceramics to metals for alkali metal applications.

On the present program two new braze alloys were subjected to 500 hour, 1600°F potassium exposure. In addition, the effect of molybdenum wetting layers and braze-diffusion on ceramic-to-metal seal strength and vacuum integrity were determined. Two braze alloy systems from all these tested for 500 hours will be subjected to 2000 hour exposure tests in the near future.

Diffusion Brazing

Diffusion brazing of active alloys was investigated because it was believed that if the intermetallic phases were responsible for weakening the ceramic-to-metal brazed joints in the presence

of potassium, the situation might be rectified by prolonging the braze cycle. Beryllium intermetallics should convert to the higher melting more stable intermetallic $CbBe_2$ and to the β-Ti-Zr-Cb-Be solid solution phases, in the BeO-(48Ti-48Zr-4Be)-Cb-1Zr system. Beryllium is soluble to the extent of 3 percent in the binary Cb-Be system at the eutectic temperature of 3632°F (reference 5). It is possible therefore that the Be component would be completely retained in the β-solid solution, Zr-V-Ti-Cb system.

The Zr-V-Ti-Cb (BeO-(56Zr-28V-16Ti)-Cb-1Zr) system appeared to be more promising since the Cb-1Zr base metal can form a solid solution with the Zr-Ti-V members and thus positively eliminate intermetallic compound formation on cooling from the braze diffusion temperature.

The secondary purpose of this study was to look for microstructure and flexural strength variations due to brazing temperature and brazing hold time differences somewhat greater than normally encountered in order to give more insight into the brazed microstructure variations noted on the previous program. These variations could not be satisfactorily explained solely on the basis of post brazing exposure times and environments.

The brazing temperature for these alloys was determined previously by trial braze runs at successively higher temperatures until satisfactory fillets, vacuum tight yields and strength were obtained. The standard vacuum brazing schedule used on this program consists of a ten minute hold just below the lowest melt temperature of the alloy system allowing the temperature to equalize within the furnace and allowing the vacuum to improve. The temperature is then rapidly raised to the predetermined brazing temperature, held for five minutes and the furnace power turned off. During the entire operation, the pressure in the furnace is not allowed to rise above 5×10^{-5} torr.

For the diffusion brazing study, the hold time at temperature was evaluated at zero minutes (actually one to five seconds), five minutes and thirty minutes. The brazing temperature with the standard five minute hold was evaluated at the predetermined temperature for each alloy and at 90°F (50°C) and 180°F (100°C) higher temperatures to accelerate diffusion. The test pieces consisted of ASTM CLM 15 geometry, Ei3-3W alumina (99.7% Al_2O_3) pieces or

99.8% beryllia modulus-of-rupture bars and cylindrical vacuum test samples. The results of these tests are presented graphically in Figure IV-10. Some interesting and readily observable trends are noted from the data. In the (48Ti-48Zr-4Be) columbium-1% zirconium system, no appreciable increase in strength is noted as a function of increasing time or temperature with either the alumina or beryllia test specimens. The reaction with the ceramic was not severe, as all but one of the alumina samples were vacuum tight. The micro leakers that occurred with the beryllia substrate must, however, be associated with the type of ceramic surface which offers a nucleation site for hard primary crystal formation, or an additional source of beryllium. These facts indicate that low intermetallics of Be in an eutectic groundmass of Cb-Ti-Zr were forming, as desired, but that no appreciable further solution of β in the solid solution phase was occurring. The results using a beryllia substrate indicate that this situation goes along with leaker formation. The braze diffusion concept was therefore discontinued for this braze system.

As discussed previously, the high temperature braze system (56Zr-28V-16Ti)-Cb-1Zr is very reactive on alumina and resulted in leakers even at zero (one to five seconds) hold time at 2273°F (1245°C).

The trend of increased strength with increased diffusion in the case of the beryllia ceramic is evident (See Figure IV-10). Indications are that the ZrV_2 phase is being absorbed into the Cb-Ti-Zr solid solution as a function both of time and temperature. This system variation holds real promise of being one that will provide better resistance to potassium attack.

Two of the three new brazed systems selected for potassium exposure testing on the current program required evaporated molybdenum wetting layers on the ceramic in order to obtain acceptable vacuum-tight assembly yields. With the first alloy, 68Ti-28V-4Be, no increase in strength was noted over that obtained during earlier screening runs with non-metallized ceramics. A strength increase noted with the 60Zr-25V-15Cb alloy was apparently due to the solution of molybdenum by the braze alloy to form a different braze structure and to the formation of a superior braze fillet.

The test results obtained from the brazed ceramic-to-metal assemblies which had been subjected to 500 hour, 1600°F potassium

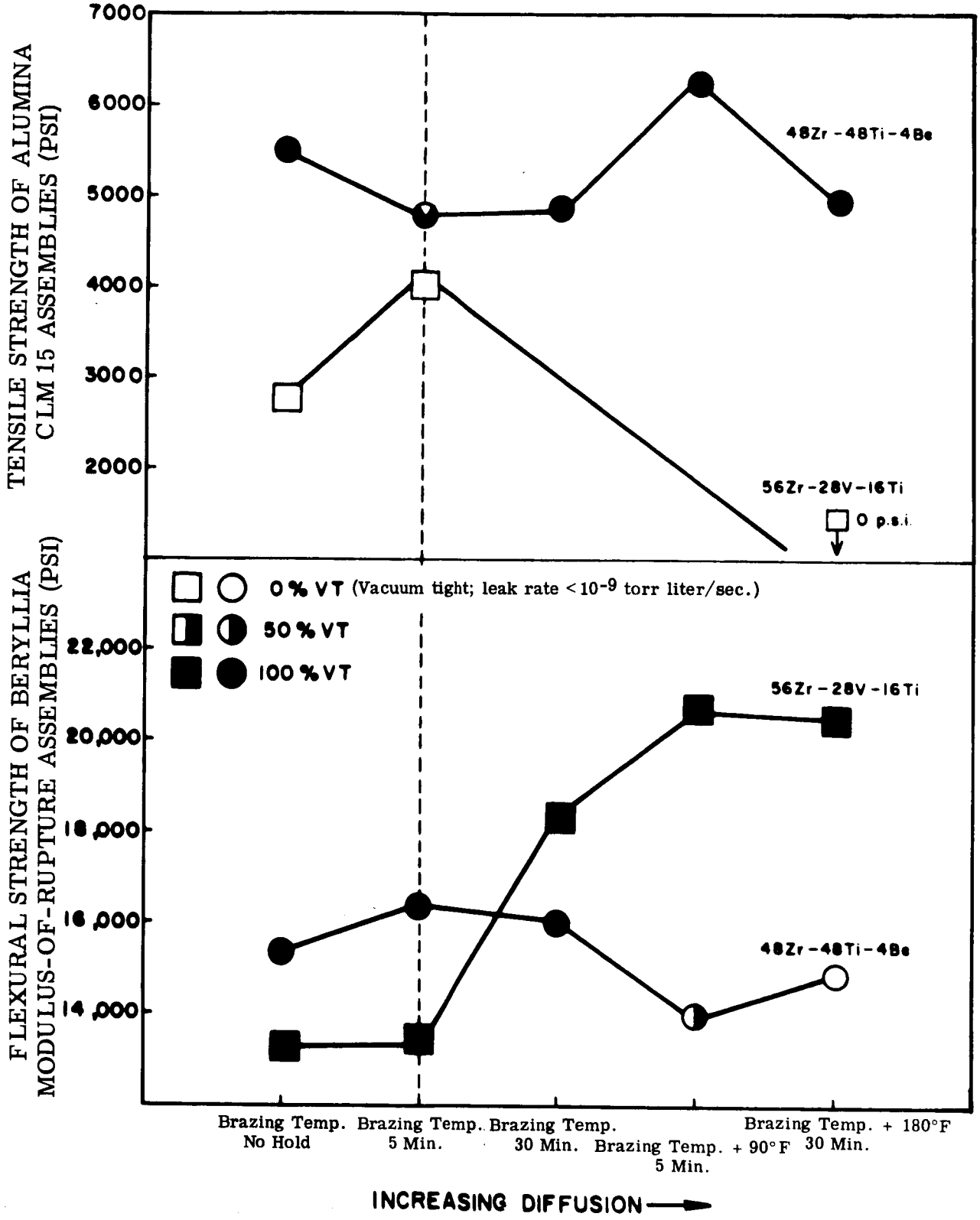

FIGURE IV-10. Effect of Increasing Diffusion on the Strength and Vacuum Integrity of Alumina - (Cb-1Zr) and Beryllia - (Cb-1Zr) Systems Brazed with Alloys 48Zr-48Ti-4Be or 56Zr-28V-16Ti

exposure on this program are presented in Table I V-13. These data indicate again that beryllium containing brazes, lead to corrosion taking place via the MBe_x phases.

The more refractory system 60Zr-25V-15Cb exhibited superior strength after exposure, indicating delayed precipitation of the ZrV_2 phase. On the basis of mechanical strength and vacuum tightness, this alloy (with Mo wetting layer) was selected for 2000 hour potassium exposure testing along with the 56Zr-28V-16Ti and 48Zr-48Ti-4Be alloys, which survived similar testing on the previous program. Braze diffusion studies and molybdenum wetting layers will be utilized to optimize joint strengths with these three alloys.

The complete list of candidate braze alloys for 2000 hours of potassium testing which can be made on the basis of work to date includes:

	56Zr-28V-16Ti	as brazed
**	56Zr-28V-16Ti	diffusion brazed
**	60Zr-25V-15Cb-Mo*	as brazed
	60Zr-25V-25Cb-Mo*	diffusion brazed
**	48Ti-48Zr-4Be	as brazed

The three braze systems indicated by the double asterisk (**) were selected as the best systems for 2000 hour alkali metal exposure tests. The single asterisk (*) indicates that a evaporated molybdenum wetting layer (1 to 3 μ thick; description of process will appear in the sixth quarterly report) was deposited on the ceramic.

c. MODEL BORE SEAL CONSTRUCTION

As a step in scaling-up from 0.5 inch outside diameter ceramic cylinders to four inch outside diameter cylinders, a two inch outside diameter intermediate size was selected for thermal cycling, high-temperature vacuum integrity evaluation and vibration testing. Two 2-inch diameter beryllia to columbium-1% zirconium seals have been made using the 56Zr-28V-16Ti active metal braze alloy. The braze alloy flowed to form a uniform fillet. The seals were vacuum-tight.

TABLE IV-13. Effect of 500 Hours 1600°F Potassium Exposure on Room Temperature Flexural and Tab Peel Strength of Beryllia to Cb-1Zr Brazed Systems

Ceramic Body	Metal Member	Braze Alloy (weight percent)	Brazing Temperature (°F)	Key	Room Temperature Flexural Strength (psi) (a)			Tab Peel Strength (b) (pounds/inch)			Vacuum Leak Test (fraction vacuum tight) (c)	
					As Brazed	Vacuum Exposed 500 hrs, 1600°F	Potassium Exposed 500 hrs, 1600°F	As Brazed	Vacuum Exposed 500 hrs, 1600°F	Potassium Exposed 500 hrs, 1600°F	Vacuum Exposed 500 hrs, 1600°F	Potassium Exposed 500 hrs, 1600°F
Thermalox 998 Beryllia 99.8% BeO	Cb-1Zr	68Ti-28V-4Be (Molybdenum wetting layer)	2372	$\bar{x}$	18 800	18 660	10 950	6.5	7.5	7.0	2/2	2/2
				s	1 240	1 660	2 540	±0.5	±1.5	±2.0	--	--
				n	4	5	4	2	2	2	2	2
Thermalox 998 Beryllia 99.8% BeO	Cb-1Zr	46Zr-46Ti-4Be-4V	2372	$\bar{x}$	17 800	13 380	11 530	6.5	10.5	6.5	2	2
				s	1 865	420	970	±0.5	±5.5	±0.5	1/2	2/4
				n	5	4	4	2	2	2	--	--
Thermalox 998 Beryllia 99.8% BeO	Cb-1Zr	60Zr-25V-15Cb (Molybdenum wetting layer)	2372	$\bar{x}$	22 170	17 560	15 250	52.5	85.0	50.0	4/4	4/4
				s	2 850	3 530	995	±2.5	±5.0	±20.0	--	--
				n	5	4	4	2	2	2	4	4

Key $\bar{x}$ - arithmetic mean
s - standard deviation
n - number of specimens tested

Notes:

(a) Strength determinations were made by four point loading on 0.1 inch x 0.1 inch x 1 inch modulus-of-rupture specimens. Load was applied at the rate of 0.1 inch per minute.
(b) Tab peel test on 0.1 inch wide by 1.0 inch long strip pulled perpendicularly at 1.0 inch per minute.
(c) Vacuum tight indicates helium leak rate of $< 10^{-9}$ torr liters/sec.

A four inch beryllia bore seal containing potassium will be tested in a generator stator on this program (Program III, Task 2). The test will be conducted at elevated temperature and a pressure of 10^{-8} torr or less. The design of the bore seal, which will be used in the stator compatibility test, is shown in Figure IV-11. The four inch diameter, four inch long Thermalox 998 beryllia tube with a 0.100 inch thick wall had been ordered from the Brush Beryllium Company. Delivery had been expected in late January. Difficulties encountered in obtaining beryllia powder of specified low-silica content and in fabrication have resulted in a delay in scheduled delivery to mid-March.

4. Program for the Next Quarter

a) Delivery of the remainder of the low-silica beryllia ceramic for test assemblies is expected.

b) The four inch model beryllia bore seal will be fabricated.

c) Fabrication of ceramic-to-metal test assemblies for alkali metal exposure will be completed. This includes testing of chemical vapor deposition of columbium on beryllia and testing of molybdenum wetting layers with the 60Zr-25V-15Cb braze alloy.

d) The 2000 hour 1600°F potassium exposure tests of ceramics which survived the 500 hour tests, and of two brazed ceramic-to-metal systems will be initiated.

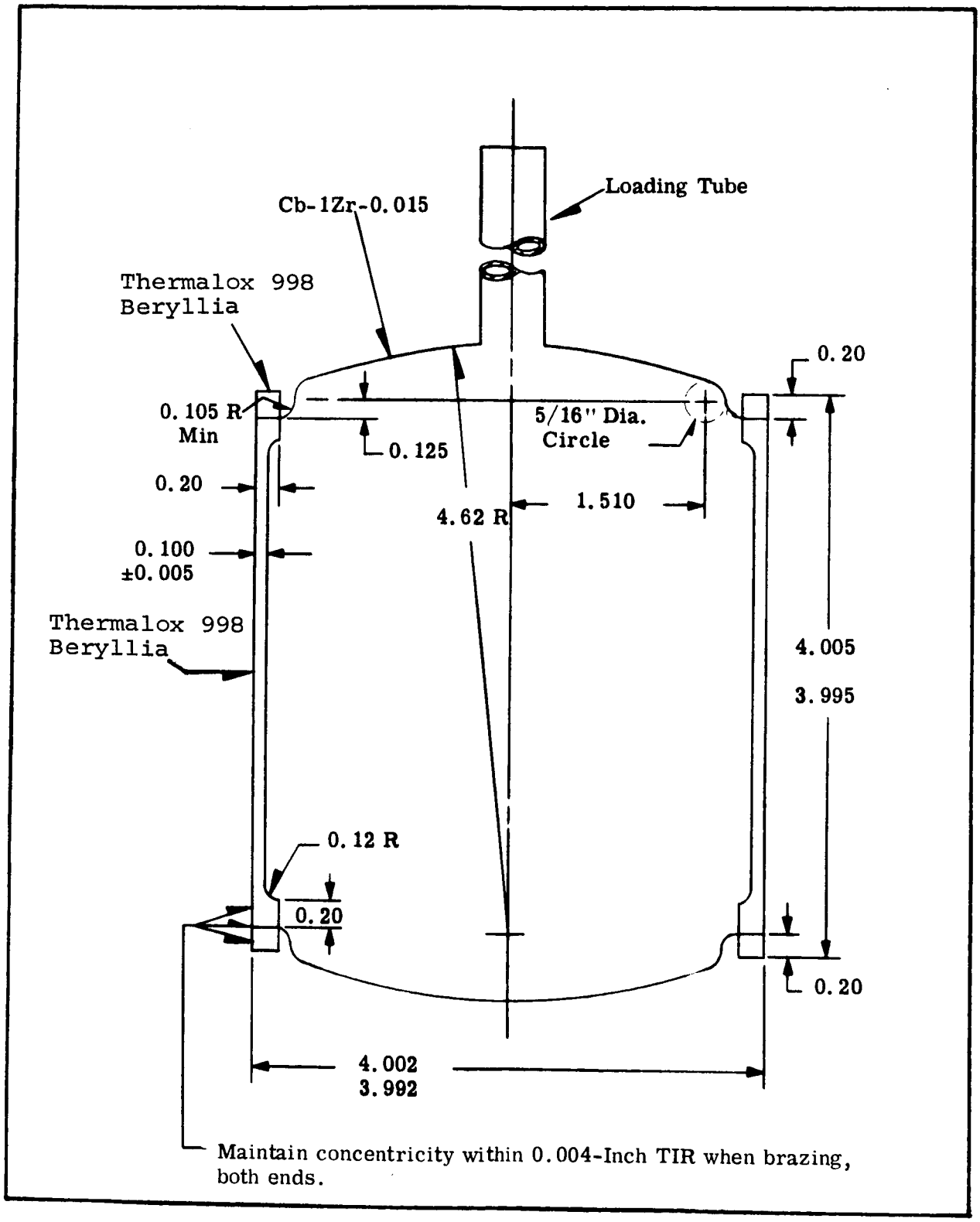

FIGURE IV-11. Bore Seal Capsule for Compatibility Test

B. TASK 2 - STATOR AND BORE SEAL

1. Summary of Technical Progress

a) A total of 2032 official endurance test hours was accumulated as of the end of the quarter.

b) Thermal chamber pressure at the beginning of the period was 5.4×10^{-7} torr. Pressure had decreased to 1.4×10^{-8} torr at the end of the report period.

c) A twelve hour plant-wide power outage resulted in a temperature reduction to approximately 350°F but with the vacuum maintained. No adverse effects have been noted.

d) Mass spectrometer residual gas analysis scans were made periodically on the test chamber atmosphere.

2. Discussion

Figure IV-12 is a cutaway drawing of the thermal vacuum chamber which shows the stator installed in the furnace hot zone. The chamber is of double wall construction with baffles between the walls to channel cooling water flow. The chamber top cover is also double walled to provide a path for cooling water. Thermocouples were placed in position in the stator just prior to installation in the chamber. Stator winding leads were inserted into short lengths of hollow alumina tubing to insulate them as they passed through the top heat shields. Thermocouple and winding leads were then passed upward through perforations in the top heat shields as the shields were set in position. Winding leads were brazed to OFHC copper feedthrough bus bars inside the furnace, using a glass bell jar with supporting frame and foil curtains to maintain an argon atmosphere during the brazing operation. Thermocouples were passed through hollow Kovar tubes and brazed externally.

The stator main frame was made from a Hiperco 27 (27% cobalt-iron) alloy forging, and the laminations were held in place in the frame by a retaining ring which was also made from a Hiperco 27 alloy forging. The magnetic stack consisted of 244 Hiperco 27 alloy laminations, 0.008-inch thick, with a sapphire-like insulation coating of plasma-arc sprayed Linde A component (Al_2O_3)

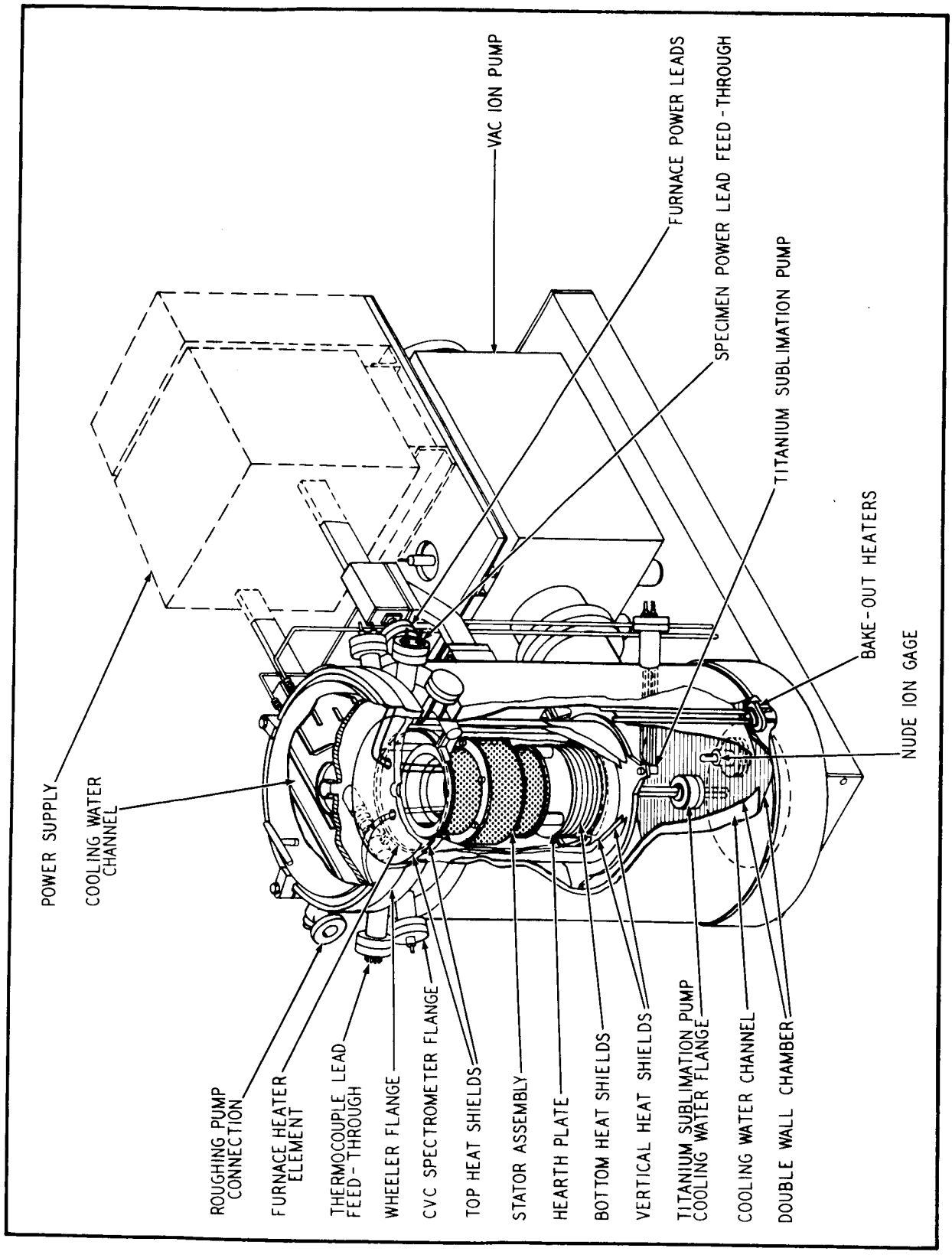

FIGURE IV-12. Cutaway View of Furnace Showing the Stator Test Specimen Installed

on one side of each lamination. Conductor wire was rectangular nickel-clad silver (20% nickel cross-sectional area) coated with a 0.006-inch thick layer of Anadur, a refractory-oxide-filled glass fiber insulation. Slot insulation was provided by ceramic (99% Al_2O_3) U-shaped channels (slot liners), spacers and wedges. Westinghouse W839 potting compound (aluminum-orthophosphate-bonded zircon) was used to fill small voids between the slot liners and slots, and extended about 3/8 inch beyond the slot liner ends to provide winding support. Hollow Al_2O_3 tubes were used as thermocouple insulators in the slot and stack areas. Thermocouples were installed in pairs in the slots of each winding, in the stack, between the stack outside diameter and frame, on the frame outside diameter and on winding end turns. Figure IV-13 shows the completed stator, except for the installation of thermocouples, sitting on three posts which were used to support the stator on the hearth plate in the thermal vacuum chamber. The stator physical size is representative of a 15 kVA generator or 12 hp a-c induction motor operating at 12,000 rpm. The stator conductor and insulation system is being tested at a current and voltage level (292 volts and 41 amperes per phase) equivalent to a 36 kVA machine.

The fourth quarterly report can be referred to for additional details on stator construction, preparations for installing the stator in the thermal vacuum chamber, and initiation of the test program.

a. STATOR TEST PROCEDURE

At the start of the report period, 172 hours of endurance test time with a slot hot-spot temperature of 1100°F had been accumulated on the stator. Thermal vacuum chamber pressure was 5.4×10^{-7} torr. During the period an additional 1860 hours of test time was completed, for a total of 2032 hours. Chamber pressure decreased slowly during the test period, reaching a value of 1.4×10^{-8} torr at the end of the period. Each stator winding carried 41.2 amperes at a potential of 292 volts a-c line-to-ground. Figure IV-14 is a schematic of the stator electrical hook-up.

Endurance time was logged only while the stator windings were energized and the hot-spot temperature was stable. Three power interruptions occurred during the report period; one planned and two unplanned. A 312 kVA, 3 phase, 400 cycle per second generator is used to supply a line-to-ground voltage of 292 volts to

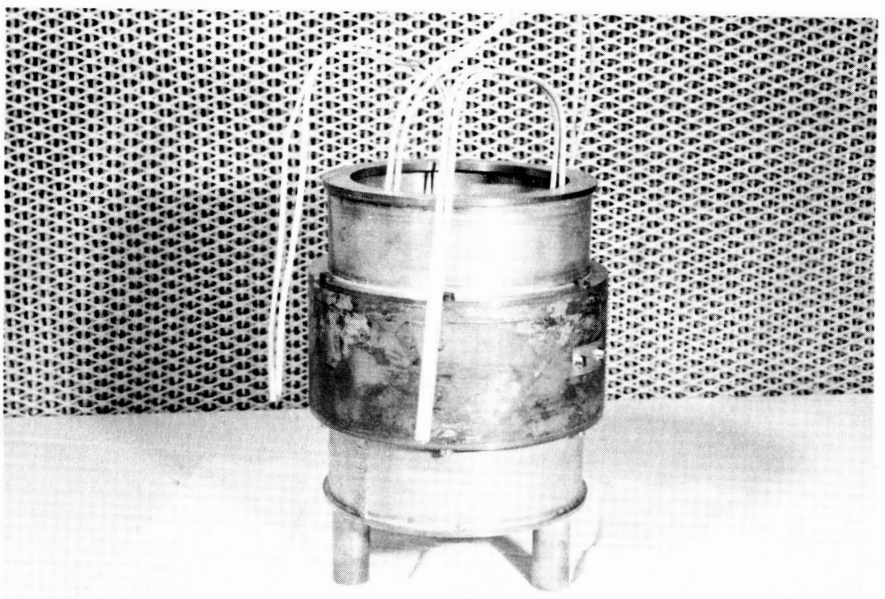

FIGURE IV-13. Stator Assembly on Furnace Supports Prior to Endurance Test

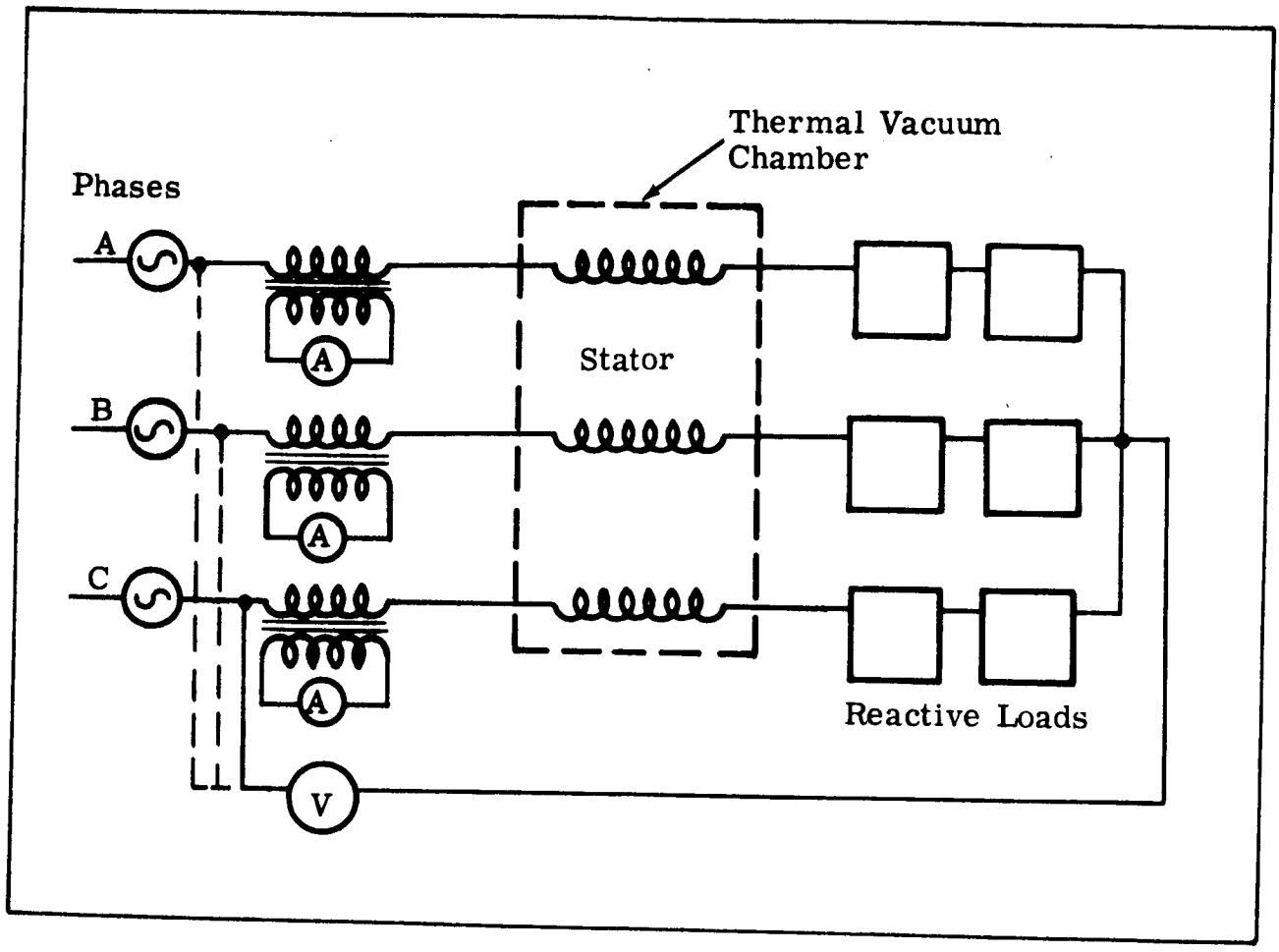

FIGURE IV-14. Schematic of Stator Electrical Hook-up

each phase of the stator (505 volts phase-to-phase). After approximately 2000 hours total operating time, this generator was shut down and the bearings were changed on a preventative maintenance basis. This step was taken to increase the reliability of the power supply, as there is no backup source available. During this power-off period the chamber furnace element power was increased enough to maintain the stator slot (hot-spot) temperature at 1100°F.

The first unexpected power interruption occurred when the Variac used to control voltage to the transformer (Task 3) became overheated. An emergency shut down was made, including the 312 kVA generator. Furnace element power was increased to maintain the stator slot at 1100°F until repairs were completed.

The second unanticipated interruption was caused by a plant-wide power outage which lasted about 11-1/2 hours. This failure occurred during the time that the 312 kVA generator was removed for the bearing change. The average generator temperature dropped to approximately 350°F during this shutdown. The sputter-ion pump and furnace element were turned on as soon as power was restored, and within five hours the stator slot temperature returned to 1050°F. Chamber pressure at the end of the power outage was in the 10^{-9} torr range. Electrical measurements taken after temperature had stabilized did not indicate any changes in electrical performance.

Static electrical measurements covering conductor resistance, d-c insulation resistance, and leakage current when subjected to an a-c voltage potential were taken once each week.

Titanium sublimation pump (TSP) bursts of two minute duration were used at intervals to see if there would be any effect on the chamber base pressure. In each case the chamber pressure was reduced for a short period of time, but it always returned to the initial value. In one instance the TSP was cycled for 20 minutes, which reduced the chamber pressure from 1.6×10^{-7} torr to 1.9×10^{-9} torr, but the pressure rapidly returned to 1.5×10^{-7} torr.

b. STATOR DATA

Figure IV-15 is a log-log plot of chamber pressure in torr vs endurance test time in days. The time scale does not necessarily

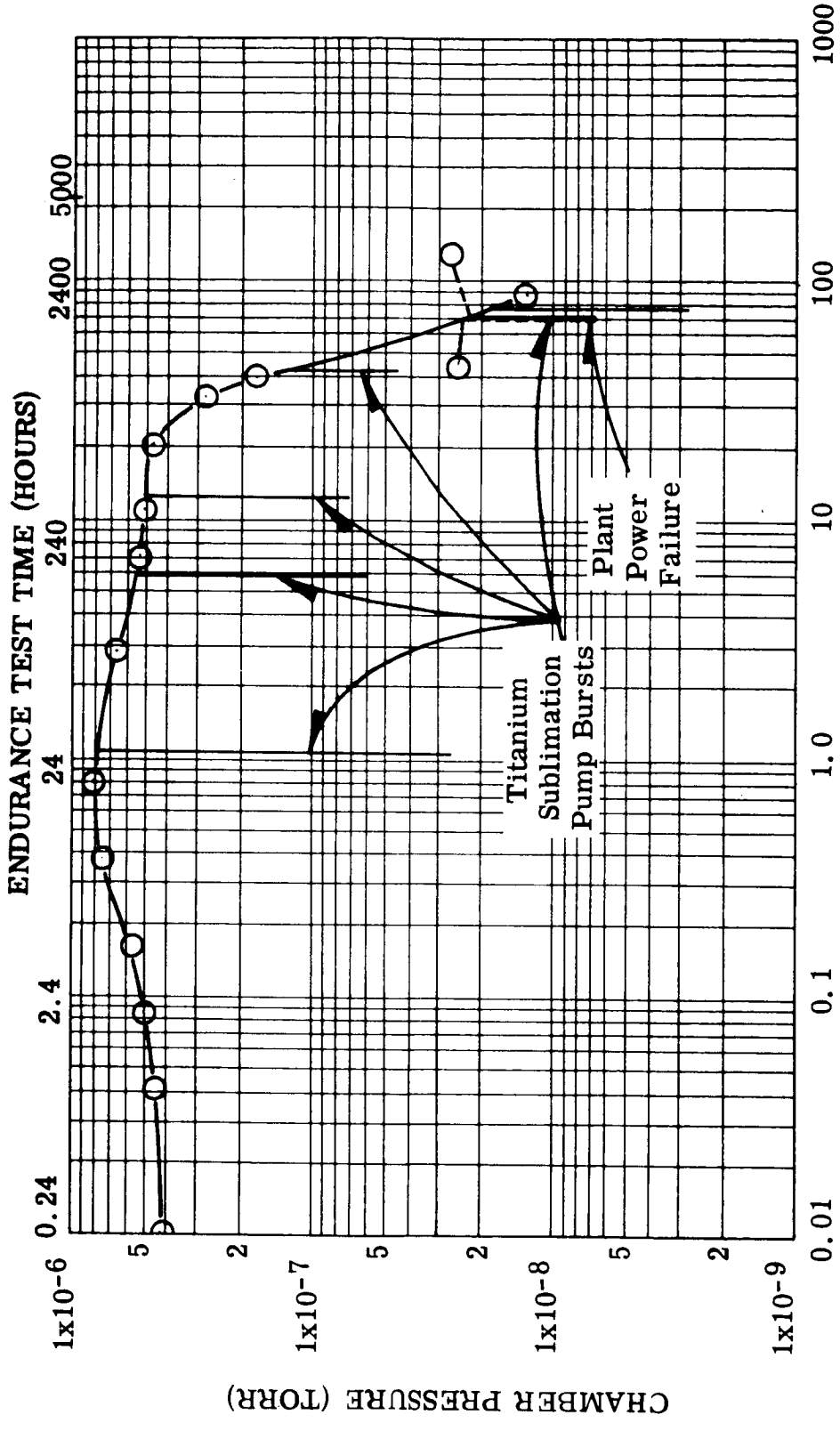

FIGURE IV-15. Stator Chamber Pressure vs. Endurance Test Time 1100°F Stator Hot Spot

Figure IV-15. Stator Chamber Pressure vs. Endurance Test Time

show consecutive calendar days, as the logging of official endurance time occurred only when the stator had voltage and current applied and was at a stable hot-spot temperature. Thus, time was not logged when the power supply generator was off the line for the bearing change. The curve as plotted shows pressure values for steady state conditions. Titanium sublimation pump pressure transients are shown as vertical lines in several places to indicate the magnitude of pressure reductions attained with titanium sublimation pumping.

Figure IV-16 is a cutaway drawing of the stator showing how the thermocouples are installed. Slot and end turn thermocouples are shown in representative locations. Two thermocouples (No. 1) are located in adjacent slots in each phase winding, as indicated by a pair of thermocouples in the drawing. Midstack thermocouples and lamination outside diameter slot thermocouples are identified as Nos. 2 & 3 respectively. One of two pairs of winding end turn thermocouples are identified as No. 5, and the two frame outside diameter thermocouples are No. 4. All but the frame outside diameter thermocouples are installed in 99% Al_2O_3 tubes, and all sensing junctions except in the end turn thermocouples are located in a plane which divides the lamination stack into two approximately equal parts where dT/dZ (T = temp, Z = cylinder axis) is zero. Six thermocouples were lost during installation of the stator in the thermal vacuum chamber, but each location had at least one functioning thermocouple because of the duality of thermocouples installed in an attempt to anticipate problems during installation.

Table IV-14 shows representative temperature readings for the various operating thermocouples.

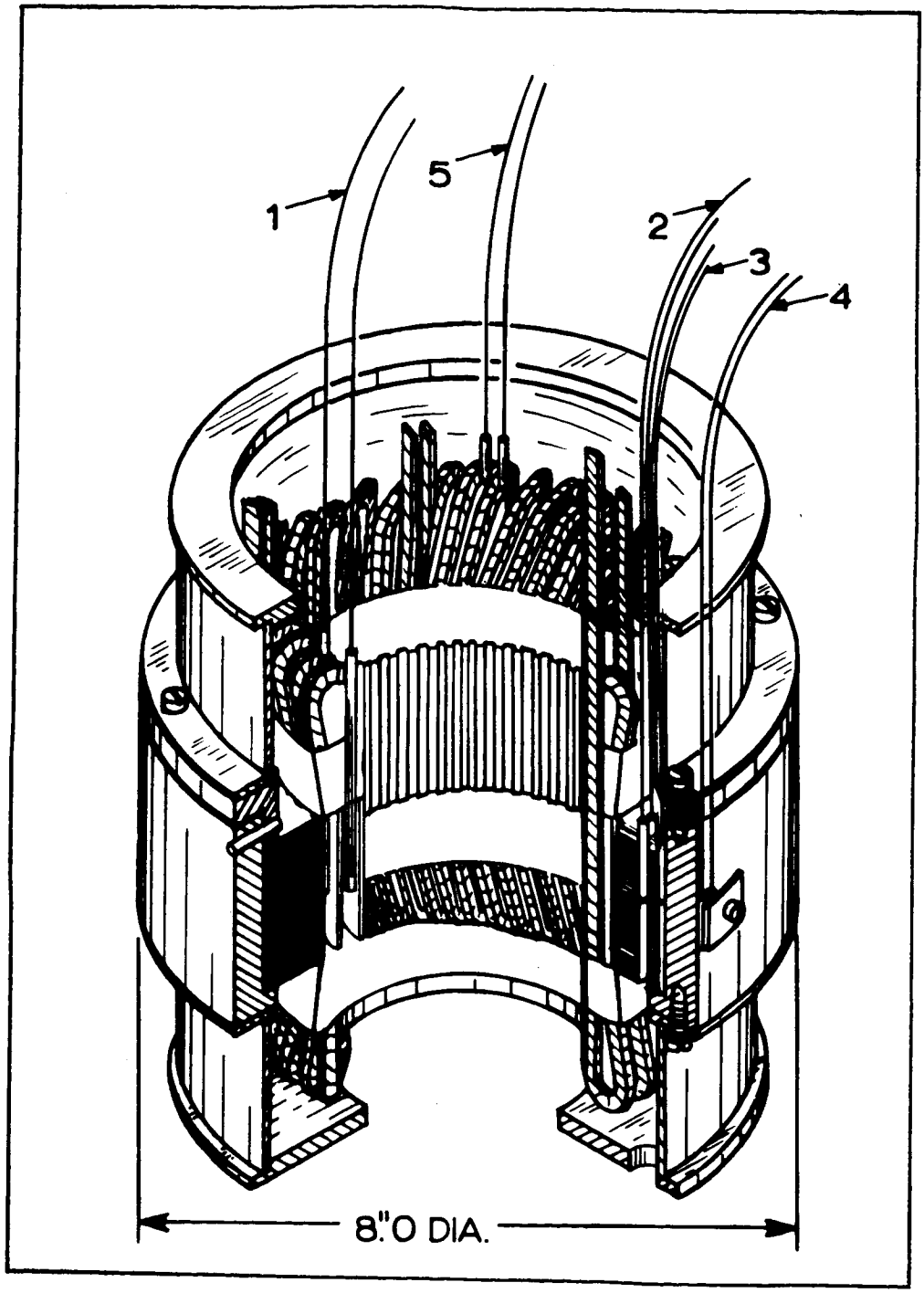

FIGURE IV-16. Stator Cross Section Showing Thermocouple Locations and Junction Positions

KEY TO FIGURE IV-16

No.	Quantity Installed	Description
1	6	Slot Liner - 2 per phase "B" Phase Thermocouple lost during assy
2	2	Stack Bore Tube
3	2	Lamination - Frame Slot One lost during assy
4	2	Frame OD One lost during assy
5	4	"B" and "C" Phase End Turns "B" phase lost during assy

TABLE IV-14. Representative Stator Temperature Distribution at 1100°F Hot-Spot Test Temperature After 1480 Hours of Endurance Test

Thermocouple Location	Temperature (°F)
Phase "A" Slot Liner	1103
Phase "A" Slot Liner	1103
Phase "C" Slot Liner	1103
Phase "C" Slot Liner	1103
Mid-Stack Bore	1080
Mid-Stack Bore	1083
Lamination OD Slot	1083
Frame OD	1080
Phase "C" End Turn	1078
Phase "C" End Turn	1078

Chamber Pressure at the time these readings were taken was 1.0×10^{-7} torr. Chamber pressure level did not have any apparent effect on temperature distribution, as this pattern and spread had been retained since the stator first reached stable test temperatures.

Initial plans were to use the stator temperature gradients to attempt to determine apparent thermal conductivity coefficients across the various materials, going radially outward from the slots. This was based on the expectation that the winding end-turn temperature would be higher than the slot temperature, as in a conventional machine. However, a comparison of slot liner and end turn temperatures from Table IV-15 shows that the end turn temperature is 25°F lower than the slot temperature,

TABLE IV-15. Stator Temperature Distributions

Winding Current - AC Amps/ Winding	Volts AC Per Winding	Stator Thermocouple Temperatures - °F						Chamber Pressure (torr)	Furnace Power (watts)	Date	Endurance Time (hours)
		Stator Slot (average)	Winding End Turn (average)	Stack Bore Tube (average)	Lamination Frame Slot	Frame OD	ΔT Slot to Frame OD				
31.2	290	451	437	430	415	415	36	4.6×10^{-10}	0	11-19-65	
31.2	290	986	980	980	975	980	6	1.2×10^{-8}	615	11-22-65	
35.6	290	1041	1008	1021	1022	1022	19	1.9×10^{-8}	615	11-23-65	
41.2	290	1092	1060	1067	1065	1065	27	4.2×10^{-7}	615	11-23-65	0
41.2	290	1099	1069	1075	1074	1071	28	6.4×10^{-7}	615	11-26-65	75
41.2	290	1112	1078	1090	1091	1082	30	5.4×10^{-7}	615	11-30-65	172

and at about the same level as the frame outside diameter temperature. The heat flow path is from the conductor volume in the stator slot to the end-turn area, where the heat is radiated to the chamber top and bottom heat shields. Water cooled cold walls are located just outside the heat shields at the top, bottom and sides of the chamber. The temperature gradient from the slot liner to the frame outside diameter is approximately the same as from the slot to the winding end turn.

This change in temperature pattern with increasing operating temperature level indicates that conduction is the primary heat transfer mode at conventional operating temperatures (300°F), but that the rapid increase in radiation emissive power (4th power of absolute temperature -°R) with increasing temperature can be used to advantage. Heat transfer in high temperature generator and motor designs can be shared between conduction and radiation modes by placing heat sinks where radiation from the end-turns can be absorbed. Depending on the absolute operating temperature, radiation may be a more efficient means of winding heat transfer than conductance paths in the stack.

The ΔT from the slot thermocouple to the mid-stack thermocouple (reference Table IV-15) is not large enough to provide a reasonable basis for calculating an apparent thermal conductivity. Temperature gradients in the Hiperco 27 alloy laminations and frame are very small, even at the lamination-frame interface, so there is no way of obtaining a check on calculations made for heat flow in the slot ceramics. Instrumentation for this test and the transformer and solenoid tests was primarily based on requirements for materials compatibility testing rather than heat transfer information.

Figure IV-17 shows conductor resistance plotted as a dimensionless ratio during the course of the endurance test. Base line ρo was 0.0134 ohms at 78°F. The effect of temperature on resistance is indicated by the temperatures shown in the figure. The conductor stability is indicated by the lack of a change in slope of the curve.

Residual gas analysis scans were made periodically on both the stator test chamber and the transformer and solenoid chamber (Tasks 3 and 4). A Consolidated Electrodynamics Corporation (CEC) Residual Gas Analyzer (RGA) Model 21-614 was used to

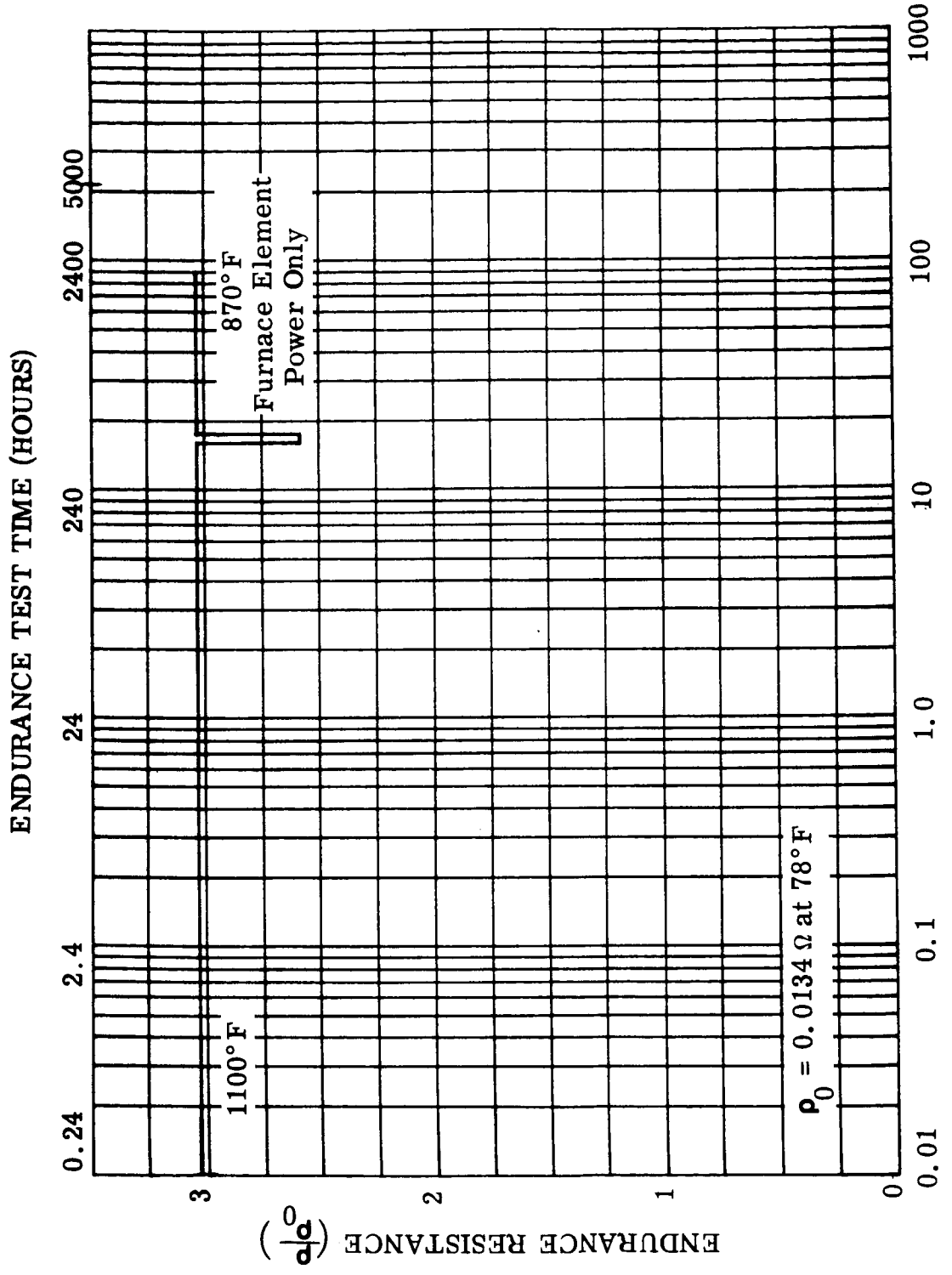

Figure IV-17. Stator Conductor Resistance vs. Endurance Test Time

FIGURE IV-17. Stator Conductor Resistance vs. Endurance Test Time at Noted Conductor Hot Spot Temperatures

determine the compounds present in the test chambers at the existing high-temperature, high-vacuum test conditions. The CEC analyzer is basically a cycloidal mass spectrometer which uses a permanent magnet to create the necessary magnetic field. The tubes used to analyze the compounds and gases coming from the test models and chamber walls have a sensitivity in the 10^{-11} to 10^{-12} torr/chart division range. The tube resolution is one atomic mass unit (amu) up to a mass-to-charge ratio (m/e) of 44. Above this value the unit resolution decreases, and the interpretation of mass spectrograms becomes more difficult.

Standard research grade gases of nitrogen, xenon, argon, and carbon dioxide were obtained from the Matheson Company. These gases were used to calibrate the analyzer with respect to mass-to-charge ratio and sensitivity. The sensitivity obtained and that given by the manufacturer are compared in Table IV-16.

TABLE IV-16. RGA* Sensitivity Data Using Calibration Gases Compared with Gas Supplier's Sensitivity Data

Gas (Matheson Co.)	Parent Mass	Sensitivity in Torr/Chart Division	
		Mfr's Data	Test Data
Nitrogen	28	5.2×10^{-11}	5.0×10^{-11}
Argon	40	4.47×10^{-11}	5.0×10^{-11}
Carbon Dioxide	44	4.45×10^{-11}	5.0×10^{-11}
Xenon	131	1.4×10^{-10}	3.1×10^{-10}

* Residual Gas Analysis

This table shows good correlation up to a parent mass of 44. Reduction in resolution becomes noticeable in the sensitivity values obtained for xenon as measurements at the parent m/e of 131 were not exact.

Figure IV-18 shows a reproduction of a mass spectrogram taken with the stator test chamber clean, dry and empty and at a temperature of 1100°F. Table IV-17 indicates which gases are contributing to the spectrum.

TABLE IV-17. Partial Pressures of the Identified Gases Contributing to the RGA Spectrum Shown in Figure IV-18

Gas	Mass-to-Charge (m/e)	Partial Pressure (torr)
H_2	2	0.40×10^{-8}
H_2O	18	6.50×10^{-8}
$N_2 + CO$	28	1.0×10^{-8}
A	40	0.10×10^{-8}
CO_2	44	1.50×10^{-8}
"Organics"	45 - 150	0.40×10^{-8}
Σ Partial Pressures (Mass Spectrometer) -		9.9×10^{-8}
Total Pressure (Ion Gauge) -		1.2×10^{-9}

Resolution of the sensing head was not sufficient to attempt to specify the components that are lumped together as "organics".

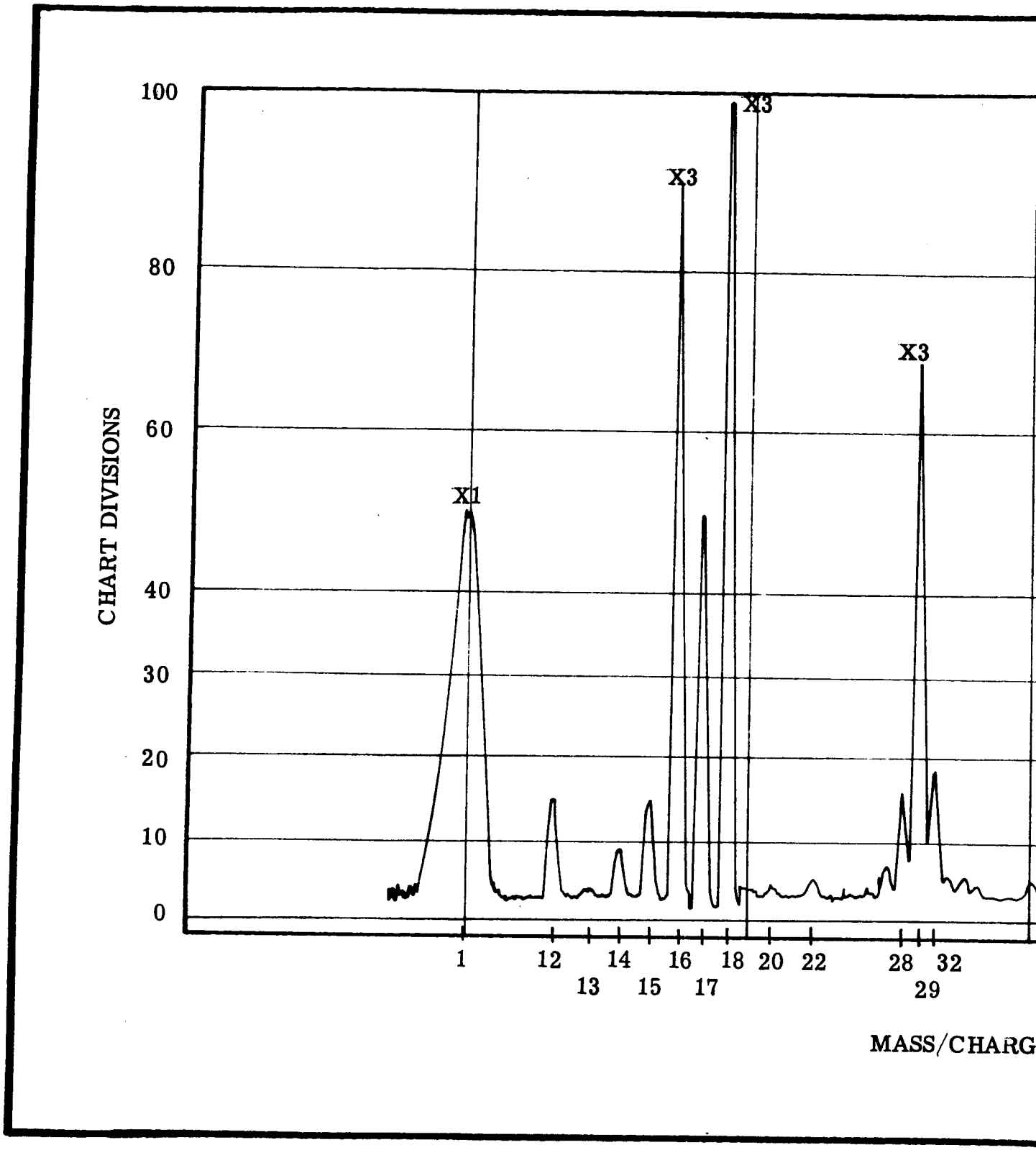

FIGURE IV-18. Replica of a Mass Spectrogram From the Stator Thermal Vacuum Chamber When Clean, Dry, and Empty and at 1100°F

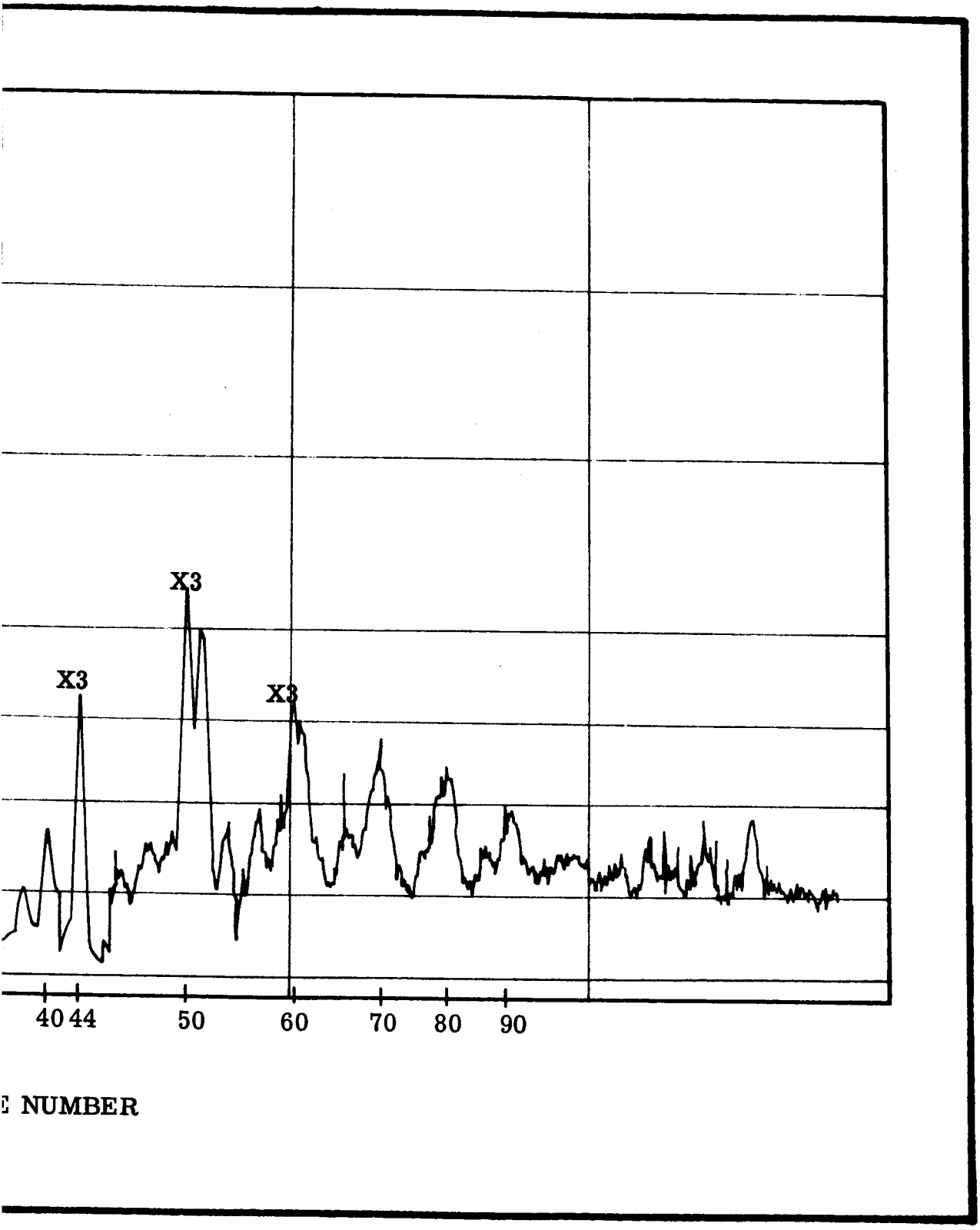

E NUMBER

The summation of partial pressures as indicated by the mass spectrometer is considerably larger than the total pressure indicated by the Bayard-Alpert type nude ion gauge. It is believed that the variation is caused in large part by the relative locations of the two sensors, in addition to the accuracy of the readouts. The ion gauge is located in the bottom of the test chamber, almost in line with the throat of the ion pump (refer to Figure IV-12). The mass spectrometer sensing head is attached to the bakeable valve at the top of the furnace. The conductance path to the ion pump is considerably more involved from the top of the chamber than it is from the vicinity of the ion gauge. More information in this pressure range will be required to determine how repeatable the condition is. The spectrometer sensing head was specifically attached to the bakeable valve so it could be removed for maintenance if necessary without disturbing the chamber.

Figure IV-19 is a plot of partial and total chamber pressures vs endurance test time in days. On the 21st day a scan was taken just prior to and immediately after a two minute titanium sublimation pump burst. The titanium caused some reduction in H_2O but the biggest change occurred in the N_2 + CO content. The other gases did not show any change. The scan plotted for the 72nd day was taken shortly after the plant-wide power failure. Slot winding temperatures were still being rebalanced to 1100°F, and were high (1123°F) at the time the scan was taken. The next scan was at 1100°F and showed a considerable decrease in pressure. As noted in the discussion of Figure IV-19, the ion gauge total pressure is consistently less than the sum of the mass spectrometer partial pressures.

c. STATOR BORE SEAL CAPSULE DESIGN

Figure IV-20 is a sketch showing the proposed construction and dimensions for a bore seal capsule which will be loaded with hot-trapped potassium under vacuum ($< 1 \times 10^{-5}$ torr). The capsule will be fitted into a stator cavity with a cold radial clearance of 0.007/0.012 inch between the capsule outside diameter and the stator stack inside diameter. When the capsule is subjected to high-temperature conditions in vacuum, the potassium vapor pressure will apply a load to the Cb-1Zr end bells, causing stresses in the metal and in the ceramic-to-metal joint. Differences in thermal expansion coefficients between the BeO and Cb-1Zr will also create stresses in the metal and in the brazed

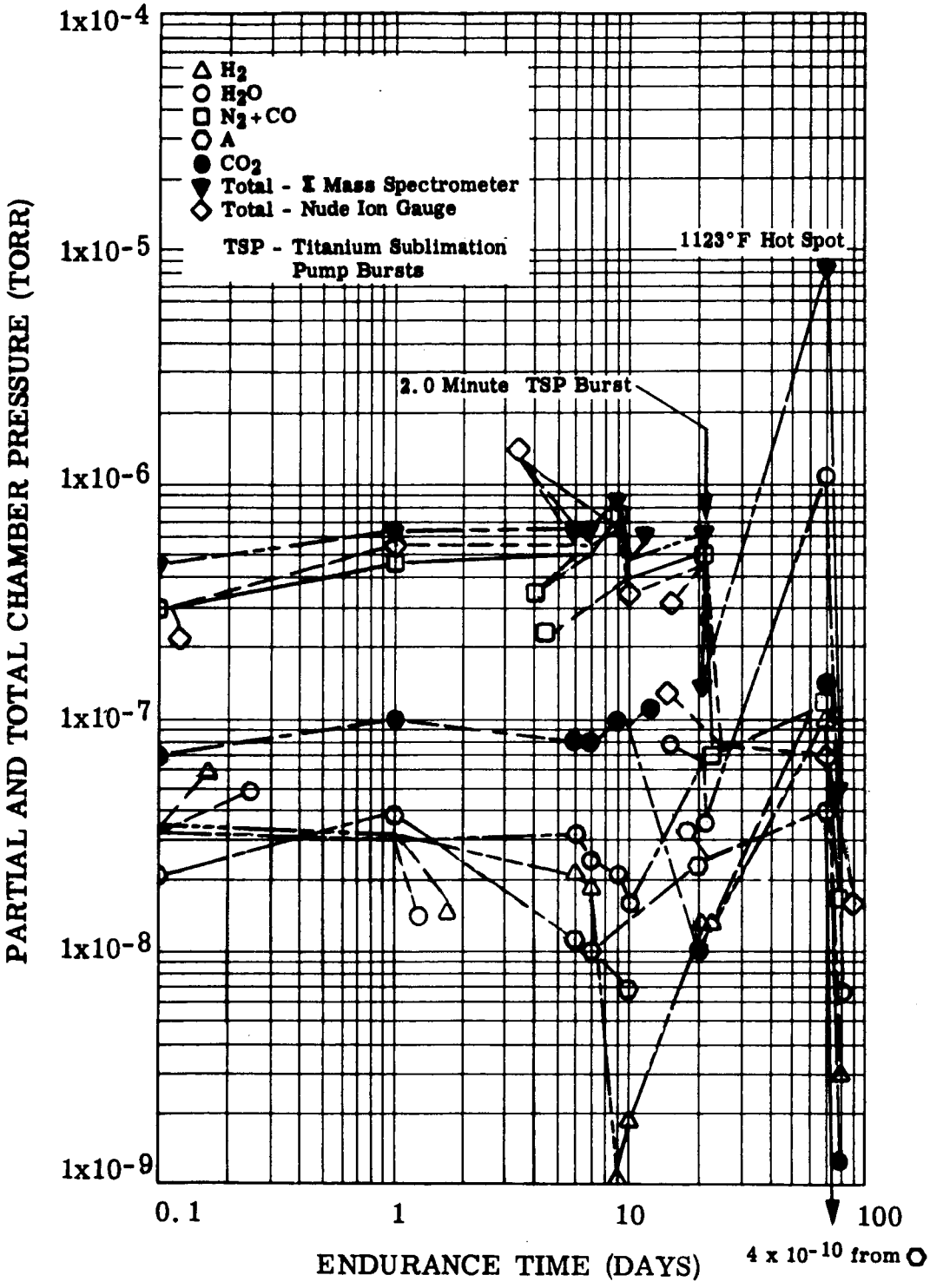

FIGURE IV-19. Time-Pressure Plot of Σ Mass Spectrometer Residual Gas Analysis Scans in Chamber No. 1 (Stator)

Figure IV-19. Time Pressure Plot of Mass Spectrometer Residual Gas Analysis Scans

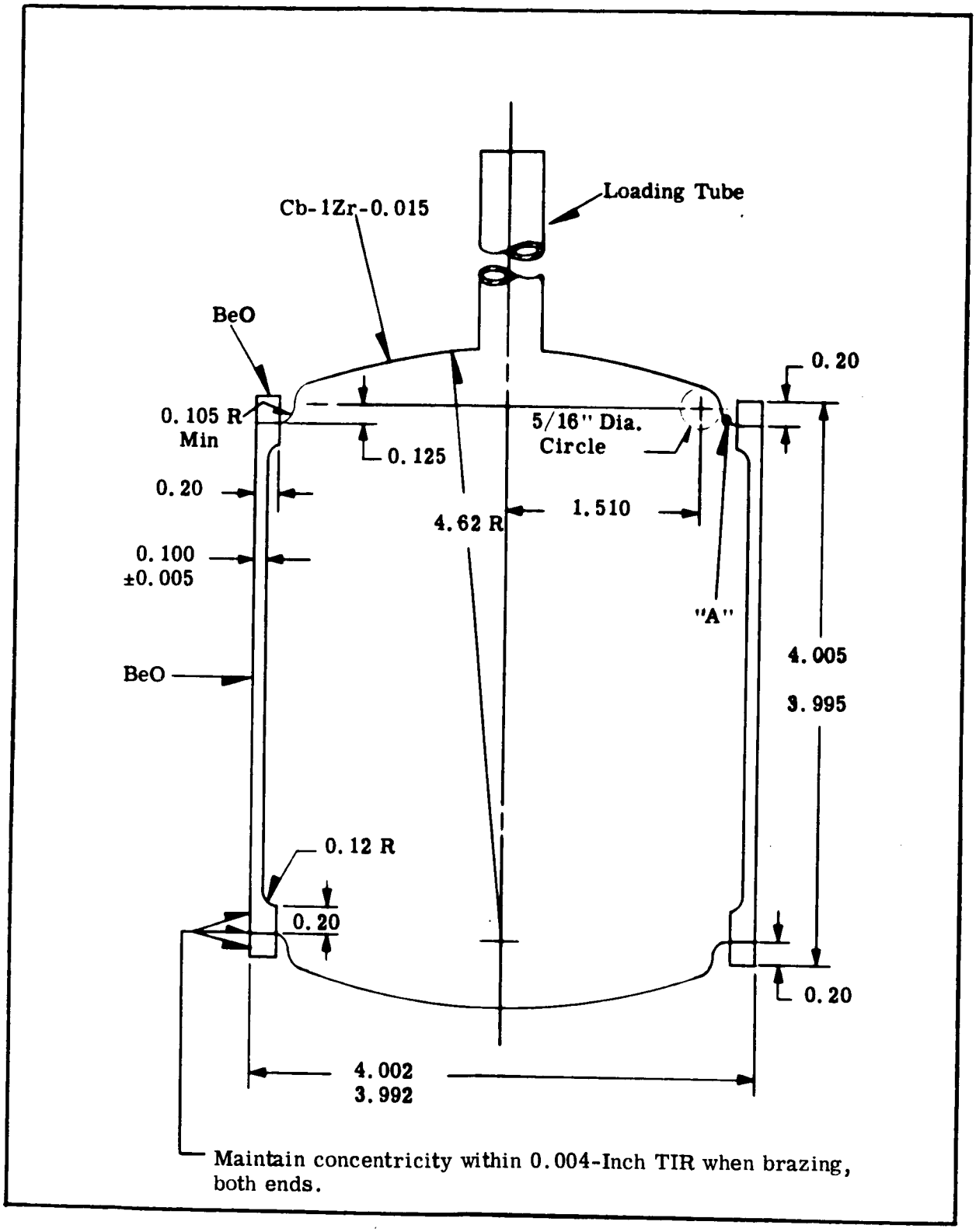

FIGURE IV-20. Bore Seal Capsule

joint. Combined pressure and thermal stresses in the metal end bell were calculated on a computer by adapting an existing computer program. The maximum stress encountered is approximately 20,000 psi and it occurs at the point designated as "A" on Figure IV-20. Creep rupture data obtained on Program NAS 3-4162 (Westinghouse Report WAED 64.54E) indicates that Cb-1Zr will withstand this stress level for more than 10,000 hours at 1400°F in a vacuum of 10^{-6} torr.

The vapor pressure of potassium at 1400°F is approximately 16 psia. This pressure will apply a circumferential load of 14.2 pounds per inch on the brazed joint at test temperature. Tab peel strength data was obtained on this program for Cb-1Zr brazed to BeO using an alloy identified as No. 9 (60Zr-25V-15Cb). After potassium exposure at 1600°F, room temperature tab peel strength was 50 pounds per inch. Assuming that the tab peel joint retains half its room temperature strength at 1400°F, it will accommodate approximately twice the load applied at the capsule joint. The tab peel specimens used do not have a back-up strip comparable to the back-up ring used in the capsule joint. The capsule joint will have more strength than the tab peel specimen because of the stiffening effect of the back-up ring.

3. Program for the Next Quarter

a) Continue the stator endurance test with a hot-spot temperature of 1100°F.

b) Continue construction of a 1400°F stator model.

c) Manufacture and load a bore seal capsule.

C. TASK 3 - TRANSFORMER

1. Summary of Technical Progress

a) A layer-to-layer short developed in the primary winding after 107 hours of endurance testing at temperature. Testing was continued because insulation aging data could be obtained.

b) An additional 1754 hours of testing with 600 volts a-c applied across both windings to ground was accumulated for a total of 1861 hours.

c) Chamber pressure at the beginning of the endurance test was 8.4×10^{-7} torr. At the end of the report period the pressure had decreased to 4.8×10^{-8} torr.

d) A twelve-hour plant-wide power outage resulted in a temperature reduction to approximately 370°F. No adverse effects have been noted.

e) Residual gas analysis scans of the test chamber atmosphere were recorded periodically.

2. Discussion

Figure IV-21 is a cutaway drawing of the thermal vacuum chamber showing the transformer and two solenoids installed in the furnace hot zone. Thermocouples and power leads were brought up through the top heat shields in the same manner as with the stator. Power leads were brazed in a controlled argon atmosphere to OFHC copper bus bar feedthroughs inside the chamber and the thermocouples were passed through hollow Kovar tube feedthroughs and brazed to the tubes outside the chamber.

The transformer design is rated at 1 kVA with 600 volts a-c on the primary winding and approximately 30 volts on the secondary winding. This 600 volt a-c single-phase design is representative of the technology for a three-phase transformer having the same phase voltage which, when coupled in a wye network with a full-wave rectifier system, would provide 1400 volts d-c.

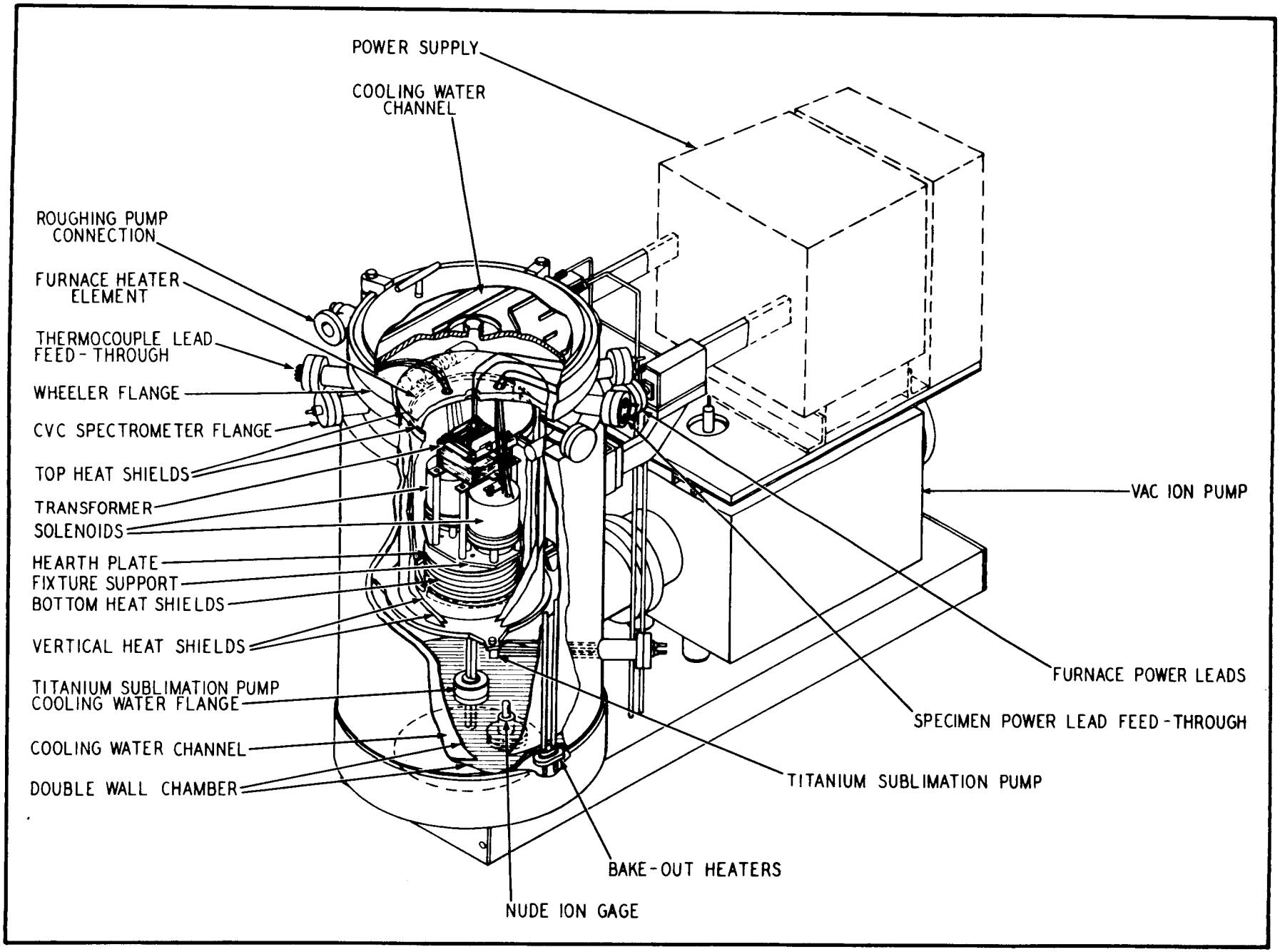

FIGURE IV-21. Cutaway View of a Vacuum Furnace Showing Installation of a Transformer and Two Solenoids

The transformer core was made from E-I style Hiperco 27 alloy laminations 0.008 inch thick with a coating of plasma-arc sprayed Linde "A" compound (Al_2O_3) on one side of each lamination (same as stator laminations). The windings were formed around a ceramic spool (99.5% Al_2O_3) which provided insulation between the windings and the center leg of the core. Alumina (99.5%) end plates and channels provided insulation between the winding ends and sides and the laminations. Non-magnetic alloy strips (Hastelloy Alloy "B") were used outside the laminations to provide lamination support. The laminations and support strips were held together by through-studs, ceramic washers and lock nuts. The primary winding was made from No. 20 AWG (0.032 dia.) nickel-clad silver wire (20% nickel cross-sectional area) coated with Anadur insulation and consisted of 174 turns in five layers. Flexible insulation (Burnil CM-2), 0.010 inch thick, was used to separate the layers. The secondary winding was a single layer 10 turn coil made from the same type wire and insulation but in No. 7 AWG (0.144 dia). Four layers of 0.010 inch thick Burnil CM-2 were installed between the outermost primary winding layer and the secondary winding. Pairs of thermocouples were installed between the primary winding and ceramic spool and between the primary and secondary windings. The stack was divided into two halves by ceramic strip spacers so that two thermocouples could be buried in ceramic tubes in the center of the core. Figure IV-22 is a photograph which shows the completed transformer, except for thermocouples, sitting on the frame which supports it and the two solenoids (Task 4) in the thermal vacuum chamber.

The fourth quarterly report shows additional details on the transformer construction, preparations for installing the transformer in the test chamber, and initiation of the test program.

a. TRANSFORMER TEST PROCEDURE

Installation of the transformer and solenoids in the thermal vacuum chamber, and bake-out of the chamber, were completed in the fourth program quarter.

Power was applied to the transformer and to the continuously activated solenoid, and adjustments were made to the solenoid input voltage to hold transformer and solenoid hot-spot temperatures near the same values. Power was then applied to the furnace element in several stages to bring the transformer and solenoid hot-spot temperatures up to 1100°F. When temperatures

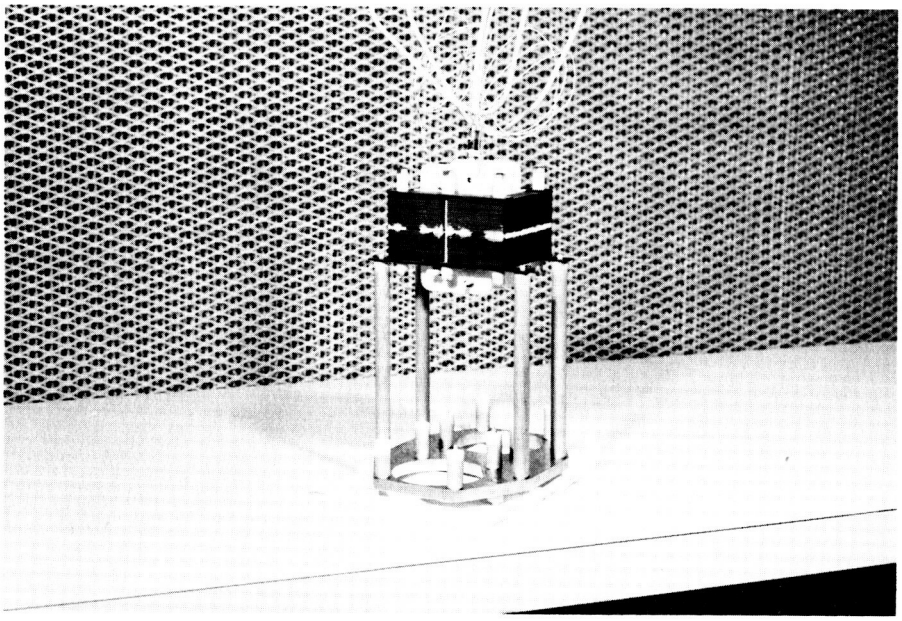

FIGURE IV-22. Transformer in Position on Furnace Mounting Frame

had reached a stable condition, electrical measurements were taken and official endurance test time was started. After approximately 107 hours of testing, the Variac supplying primary winding power and the primary circuit voltmeter were damaged by excessive current. The first analysis was that one or the other had developed a short. These two components were sitting side by side and the metal handle on the voltmeter case might have provided a path to ground through the metal case of the Variac. When power was reapplied to the transformer, however, it was found that the primary winding had developed a layer-to-layer short circuit. The Variac was supplying the transformer primary winding with 600 volts through a 1:4 step-up transformer. Source voltage was 292 volts. A short in the Variac might have applied a voltage surge high enough to break down the transformer insulation, but it is more likely that the primary winding insulation system had failed and that increased current eventually caused the Variac to overheat.

The Burnil CM-2 flexible sheet insulation is composed of synthetic-mica platelets of a complex composition of lithium magnesium silicate. Voltage breakdown as established on Program NAS 3-4162 (Westinghouse Report WAED 64.53E) was 208 volts/mil at 932°F and 400 cps. Voltage breakdown for the Anadur conductor insulation was 62 volts/mil at 1112°F and 400 cps. The expected maximum voltage gradient layer-to-layer in the primary winding was 271 volts. The Anadur thickness between two conductors is 14 mils, giving a breakdown strength of 868 volts at 1100°F. The Burnil CM-2 thickness is 10 mils between winding layers, giving a breakdown strength of 2080 volts at 932°F. This value would be lower at 1100°F but is still additive to the Anadur voltage breakdown strength. Further analysis of the mechanism of failure will have to wait until the transformer is removed from the chamber. Work has been initiated on an independent Westinghouse program to define a better flexible layer insulation. Changes in electrical test data as a result of the failure are covered in the data discussion.

Electrical performance measurements were taken and the results indicated that considerable value could be obtained from the component by unloading the transformer and providing a 600 volt a-c winding-to-ground potential to each winding. This will give continuing information on insulation resistance and conductor performance. Figures I V-23 and I V-24 are schematics of the

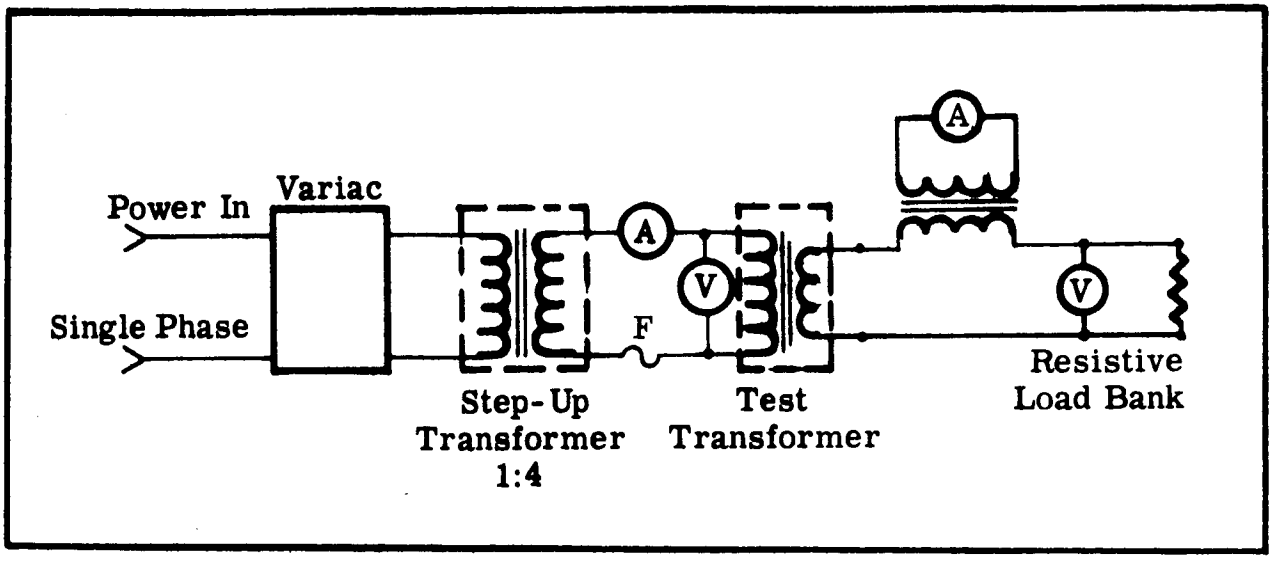

FIGURE IV-23. Electrical Test Schematic for the 1 kVA Rated Transformer

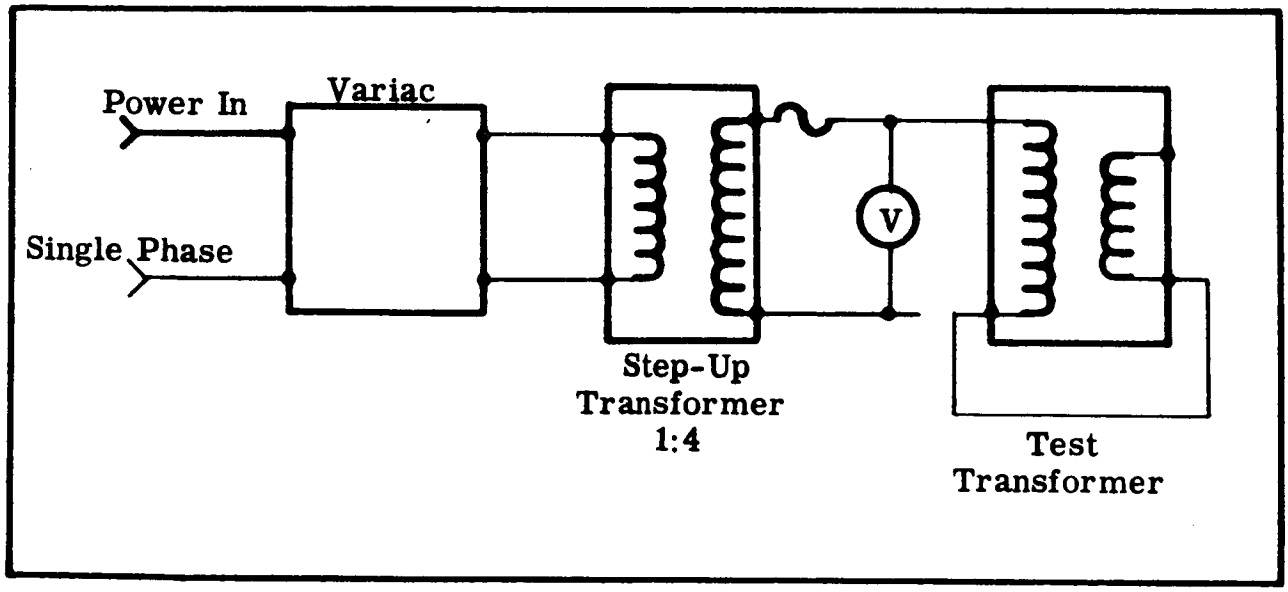

FIGURE IV-24. Transformer Electrical Test Schematic After Primary Winding Short

transformer test connections prior to and following the occurrence of the primary winding short circuit.

During the plant-wide power failure the average temperature in the transformer decreased to approximately 400°F and the vacuum was maintained. Furnace element power was applied and the sputter-ion pump was turned on as soon as plant power was restored. Chamber pressure was in the low 10^{-9} torr range. By the following morning the transformer temperature was stabilized at 1035°F.

Static electrical measurements covering conductor resistance, d-c insulation resistance, and leakage current when subjected to an a-c voltage potential were taken once each week during the program quarter. Titanium sublimation pump (TSP) bursts of two minute duration were used at intervals to determine their effect on the chamber pressure. In each case, the chamber pressure was reduced temporarily, but returned to the initial setting within a short time ($<$ 2 minutes).

b. TRANSFORMER DATA

Figure IV-25 is a plot of chamber pressure vs endurance test time. The power supply for the transformer is one phase of the generator which also supplies the stator. The curve shows the temporary pressure reductions that occurred when two minute titanium sublimation pump bursts were applied. It also shows the pressure decreases which accompanied the removal of power when primary winding and instrumentation were damaged and when the plant-wide power failure occurred. Chamber pressure was read by a Bayard-Alpert type hot cathode nude ionization gauge.

Figure IV-26 is a sketch showing the location of thermocouples in the transformer assembly. The lamination stack was split into two approximately equal halves so that the thermocouples designated No. 1 could be inserted. The No. 2 thermocouples are installed between the primary winding inside diameter and the ceramic winding spool. The No. 3 thermocouples are located between the primary and secondary windings and those designated No. 4 are installed between the secondary winding outside diameter and the ceramic plates that insulate the winding from the stack. All thermocouples are installed in ceramic tubes, and the sensing junctions are located at the mid-planes of the assembly.

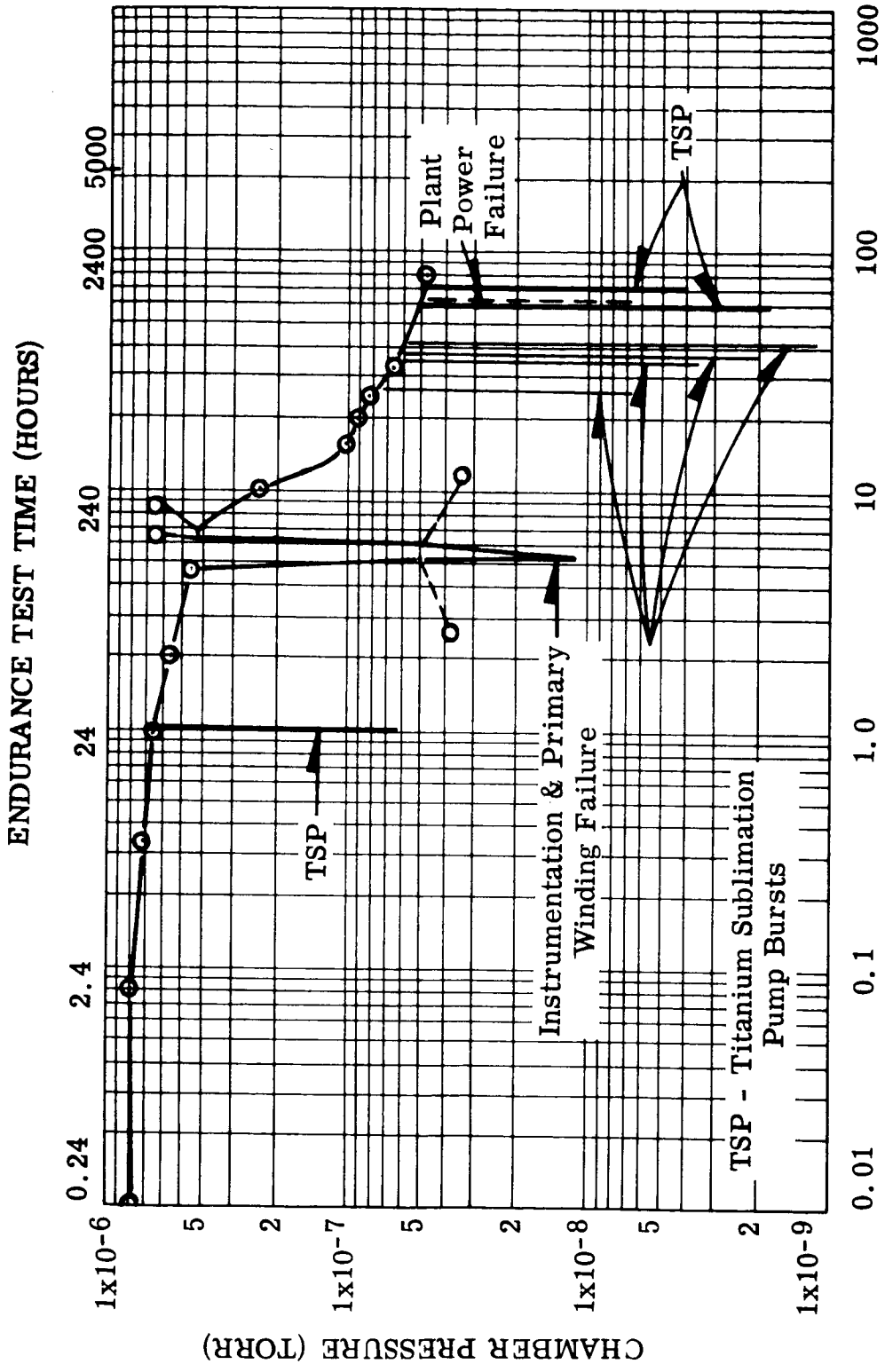

FIGURE IV-25. Transformer and Solenoid Chamber Pressure vs. Endurance Test Time

Figure IV-25. Transformer and Solenoid Chamber Pressure vs. Endurance Test Time

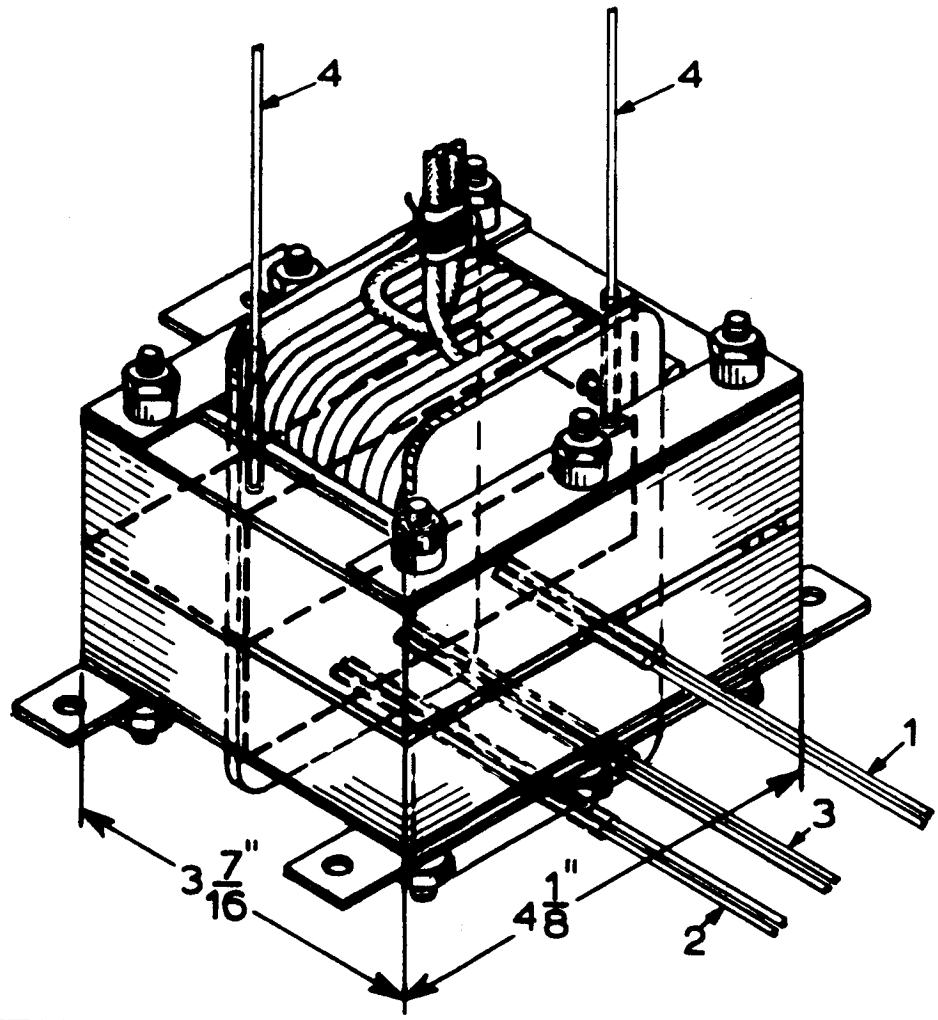

No.	Quantity Installed	Description
1	2	Mid-stack
2	2	Primary ID-Spool One lost during assy
3	2	Primary-Secondary windings
4	2	Secondary OD One lost during assy

FIGURE IV-26. Transformer Assembly Showing Thermocouple Locations and Junction Positions

Thermocouples were installed in pairs to provide a check on readings and also to guard against the loss of sensors during installation of the transformer in the test chamber. Two thermocouples were lost during the Kovar tube feedthrough brazing operation, but from different locations, so that each location to be monitored has at least one functioning thermocouple.

Table IV-18 shows representative temperature readings taken before the primary winding developed a short circuit and operating with a 1 kVA load.

TABLE IV-18. Representative Operational Transformer Temperatures After 24 Hours of Endurance Test

Thermocouple Location	Temperature (°F)
Mid-stack	1088
Mid-stack	1088
Primary Winding ID-Spool	1095
Primary-Secondary Winding	1082
Primary-Secondary Winding	1078
Secondary Winding OD	1062

Chamber pressure level at the time these readings were taken was 6.1×10^{-7} torr. Transformer temperature will be reviewed to determine if the apparent thermal conductivities for the construction can be realized. This effort will have to be carried into the next program quarter.

Figure IV-27 is a plot of the transformer primary and secondary conductor resistance as a dimensionless ratio of endurance test

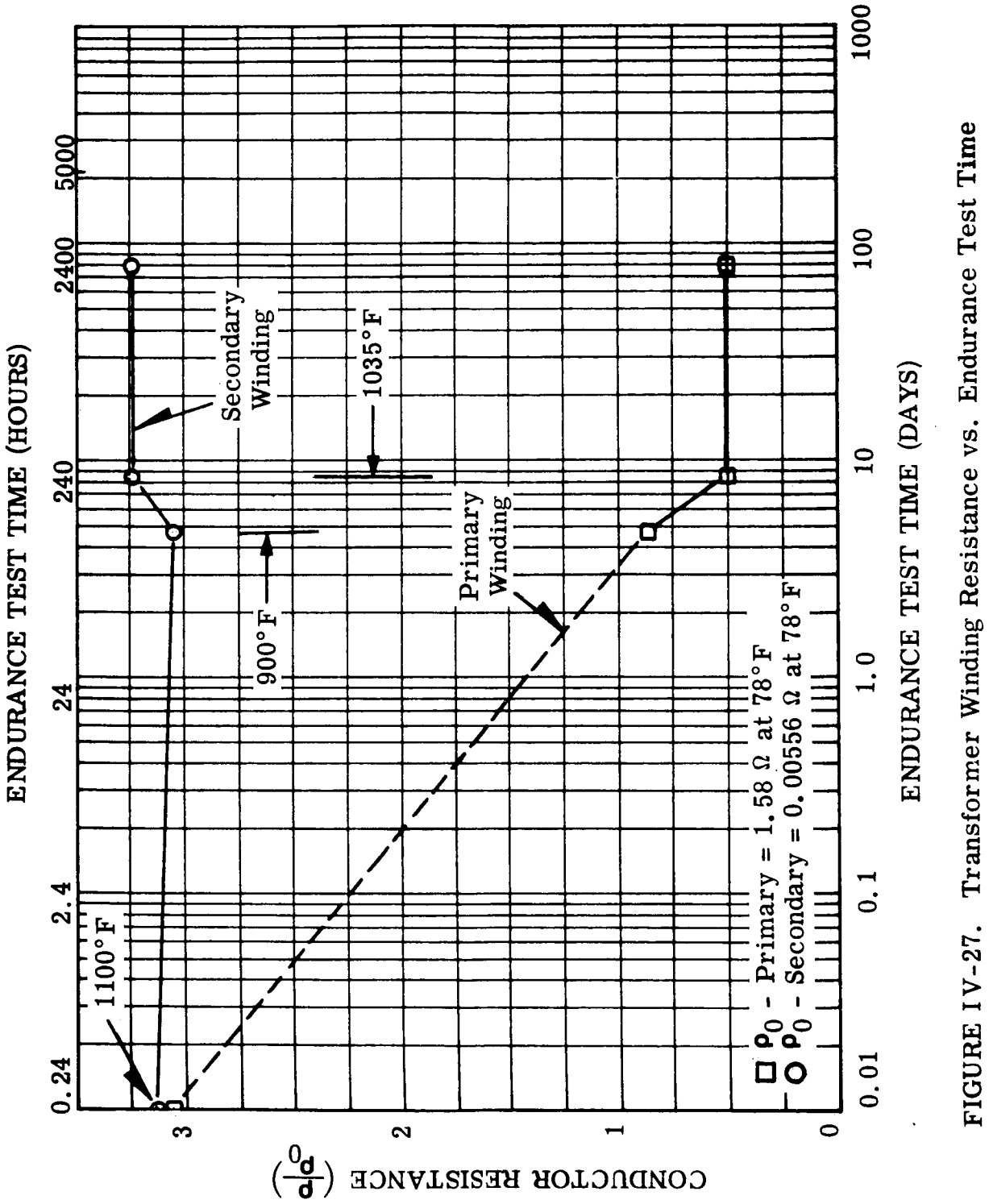

FIGURE IV-27. Transformer Winding Resistance vs. Endurance Test Time

Figure IV-27. Transformer Winding Resistance vs. Endurance Test Time

time. The secondary winding showed very little change with time. The primary resistance decreased from 3.08 at the start of the test (at 1100°F hot-spot) to 0.85 at the time the layer-to-layer short circuit was discovered. The shape of the resistance curve in the intervening time is not known. There was a further decrease in winding resistance between the 5th and 9th days, although the temperature was increased from 900°F to 1035°F. This would appear to indicate further shorting in the primary winding layers.

Residual gas analysis traces were taken in the same manner as for the stator chamber. Calibration of the sensing head was done using the same gases and test setup as for the stator chamber.

Figure IV-28 is a reproduction of a mass spectrogram taken with the furnace clean, dry and empty and at a temperature of 1100°F. Table IV-19 shows the relative magnitudes of the gases present in the chamber as indicated by the spectrogram.

TABLE IV-19. Partial Pressures of the Identified Gases Contributing to the RGA* Spectrum Shown in Figure IV-28

Gas	Mass/charge	Partial Pressure (torr)
H_2	2	0.50×10^{-8}
H_2O	18	2.80×10^{-8}
N_2+CO	28	1.30×10^{-8}
A	40	0.20×10^{-8}
CO	44	0.80×10^{-8}
"Organics"	45-150	0.40×10^{-8}

* Residual Gas Analysis

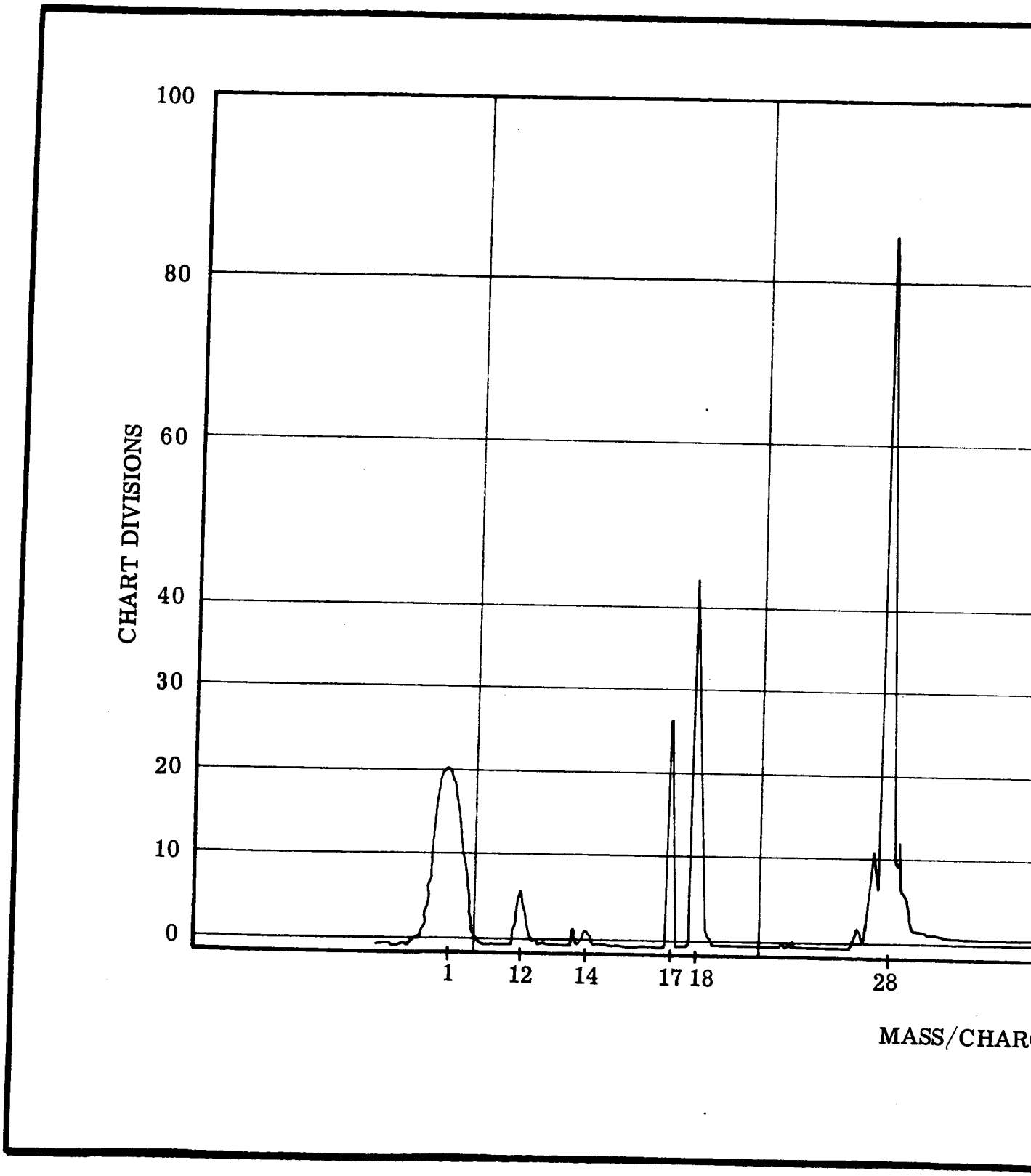

FIGURE IV-28. Replica of a Mass Spectrogram From the Transformer and Solenoid Thermal Vacuum Chamber When Clean, Dry and Empty and at 1100°F

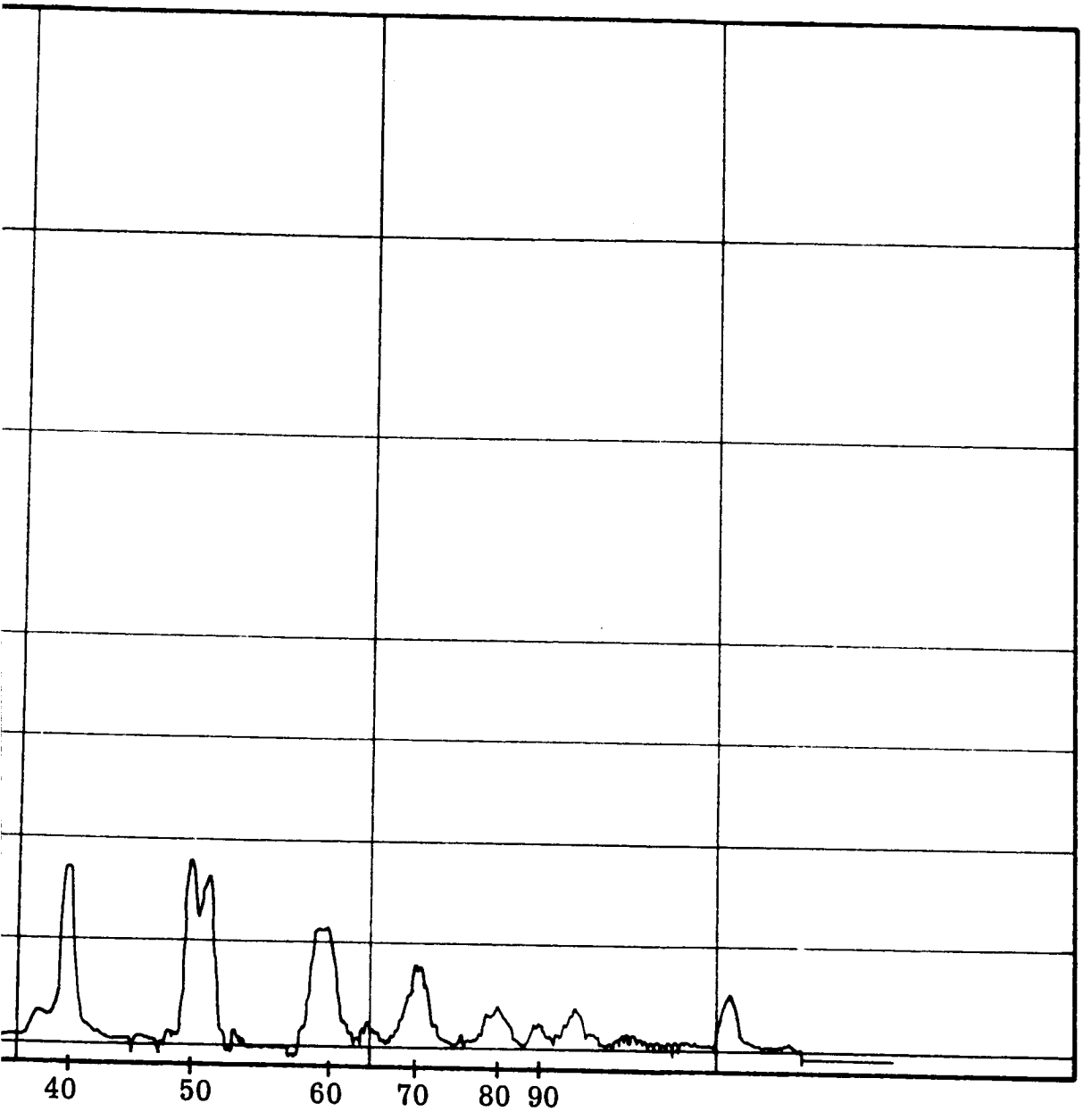

GE NUMBER

Resolution for the higher mass numbers was not sufficient to determine the components classed as "organics". The summation of the mass spectrometer partial pressures was 7.0×10^{-8} torr as compared to a total nude ion gage pressure of 1.2×10^{-9} torr. This pressure spread is similar to that noted in the stator chamber. The mass spectrometer sensing heads and ion gauge filaments are installed in the same relative locations in both chambers.

Figure IV-29 is a plot of partial and total chamber pressures vs endurance test time in days.

3. Program for the Next Quarter

a) Continue the transformer endurance test with 600 volts a-c potential across each winding to ground.

b) Begin construction of a 1400°F hot-spot transformer model.

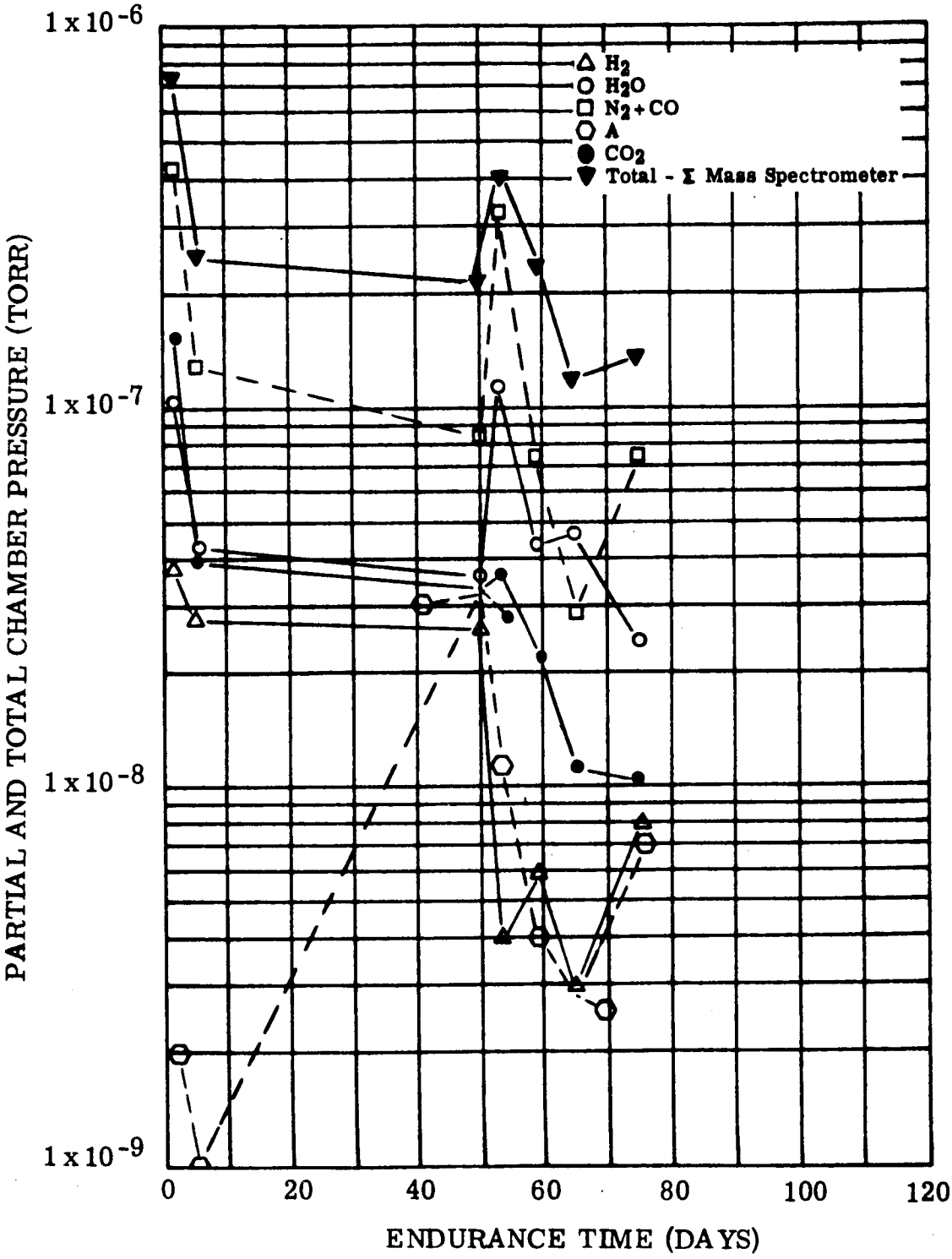

FIGURE IV-29. Time-Pressure Plot of Mass Spectrometer Residual Gas Analysis Scans in Chamber No. 2 (Transformer & Solenoids)

Figure IV-29. Time-Pressure Plot of Mass Spectrometer Residual Gas Analysis Scans

D. TASK 4 - SOLENOID

1. Summary of Technical Progress

a) A total of 1885 hours of endurance test time was accumulated with one solenoid energized continuously and the other one unenergized.

b) Chamber pressure decreased from 8.4×10^{-7} torr at the beginning of the test to 4.8×10^{-8} torr at the end of the program quarter.

c) A twelve hour plant-wide power loss resulted in a temperature reduction to approximately 400°F. No adverse effects have been noted.

2. Discussion

The transformer installation cutaway drawing, Figure IV-21, also shows how the two solenoids were fitted into the chamber. All three components were installed at the same time.

The solenoid magnetic housing, cover, and plunger are made from Hiperco 27 alloy forged material. The coil is wound on an alumina (99%) spool which provides insulation between the winding and the plunger and housing center core. Alumina end plates insulate the sides of the winding from the housing and cover. Bearing surfaces for the plunger consist of an alumina guide rod at one end of the plunger and an alumina bushing at the opposite end. The winding was formed from 1860 turns of No. 20 AWG (0.032 dia.) nickel-clad silver wire with an Anadur insulation system. This is the same wire that was used for the transformer primary winding. The solenoid is rated at 1530 ampere turns when energized with 28 volts d-c at a winding temperature of 1100°F.

Pairs of thermocouples were installed between the winding inside diameter and the ceramic spool, at the radial mid-winding point, between the winding outside diameter and the housing and on the housing outside diameter. All except the housing outside diameter thermocouples were installed in 99% alumina tubes. Figure IV-30 shows the completed solenoids, except for the installation of thermocouples.

The fourth quarterly report gives additional details on solenoid construction, preparations for installing the solenoids in the test chamber, and initiation of the test program.

a. SOLENOID TEST PROCEDURE

Installation of the solenoids and transformer in the thermal vacuum chamber and chamber bake-out were completed in the fourth program quarter.

Power was applied to the continuously activated solenoid and to the transformer. Solenoid input voltage was adjusted downward several times to hold the solenoid and transformer hot-spot temperatures near the same value. Power was then applied to the furnace element in several stages to bring the solenoid and transformer hot-spot temperatures up to approximately 1100°F. When temperatures had reached a stable condition, electrical measurements were taken and official endurance test time was started. Figure IV-31 is a schematic of the energized solenoid electrical connection.

The transformer instrumentation damage that occurred after 107 hours of testing did not affect the solenoid operations. Power was removed from the solenoid and all three specimens were maintained at a temperature of approximately 930°F by applying power at the previously existing setting to the furnace heater element. After repairs to the transformer instrumentation, the furnace element power was increased to bring the solenoid hot-spot temperature back up to 1100°F. When temperatures became stable, the logging of time was continued.

During the 12-hour plant-wide power loss the average temperature in each solenoid dropped to approximately 400°F. Within five hours after power was restored, the energized solenoid hot-spot temperature was up to 1020°F and increasing slowly. Electrical measurements taken after temperatures had stabilized did not indicate any changes in electrical performance.

Static electrical measurements covering winding resistance, d-c insulation resistance, and leakage current when subjected to an a-c voltage potential, were taken once each week. Pick-up and drop-out voltages and currents were also measured on each solenoid to verify that the plungers were free to move.

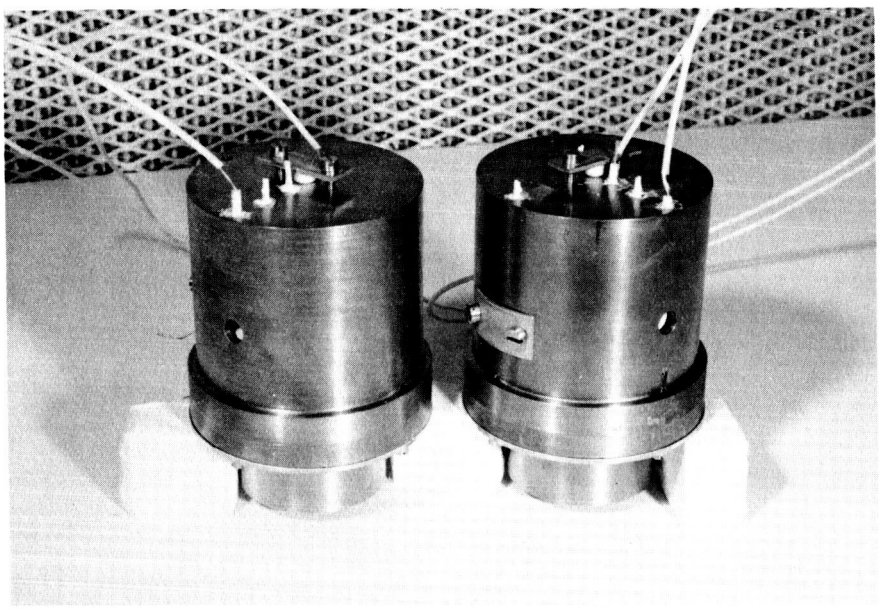

FIGURE IV-30. Solenoid Assemblies Complete Except for Thermocouples

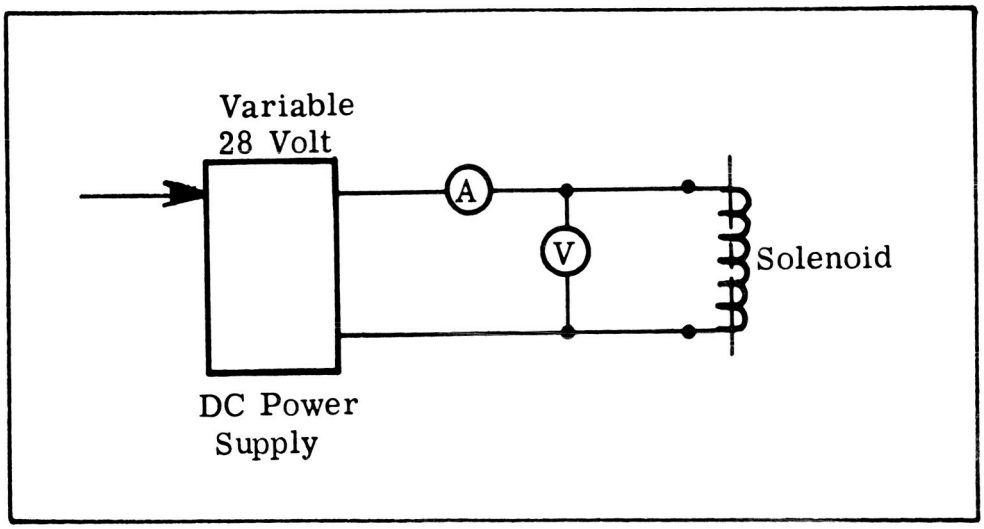

FIGURE IV-31. Solenoid Circuitry

b. SOLENOID DATA

Each solenoid accumulated 1885 endurance test hours during the report period. One solenoid was energized continuously except during the taking of electrical readings and during power outages. The other was unenergized except for periodic checks on plunger movability.

Figure IV-25 shows the chamber pressure vs test time curve which is also applicable to the solenoids. Pressure readings were taken with a Bayard-Alpert type nude ion gauge which is mounted in the bottom of the test chamber.

Figure IV-32 is a cutaway drawing of a solenoid showing how the thermocouples are installed. The sensing tips were inserted so as to be located halfway between the top and bottom of the coil as it is shown in the picture. As in the other test models, thermocouples were installed in pairs at each location in both solenoids.

Table IV-20 shows representative temperature readings from the energized solenoid.

TABLE IV-20. Energized Solenoid Representative Temperatures After 1477 Hours of Endurance Test

Thermocouple Location	Temperature (°F)
Winding ID - Spool	1095
Winding ID - Spool	1088
Mid-Winding	1120
Mid-Winding	1115
Winding OD - Housing	1065
Winding OD - Housing	1075
Housing OD	1085
Housing OD	1075

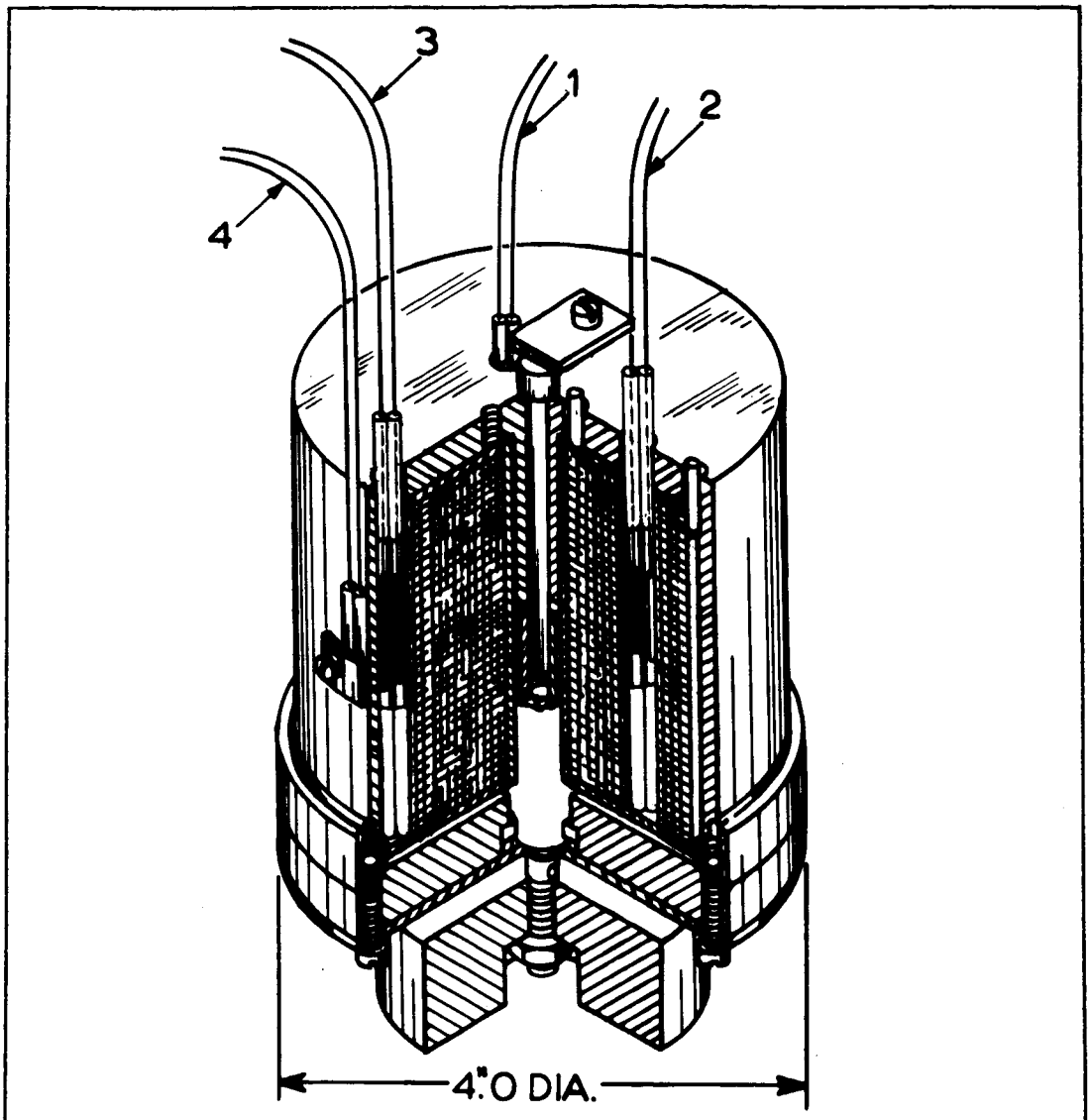

No.	Quantity Installed	Description
1	2	Winding ID
2	2	Mid-winding
3	2	Winding OD-Housing
4	2	Housing OD One lost on S/N2 during assy

FIGURE IV-32. Solenoid Assembly Showing Thermocouple Locations and Junction Positions

Chamber pressure at the time these readings were taken was 8.4×10^{-8} torr. All thermocouples in the unenergized solenoid read 1060°F.

Solenoid temperature data are being reviewed for the possibility of determining apparent thermal conductivities for the construction.

Minimum pick-up and holding voltage and current readings were taken periodically. Table IV-21 compares the ambient temperature bench test values with those obtained at a stable test temperature (1100°F hot-spot) in the thermal vacuum chamber.

TABLE IV-21. Minimum Pick-up and Holding Electrical Measurements for Solenoid Weight and Plunger

	Bench Test		Chamber Test*	
	S/N 1	S/N 2	S/N 1	S/N 2
Minimum Pick-up Voltage, d-c	4.9	3.9(a)	15.0	12.0(a)
Minimum Pick-up Current, AMPS	0.41	0.34	0.39	0.34
Minimum Holding Voltage, d-c	0.9	0.85	1.9	2.1
Minimum Holding Current, AMPS	0.065	0.056	0.05	0.06

(a) The increase in voltage required to maintain a constant current is caused by the increase in wire resistance as conductor temperature increases.

* After 1788 Endurance Test Hours

Steady state test voltage and current readings were 13.0 volts and 0.35 amperes.

Figure IV-33 is a plot of winding conductor resistance as a dimensionless ratio vs time for both solenoids. The curves are very close together because while S/N 1 is at a hot-spot temperature of 1100°F, most of the winding is at a lower temperature.

Section IV-C concerns the discussion on residual gas analysis of the transformer test which is also applicable to the solenoid.

3. Program for the Next Quarter

a) Continue the solenoid endurance test with a hot-spot temperature of 1100°F.

b) Begin construction of a 1400°F solenoid model.

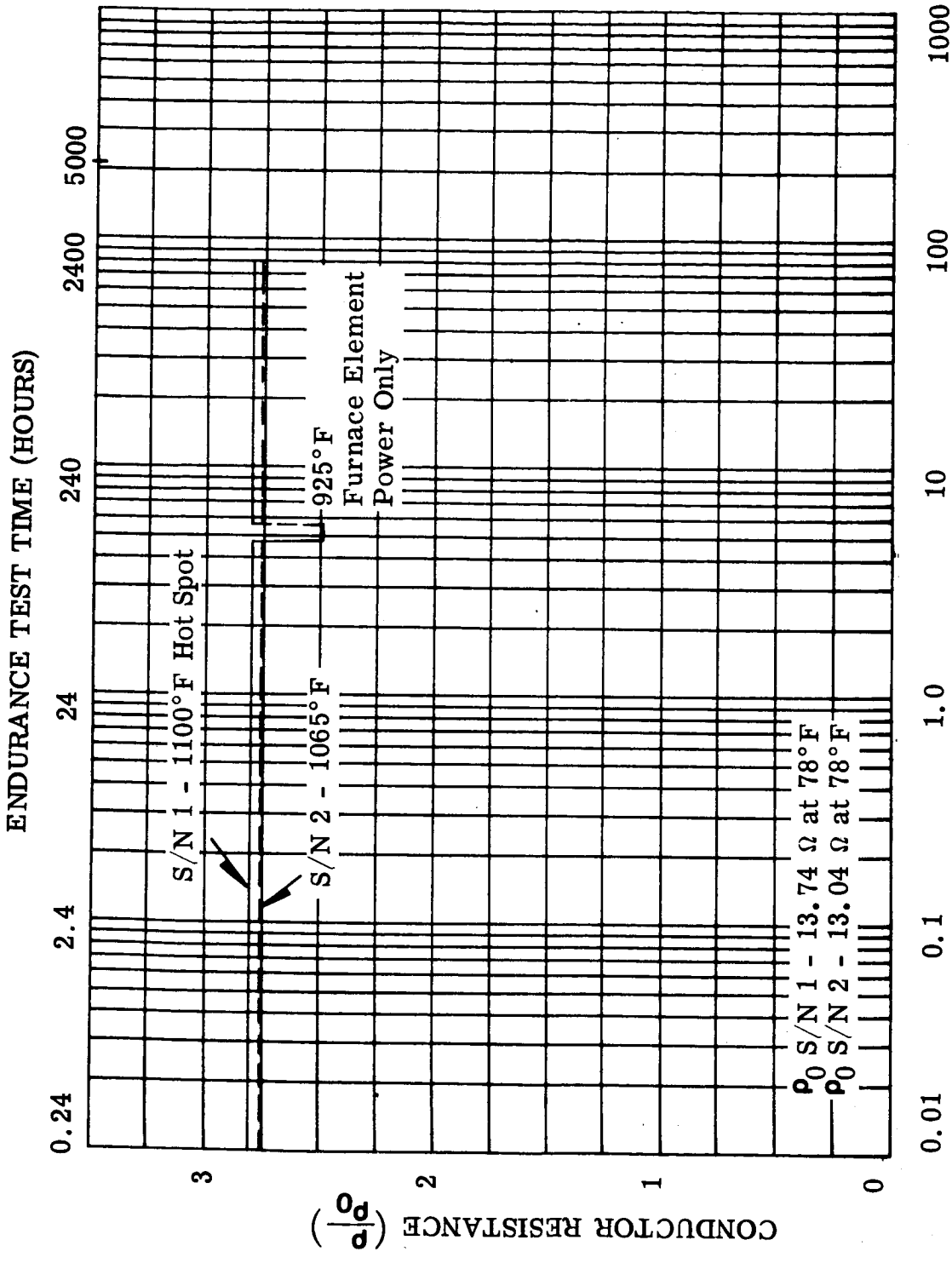

FIGURE IV-33. Solenoid Conductor Resistance vs. Endurance Test Time

Figure IV-33. Solenoid Conductor Resistance vs. Endurance Test Time

SECTION V

REFERENCES

Reports published on this program are:

Kueser et al, P.E., "Development and Evaluation of Magnetic and Electrical Materials Capable of Operating in the 800° to 1600°F Temperature Range", First Quarterly Report, NASA-CR-54354, March 1965.

Kueser et al, P.E., "Development and Evaluation of Magnetic and Electrical Materials Capable of Operating in the 800° to 1600°F Temperature Range", Second Quarterly Report, NASA-CR-54355, June 1965.

Kueser et al, P.E., "Development and Evaluation of Magnetic and Electrical Materials Capable of Operating in the 800° to 1600°F Temperature Range", Third Quarterly Report, NASA-CR-54356, September 1965.

Kueser et al, P.E., "Development and Evaluation of Magnetic and Electrical Materials Capable of Operating in the 800° to 1600°F Temperature Range", Fourth Quarterly Report, NASA-CR-54357, December 1965.

References cited in this report follow and are grouped by Program and Task.

Section II

Program I - Magnetic Materials For High-Temperature Operation

References for Task 1 - Optimized Precipitation Hardened Magnetic Materials for High-Temperature Application

1. Glenn, R. C., R. D. Schoone, "Electropolishing Unit for Rapid Thinning of Metallic Specimens for Transmission Electron Microscopy", Rev. Sci. Instr., v. 35, p. 1223, 1965.

2. Mitchel, W. J., "Increase in Strength and Hardness in a Complex Nickel Base Alloy", Z. Metallkunde, v. 55, p. 613, 1964.

3. Reisdorf, B. G., "Identification of Precipitates in 18, 20, and 25% Nickel Maraging Steels", Trans. ASM, v. 56, p. 783, 1963.

4. Baker, A. J., P. R. Swann, "The Hardening Mechanism in Maraging Steels", Trans. ASM, v. 57, p. 1008, 1964.

5. Speich, G. R., "Age-Hardening of Fe-20-Pct, Ni, Martensites", Trans. AIME, v. 227, p. 1426, 1963.

6. Miller, G. P., W. J. Mitchel, J. Iron Steel Inst., v. 203, p. 899, 1965.

7. Chen, C. W., "Temperature Dependence of Magnetic Properties of Silicon-Iron", J. Appl. Phys., v. 29, p. 1337, 1958

8. Speich, G. R., "Cellular Precipitation in an Austenitic Fe-30Ni-6Ti Alloy", Trans. AIME, v. 227, p. 754, 1963.

9. Detert, K., H. Pohl, "Investigation of Precipitation Processes in Co-Ni Alloys with Al and Ti additions", Z. Metallkunde, v. 57, 1966.

10. Kueser, P. E., et al, "Magnetic Materials Topical Report", Westinghouse Electric Corporation Report WAED 64.52E, Contract NAS3-4162, p. 72, September 1964.

References for Task 3 - Dispersion-Strengthened Magnetic Materials for Application in the 1200-1600°F Range.

11. Stadelmaier, H. H., "Ternary Borides with the Cubic Chromium Carbide Structure", Met. Soc. AIME, Nuclear Metallurgy, v. 10, p. 159-166, 1964.

12. Stadelmaier, H. H. and G. Hofer, "Cobalt-Rich Corner of the Cobalt-Tantalum-Boron System and the $Co_{21}Ta_2B_6$ Phase", Metall., v. 18, no. 5, p. 460-462, May 1964.

13. Stadelmaier, H. H. and J. D. Schobel, "Die Kobaltecke im Dreistoff-system Kobalt-Niob-Bor", Metall., Jan. 1966.

14. Anon., "TD Nickel, Dispersion-Strengthened Nickel", Du Pont Metal Products, Production Information A-41076, E. I. du Pont de Nemours & Co., Wilmington, Del.

Section III

Program II - High-Temperature Capacitor Feasibility References

1. Anon., Englehard Industries, Inc., Baker Platinum Division

2. Dummer, G. W. A. and H. M. Nordenberg, "Fixed and Variable Capacitors," McGraw Hill Book Co., 1960.

Section IV

Program III - Bore Seal Development and Combined Material

References for Task 1 - Bore Seal Development

1. Steel, E. L., H. R. Lukens, Jr., V. P. Guinn, Development of Neutron Activation Analysis Procedure for the Determination of Oxygen in Potassium, Final Report NASA CR-54100 on Contract NAS 3-2537, 1964.

2. Kueser, P. E. et al, "Bore Seal Technology", Westinghouse Electric Corporation, NASA-CR-54093, Contract NAS 3-4162, 1964.

3. Reed, L., et al, "Metallurgical Research and Development for Ceramic Electron Devices", Final Report on Contract DA-36-039SC90903, 1965.

4. McKisson, R., Atomics International, Canoga Park, Calif., Private Communication.

5. Aszbanyl, P. M., et al, "Investigation of the System Niobium-Beryllium", Doklady Akademii Nauk SSSR, v. 150, 1964.

6. Goldschmidt, H. J. "Phase Constitutions of Transition Metal Systems", J. of Less-Common Metals, v. 2, p. 138, 1960.

7. Young, R. General Electric Co., Cincinnati, Ohio, Private Communication.